NUMERICAL STUDIES OF THREE DIMENSIONAL TURBULENCE WITH POLYMER ADDITIVES AND TWO DIMENSIONAL TURBULENCE IN THIN FILMS
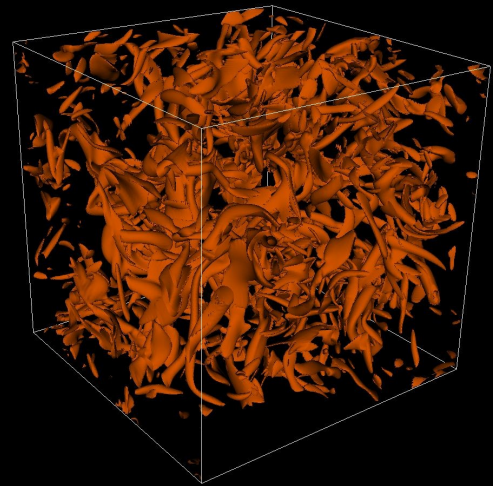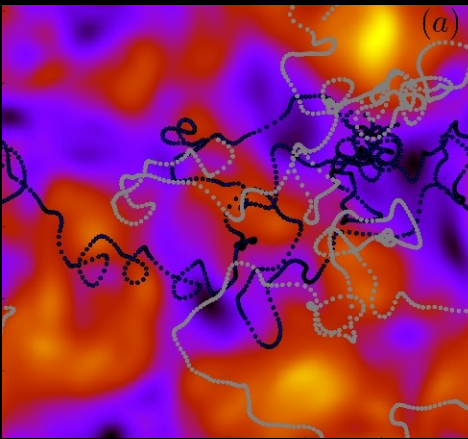
A thesis submitted for the degree of
Doctor of Philosophy
in the Faculty of Science

Prasad Perlekar

Department of Physics
Indian Institute of Science
Bangalore – 560012
India

July 2009

Declaration

The work reported in this thesis is original and was carried out by me during my tenure as a PhD student at the Department of Physics, Indian Institute of Science, Bangalore. This thesis has not formed the basis for the award of any degree, diploma, associateship, membership or similar title of any university or institution.

(Prasad Perlekar)
July, 2009

Department of Physics,
Indian Institute of Science,
Bangalore - 560012,
India

Acknowledgements

The work in this PhD. thesis was done under the guidance of Prof. Rahul Pandit. I am greatly indebted to him for his constant support and encouragement. Along with Rahul, I was very fortunate to have worked with Dhrubaditya Mitra (Dhruba). Most of the ideas that constitute this thesis came out of discussions with Rahul and Dhruba. The discussions, physics or otherwise, with Dhruba will always be remembered. I am also grateful to Dhruba and his family for their hospitality during my visit to England.

I have learnt a lot from the discussions and courses taught by Prof. R. Pandit, Prof. S. Ramaswamy, Prof. C. DasGupta, and Prof. H.R. Krishnamurthy. I also thank Prof. R. Govindarajan and Prof. B. Mukhopadhyay for the discussions.

I am grateful to Prof. J. Bec, Prof. U. Frisch, Prof. D. Vincenzi, and Prof. F. Toschi for their hospitality and discussions during my visits to the Netherlands and France. I am greatly indebted to Dr. Sadhna Relia (DST, India) for her help during my visit to Trieste, Italy.

I am also grateful to Prof. A. Gangal (University of Pune) and Prof. D.G. Kanhere (University of Pune) for their guidance. The course by Prof. D.G. Kanhere on Computational Physics is one of the best courses that I have ever taken.

Special thanks are due to Vijay Kumar Krishnamurthy. I have learnt a lot of physics by having discussions and debates with him. I am also grateful to Samriddhi Sankar Ray and Sagar Chakraborty for many discussions on fluid dynamics.

The time spent with my cousin Sughosh and friends Nishit, Sumonto, Satish, Sourav, Ankit, and Forum at different coffee houses in Bangalore will never be forgotten. The presence of my University of Pune friends Bishwanath, Sunita, and Arvind helped me a lot during my first two years in IISc. All the past and present members of

Contents

FRONTISPIECE

Left panel: Pseudocolor plot of the streamfunction filed and representative particle tracks from a direct-numerical simulation (with 1024^2 grid points) of the two-dimensional, incompressible, Navier-Stokes equations with Ekman friction term.

Right panel: Isosurfaces of intense vorticity from a direct-numerical simulation (with 512^3 grid points) of the three-dimensional, incompressible, Navier-Stokes equations.

Preface

. . . there might be hope to 'break the deadlock' by extensive, but well-planned, computational efforts. It must be admitted that the problems in question are too vast to be solved by a direct computational attack, that is, by an outright calculation of a representative family of special cases. There are, however, strong indications that one could name certain strategic points in this complex, where relevant information must be obtained by direct calculations. If this is properly done, and the operation is then repeated on the basis of broader information then becoming available, etc., there is a reasonable chance of effecting real penetrations in this complex of problems and gradually developing a useful, intuitive relationship to it.

– von Neumann

Fluid turbulence is ubiquitous in nature. In most physical situations the effect of the turbulence is to enhance the dissipation. It is therefore, not surprising that a lot of effort has gone into devising new ways to reduce turbulent dissipation. One way by which a dramatic reduction in the turbulent dissipation is observed is by adding small quantities of polymers to the turbulent fluid. The addition of polymers changes the fluid properties from Newtonian to Viscoelastic. Understanding the properties of such a viscoelastic turbulent fluid is a very challenging problem. In Chapters 2 and 3 of this thesis we conduct direct numerical simulations of forced and decaying turbulence in polymer solutions to unravel the effects of polymer additives on fluid turbulence.

Fluid turbulence in two dimensions is dramatically different from its three-dimensional counterpart. One of the major challenges is to

understand the statistical properties of fluid turbulence in two dimensions. Experimentally, two-dimensional turbulence is realised in thin layers of fluid. In Chapters 4, 5, and 6 we study different aspects of turbulence in two-dimensions.

Below we present an overview of different Chapters in this thesis.

CHAPTER 1 We present a brief introduction to the statistical properties of turbulence and the underlying Navier-Stokes equations. Topological properties of the three-dimensional fluid flows, the experimental results, and the earlier numerical studies of polymer solutions are discussed. We then discuss the dramatic change in the statistical properties of turbulent flows on going from three to two dimensions. We introduce the modified Navier-Stokes equations to model thin film of fluids. We discuss earlier experimental studies on thin-films of fluids and introduce the idea of persistence in two-dimensional turbulence.

CHAPTER 2 In this Chapter we investigate the presence of drag-reduct-ion type phenomenon in homogeneous, isotropic turbulence. We carry out a high-resolution direct numerical simulation (DNS) of *decaying*, homogeneous, isotropic turbulence with polymer additives. Our study reveals clear manifestations of drag-reduction-type phenomena: On the addition of polymers to the turbulent fluid we obtain a reduction in the energy dissipation rate, a significant modification of the fluid energy spectrum especially in the deep-dissipation range, a suppression of small-scale intermittency, and a decrease in small-scale vorticity filaments. We show that the analogue of drag reduction in wall-bounded flows is dissipation reduction in homogeneous, isotropic turbulence.

CHAPTER 3 In this Chapter we carry forward our study to the case of statistically steady, forced, homogeneous, isotropic turbulence. Our study reveals clear manifestations of dissipation-reduction phenom-

ena: On the addition of polymers to the turbulent fluid, we obtain a reduction in the energy dissipation rate, a significant modification of the fluid energy spectrum especially in the deep-dissipation range, a suppression of small-scale intermittency, and a decrease in small-scale vorticity filaments.

CHAPTER 4 In this Chapter we present the results of a detailed direct numerical simulation (DNS) of the two-dimensional Navier-Stokes equation with the incompressibility constraint and air-drag-induced Ekman friction. We investigate the combined effects of walls and such friction on turbulence in forced thin films. We concentrate on the forward-cascade regime and study the velocity and vorticity structure functions. To understand the topological properties of two dimensional turbulence we study the probability distribution function of the Weiss parameter Λ, which distinguishes between regions with centers and saddles, i.e., vortical regions and strain-dominated regions.

CHAPTER 5 In this Chapter we perform a DNS of the two-dimensional Navier-Stokes equations. The forcing is chosen such that, at low Reynolds (Re) numbers, the steady state of the soap film is a square lattice of vortices. We find that, as we increase Re, this lattice undergoes a series of nonequilibrium phase transitions, first to a crystal with a different reciprocal lattice and then to a sequence of crystals that oscillate in time. Initially the temporal oscillations are periodic; this periodic behavior becomes more and more complicated with increasing Re until the soap film enters a spatially disordered nonequilibrium statistical steady that is turbulent. We study this sequence of transitions by using fluid-dynamics measures, such as the Okubo-Weiss parameter, ideas from nonlinear dynamics, e.g., Poincaré maps, and theoretical methods that have been developed to study the melting of an equilibrium crystal or the freezing of a liquid, for instance, the behavior of the autocorrelation function $G(r)$ in crystalline and liquid phases.

CHAPTER 6 In this Chapter we introduce the *persistence* phenomenon in two-dimensional turbulence. We show, in particular, that the Okubo-Weiss parameter provides us with a natural way for studying persistence. We distinguish two types of persistence: (A) In the Eulerian framework we consider a point (x, y) and determine how long the flow at this point remains vortical (extenstional) if the flow at this point became vortical (extensional) at some earlier time; (B) in the Lagrangian framework we consider how long a Lagrangian particle resides in a vortical (extensional) region if this particle entered that vortical (extensional) region at an earlier time. Our study shows that, in the Eulerian framework, the persistence PDFs show exponential tails. In the Lagrangian framework the persistence PDF for the residence time of the particle in vortical regions shows a power-law whereas the persistence PDF for the residence time of the particle in straining regions shows an exponential tail. We also study the autocorrelation functions of Λ and the velocity derivatives.

References:

[1] 'Manifestations of Drag Reduction by Polymer Additives in Decaying, Homogeneous, Isotropic Turbulence', Prasad Perlekar, Dhrubaditya Mitra, and Rahul Pandit, *Phys. Rev. Lett.*, **97**, 264501 (2006).

[2] 'Statistically steady turbulence in thin films: direct numerical simulations with Ekman friction', Prasad Perlekar and Rahul Pandit, *New. J. Phys.*, **11**, 073003 (2009).

[3] 'Statistical properties of turbulence: An overview', Rahul Pandit, Prasad Perlekar, Samriddhi Sankar Ray, *Pramana*, **73**, 179 (2009).

[4] 'Turbulence-induced melting of a nonequilibrium vortex lattice in a forced soap film', Prasad Perlekar and Rahul Pandit, to be submitted.

[5] 'Lifetime of topological structures in two-dimensional turbulence', Prasad Perlekar, Samriddhi Sankar Ray, Dhrubaditya Mitra, and Rahul Pandit, to be submitted.

Chapter 1

Introduction

The advection of smoke emanating from a volcanic eruption, the flow of water through rapids, in a jet, or behind a racing car are all examples of turbulence in fluids. The above examples cover a wide range of phenomena and, therefore, obvious questions come to mind: "What is turbulence? How can we describe it?"

Turbulence is a multifaceted phenomenon. It is generally associated with a flow or fluid motion in which a large range of length and time scale are excited. In most physical situations turbulence is generated by high-speed flows of fluids over walls, past obstacles, through orifices, or grids. The flow changes from laminar to turbulent flow via a series of transitions that yield ever more complicated flow patterns. The exact natures of these transitions depend sensitively on the boundary conditions and external forcing mechanisms. Indeed, a lot of effort in fluid dynamics has put in to studying the route to turbulence in different flows such as the Taylor-Couette, plane-Poiseuille, and planar-Couette flows (see, e.g., Refs. [1, 2, 3, 4] and the books by Drazin [5], Chandrasekhar [6], and Lin [7]).

Once turbulence sets in, the fluid motion can be divided into a mean flow, generated by the boundary conditions or external forcing, and the turbulent fluctuations. The statistical properties of these fluctuations do not depend strongly on the boundary conditions or on the exact na-

ture of the external forcing if we concentrate at small spatial scales (much smaller than the length scale at which the fluid is forced) and if we look far away from boundaries. These turbulent fluctuations are, then, homogeneous and isotropic to a very good approximation. If the turbulent flow velocity u is close to or larger than the velocity of sound c in the fluid (i.e., the Mach number $M \equiv u/c_s \geq 0.3$) then compressibility effects are important; otherwise the flow can be considered to be incompressible. We will study incompressible flows.

In this thesis we conduct a detailed study of homogeneous, isotropic, turbulence in different settings. In Chapters 2 and 3, we study the effects of polymer additives on, respectively, three-dimensional decaying and forced homogeneous, isotropic turbulence. In Chapters 4, 5, and 6 we study the statistical and topological properties of flows in two dimensional thin layers of fluids, both in Eulerian and Lagrangian frameworks.

The remaining part of this Chapter is arranged as follows. In Section 1.1 we present an introduction to the three dimensional turbulence. In Subsection 1.1.1 we introduce the equations and conservations laws of fluid dynamics for the systems we study. We then provide, in Subsection 1.1.2, a short introduction to the statistical and topological properties of three-dimensional turbulence. In Subsection 1.1.3 we discuss the non-dimensionalization of the fluid dynamics equations. This is followed by an introduction to the three dimensional, homogeneous, isotropic turbulence (Subsection 1.1.4 and 1.1.5). In Subsections 1.1.6 we give an overview of the studies on the effects of polymer additives on turbulent fluids (details are discussed again in Chapters 2 and 3). We then discuss the dramatic change in the statistical properties of turbulent flows on going from three to two dimensions (Section 1.2). In Subsections 1.2.3-1.2.6 we discuss the turbulence generated in thin-film of fluids (details are discussed again in Chapters 4-5). Finally, in Subsection 1.2.7 we introduce the idea of

persistence in two-dimensional flows (details are again discussed in Chapter 6).

For more detailed accounts of homogeneous, isotropic turbulence we refer the reader to the books by Frisch [8], Lesieur [9], and the classic texts by Monin and Yaglom [10] and Batchelor [11].

1.1 Three-dimensional Turbulence

In this Section we give an overview of the equations and the corresponding conservation laws for the fluid systems we consider.

1.1.1 Equations and Conservation Laws

The equations that govern the motion of neutral, uniform-density, incompressible fluids were first given by Navier and Stokes and are known, therefore, as the Navier-Stokes (NS) equations [Eq. (1.1)]; they are:

$$\frac{D\mathbf{u}}{Dt} = \nu\nabla^2\mathbf{u} - \nabla p + \mathbf{f}; \tag{1.1}$$

$$\nabla \cdot \mathbf{u} = 0; \tag{1.2}$$

we use units in which the density $\rho = 1$, $\frac{D}{Dt} \equiv \frac{\partial}{\partial t} + \mathbf{u} \cdot \nabla$ is the material derivative, the Eulerian velocity at point $\mathbf{x}$ and time t is $\mathbf{u}$, the kinematic viscosity is ν, the pressure is p, and $\mathbf{f}$ denotes an external body force (per unit volume) imposed on the fluid. The incompressibility condition [Eq. (1.2)] can be used to eliminate the pressure from Eq. (1.1). The form of the Navier-Stokes equations written in terms of the velocity $\mathbf{u}$ and the pressure p is known as *primitive variable formulation*.

The Navier-Stokes equations [Eqs. (1.1) and (1.2)] are density and momentum conservation laws. By taking the dot product of $\mathbf{u}$ with

Eq. (1.1) and integrating over the volume we get the energy-balance relation

$$\frac{dE}{dt} = -\epsilon_\nu + \epsilon_{inj}, \tag{1.3}$$

where the energy $E \equiv \frac{1}{2V}\int_V |\mathbf{u}|^2$, the energy-dissipation rate $\epsilon_\nu \equiv 2\nu\Omega$, the enstrophy $\Omega \equiv \frac{1}{2V}\int_V |\boldsymbol{\omega}|^2$, and the energy-injection rate $\epsilon_{inj} \equiv \frac{1}{2V}\int_V \mathbf{f}\cdot\mathbf{u}$. In a statistically steady state, $\langle dE/dt\rangle = 0$ and $\epsilon_{inj} = \epsilon_\nu$. For the inviscid, unforced case, $\nu = 0$ and $\mathbf{f} = 0$, so Eq. (1.3) yields energy conservation.

Equations (1.1) and (1.2) can be reformulated in terms of the vorticity and the velocity (this is known as the *vorticity-velocity formulation*) by taking the *curl* of Eq. (1.2):

$$\frac{\partial\boldsymbol{\omega}}{\partial t} = \nabla\times(\mathbf{u}\times\boldsymbol{\omega}) + \nu\nabla^2\boldsymbol{\omega}; \tag{1.4}$$

here the vorticity $\boldsymbol{\omega} = \nabla\times\mathbf{u}$ and the velocity at every time step is obtained by solving the Poisson equation

$$\nabla^2\mathbf{u} = -\nabla\times\boldsymbol{\omega}, \tag{1.5}$$

obtained by taking the *curl* of the vorticity and by using the incompressibility condition [Eq. (1.2)]. The pressure is eliminated naturally here. This formulation becomes especially useful in two dimensions since the vorticity becomes a pseudo-scalar in this case. Specifically, in two dimensions, the NS equation can be written in terms of the vorticity ω and the streamfunction ψ:

$$\frac{\partial\boldsymbol{\omega}}{\partial t} = \nabla\times(\mathbf{u}\times\boldsymbol{\omega}) + \nu\nabla^2\boldsymbol{\omega}; \tag{1.6}$$

$$\nabla^2\psi = \boldsymbol{\omega}; \tag{1.7}$$

$$\mathbf{u} \equiv \left(-\frac{\partial\psi}{\partial y}, \frac{\partial\psi}{\partial x}\right). \tag{1.8}$$

By taking the dot product of $\mathbf{u}$ with Eq. (1.4) and integrating over the volume we get the helicity-balance relation

$$\frac{dH}{dt} = -2\nu H_{\boldsymbol{\omega}}, \tag{1.9}$$

where $H \equiv \frac{1}{2V} \int_V \mathbf{u} \cdot \boldsymbol{\omega}$, $H_{\boldsymbol{\omega}} \equiv \frac{1}{2V} \int_V |\boldsymbol{\omega} \cdot \nabla \times \boldsymbol{\omega}|^2$. In the inviscid limit the above equation yields helicity conservation.

The Navier-Stokes equation Eq. (1.1) can be modified to study the motion of dyes or pollutants advected by the fluid. The motion of *passive scalars* is modelled by an advection-diffusion equation

$$\frac{D\theta}{Dt} = \nu \nabla^2 \theta + \mathbf{f}_\theta, \tag{1.10}$$

where θ is the passive-scalar field, the advecting velocity field satisfies the Navier-Stokes equation Eq. (1.1), and $\mathbf{f}_\theta$ is an external force which mimics the source of the passive scalar. The field θ is passive because it does not act on or modify $\mathbf{u}$.

The addition of small amounts of polymers or surfactants to the fluid leads to dramatic changes in the flow properties of the fluid. Solutions of fluids with polymers or surfactants provide us with examples of non-Newtonian fluid. The NS equations coupled to the finitely extensible nonlinear elastic Peterlin (FENE-P) model for the polymers is used to study the dynamics of dilute polymer solutions. This model is defined by the following equations:

$$\partial_t \mathbf{u} + (\mathbf{u}.\nabla)\mathbf{u} = \nu \nabla^2 \mathbf{u} + \frac{\mu}{\tau_P} \nabla.[f(r_P)\mathcal{C}] - \nabla p; \tag{1.11}$$

$$\partial_t \mathcal{C} + \mathbf{u}.\nabla \mathcal{C} = \mathcal{C}.(\nabla \mathbf{u}) + (\nabla \mathbf{u})^T.\mathcal{C} - \frac{f(r_P)\mathcal{C} - \mathcal{I}}{\tau_P}. \tag{1.12}$$

Here ν is the kinematic viscosity of the fluid, μ the viscosity parameter for the solute (FENE-P), τ_P the polymer relaxation time, ρ the solvent density, p the pressure, $(\nabla \mathbf{u})^T$ the transpose of $(\nabla \mathbf{u})$, $\mathcal{C}_{\alpha\beta} \equiv \langle R_\alpha R_\beta \rangle$ the elements of the polymer-conformation tensor $\mathcal{C}$ (angular brackets indicate an average over polymer configurations), $\mathcal{I}$ the identity tensor with elements $\delta_{\alpha\beta}$, $f(r_P) \equiv (L^2 - 3)/(L^2 - r_P^2)$ the FENE-P potential that ensures finite extensibility, $r_P \equiv \sqrt{Tr(\mathcal{C})}$ and L the length and the maximum possible extension, respectively, of the polymers, and $c \equiv \mu/(\nu + \mu)$ a dimensionless measure of the polymer concentration [12].

The Navier-Stokes equations, when coupled with Maxwell's equations of electrodynamics, can be used to study the motion of a charged fluid, such as a plasma; given some approximations [13] this yields the equations of magnetohydrodynamics (MHD). In the regime where the external magnetic field is very large, the field acts on the fluid as an external driving force. In thin layers of, say, soap films, a magnetic field is coupled with external currents to drive the fluid to a turbulent state. The motion of fluid in thin layers of, e.g., soap-film is governed by the two-dimensional incompressible, Navier-Stokes equation with an additional, air-drag induced Ekman friction term (provided corrections arising from compressibility and Marangoni effects can be ignored [14, 15]). The two-dimensional Navier-Stokes equations, which we will used to model flow in thin films, can be written in $\omega - \psi$ formulation as follows:

$$\frac{D\omega}{Dt} = \nu\nabla^2\omega - \alpha\omega + f_\omega; \tag{1.13}$$

$$\nabla^2\psi = \omega; \tag{1.14}$$

$$\mathbf{u} \equiv \left(-\frac{\partial\psi}{\partial y}, \frac{\partial\psi}{\partial x}\right). \tag{1.15}$$

Here $f_\omega = IB\sin(\theta)$ is the Lorentz force which drives the soap-film, I is the current passing through the soap-film, B is the external magnetic field, θ is the angle formed between I and B, and α the strength of the Ekman friction.

This concludes our brief overview of the equations that we have used in the studies we present in the following Chapters.

1.1.2 Topological Properties of Three-dimensional Flows

In this Section we present a discussion of topological properties of three-dimensional flows with a special emphasis on the topological properties in a homogeneous, isotropic state.

In Fig. 1.1 we show an iso-$|\boldsymbol{\omega}|$ plot for the high-Re_λ numerical simulations of Mitsuo, *et al.* [16] for fluid turbulence.

The isosurfaces consist of tube-like and some sheet-like regions. To answer the question about how these structures are distributed in a turbulent flow we need to understand the topological properties of a three-dimensional flow.

Consider the motion of a particle inside a turbulent fluid. It visits regions of vorticity and regions that are strain dominated. The motion of a particle in an inviscid fluid is governed by

$$\dot{\mathbf{x}} = A\mathbf{x}, \tag{1.16}$$

where $A = \nabla\mathbf{u}$ is the velocity-gradient tensor. If λ_1, λ_2, and λ_3 are the eigenvalues of A, then A satisfies

$$A\psi = \lambda\psi \tag{1.17}$$

and the eigenvalues $\lambda \equiv (\lambda_1, \lambda_2, \lambda_3)$ can be determined by solving the characteristic equation

$$\det(A - \lambda\mathcal{I}) = 0, \tag{1.18}$$

where $\mathcal{I}$ is the identity tensor. By expanding the above equation we get

$$\lambda^3 + P\lambda^2 + Q\lambda + R = 0, \tag{1.19}$$

where

$$\begin{aligned}
P &= \text{Tr}(A), \\
Q &= \frac{1}{2}(P^2 - \text{Tr}(A^2)), \text{and} \\
R &= \frac{1}{3}(-P^3 + 3PQ - \text{Tr}(A^3)).
\end{aligned}$$

For incompressible flows, $P \equiv \text{Tr}(A) \equiv \lambda_1 + \lambda_2 + \lambda_3 = 0$. Therefore, for three-dimensional, incompressible flows we have two invariants,
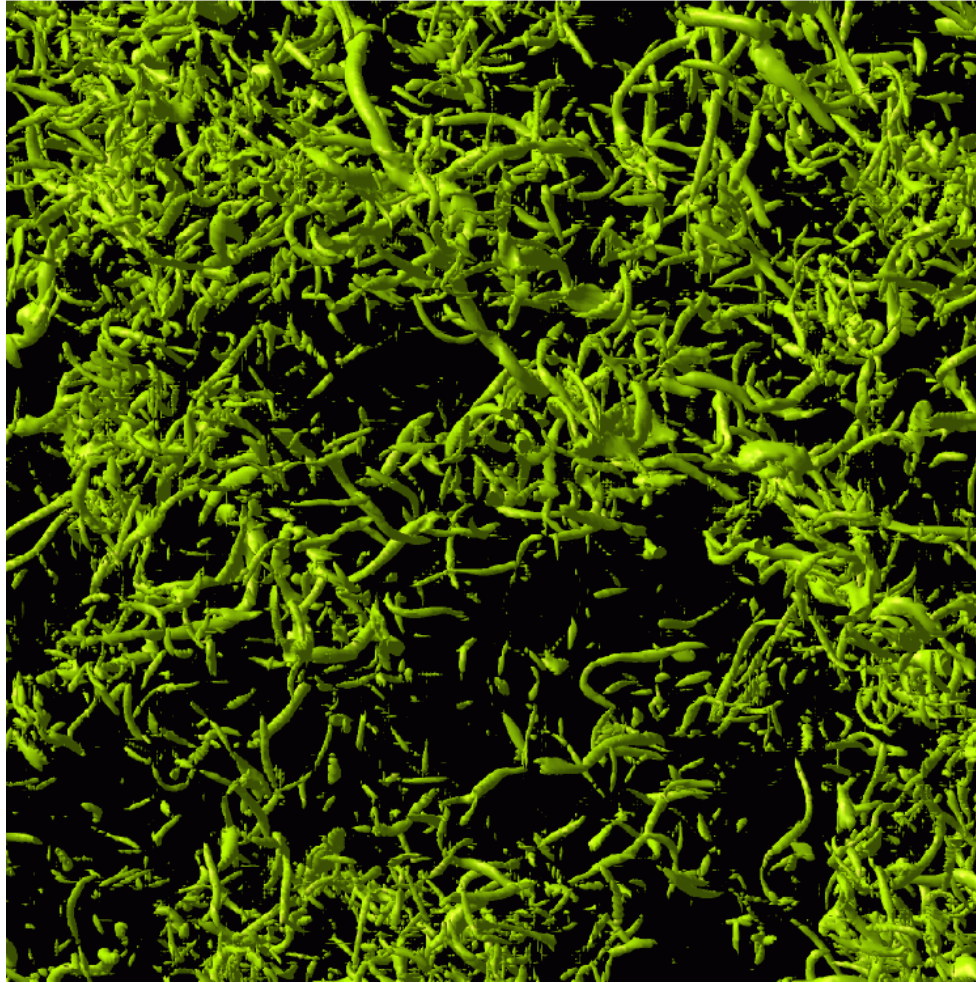
Figure 1.1: Iso-ω surfaces showing regions where $\mid \omega \mid > \overline{\omega} + 4\sigma$; ω is the vorticity, and $\overline{\omega}$ and σ are its mean value and the standard deviation, respectively. The size of the display domain is $748^2 \times 1496\eta$ in the vertical and the horizontal directions; $\eta = 0.00105$ is the Kolmogorov dissipation length scale and $Re_\lambda = 732$ is the Taylor-microscale Reynolds number. The simulations are done with 2048^3 collocation points. The figure is taken from Ref. [16].

namely, $Q = -\text{Tr}(A^2)/2$ and $R = -\text{Tr}(A^3)/3$. There are three possibilities for the roots of the characteristic equation: (a) all roots can be real and distinct; (b) all roots can be real with two of them equal to each other; and (c) one of the roots can be real and the other two are complex and conjugates of each other. The incompressibility constraint rules out the possibility of having all roots real and equal. Topological properties of a flow can now be classified in the QR plane as shown schematically in Fig. 1.2.

Data for the velocity field from a direct numerical simulation of the three-dimensional Navier-Stokes equations can be used to determine the joint probability distribution function (PDF) $P(Q, R)$; this shows a characteristic tear-drop shape that is shown in Fig. 1.3.

1.1.3 Non-dimensional Parameters

For the case of pressure-driven flows (e.g., the Poiseuille flow) or for flows in which the forcing is provided by the boundaries (e.g., shear flows) the natural non-dimensional parameter is the Reynolds number. On rescaling length by a typical length scale L, velocity by a typical velocity U, and for $\mathbf{f} = 0$ Eq. (1.1) reduces to

$$\frac{D\mathbf{u}}{Dt} = \frac{\nabla^2 \mathbf{u}}{Re} - \nabla p,$$

where $Re \equiv UL/\nu$ is the Reynolds number of the fluid. If we fix the geometry, then this equation depends only on a single parameter Re. As we increase Re, the fluid undergoes a series of transitions from a laminar state to one that is, finally, turbulent. Note that, if we keep the geometry and shape of our domain fixed, then all the properties of the flow are governed by a single parameter, namely, the Reynolds number Re. This is the famous similarity principle of fluid dynamics.

In the presence of an external force acting on the fluid, the natural normalization is obtained by rescaling length by a typical length scale L, velocity by L/ν, and force by $||f||_2/L^{d/2}$, where $||f||_2 \equiv [\int_V f]^{1/2}$, V
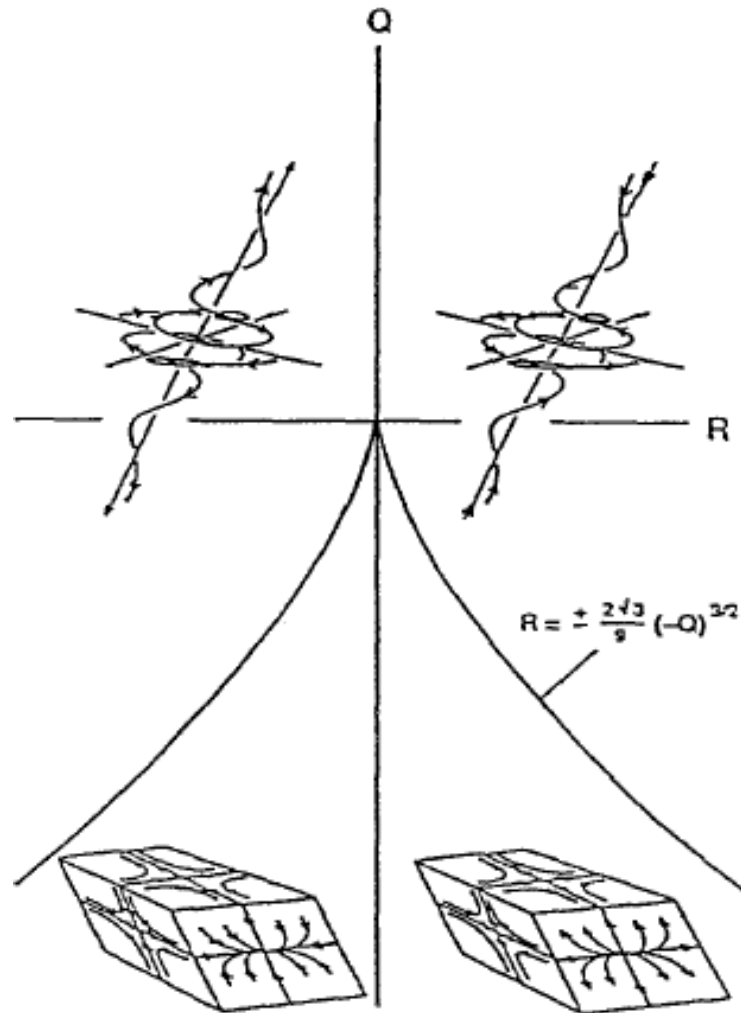
Figure 1.2: Three-dimensional flow topologies indicated schematically in the QR plane. The topologies are classified as (reading counter clockwise from the top-right corner) unstable focus/contracting, stable focus/stretching, stable node/saddle/saddle, and unstable node/saddle/saddle. This sketch is taken from Ref. [17].
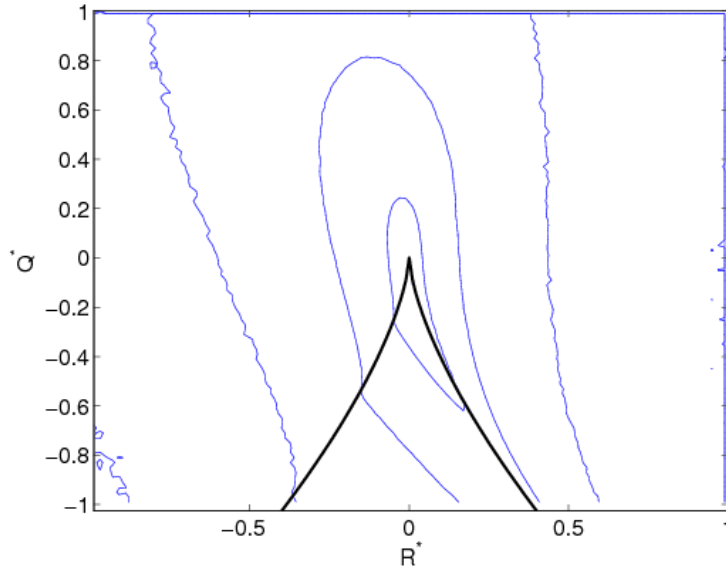
Figure 1.3: A representative joint PDF $P(Q^*, R^*)$ of $R^* = R/\langle S_{ij}S_{ij}\rangle^{3/2}$ and $Q^* = Q/\langle S_{ij}S_{ij}\rangle$ calculated from our DNS of the three-dimensional Navier-Stokes equation. The black curve represents the zero-discriminant (or Vieillefosse) line $27R^2/4 + Q^3 = 0$; here $Re_\lambda \equiv 122$. The contour levels are logarithmically spaced.

is the volume, and d is the dimension. With the above normalization Eq. (1.1) reduces to

$$\frac{D\mathbf{u}}{Dt} = \nabla^2\mathbf{u} - \nabla p + \mathcal{G},$$

where $\mathcal{G} \equiv \frac{L^{3-d/2}}{\nu^2||f||_2}\mathbf{f}$ is the Grashof number. For a given geometrical shape and a given form of the forcing, $\mathcal{G}$ is the only control parameter.

1.1.4   Three-dimensional Homogeneous Isotropic Turbulence

To explain homogeneous, isotropic turbulence we follow the example of flow past a cylinder given in Chapter-1 of Ref. [8].

   Consider the flow past a cylinder at low Reynolds numbers (Fig. 1.4). The inlet velocity is $\mathbf{u} = (V, 0, 0)$, L is the diameter of the cylinder, and ν is the viscosity of the fluid. The control parameter for the flow is the Reynolds number $Re \equiv VL/\nu$.
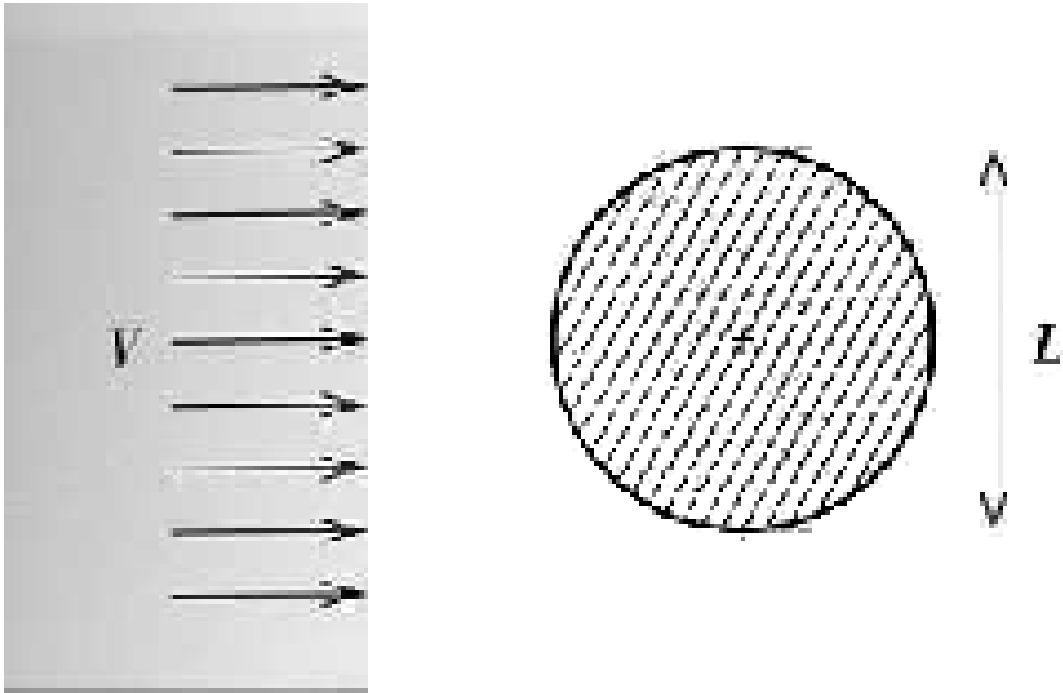
Figure 1.4: A sketch of flow past a cylinder. The $x - y$ axis are in plane. The flow is along the $x-$direction and the $z-$axis is pointing out of the page. The sketch is taken from the book of Frisch [8].

At low $Re = 0.16$ the flow has up-down(y-reversal), time-translation, and space translation (parallel to the z-axis of the cylinder) symmetries (Fig. 1.5).

At large values of the Reynolds number, say $Re = 140$, a Kármán vortex street is formed behind the cylinder (Fig. 1.5) and the continuous time symmetry is broken.

Now consider a situation where the flow is generated not by one but a large number of cylinders arranged in a manner so as to form a grid. The flow behind every cylinder, at sufficiently large Re, interacts with that behind the neighbouring cylinder and becomes turbulent. Figure 1.7 shows such turbulent flow behind a grid.

We now quote the following paragraphs describing homogeneous, isotropic, turbulence from the book of Frisch:
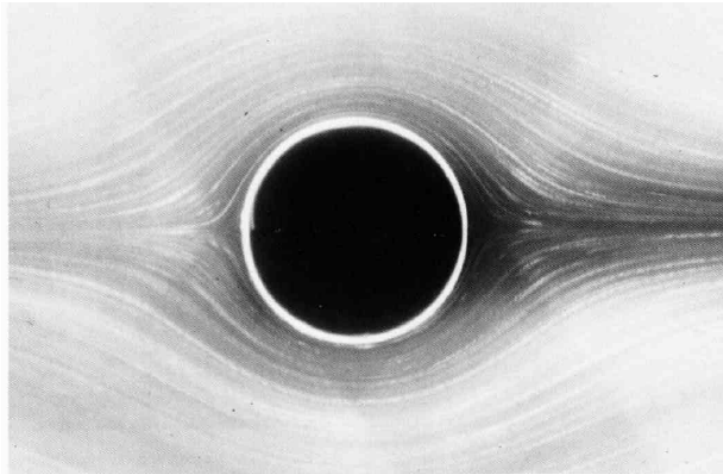
Figure 1.5: Flow past a cylinder at $Re = 0.16$. The photograph is taken from the book by Frisch [8] and is the same as Fig. 6 on page-11 of the book by Van Dyke [18].

Figure 1.6: Flow past a cylinder at $Re = 0.16$. The photograph is taken from the book by Frisch [8] and is the same as Fig. 94 on page-56 of the book by Van Dyke [18].

"Far enough behind the grid (say, $10 - 20$ meshes) the flow displays a form of spatial disorder known since Lord Kelvin (1887) as *homogeneous, isotropic, turbulence* because its overall aspect seems not to change under translations and rotations. This, of course, can only be a statistical statement.
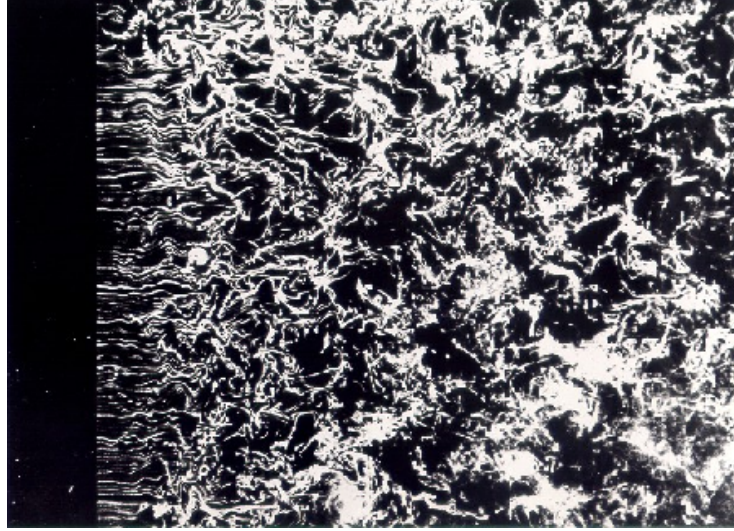
Figure 1.7: Homogeneous turbulence behind a grid. The figure is downloaded from Prof. Nagib's web page http://fdrc.iit.edu/research/nagibResearch.php.

At very high Reynolds number, there appears a tendency to *restore* the symmetries in a statistical sense far from the boundaries."

By statistical symmetries we mean that the symmetries are restored in the averages of measured quantities. Consider two points separated by a distance ℓ. Then the velocity difference between these two points is

$$\delta\mathbf{u}(\mathbf{r}, \ell) \equiv (\mathbf{u}(\mathbf{r} + \ell) - \mathbf{u}(\mathbf{r})). \tag{1.20}$$

The flow is considered to be homogeneous in velocity increments if $\langle \delta\mathbf{u}(\mathbf{r} + \rho, \ell) \rangle \equiv \langle \delta\mathbf{u}(\mathbf{r}, \ell) \rangle$, for all increments ℓ and all displacements ρ that are small compared to the integral scales (at which energy is pumped into the system). Similarly isotropy means that the statistical properties of velocity increments are invariant under simultaneous rotations of ℓ and $\delta\mathbf{u}$.

We present now the following two hypotheses about homogeneous, isotropic turbulence given by Frisch, *op. cit.*:

H1 In the limit of infinite Reynolds numbers, all the possible symmetries of the Navier-Stokes equation, usually broken by the mecha-

nism of producing the turbulent flow, are restored in a statistical sense at small scales and away from the boundaries.

H2 Under the same assumptions as H1, the turbulent flow is self-similar at small scales. There exists a unique scaling exponent $h \in \mathbb{R}$

$$\langle \delta \mathbf{u}(\mathbf{r}, \lambda \ell) \rangle = \lambda^h \langle \delta \mathbf{u}(\mathbf{r}, \ell) \rangle, \forall \lambda \in \mathbb{R}_+ \tag{1.21}$$

1.1.5 Structure Functions and the Energy Spectrum

The two quantities which are studied exhaustively and for which some analytical or phenomenological results are known are the order-p structure functions

$$S_p(\ell) \equiv < [(\mathbf{u}(\mathbf{x} + \boldsymbol{\ell}) - \mathbf{u}(\mathbf{x})).(\boldsymbol{\ell}/\ell)]^p >, \tag{1.22}$$

and the energy spectrum

$$E(k) \equiv \int_{\Omega_s} 4\pi k^2 |\mathbf{u_k}|^2 \tag{1.23}$$

where Ω_s is the solid angle (for specificity we give $E(k)$ for the three-dimensional case). The energy spectrum is related to the velocity-velocity autocorrelation by a Fourier transform.

The following cascade picture of turbulence, due to Richardson, has played an important part in the development of the phenomenology of turbulence. Consider eddies of various sizes. The largest eddies of size ℓ_0 correspond to the forcing scale. According to the cascade picture the energy flows through successive generation of eddies, each of size $\ell_n = r\ell_{n-1}$, till it is dissipated at and beyond the *Kolmogorov dissipation scale*. Here the subscript n indicates the generation of an eddy, with 0 denoting the first mother eddy and $0 < r < 1$. It is also assumed that these eddies are space filling as shown in the schematic diagram of Fig. 1.8. The energy is injected at the *forcing scales*. In
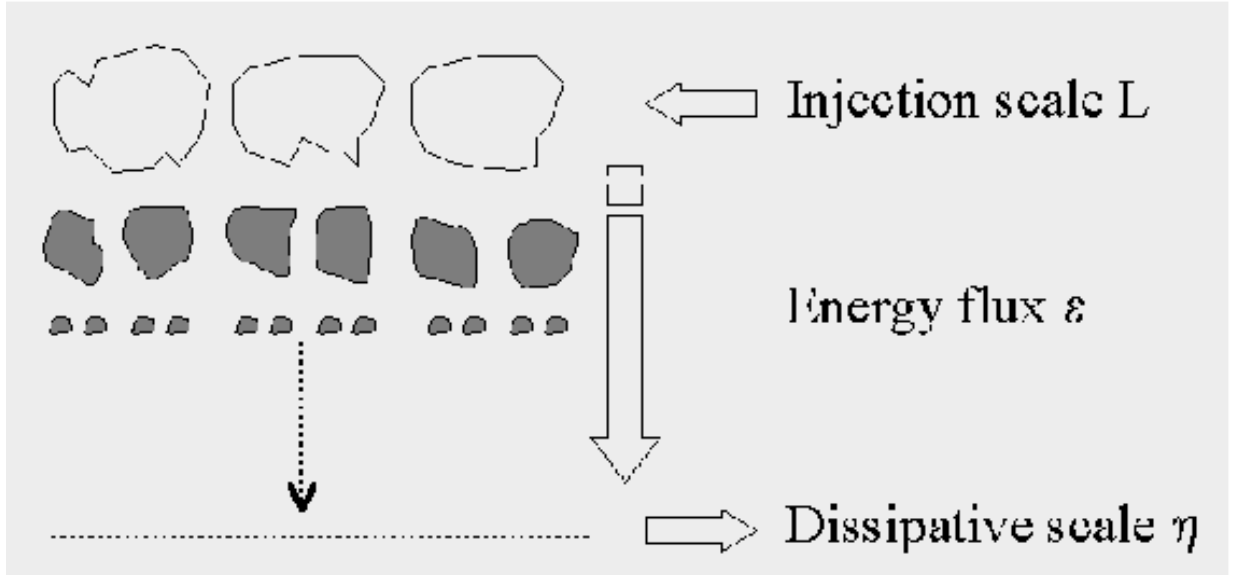
Figure 1.8: A schematic diagram of the Richardson cascade that plays an important role in Kolmogorov's phenomenology of turbulence.

the *inertial range* a constant flux is maintained till, finally, the energy reaches the scales where it is dissipated because of viscous losses.

Kolmogorov made a further assumption that, in the limit of infinite Reynolds number, all small-scale properties are uniquely and universally determined by the scale ℓ and the energy dissipation rate ϵ. The dimension of $S_p(\ell)$ is $[L]^p[T]^{-p}$. Therefore, by using Kolmogorov's assumption above we get,

$$S_p^{K41}(\ell) \sim \epsilon^{p/3}\ell^{p/3}, \tag{1.24}$$

where the superscript $K41$ stands for Kolomogorov's phenomenological theory [19, 8] of 1941. At large, but not infinite, Reynolds numbers, the above scaling form (and its multiscaling generalisations that are described below) holds for separations ℓ in the *inertial range* $l_d << \ell << L$, where l_d is the dissipation scale (see below) and L the length at which energy is injected into the system. In particular, the second-order structure function scales as

$$S_2^{K41}(r) \sim \epsilon^{2/3}\ell^{2/3}, \tag{1.25}$$

whence we get

$$E^{K41}(k) \sim k^{-5/3}. \tag{1.26}$$

We now define the dissipation length scale l_d, at which the dissipation becomes significant, the Taylor microscale λ, and the integral scale l_0, which corresponds to the sizes of large eddies.

$$l_d \simeq (\nu^3/\epsilon)^{1/4}, \tag{1.27}$$

$$\lambda \simeq \sqrt{\frac{\sum_k E(k)}{\sum_k k^2 E(k)}}, \text{ and} \tag{1.28}$$

$$l_0 \simeq \frac{\sum_k k^{-1} E(k)}{\sum_k E(k)} \tag{1.29}$$

From these length scales we can define the Taylor-microscale Reynolds number $Re_\lambda = u_{rms}\lambda/\nu$ and the integral scale Reynolds number $Re_0 = u_{rms}l_0/\nu$.

Furthermore, by using the Kármán-Howarth-Monin relation for the energy flux [8], Kolmogorov derived the exact relation for the third-order structure function in homogeneous, isotropic, turbulence, namely,

$$S_3(\ell) = -\frac{4}{5}\epsilon\ell. \tag{1.30}$$

This is also called the fourth-fifths law.

In Figure 1.9 we give representative results for the second-order structure function and the energy spectrum; these show good agreement K41 predictions.

Deviations from the predictions of K41 became apparent when experiments studied high-order structure functions $(p > 3)$ as shown, e.g., in Fig. 1.10; this figure shows that the exponent ζ_p, which characterises the inertial-range scaling behaviour of $S_p(r)$, deviates significantly from $\zeta_p^{K41} = p/3$. This deviation of ζ_p from the simple, scaling K41 prediction $p/3$ is referred to as multiscaling. It can be rationalised in terms of the multifractal model for turbulence. For a detailed dis-
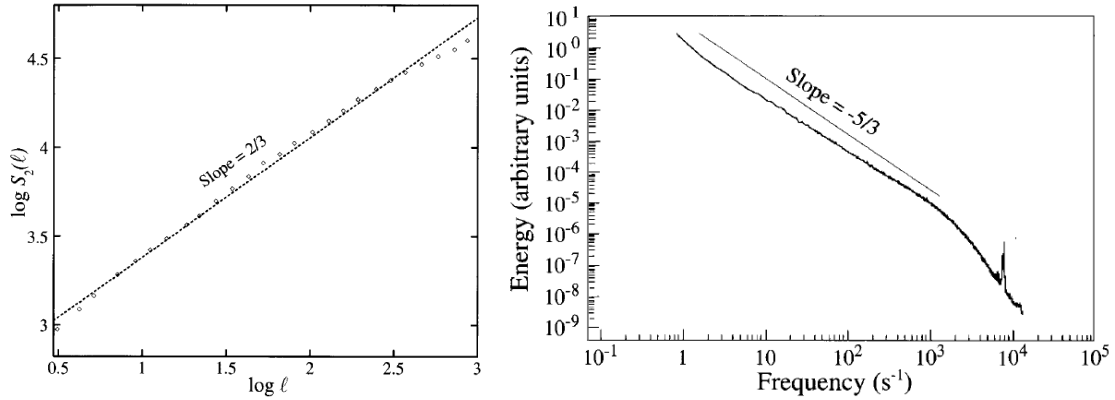
Figure 1.9: Plots of the second-order structure function and the energy spectrum in the frequency domain for data from the S1 wind-tunnel at ONERA (see Ref. [8] for details).
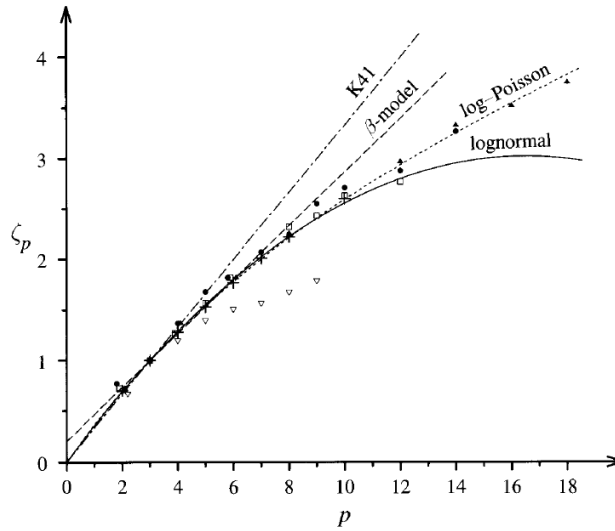
Figure 1.10: Plots of the exponent ζ_p, which characterises the inertial-range scaling behaviour of $S_p(r)$, showing significant deviations from $\zeta_p^{K41} = p/3$. This plot is the same as Fig. 8.8 in the book by Frisch, *op. cit.*, to which we refer the reader for details.

cussion of multifractality we refer the reader to Ref. [8]; we will touch on it only briefly in some of the studies presented in this thesis.

1.1.6 Effects of Polymer Additives on Three-dimensional Turbulence

The dramatic reduction of drag by the addition of small concentrations of polymers to a turbulent fluid continues to engage the attention of engineers and physicists. Drag reduction was discovered by Toms in 1949. He found that, by the addition of small amounts of polymers, one can sustain a given flow rate in a pipe with a pressure gradient that is less than that required in the absence of polymers. Significant advances have been made in understanding this drag reduction both experimentally [20, 21, 22] and theoretically [23, 24, 25, 26] in channel flows or the Kolmogorov flow [27]. In this Section we present an overview of earlier experimental and numerical studies that have investigated the effects of polymer additives on turbulence. We then summarize the results of our simulations and contrast them with these earlier studies. The details of our numerical studies are given in Chapters-2 and 3.

1.1.7 Experimental Studies of Fluids with Polymers

In wall-bounded flows polymer additives modify the viscosity in a scale-dependent manner in such a way that the viscous sublayer thickens and the mean velocity increases [23, 26]. In particular, polymers modify the log-law in a channel flow and so the mean velocity increases. The plot in Fig. 1.11 shows the modification of the log-law profile on the addition of polymers to a channel flow.

In pressure-driven flows (channel or pipe) the percentage drag reduction (DR) is defined as

$$DR = (\frac{\Delta P_f - \Delta P_p}{\Delta P_p}) \times 100 \qquad (1.31)$$
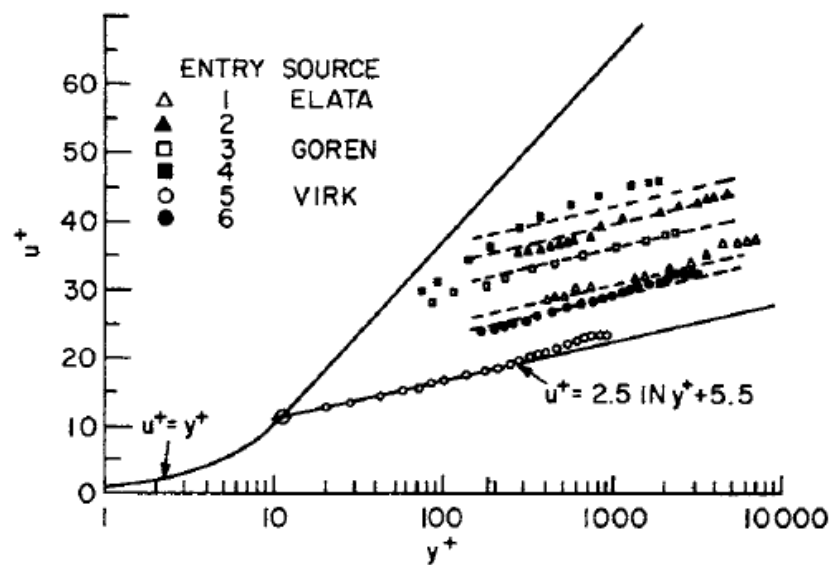
Fig. 5. Mean velocity profiles during drag reduction. The solid line approximates the envelope of the buffer layers for increasing drag reduction. After Virk et al. (1970).

Figure 1.11: Plot of mean velocity profiles during drag reduction. The solid lines approximate the envelope of the buffer layers for increasing drag reduction. The plot and the caption is taken from Virk, *et. al.* [20]. Here $u^+ = U(y)/\sqrt{\nu \partial_y U}$, $y^+ = y/\delta$, and δ is the thickness of the viscous sublayer.
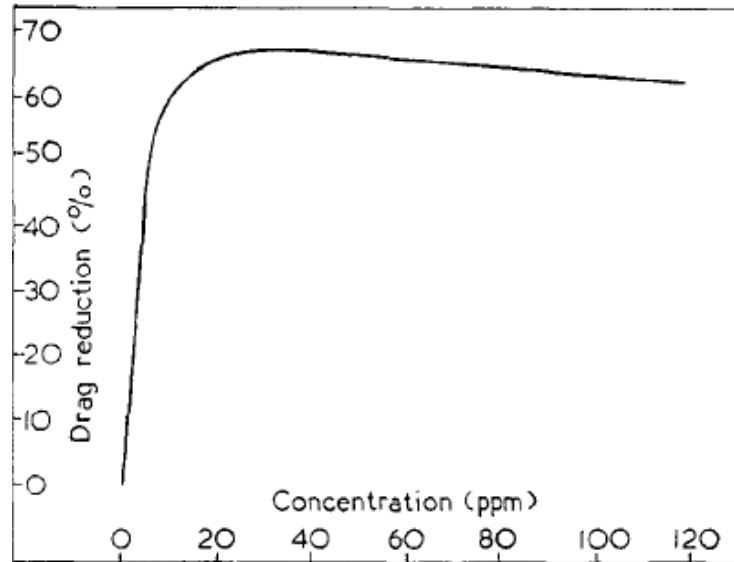
Figure 1.12: DR versus c for Polyox WSR-301. from the experiment of Colleyer, *et al.* [28]. DR increases, reaches a maximum, and then decreases mildly.

In Fig. 1.12 we present a plot of DR versus the concentration c from the experiment of Colleyer, *et al.* [28]. DR increases, reaches a maximum, and then decreases mildly.

Figure 1.13 shows how the friction factor $f \equiv (4a\Delta p)/(\rho L U^2)$ changes with the Reynolds number for different polymer concentrations. Here a is the radius of the pipe, ρ is the fluid density, and U is the mean velocity. For a given Reynolds number there is a minimum friction factor or maximum DR that one can attain (this is independent of the polymer concentration). The curve of the minimum friction factor as a function of the Re is known as Virk's maximum-drag-reduction asymptote.

Polymer additives also lead to dramatic changes in the structure of a flow in a turbulent jet as shown in Fig. 1.14. In the absence of polymers there is a lot of spray formation; but the addition of polymers suppresses spray formation and thereby reduces small-scale structures in the flow.
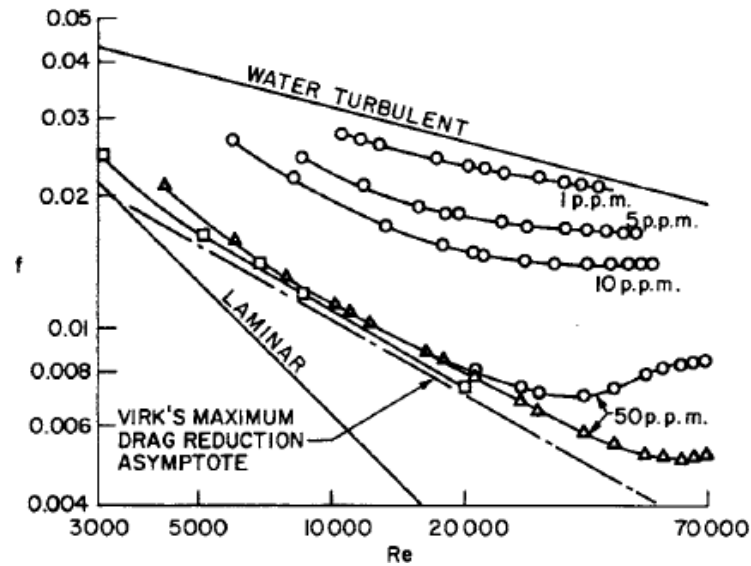
Figure 1.13: Pipe friction factor versus the Reynolds number for various polymer solutions [from Virk, *et al.*, [20]].
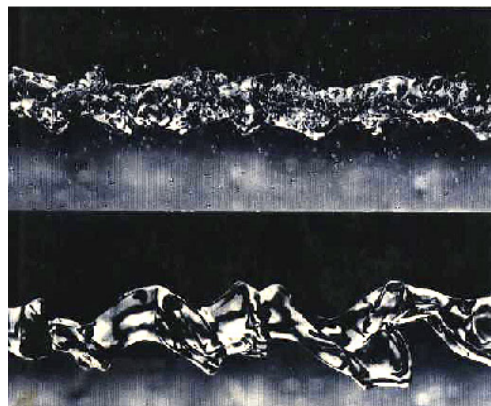
Figure 1.14: Turbulent jet of water without (top) and with 50ppm polyethylene oxide(PEO) (bottom) at $Re \sim 225$ (from Hoyt *et al.* [29].).

Results similar to those described above for a turbulent jet have also been obtained in the grid-turbulence experiments of McComb, *et al.* [30]. Visualisation by a dye injected at the inlet has displayed that the turbulent structure is considerably reduced on the addition of polymers as shown in Fig. 1.15 for various polymer concentrations. The corresponding energy spectra $E(k)$ are shown in Fig. 1.16 for different polymer concentrations. These spectra show that the energy content of the polymer solution is marginally increased at large spatial scales (low k) for large polymer concentrations whereas it is reduced in inertial-range scales. Dissipation-range Fourier modes are under resolved in this experiment.

A recent experiment [31] has studied the effects of polymer additives on the second-order structure function $S_2(r)$. This study shows that, at large polymer concentrations, the value of $S_2(r)$ is suppressed in the inertial range. The normalized $S_2(r)$ shows that some cross-over takes place, for small polymer concentrations, at the beginning of the dissipation range [see Fig. 1.17 for a plot of $S_2(r)$ ($D_{NN}(r)$ in the plot)]. However, this is not absolutely conclusive since, in this experiment, the estimated dissipation length scale for the pure fluid is $\eta_w = 84\mu m$ and the smallest resolved scale in the experiment is $r/\eta_w = 1$. Thus the dissipation range is not very well resolved.

The statistical properties of the fluid turbulence in the presence of polymer additives have been studied by Liberzon, *et al.* [32, 33]. The forcing is produced by four counter-rotating disks. In one case the disks have baffles (the forcing thus generated is called inertial forcing); in the other case the disks are smooth (the forcing thus generated is called frictional forcing). Furthermore, in the former case the average energy input remains constant both in the absence and in the presence of polymers. The Reynolds number in these experiments is $Re \simeq 40$. For both types of forcing a reduction in the small-scale structure is observed. In the smooth-disk case the turbulence is generated
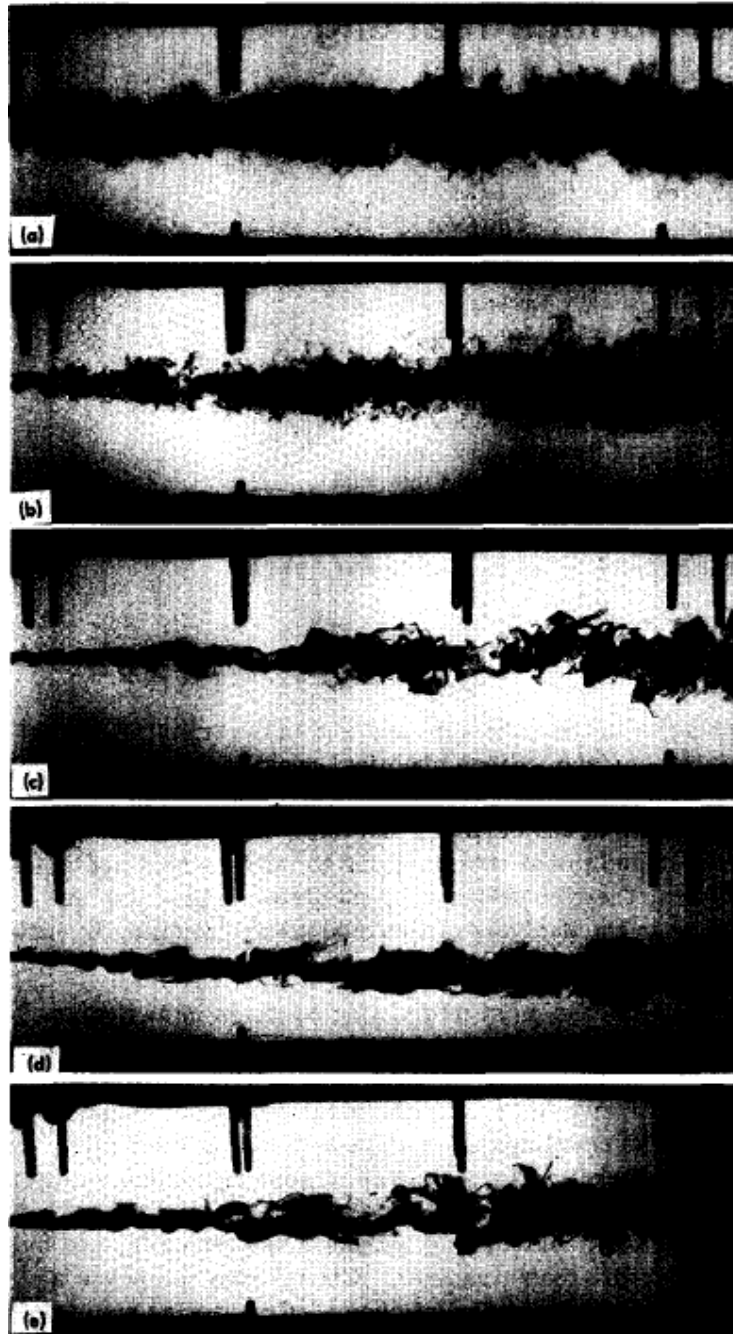
Figure 1.15: Effect of polymer additive(Polyox WSR 301) on the dye traces at concentrations (a) $c = 0$(water), (b) $c = 50$ppm, (c) $c = 100$ppm, (d) $c = 250$ppm, and (e) $c = 500$ppm (from McComb, *et al.*, [30]).
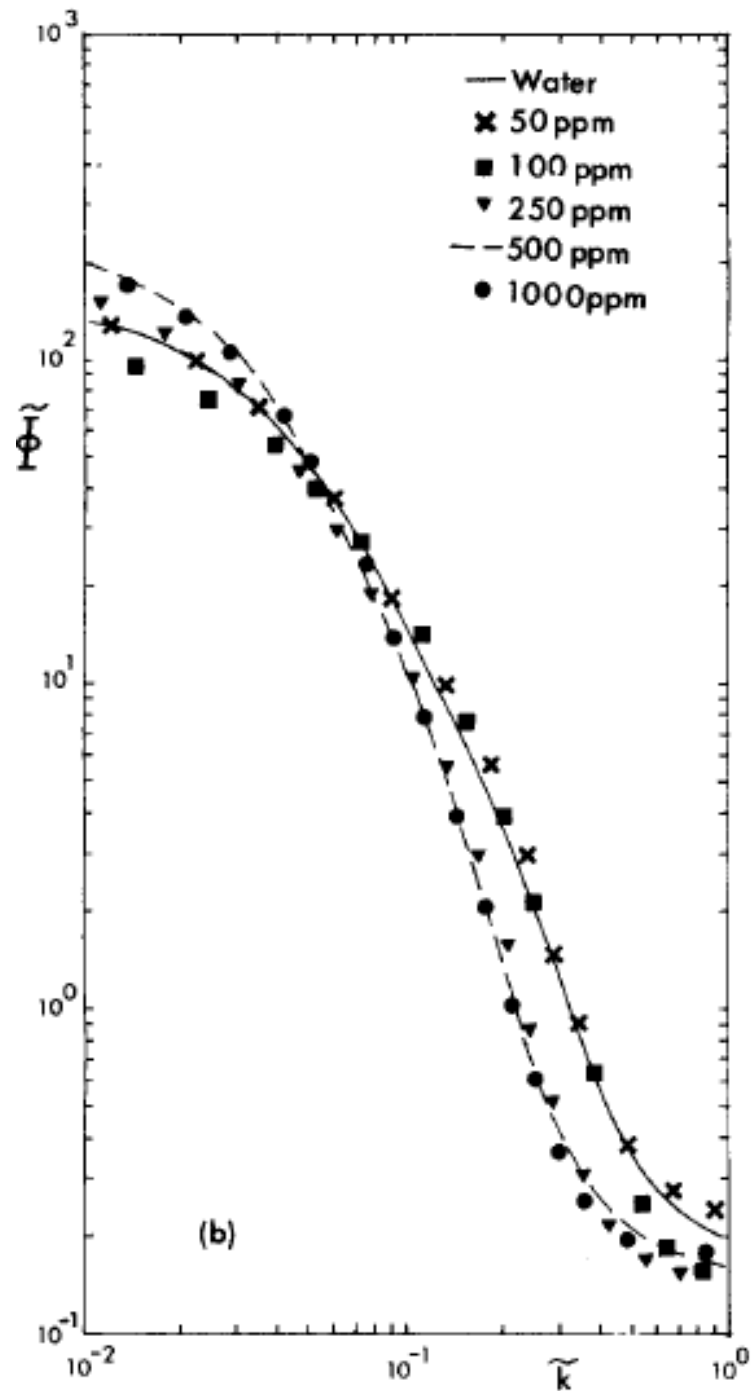
Figure 1.16: Energy spectra $E(k)$ versus k for various polymer concentrations (from McComb, *et al.*, [30]).
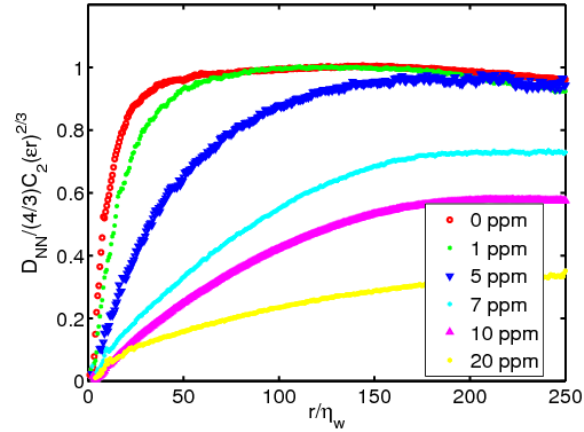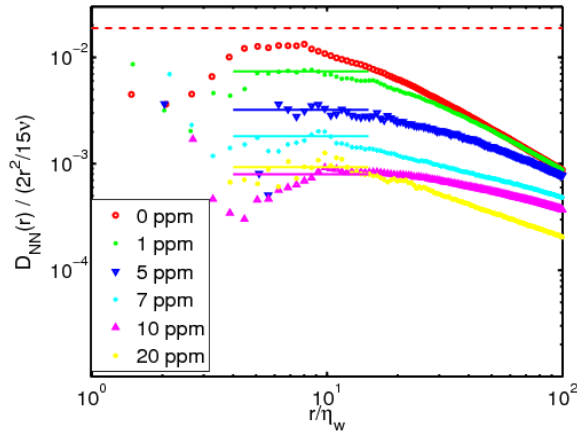
Figure 1.17: The effect of polymer additives on the second-order structure functions
. The Reynolds number of the water flow (before the addition of polymers) is $Re_\lambda = 350$ (corresponding to $We = 6.0$ with polymers) and the Kolmogorov length scale is $\eta_w = 84\mu$m. The structure functions compensated by (a) the inertial-range scaling prediction and (b) the dissipation-range scaling prediction. The dashed line in (b) indicates $\epsilon_T(0)$ as measured in the pure-water flow.(Our caption follows the caption of Fig. 1 in Ref. [31].)
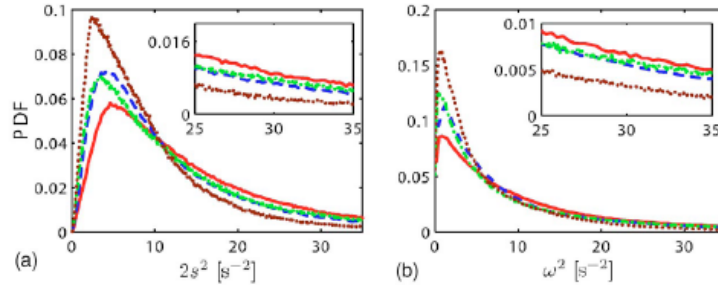
Figure 1.18: PDFs of s^2 and ω^2 for four cases: (a) water flow forced by smooth disks [solid line(-)]; (b) dilute polymer solution forced by smooth disks [dashed line(–)]; and then the flows forced by baffles: (c) pure water [chain like(-.-)]; and (d) with polymers [dotted line (...)]. Our caption follows that of Fig. 3 in Ref. [33].

in the boundary layer whereas, if the disk has baffles the turbulence is not boundary-layer driven. Since a reduction in small-scale structures is also observed in the inertial-forcing case, it was argued that polymers do modify the bulk fluid turbulence away from the boundaries. In Fig. 1.18 we present the PDF of the strain squared s^2 and ω^2 for these two types of forcing, with and without polymers. Note that the presence of polymers leads to a suppression of regions of large strain and large vorticity in the flow. To understand the effect of the polymer additives on the topological properties of the flow, QR plots (Fig. 1.19) were analysed in Ref. [33]. Although the typical tear-drop shape of the QR plot remains on the addition of polymers, its size shrinks. This gives a very strong indication that the structural properties of the turbulent flow are changed on the addition of the polymers.

1.1.8 Numerical Studies of Fluids with Polymers

Dilute solutions of polymers are modelled by coupling a constitutive equation for the polymer conformation tensor with the Navier-Stokes equations. The constitutive equation we use is the Finitely Extensible Nonlinear Elastic-Peterlin (FENE-P) equation. A drag-reducing polymer molecule such as PEO consists of a large number of monomers
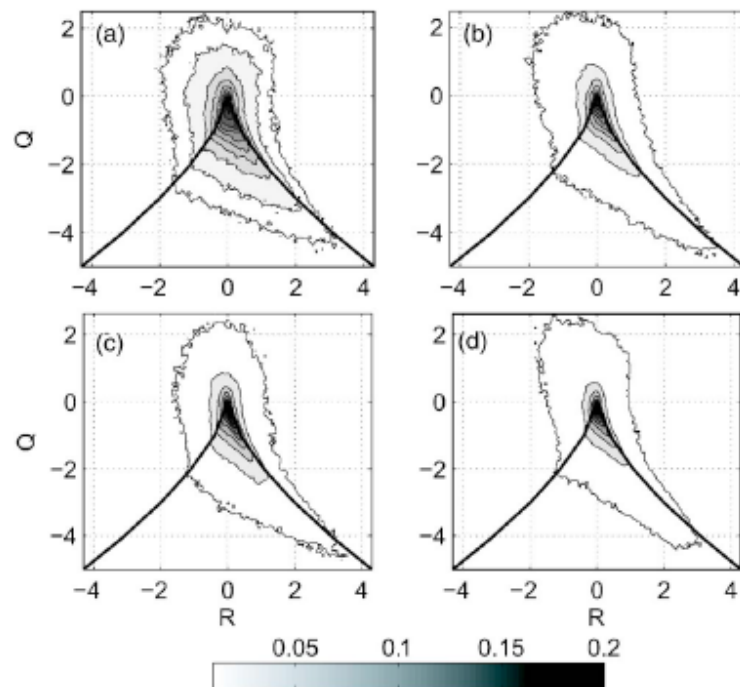
Figure 1.19: Joint PDFs $P(Q, R)$ for (a) water with smooth disks; (b) with polymers and smooth disks; (c) water with baffles; and (d) with polymers and with baffles. Contour lines are from 0.01 to 1 in steps of 0.1. (Liberzon, *et al.*, Ref. [33].)

($\approx 10^4$), has a high molecular weight, a large number of time-scales, and an end-to-end maximal extension ($\approx 34\mu m$) smaller than the Kolmogorov dissipative scale. In the FENE-P equation the complicated polymer molecule is modelled by a dumbbell with a single relaxation time τ_P and a finite maximal extension L. The contribution of the polymer to the fluid is modelled by an additional stress term that is added to the Navier-Stokes equation [Eq. (1.1)]. For the details of such modelling we refer the reader to Refs. [34, 35]. Some simulations have also used the Oldroyd-B equation as a polymer model. The Oldroyd-B model is a special case of the FENE-P model with $L = \infty$. Although the FENE-P model appears over simplified, it has been used successfully in channel-flow simulations to obtain the modification of the log-law profile observed in experiments [25, 36, 37].

In this thesis we restrict our discussion to numerical studies of homogeneous, isotropic turbulence in the presence of polymer additives by using direct numerical simulations. For a discussion on earlier shell model studies we refer the reader to Refs. [38, 39]. For issues regarding the numerical schemes and their implementation we refer the reader to Chapter 2. The first numerical studies on the effect of polymers on homogeneous, isotropic turbulence were conducted in Ref. [40]; stochastic forcing was used and the forcing-scale Reynolds number was $Re = (L^3 f)^{1/2}/\nu_T$, with L the linear size of the box, and ν_T the total viscosity (the sum of the polymer and the fluid viscosities) kept fixed. The polymer was modelled by using a FENE-P model and an artificial diffusivity term was added to the FENE-P equations for stability. The main results of this study are: (a) A reduction of vorticity filaments on the addition of polymers; (b) an overall reduction in the dissipation rate with polymers. The energy input in these simulations changes with change in parameters, hence a direct comparison with the experiments cannot be attempted.

In a series of numerical experiments Vaithianathan,*et al.*, have proposed new numerical schemes and a RANS-type model [12, 41, 42] to study the coupled NS+FENE-P equations in the presence of shear and for the case of homogeneous, isotropic turbulence. They have found the following: (a) A suppression of the energy spectrum on the addition of polymers; (b) an increases in the polymer extension with an increase in the polymer relaxation time.

In another study Berti, *et al.*, have modelled the polymers by a linear viscoelastic model. Their study also shows attenuation of the spectrum in the inertial range; but they have found a mild increase in the viscous dissipation with an increase in the polymer relaxation time.

We have conducted very detailed, high-resolution direct numerical simulations, both for forced and decaying homogeneous, isotropic fluid turbulence in the presence of polymer additives. For decaying turbulence our study shows that: (a) The addition of polymers leads to dissipation reduction; (b) the energy spectrum is attenuated at most of the scales except in the deep-dissipation range where the polymers inject energy back into the fluid; (c) small-scale intermittency is reduced on the addition of polymers; (d) there is a reduction in large-vorticity and large-strain regions on the addition of polymers. This is in agreement with the experiments of Liberzon, *et al.*, *op. cit.*.

Our study of forced fluid with polymer additives is divided into two parts. In the first part we study the effect of polymers on the turbulent fluid at moderate Reynolds numbers, comparable to those in the experiments of Liberzon, *et al.*, *op. cit.*. The forcing scheme used is such that the energy injection, and hence the *total dissipation*, is held at a constant value, both with and without polymers. Our results are in qualitative agreement with those of Liberzon, *et al.*, it op. cit. In the second part we have looked at the modification of the energy spectrum in the presence of polymer additives. These simulations are

conducted at a low Reynolds number as a well-resolved dissipation range is required to uncover the modification of the spectrum in the deep dissipation range. In agreement with our earlier study of decaying turbulence, we find that the energy spectrum is attenuated at most spatial scales except in the deep dissipation range where the polymers inject energy back into the fluid.

1.2 Flow in two dimensions

When the motion of the fluid is confined to a plane the flow is two-dimensional. Consider the situation in which $\mathbf{u} \equiv \mathbf{u}(x, y)$, $p \equiv p(x, y)$, and $\mathbf{f} \equiv \mathbf{f}(x, y)$ are independent of the z-direction. By writing the equations for the different components of $\mathbf{u}$ in Eq. (1.1) and Eq. (1.2) we get

$$\frac{\partial u_x}{\partial t} + u_x \frac{\partial u_x}{\partial x} + u_y \frac{\partial u_x}{\partial y} = \nu(\frac{\partial^2 u_x}{\partial x^2} + \frac{\partial^2 u_x}{\partial y^2}) - \frac{\partial p}{\partial x} + f_x, \quad (1.32)$$

$$\frac{\partial u_y}{\partial t} + u_x \frac{\partial u_y}{\partial x} + u_y \frac{\partial u_y}{\partial y} = \nu(\frac{\partial^2 u_y}{\partial x^2} + \frac{\partial^2 u_y}{\partial y^2}) - \frac{\partial p}{\partial y} + f_y, \quad (1.33)$$

$$\frac{\partial u_z}{\partial t} + u_x \frac{\partial u_z}{\partial x} + u_y \frac{\partial u_z}{\partial y} = \nu(\frac{\partial^2 u_z}{\partial x^2} + \frac{\partial^2 u_z}{\partial y^2}) + f_z, \quad (1.34)$$

$$\frac{\partial u_x}{\partial x} + \frac{\partial u_y}{\partial y} = 0. \quad (1.35)$$

We observe now that the equation for the time evolution of u_z is similar to the equation of a passive scalar. It does not affect the motion of the velocities u_x and u_y. Therefore, when the motion is constrained to be in a plane, the time-evolution of u_x and u_y completely determines the dynamics in the plane. By defining the vorticity $\boldsymbol{\omega} \equiv (\partial_x u_y - \partial_y u_x)$ and using $u_x \equiv -\partial \psi / \partial y$ and $u_y \equiv \partial \psi / \partial x$, we get

$$\frac{\partial \boldsymbol{\omega}}{\partial t} + u_x \frac{\partial \boldsymbol{\omega}}{\partial x} + u_y \frac{\partial \boldsymbol{\omega}}{\partial y} = \nu(\frac{\partial^2 \boldsymbol{\omega}}{\partial x^2} + \frac{\partial^2 \boldsymbol{\omega}}{\partial y^2}) + f_{\boldsymbol{\omega}}, \quad (1.36)$$

$$\nabla^2 \psi = \boldsymbol{\omega}, \quad (1.37)$$

where $f_\omega = (\partial_x f_y - \partial_y f_x)$ and ψ is the streamfunction. In the above formulation (conventionally called the streamfunction-vorticity formulation) the incompressibility constraint [Eq. (1.2)] is satisfied by construction. Note that in two dimensional flows the vortex stretching mechanism is absent, namely, $\boldsymbol{\omega} \cdot \nabla \mathbf{u} = 0$.

1.2.1 Conservation Laws

In addition to the energy conservation, there is an additional balance equation for enstrophy. The energy and enstrophy conservation laws follow from the balance equations

$$\frac{dE}{dt} = -2\nu\Omega, \text{and} \tag{1.38}$$

$$\frac{d\Omega}{dt} = -2\nu P, \tag{1.39}$$

where $P \equiv \frac{1}{2V} \int_V |\nabla \times \boldsymbol{\omega}|^2$. The limit $\nu \to 0$ leads to energy and enstrophy conservation. [In the two-dimensional case, integrals of all powers of $\boldsymbol{\omega}$ are conserved in the unforced, inviscid limit.]

1.2.2 Topological Properties of Two-dimensional Flows

In Section 1.1.2 we presented a way of studying the topological properties of three-dimensional flows. For two-dimensional flows we note that $A^2 = -\det(A)\mathcal{I}$, where A is the velocity-derivative matrix. Therefore $P = R = 0$ (by incompressibility) and $Q = -\det(A)$ is the only invariant of two-dimensional turbulence in the inviscid case. This invariant is often the Okubo-Wiess parameter and is conventionally denoted by the symbol Λ; if $\Lambda = -\det(A) > 0$, the flow is vorticity dominated, whereas, if $\Lambda = -\det(A) < 0$, the flow is strain dominated.
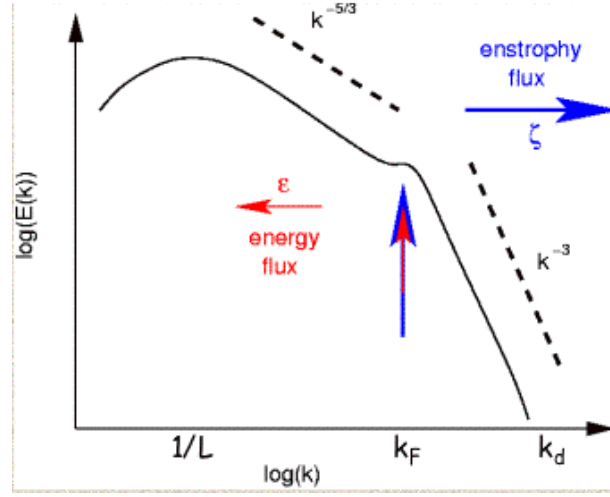
Figure 1.20: A sketch showing the forward and the inverse cascades in the energy spectrum for two-dimensional turbulence. This figure is taken from the talk of Prof. G. Boeffetta that is available at the URL http://personalpages.to.infn.it/b̃offetta/Seminars/conformalturbo.htm.

1.2.3   Two-dimensional Turbulence

According to Frisch, *op. cit.*, the study high-Reynolds number solutions of Eq. (1.37) is two-dimensional turbulence. Because of the additional conservation of enstrophy, there is a dual cascade in two-dimensional turbulence. There is an inverse energy cascade, from forcing scales to large spatial scales, and a forward cascade of enstrophy, from forcing scales to small spatial scales, as suggested first by Kraichnan [43]. By using dimensional arguments it was predicted that, in the inverse-cascade regime, $E(k) \sim k^{-5/3}$, whereas, in the forward-cascade regime, $E(k) \sim k^{-3}$. These scaling laws were independently predicted by Kraichnan, Leith, and Batchelor [43, 44, 45]. A schematic sketch of the energy spectrum, showing the two cascade regimes in two-dimensional turbulence, is given in Fig. 1.20. From the conservation laws given in Section 1.2.1 we find that, in the limit $\nu \to 0$, Ω attains a constant value, whereas $E \to 0$. Thus there is a dissipative anomaly for the enstrophy but no dissipative anomaly

for the energy in two-dimensional turbulence. By contrast, three-dimensional fluid turbulence displays a dissipative anomaly for the energy in so far as the energy dissipation rate seems to asymptote to a positive number as $Re \to \infty$, i.e., $\nu \to 0$.

1.2.4   Quasi-two-dimensional Turbulence: Ekman Friction

Experiments can only realise quasi-two-dimensional flows. Such flows have an additional dissipative mechanism that inhibits the inverse cascade of the energy and steepens the slope of the energy spectrum in the forward-cascade region. This additional dissipative mechanism is modelled by adding a linear drag term (called the Ekman friction) to the Navier-Stokes equations:

$$\frac{D\mathbf{u}}{Dt} = \nu\nabla^2\mathbf{u} - \alpha\mathbf{u} + \mathbf{f}, \text{and} \tag{1.40}$$

$$\nabla \cdot \mathbf{u} = 0, \tag{1.41}$$

here α is the Ekman friction coefficient. The origin of the Ekman friction and its effect on the topological properties of the fluid are discussed in the next Section and in Chapter-4. Because of the Ekman friction the energy spectrum in the forward cascade regime steepens to $E(k) \sim k^{-(3+\delta)}$ and the enstrophy flux shows, at variance with pure two-dimensional turbulence, a power-law decay $k^{-\delta}$, with $\delta > 0$ [46]. Furthermore [46], at the dissipation wavenumber $k_d \sim \nu^{-1}$ the enstrophy flux is stopped by a viscous dissipation, with a viscous dissipation rate $\epsilon_\omega = \nu^\delta$, the enstrophy dissipation vanishes in the inviscid limit $\nu \to 0$, since $\delta > 0$. Therefore, in quasi-two-dimensional turbulence with Ekman friction there is neither a dissipative anomaly nor an enstrophy anomaly.

In the inverse-cascade regime, where the energy scales as $E(k) \sim k^{-5/3}$, from dimensional arguments, similar to those in K41 (see Section 1.1.5), we get $S_p(r) \sim \epsilon^{2/3}r^{2/3}$. In the forward-cascade regime,

where the energy scales as $E(k) \sim k^{-3+\alpha}$, the velocity field is smooth so Taylor expansion yields $S_p(r) \sim r^p$.

1.2.5 Two-dimensional Turbulence in Thin Films

The first experimental realisation of two-dimensional turbulence was obtained in atmospheric-turbulence experiments [44] where a k^{-3} spectrum was observed. More recently, quasi-two dimensional turbulence has been realized in laboratory flows of thin layers of soap films or other conducting fluids. In the former case, the experimental apparatus consists of a soap film suspended on a wire-frame. To study decaying two dimensional turbulence, the flow is driven by gravity and passed through a wire comb to generate turbulence behind a grid [47]. Since a soap film is an electrolyte solution, for forced-turbulence studies, the soap film is suspended above an array of magnets and a current is passed through it. This generates a Lorentz force that acts as a forcing mechanism for the soap film. For a detailed overview of two-dimensional turbulence theory, numerical simulations, and experiments we refer the reader to Refs. [48, 49, 50, 51]. Since we are interested in forced-turbulence experiments, we concentrate on the electromagnetically forced soap films of Refs. [52, 53, 54, 55, 56].

A sketch of the forced, quasi-two-dimensional turbulence experiments of Refs. [52, 53, 54, 55, 56] is shown in Fig. 1.21. In all the soap-film experiments, the soap-film is in contact with the air outside. The friction between the soap-film and air leads to an additional air-drag induced dissipative mechanism (also called air-drag induced Ekman friction) that extracts energy from large scales and inhibits the inverse cascade of energy. In Ref. [53] it was shown that dissipation because of the air-drag induced Ekman friction is as large as the viscous dissipation. In Ref. [54, 55] topological properties of two-dimensional turbulence were studied by using the Okubo-Weiss parameter Λ; the turbulent kinetic energy was maintained at a constant
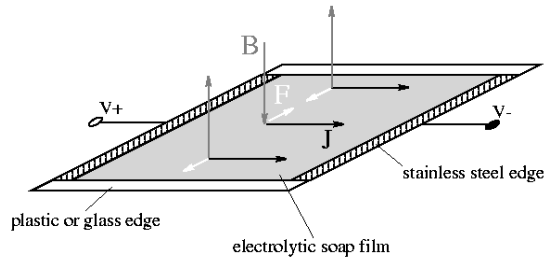
Figure 1.21: Sketch of the experimental apparatus used in the studies of Refs. [52, 53, 54, 55, 56] (this figure from the Ph.D. thesis of M. Rivera.)
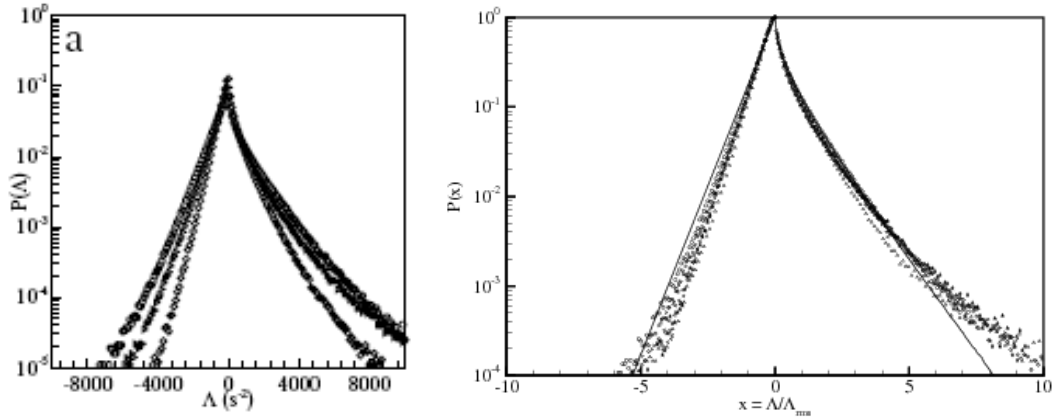
Figure 1.22: The PDFs (a) $P(\Lambda)$ versus Λ and (b) $P(\Lambda/\Lambda_{rms})$ versus Λ/Λ_{rms} for different values of the Ekman friction ($\gamma = 0.28$(diamond), $\gamma = 0.56$(triangle), $\gamma = 0.97$(circle).) from Ref. [54].

value for different values of the Ekman friction α (or γ, to use the notations of the experiments to which we refer). The plot in Fig. 1.22 shows the PDF $P(\Lambda)$ and the normalized PDF $P(\Lambda/\Lambda_{rms})$ for different values of γ. The normalization of the PDF leads to the overlap of all the distributions; and the PDF of Λ shows a cusp singularity at $\Lambda = 0$.

Another set of experiments [55] studied the joint distributions of Λ with the longitudinal and the transverse component of the velocity. These joint distribution indicate that, for large Λ, large transverse
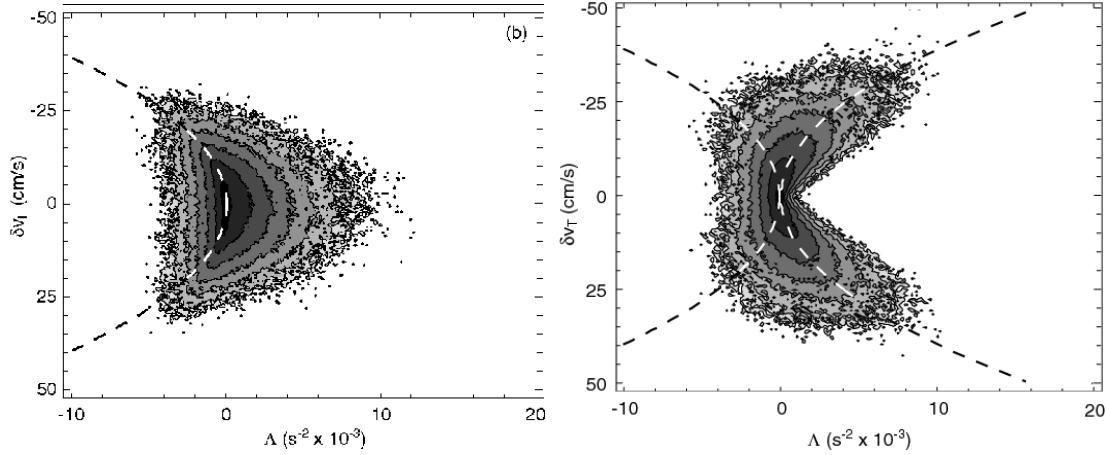
Figure 1.23: Joint PDF of Λ and (a) the longitudinal velocity difference and (b) the transverse velocity difference. This figure is extracted from Ref. [52].

velocity gradients are more probable than large longitudinal velocity differences (Fig. 1.23).

The experiments of Refs. [56] have studied Eulerian and Lagrangian velocity structure functions of order $1 \leq p \leq 6$. In the inverse-cascade regime they find that the Eulerian structure functions show simple scaling whereas in the forward-cascade regime there is small deviation from simple scaling. The corresponding Lagrangian structure functions show significant deviations from simple-scaling predictions. To the best of our knowledge there has been no experimental investigation of the vorticity structure functions in forced soap-film turbulence experiments. Numerical studies with periodic boundary conditions and with very high Reynolds numbers [46, 57] have observed multiscaling of the vorticity structure functions.

In this thesis we have conducted a detailed direct numerical simulation (DNS) of the two-dimensional Navier-Stokes equation with the incompressibility constraint and air-drag-induced Ekman friction. We have investigated the combined effects of walls and such friction on turbulence in forced thin films. We have concentrated on the forward-cascade regime and have extracted the isotropic parts of velocity and

vorticity structure functions and thence the ratios of multiscaling exponents. Our study shows velocity structure functions display simple scaling whereas their vorticity counterparts show multiscaling; and the probability distribution function of the Okubo-Weiss parameter Λ, which distinguishes between regions with centers and saddles, is in quantitative agreement with experiments. The details of the numerical simulations and the results is given in Chapter 4.

1.2.6 Turbulence-induced Melting in a Vortex Crystal

In Section 1.2.2 we had discussed how the topological properties of a two-dimensional fluid can be quantified by the Okubo-Weiss parameter Λ. Recently an experiment was conducted a on two-dimensional soap-film with an external forcing [58]. This forcing generates a cellular flow pattern with a square lattice of vortices with alternating sign. The corresponding Λ field is a square array of alternating regions of positive (vortex cores) and negative (strain-dominated or extensional flow) Λ. On increasing the Reynolds number, this array undergoes a transition and finally becomes turbulent. Snapshots of the velocity, vorticity, and the Λ field from these experiments [58] is shown in Fig. 1.24. This study considered the regions of large curvatures as topologically special points. The radial distribution function [13] of these points showed crystal-like behaviour at low Reynolds numbers; but, at large Reynolds number when the fluid became turbulent, the behaviour became like that of a liquid (Fig. 1.25).

An earlier numerical study [59] investigated the transition to turbulence in a square array of forced vortices from a purely dynamical-systems perspective. The control parameter was the Grashof number. On increasing the Grashof number they found the formation of large-scale structures. Recently Brons, *et al.* [60] conducted a numerical simulation that mimicked the experiments of Ref. [58] and studied the rate of annihilation of topologically special points.

Figure 1.24: Veloctiy, vorticity, and the logarithm of the curvature (Λ) fields for $Re = 32$(a,d), 93(b,c), and 245(c,f). In (a-c) the dark red regions correspond to regions of large vorticity whereas dark blue regions correspond to regions of large negative vorticity. In (d-f) regions with large curvature are marked red whereas regions of small curvatures are marked blue (our caption and figure follow Ref. [58]).
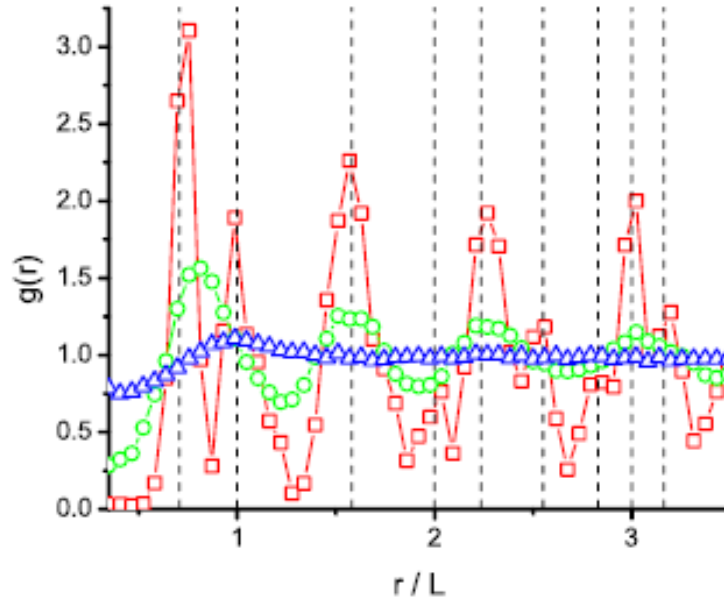
t

Figure 1.25: The radial distribution function of topologically special points, shown for $Re = 32(\square)$, $93(o)$, and $245(\triangle)$; this is from Ref. [58].

We perform a DNS of the two-dimensional Navier-Stokes equations. The forcing is chosen such that, at low Reynolds (Re) numbers, the steady state of the soap film is a square lattice of vortices. We find that, as we increase Re, this lattice undergoes a series of nonequilibrium phase transitions, first to a crystal with a different reciprocal lattice and then to a sequence of crystals that oscillate in time. Initially the temporal oscillations are periodic; this periodic behavior becomes more and more complicated with increasing Re until the soap film enters a spatially disordered nonequilibrium statistical steady that is turbulent. We study this sequence of transitions by using fluid-dynamics measures, such as the Okubo-Weiss parameter, ideas from nonlinear dynamics, e.g., Poincaré maps, and theoretical methods that have been developed to study the melting of an equilibrium crystal or the freezing of a liquid, for instance, the behavior of the pair-correlation function $G(r)$ in crystalline and liquid phases.

1.2.7   Persistence of particles in vortical regions

For a nonequilibrium fluctuating field persistence is the probability $P_0(\tau)$ that sign of the field at a point in space does not change upto time τ [61]. This probability can be analytically determined for a number of models, e.g., simple diffusion equation with Gaussian random initial conditions [61, 62]. Such questions have also been studied for several other models including, reaction-diffusion systems, fluctuating interfaces, granular medium, and population dynamics. In all these cases the persistence probability shows power-law decay for large τ, i.e., $P_\theta(\tau) \sim \tau^\theta$ where θ is negative and is often called the persistence exponent [63, 64].

We have investigated the presence of persistence exponent in two-dimensional turbulence. We perform a DNS of the two-dimensional Navier-Stokes equations and choose Kolmogorov forcing to mimic soap-film experiments. We evaluate the persistence times and autocorrelation functions for the Okubo-Weiss parameter Λ in Eulerian and Lagrangian frameworks. Our study reveals qualitatively different behaviours for the probability distribution functions for persistence times in different frames. In the Eulerian case, the PDF for residence time in vortical regions shows exponential decay whereas in the Lagrangian case it shows power law tail (details in Chap. 6).

Bibliography

[1] G.I. Taylor, *Phil. Trans. Royal Society* **A223**, 289 (1923).

[2] C.D. Andereck, S.S. Liu, and H.L. Swinney, *J. Fluid Mech.* **164**, 155 (1986).

[3] S.A. Orszag and C.K. Lawrence, *J. Fluid Mech.* **96**, 159 (1980).

[4] B. Eckhardt, T.M. Schneider, B. Hof, and J. Westerweel, *Ann. Rev. Fluid Mech.* **39**, 447 (2007).

[5] P.G. Drazin, *Introduction to Hydrodynamic Stability* (Cambridge University Press, Cambridge, 2002).

[6] S. Chandrasekhar, *Hydrodynamic and Hydromagnetic Stability* (Dover Publications, Oxford, England, 1981).

[7] C.C. Lin, *The theory of hydrodynamic stability* (Cambridge University Press, Cambridge, 1955).

[8] U. Frisch, *Turbulence the legacy of A.N. Kolmogorov* (Cambridge University Press, Cambridge, 1996).

[9] M. Lesieur, *Turbulence in Fluids*, Vol. 40 of *Fluid Mechanics and Its Applications* (Kluwer, Springer, The Netherlands, 1997).

[10] A.S. Monin and A.M. Yaglom, *Statistical fluid mechanics* (MIT Press, Cambridge, Massachusetts, 1975).

[11] G.K. Batchelor, *The theory of homogeneous turbulence* (Cambridge University Press, Cambridge, 1953).

[12] T. Vaithianathan and L.R. Collins, *J. Comp. Phys.* **187**, 1 (2003).

[13] P.M. Chaikin and T.C. Lubensky, *Principles of condensed matter physics* (Cambridge, Cambridge University Press, UK, 1998).

[14] J.M. Chomaz and B. Cathalau, *J. Fluid Mech.* **442**, 387 (2001).

[15] J.M. Chomaz, *J. Fluid Mech.* **442**, 387 (2001).

[16] Y. Mitsuo, K. Itakura, A. Uno, T. Ishihara, and Y. Kaneda in *In Proc. SC2002, CD-ROM* (2002).

[17] A.E. Perry and M.S. Chong, *Appl. Sci. Res.* **53**, 357 (1994).

[18] M. Van Dyke, *An album of fluid motion* (The Parabolic Press, Stanford, California, 1982).

[19] A.N. Kolmogorov, *Dokl. Acad. Nauk* **30**, 9 (1941).

[20] P. Virk, *AIChE* **21**, 625 (1975).

[21] P.H.J. vanDam, G. Wegdam, and J. van der Elsken, *J. Non-Newtonian Fluid Mech.* **53**, 215 (1994).

[22] J.M.J. Den Toonder, M.A. Hulsen, G.D.C. Kuiken and F. Nieuwstadt, *J. Fluid. Mech.* **337**, 193 (1997).

[23] J.L. Lumley, *J. Polymer Sci* **7**, 263 (1973).

[24] K.R. Sreenivasan and C.M. White, *J. Fluid Mech.* **409**, 149 (2000).

[25] P.K. Ptasinski, B.J. Boersma, E.T.M. Nieuwstadt, M.A. Hulsen, B.H.A.A. Van den Brule and J.C.R. Hunt *J. Fluid Mech.* **490**, 251 (2003).

[26] V.S. L'vov, A. Pomyalov, I. Procaccia, and V. Tiberkevich, *Phys. Rev. Lett.* **92**, 244503 (2004).

[27] G. Boffetta, A. Celani, and A. Mazzino, *Phys. Rev. E* **71**, 036307 (2005).

[28] A.A. Collyer, *Phys. Educ.* **10**, 305 (1975).

[29] J. Hoyt and J. Taylor, *Phys. Fluids* **20**, S253 (1977).

[30] W. McComb, J. Allan, and C. Greated, *Phys. Fluids* **20**, 873 (1977).

[31] N.T. Ouellette, H. Xu, and E. Bodenschatz, *J. Fluid Mech.* **629**, 375 (2009).

[32] A. Liberzon, M. Guala, B. Luthi, W. Kinzelbach and A. Tsinober, *Phys. Fluids* **17**, 031707 (2005).

[33] A. Liberzon, M. Guala, W. Kinzelbach, and A. Tsinober, *Phys. Fluids* **18**, 125101 (2006).

[34] R. Bird, C. Curtiss, R. Armstrong, and O. Hassager, *Dynamics of Polymeric Liquids* (Wiley, New York, 1987).

[35] N. Phan-Thien, *Understanding Viscoelasticity* (Springer, Berlin, 2002).

[36] Y. Dubief and S.K. Lele, *Annual Research Briefs*, Center for Turbulence Research (unpublished).

[37] Y. Dubief, C. M. White, V. E. Terrapon, E.S.G. Shafeh, P. Moin, and S.K. Lele, *J. Fluid Mech.* **514**, 271 (2004).

[38] R. Benzi, E. De angelis, R. Govindarajan, and I. Procaccia, *Phys. Rev. E* **68**, 016308 (2003).

[39] C. Kalelkar, R. Govindarajan, and R. Pandit, *Phys. Rev. E* **72**, 017301 (2004).

[40] E. De angelis, C.M. Casicola, R. Benzi, and R. Piva, *J. Fluid Mech.* **531**, 1 (2005).

[41] T. Vaithianathann, A. Robert, J. Brasseur, and L.R. Collins, *J. Non-newtonian Fluid Mech.* **140**, 3 (2006).

[42] D. Vincenzi, S. Jin, E. Bodenschatz, and L. Collins, *Phys. Rev. Lett.* **98**, 024503 (2007).

[43] R.H. Kraichnan, *Phys. Fluids* **10**, 1417 (1967).

[44] C.E. Leith, *Phys. Fluids* **11**, 671 (1968).

[45] G.K. Batchelor, *Phys. Fluids Suppl. II* **12**, 233 (1969).

[46] G. Boffetta, A. Celani, S. Musacchio, and M. Vergassola, *Phys. Rev. E* **66**, 026304 (2002).

[47] C.H. Bruneau, O. Greffier, and H. Kellay, *Phys. Rev. E* **60**, R1162 (1999).

[48] S.D. Danilov and D. Gurarie, *Physics-Uspekhi* **43**, 863 (2000).

[49] H. Kellay and W.I. Goldburg, *Rep. Prog. Phys.* **65**, 845 (2002).

[50] P. Tabeling, *Physics Reports* **362**, 1 (2002).

[51] H.J.H. Clercx and G.J.F. van Heijst, *Appl. Mech. Rev.* **62**, 020802 (2009).

[52] W.B. Daniel and M.A. Rutgers, *arXiv:nlin/005008v1* (2000).

[53] M. Rivera and X.L. Wu, *Phys. Rev. Lett.* **85**, 976 (2000).

[54] M. Rivera, X.L. Wu, and C. Yeung, *Phys. Rev. Lett.* **87**, 044501 (2001).

[55] W.B. Daniel and M.A. Rutgers, *Phys. Rev. Lett.* **89**, 134502 (2002).

[56] M. Rivera and R.E. Ecke, *arXiv:0710.5888v1* (2007).

[57] K. Nam, E. Ott, Jr. T.M. Antonsen, and P.N. Guzdar, *Phys. Rev. Lett.* **84**, 5134 (2000).

[58] N.T. Ouellette and J.P. Gollub, *Phys. Rev. Lett.* **99**, 194502 (2007).

[59] R. Braun, F. Feudel, and N. Seehafer, *Phys. Rev. E* **55**, 6979 (1997).

[60] A. Brons, A. Skajaa, and O. Skovgaard, *arXiv:0806.4757*, (2008).

[61] S. Majumdar, C. Sire, A. Bray, and S. Cornell, *Phys. Rev. Lett.* **77**, 2867 (1996).

[62] B. Derrida, V. Hakim, and R. Zeitak, *Phys. Rev. Lett.* **77**, 2871 (1995).

[63] S. Watanbe, *Proc. Symp. Pure Math.* **57**, 157 (1995).

[64] S. Majumdar, *Curr. Sci.* **77**, 370 (1999).

Chapter 2

Effect of polymer additives on decaying turbulence

In this chapter we investigate the presence of drag-reduction type phenomenon in homogeneous, isotropic turbulence. A shorter version of this Chapter was published in *Physical Review Letters* [1].

The existence of drag reduction by polymer additives, well established for wall-bounded turbulent flows, is controversial in homogeneous, isotropic turbulence. We carry out a high-resolution direct numerical simulation (DNS) of *decaying*, homogeneous, isotropic turbulence with polymer additives. Our study reveals clear manifestations of drag-reduction-type phenomena: On the addition of polymers to the turbulent fluid we obtain a reduction in the energy dissipation rate, a significant modification of the fluid energy spectrum especially in the deep-dissipation range, a suppression of small-scale intermittency, and a decrease in small-scale vorticity filaments. The analogue of drag reduction in wall-bounded flows turns out to be dissipation reduction in homogeneous, isotropic turbulence.

2.1 Introduction

The dramatic reduction of drag by the addition of small concentrations of polymers to a turbulent fluid continues to engage the atten-

tion of engineers and physicists. Drag reduction was discovered by Toms in 1949; he found that on the polymers to a turbulent flow in a pipe, the pressure difference required to maintain the required volumetric flow rate decreases, i.e., the drag is reduced and a percentage drag reduction can be obtained from the percentage reduction in the pressure gradient. Subsequently, significant advances have been made in understanding drag reduction both experimentally [2, 3, 4] and theoretically [5, 6, 7, 8, 9] in channel flows or the Kolmogorov flow [10]. In wall-bounded flows the effect of the polymer additives is to modify the viscosity in a scale dependent manner in such a way that the viscous sublayer thickens and the mean velocity increases [5, 8, 9]. However, the effect of polymers on the turbulence away from the walls, i.e., the regime where the turbulence is homogeneous and isotropic [1, 11, 12, 13, 14, 15, 16, 17, 18, 19, 20, 21, 22, 23] remains controversial. Some experimental [19, 20, 21, 22], numerical [1, 13, 14, 15, 16, 17, 18, 24], and theoretical [11, 12] studies have suggested that drag reduction should occur even in homogeneous, isotropic turbulence; but other studies have refuted this claim [23]. Recent experiments have also looked at how the polymers affect the topological properties of the turbulent fluid by comparing the probability distribution of the strain and its tensorial products. These studies clearly show that the effect of the polymer additives is to suppress small-scale structures in turbulent flows [25, 26].

We present the results of our extensive direct numerical simulation (DNS) of decaying, homogeneous, isotropic turbulence in the presence of polymer additives. Our results are divided into three Parts.

In Part-I (Sec. 2.5.1), we monitor the decay of turbulence from initial states in which the kinetic energy of the fluid is concentrated at small wave vectors; this energy then cascades down to large wave vectors where it is dissipated by viscous effects; the energy-dissipation rate ϵ attains a maximum at t_m, roughly the time at which the cas-

cade is completed. An earlier shell-model study [15] has suggested that this peak in ϵ can be used to quantify drag reduction by polymer additives. Since shell models are far too simple to capture the complexities of real flows, we have studied decaying turbulence in the Navier-Stokes (NS) equation coupled to the Finitely Extensible Nonlinear Elastic Peterlin (FENE-P) model [27] for polymers. Our study, designed specifically to uncover drag-reduction-type phenomena, shows that the position of the maximum in ϵ depends only mildly on the polymer concentration c; however, the value of ϵ at this maximum falls as c increases. We use this decrease of ϵ to define the percentage dissipation reduction DR in decaying homogeneous, isotropic turbulence.

In Part-II (Secs. 2.5.2-2.5.3), we study the effect the polymer additives on the energy spectrum for various polymer concentrations c. We find that, on the addition of polymers ($c \neq 0$), the energy at the intermediate wave-numbers is lesser than the energy content for the pure fluid ($c = 0$), whereas in the deep dissipation range it is larger than in the pure fluid.

In Part-III (Secs. 2.5.4-2.5.5), we look at the effects of polymer additives on the structural properties of turbulent flows. We calculate the probability distribution function (PDF) of the modulus of the vorticity, the strain, and the eigenvalues of the strain tensor as a function of the polymer concentration. We show that regions of large strain and vorticity are suppressed on the addition of polymers. This is in agreement with the experimental studies of Liberzon, *et al.* [25, 26]. We further quantify the above observations by looking at the hyperflatness and also the isosurfaces of the modulus of the vorticity with and without polymers. The addition of polymer reduces the growth in this hyperflatness at small length scales; large-$|\omega|$ tubes, which appear in isosurface plots, are also depleted in the presence of polymers. We also study the effect of the polymer concentration and polymer re-

laxation time on the polymer extension. Our study reveals that the polymer extension increases on increasing the Weissenberg number We whereas it decreases on increasing the polymer concentration c.

2.2 Model and Equations

The polymeric fluid solution is modelled by the Navier-Stokes equations for the fluid coupled with the Finite Extension Nonlinear Elastic-Peterlin (FENE-P) equation for the polymer additives. The polymer contribution to the fluid is modelled by an extra stress term in the NS equations. The FENE-P equation approximates a polymer molecule by a nonlinear dumbbell with an upper bound on the maximum extension and with a single relaxation time. The NS and FENE-P (henceforth NSP) equations are

$$D_t\mathbf{u} \;=\; \nu\nabla^2\mathbf{u} + \frac{\mu}{\tau_P}\nabla.[f(r_P)\mathcal{C}] - \nabla p; \tag{2.1}$$

$$D_t\mathcal{C} \;=\; \mathcal{C}.(\nabla\mathbf{u}) + (\nabla\mathbf{u})^T.\mathcal{C} - \frac{f(r_P)\mathcal{C} - \mathcal{I}}{\tau_P}. \tag{2.2}$$

Here $\mathbf{u}(\mathbf{x},t)$ is the fluid velocity at point $\mathbf{x}$ and time t, incompressibility is enforced by $\nabla.\mathbf{u} = 0$, $D_t = \partial_t + \mathbf{u}.\nabla$, ν is the kinematic viscosity of the fluid, μ the viscosity parameter for the solute (FENE-P), τ_P the polymer relaxation time, ρ the solvent density (set to 1), p the pressure, $(\nabla\mathbf{u})^T$ the transpose of $(\nabla\mathbf{u})$, $\mathcal{C}_{\alpha\beta} \equiv \langle R_\alpha R_\beta \rangle$ the elements of the polymer-conformation tensor $\mathcal{C}$ (angular brackets indicate an average over polymer configurations), $\mathcal{I}$ the identity tensor with elements $\delta_{\alpha\beta}$, $f(r_P) \equiv (L^2 - 3)/(L^2 - r_P^2)$ the FENE-P potential that ensures finite extensibility, $r_P \equiv \sqrt{Tr(\mathcal{C})}$ and L the length and the maximum possible extension, respectively, of the polymers, and $c \equiv \mu/(\nu + \mu)$ a dimensionless measure of the polymer concentration [24]. $c = 0.1$ corresponds, roughly, to 100ppm for polyethylene oxide [2].

2.3 Numerical Scheme

We consider homogeneous, isotropic, turbulence, so we use periodic boundary conditions and solve Eq. (2.1) by using a massively parallel pseudospectral code [28, 29], which we have developed. We use N^3 collocation points in a cubic domain (side $\mathbb{L} = 2\pi$). We eliminate aliasing errors by the 2/3 rule [28, 29], to obtain reliable data at small length scales, and use a second-order, slaved Adams-Bashforth scheme for time marching (Appendix A.2 and A.4). For Eq. (2.2) we use an explicit sixth-order central-finite-difference scheme (Appendix A.1) in space and a second-order Adams-Bashforth method for temporal (Appendix A.3) evolution. The numerical error in r_P must be controlled by choosing a small time step δt, otherwise r_P can become larger than L, which leads to a numerical instability; this time step is much smaller than what is necessary for a pseudospectral DNS of the NS equation alone. Table 2.1 lists the parameters we use. We preserve the symmetric-positive-definite (SPD) nature of $\mathcal{C}$ at all times by using [24] the following Cholesky-decomposition scheme: If we define

$$\mathcal{J} \equiv f(r_P)\mathcal{C}, \tag{2.3}$$

Eq. (2.2) becomes

$$D_t\mathcal{J} = \mathcal{J}.(\nabla\mathbf{u}) + (\nabla\mathbf{u})^T.\mathcal{J} - s(\mathcal{J} - \mathcal{I}) + q\mathcal{J}, \tag{2.4}$$

where

$$
\begin{aligned}
s &= (L^2 - 3 + j^2)/(\tau_P L^2), \\
q &= [d/(L^2 - 3) - (L^2 - 3 + j^2)(j^2 - 3)/(\tau_P L^2(L^2 - 3))], \\
j^2 &\equiv Tr(\mathcal{J}), \text{and} \\
d &= Tr[\mathcal{J}.(\nabla\mathbf{u}) + (\nabla\mathbf{u})^T.\mathcal{J}].
\end{aligned}
\tag{2.5}
$$

Since $\mathcal{C}$ and hence $\mathcal{J}$ are SPD matrices, we can write $\mathcal{J} = \mathcal{L}\mathcal{L}^T$, where $\mathcal{L}$ is a lower-triangular matrix with elements ℓ_{ij}, such that $\ell_{ij} =$

0 for $j > i$, and

$$\mathcal{J} \equiv \begin{pmatrix} \ell_{11}^2 & \ell_{11}\ell_{21} & \ell_{11}\ell_{31} \\ \ell_{11}\ell_{21} & \ell_{21}^2 + \ell_{22}^2 & \ell_{21}\ell_{31} + \ell_{22}\ell_{32} \\ \ell_{11}\ell_{31} & \ell_{21}\ell_{31} + \ell_{22}\ell_{32} & \ell_{31}^2 + \ell_{32}^2 + \ell_{33}^2 \end{pmatrix}. \tag{2.6}$$

Equation (2.4) now yields ($1 \le i \le 3$ and $\Gamma_{ij} = \partial_i u_j$) the following:

$$\begin{aligned} D_t \ell_{i1} &= \sum_k \Gamma_{ki}\ell_{k1} + \frac{1}{2}\left[(q-s)\ell_{i1} + (-1)^{(i \bmod 1)}\frac{s\ell_{i1}}{\ell_{11}^2}\right] \\ &\quad + (\delta_{i3} + \delta_{i2})\frac{\ell_{i2}}{\ell_{11}}\sum_{m>1}\Gamma_{m1}\ell_{m2} \\ &\quad + \delta_{i3}\Gamma_{i1}\frac{\ell_{33}^2}{\ell_{11}}, \text{ for } i \ge 1; \\ D_t \ell_{i2} &= \sum_{m \geqslant 2}\Gamma_{mi}\ell_{m2} - \frac{\ell_{i1}}{\ell_{11}}\sum_{m \geqslant 2}\Gamma_{m1}\ell_{m2} \\ &\quad + \frac{1}{2}\left[(q-s)\ell_{i2} + (-1)^{(i+2)}s\frac{\ell_{i2}}{\ell_{22}^2}\left(1 + \frac{\ell_{21}^2}{\ell_{11}^2}\right)\right] \\ &\quad + \delta_{i3}\left[\frac{\ell_{33}^2}{\ell_{22}}\left(\Gamma_{32} - \Gamma_{31}\frac{\ell_{21}}{\ell_{11}}\right) + s\frac{\ell_{21}\ell_{31}}{\ell_{11}^2\ell_{22}}\right], \text{ for } i \ge 2; \\ D_t \ell_{33} &= \Gamma_{33}\ell_{33} - \ell_{33}\left[\sum_{m<3}\frac{\Gamma_{3m}\ell_{3m}}{\ell_{mm}}\right] + \frac{\Gamma_{31}\ell_{32}\ell_{21}\ell_{33}}{\ell_{11}\ell_{22}} \\ &\quad - s\frac{\ell_{21}\ell_{31}\ell_{32}}{\ell_{11}^2\ell_{22}\ell_{33}} + \frac{1}{2}\Big[(q-s)\ell_{33} \\ &\quad + \frac{s}{\ell_{33}}\left(1 + \sum_{m<3}\frac{\ell_{3m}^2}{\ell_{mm}^2}\right) + \frac{s\ell_{21}^2\ell_{32}^2}{\ell_{11}^2\ell_{22}^2\ell_{33}}\Big]. \end{aligned} \tag{2.7}$$

The SPD nature of $\mathcal{C}$ is preserved by Eq. (2.7) if $\ell_{ii} > 0$, which we enforce explicitly [24] by considering the evolution of $\ln(\ell_{ii})$ instead of ℓ_{ii}.

2.4 Initial conditions

We use the following initial conditions (superscript 0): $\mathcal{C}^0_{mn}(\mathbf{x}) = \delta_{mn}$ for all $\mathbf{x}$; and $u^0_m(\mathbf{k}) = P_{mn}(\mathbf{k})v^0_n(\mathbf{k})\exp(\iota\theta_n(\mathbf{k}))$, with $m, n = x, y, z$, $P_{mn} = (\delta_{mn} - k_m k_n/k^2)$ the transverse projection operator, $\mathbf{k}$ the wavevector with components $k_m = (-N/2, -N/2 + 1, \ldots, N/2)$, $k = |\mathbf{k}|$, $\theta_n(\mathbf{k})$ random numbers distributed uniformly between 0 and 2π, and $v^0_n(\mathbf{k})$ chosen such that the initial kinetic-energy spectra are either of type I, with $E^I(k) = k^2\exp(-2k^4)$, or of type II, with $E^{II}(k) = k^4\exp(-2k^2)$. Physically both these initial conditions correspond to states in which the fluid energy is concentrated, to begin with, at small k (large length scales); and all the polymers are in the coiled state at $t = 0$.

2.5 Results

We now present the results that we have obtained from our DNS. In addition to $\mathbf{u}(\mathbf{x}, t)$, its Fourier transform $\mathbf{u_k}(t)$, and $\mathcal{C}(\mathbf{x}, t)$ we monitor the vorticity $\omega \equiv \nabla \times \mathbf{u}$, the kinetic-energy spectrum $E(k, t) \equiv \sum_{k-1/2 < k' \leq k+1/2} |\mathbf{u}^2_{\mathbf{k}'}(t)|$, the total kinetic energy $\mathcal{E}(t) \equiv \sum_k E(k, t)$, the energy-dissipation-rate $\epsilon(t) \equiv \nu \sum_k k^2 E(k, t)$, the cumulative probability distribution of scaled polymer extensions $P^C(r_P^2/L^2)$, the hyperflatness $\mathcal{F}_6(r) \equiv \mathcal{S}_6(r)/\mathcal{S}_2^3(r)$, where $\mathcal{S}_p(r) \equiv \langle\{[\mathbf{u}(\mathbf{x} + \mathbf{r}) - \mathbf{u}(\mathbf{x})] \cdot \mathbf{r}/r\}^p\rangle$ is the order-p longitudinal velocity structure function, the PDF of the strain and the modulus of the vorticity, the eigenvalues of the strain tensor, and the angular brackets denote an average over our simulation domain at t_m, the time at which the energy cascade is completed. For notational convenience, we do not display the dependence on c explicitly.

2.5.1   Time evolution of the energy dissipation rate

In decaying homogeneous, isotropic fluid turbulence simulations with type-I or type-II initial conditions, where energy is stored initially in the first few Fourier modes, the energy dissipation rate increases, reaches a peak at a time $t = t_m$, and then decreases. The time $t = t_m$ corresponds to the cascade completion. In this Section we study the effect of the polymer additives on the time evolution of the energy dissipation rate ϵ. Figure 2.1 shows that ϵ first increases with time, reaches a peak, and then decreases; for $c = 0$ this peak occurs at $t = t_m$. The position of this peak changes mildly with c but its height goes down significantly as c increases. This suggests the following natural definition [15] of the percentage dissipation reduction for decaying homogeneous, isotropic turbulence:

$$\text{DR} \equiv \left(\frac{\epsilon^{f,m} - \epsilon^{p,m}}{\epsilon^{f,m}} \right) \times 100; \tag{2.8}$$

here (and henceforth) the superscripts f and p stand, respectively, for the fluid without and with polymers and the superscript m indicates the time t_m. Figure 2.2 shows plots of DR versus c, for the Weissenberg number, a ratio of the polymer relaxation time and typical shearing time in the flow, $We \equiv \tau_P \sqrt{\epsilon^{f,m}/\nu} \simeq 0.35$, and versus We, for $c = 1/11 \simeq 0.1$. DR increases with c in qualitative accord with experiments on channel flows (where DR is the drag reduction that is defined via a normalized pressure difference); but it drops gently as We increases, in contrast to the behavior seen in channel flows (in which τ_P is varied by changing the polymer). We will come back to this mild increase in the energy dissipation rate with We in the next chapter.

2.5.2   Energy spectra

In this Section we study the effects of the polymer additives on the fluid energy spectrum with varying polymer concentration. As a check
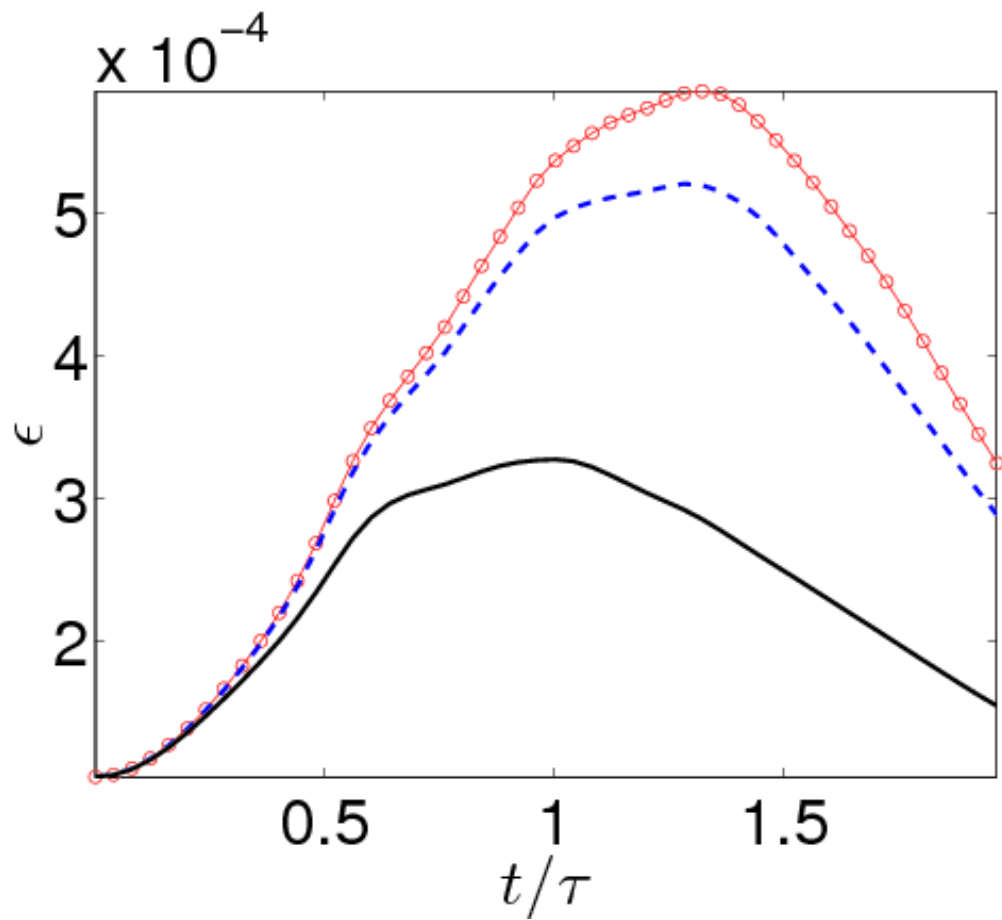
Figure 2.1: Temporal evolution of the energy dissipation rate ϵ (run `NSP-256B`) for concentrations $c = 0.1(--)$ and $c = 0.4$(solid line), with $\tau \equiv \sqrt{2\mathcal{E}(t=0)/3\mathbb{L}^2}$.
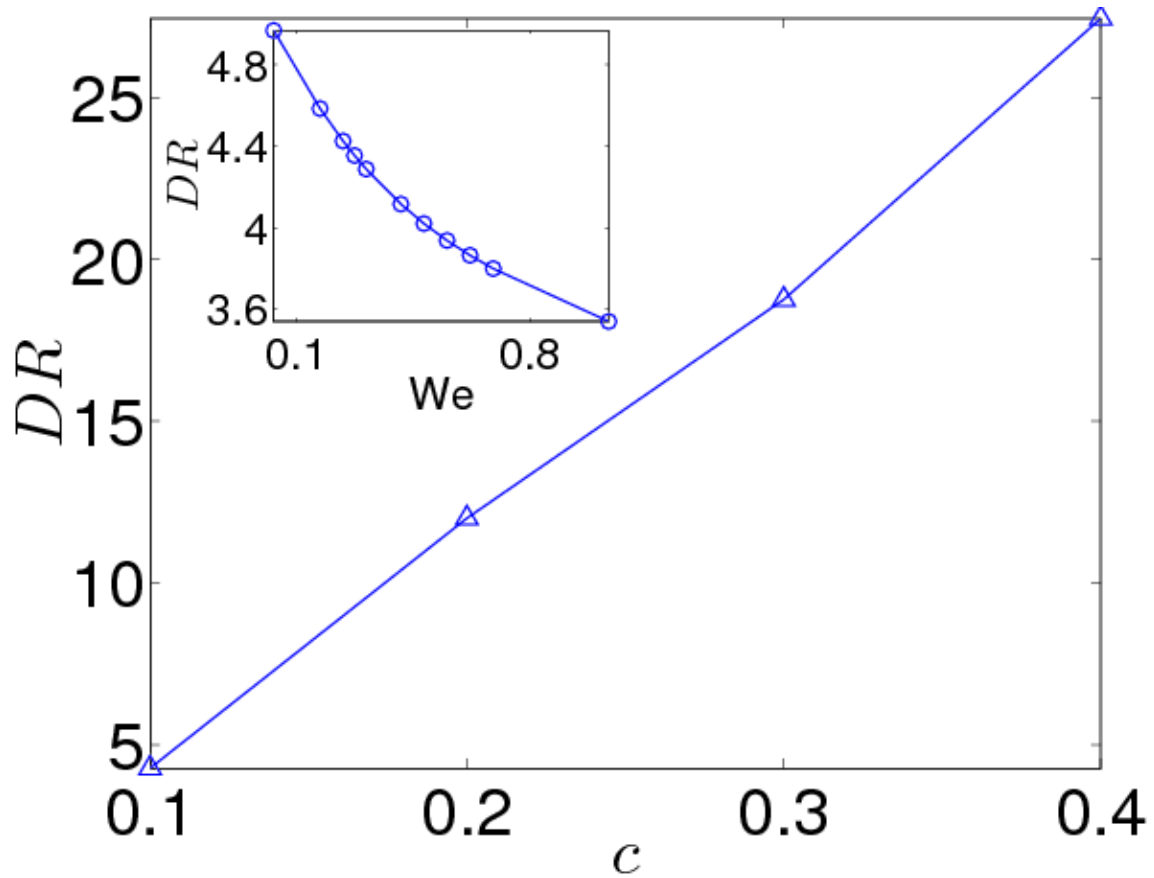
Figure 2.2: Percentage drag-reduction DR versus c (run `NSP-192`); the inset shows the mild variation in DR with We (runs `NSP-96`).
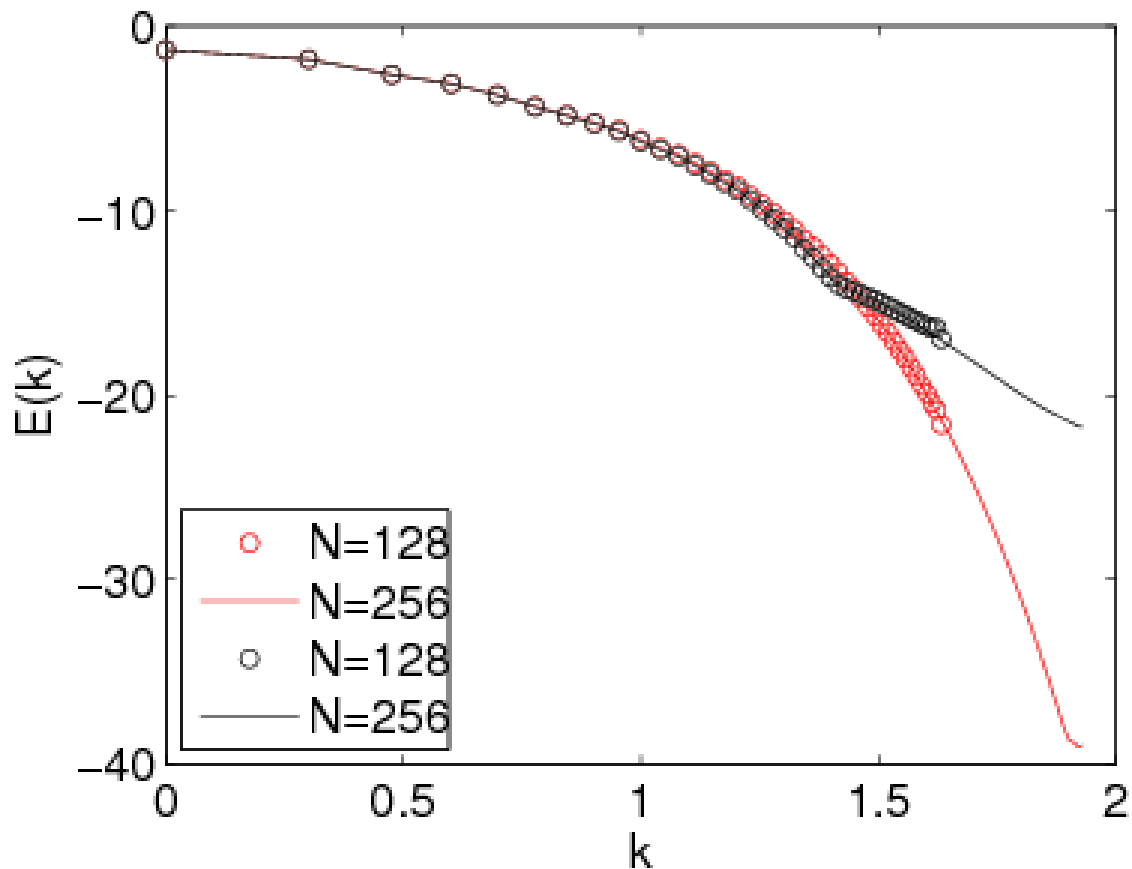
Figure 2.3: Log-log plots of the energy spectrum $E(k)$ versus the wave vector k for our runs `NSP = 128A` (black circle) and `NSP = 256A` (black line) for $c = 0.1$ and $\tau_P = 1$. The corresponding plots for the pure NS runs for $N = 128$ (red circles) and $N = 256$ (red line) are also shown for comparison.

on the numerical resolution we compare our DNS for runs `NSP − 128A` and `NSP − 256A` (see Table 2.1); in the latter the grid resolution is increased but all other parameters are kept the same. The plots in Fig. 2.3 show superimpositions of the spectra obtained from our runs different resolutions. The agreement between spectra obtained from runs with different resolutions indicate that our numerical simulations are well resolved. Polymer additives have a dramatic effect on the dissipation range, so we restrict ourselves to moderate Reynolds numbers for which we can resolve the dissipation range well.

We find that the polymers affect the fluid spectrum not only in the inertial range but also in the deep dissipation range. At low Reynolds number where the dissipation range is well resolved, for small concentrations ($c \simeq 0.1$) the spectra with and without polymers differ substantially only in the deep dissipation range, where $E^{f,m}(k) \ll E^{p,m}(k)$. As c increases, to say $c \simeq 0.4$, $E^{p,m}(k)$ is reduced relative to $E^{f,m}(k)$ at intermediate values of k [Fig. 2.4]; however, deep in the dissipation range $E^{f,m}(k) \ll E^{p,m}(k)$.

Figure 2.5 is a large-Re analog of Fig. 2.5. Given that Re is larger here than in run $\mathtt{NSP-256A}$, we have not been able to resolve enough of the dissipation range in this case to detect the effects of polymer additives on this range. At small k we observe a small increase in the spectrum on the addition of the polymers (see inset of Fig. 2.5). In the inertial lengths the polymer energy spectrum is suppressed in comparison to the fluid energy spectrum.

2.5.3 Time evolution of the energy

In decaying turbulence, the total kinetic energy $\mathcal{E}(t)$ of the fluid falls as t increases; the rate at which it falls increases with c (Fig. 2.6), which suggests that the addition of polymers increases the effective viscosity of the solution. This is not at odds with the decrease of ϵ with increasing c since the effective viscosity because of polymers turns out to be *scale-dependent*. We confirm this by obtaining the kinetic-energy spectrum $E^{p,m}(k)$ for the fluid in the presence of polymers at $t = t_m$. We now define [14] the effective scale-dependent viscosity

$$\nu_e(k) \equiv \nu + \Delta\nu(k). \tag{2.9}$$

From the scale-by-scale energy balance of Eq. (2.1) in Fourier space we get

$$\frac{DE_{\mathbf{k}}}{Dt} = -\nu \sum_{k-1/2 < k' \leq k+1/2} k^2 |u_{\mathbf{k}}|^2 + \frac{\mu}{\tau_P} \sum_{k-1/2 < k' \leq k+1/2} \mathbf{u}_{\mathbf{k}'} \cdot (\nabla \cdot \mathcal{J})_{-\mathbf{k}'}, \tag{2.10}$$
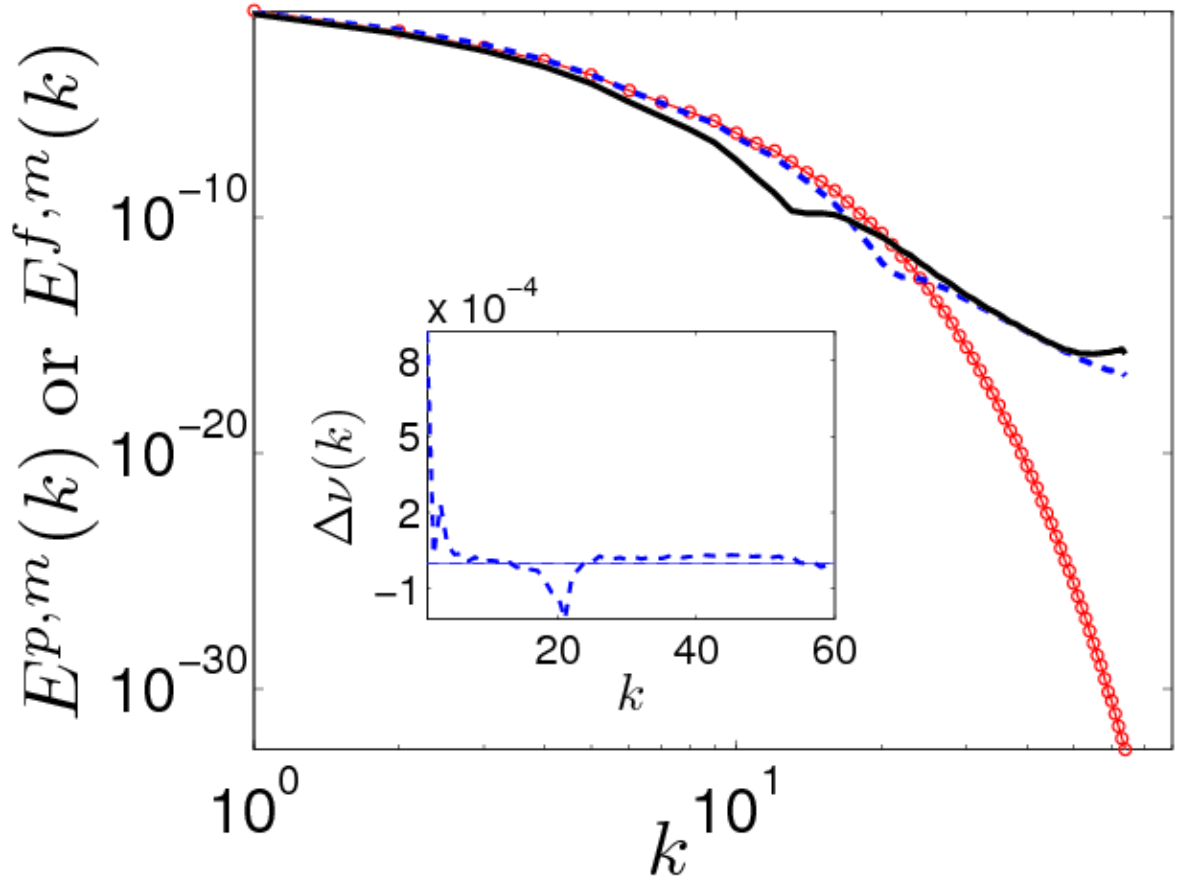
Figure 2.4: Plots of the energy spectra $E^{p,m}(k)$ or $E^{f,m}(k)$ versus k (run `NSP-192`) for $c = 0.1(--)$ and $c = 0.4$(solid line) [$E^{p,m}(k)$ is unchanged if we use $N = 256$, with all other parameters the same (run `NSP-256A`)]; inset: polymer contribution to the scale-dependent viscosity $\Delta\nu(k)$ versus k for $c = 0.1(--)$; $\Delta\nu(k) = 0$ (solid line) is also shown for reference. The corresponding plot with $c = 0$ ($o-$) is shown for comparison.
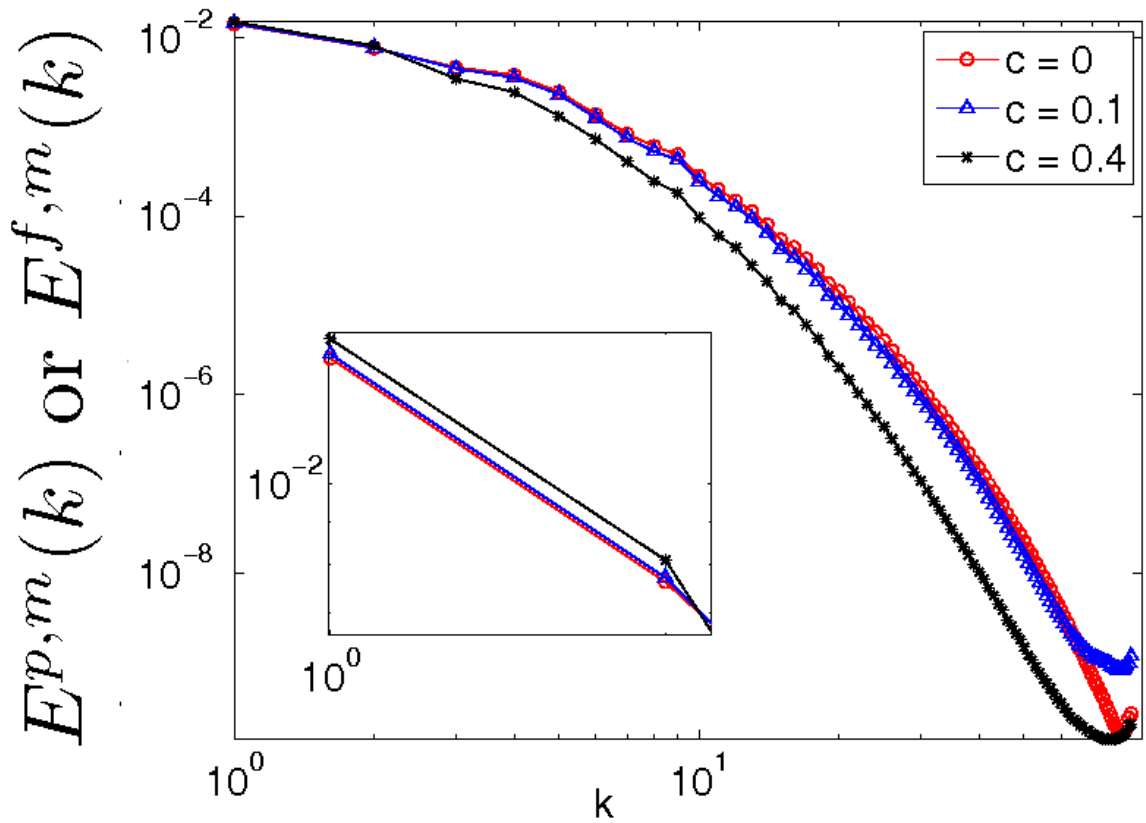
Figure 2.5: Plots of the energy spectra $E^{p,m}(k)$ or $E^{f,m}(k)$ versus k (run NSP-256B)for different polymer concentrations. The inset shows the small increase in the spectrum, on the addition of polymers, at small k.
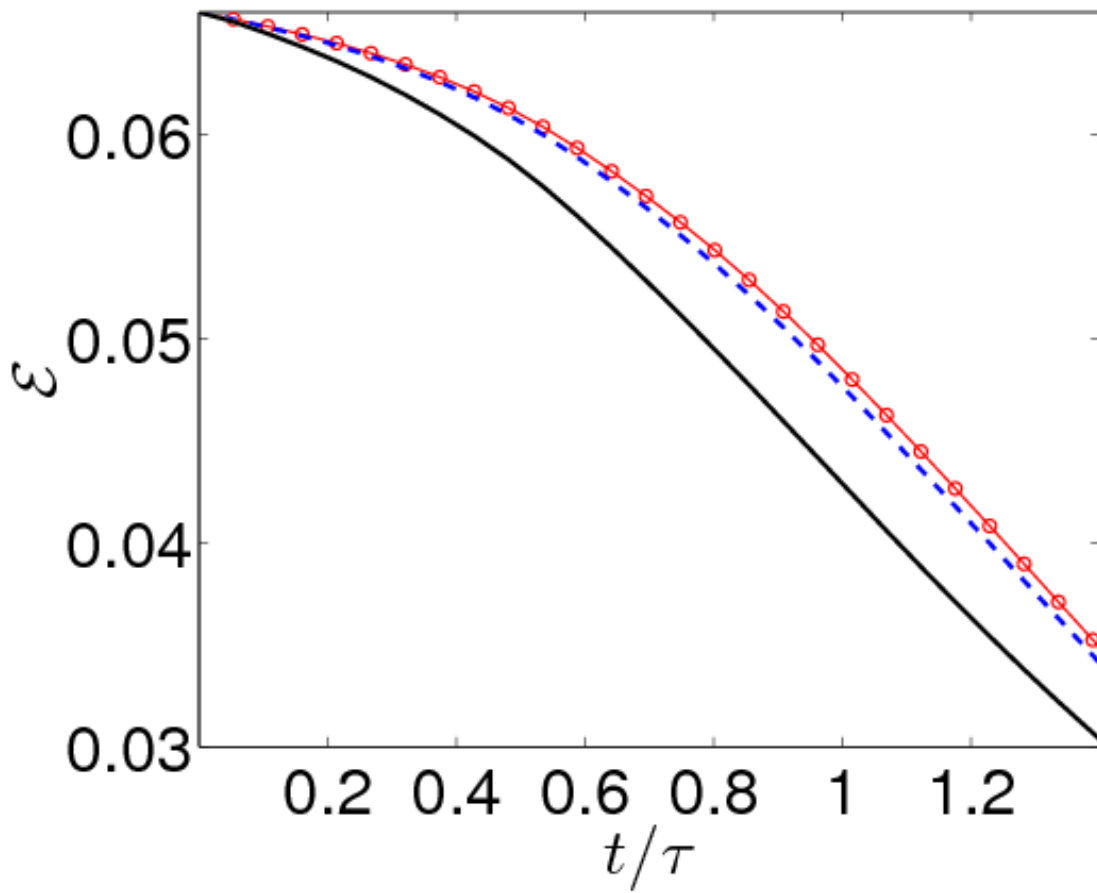
Figure 2.6: Temporal evolution of the total fluid energy $\mathcal{E}$ for concentrations $c = 0.1 (--)$ and $c = 0.4$(solid line) (runs `NSP-256B`). The plot for $c = 0$ $(o-)$ is shown for comparison.

where $(\nabla \cdot \mathcal{J})_{\mathbf{k}}$ is the Fourier transform of $\nabla \cdot \mathcal{J}$. To obtain a scale-dependent viscosity we replace the second term inside the summation on the RHS of Eq. (2.10) by a scale-dependent viscosity $\Delta\nu(k) \equiv \nu(k)|u_{\mathbf{k}}|^2$. On comparison with Eq. (2.10) we get

$$\Delta\nu(k) \equiv -\mu \sum_{k-1/2<k'\leq k+1/2} \mathbf{u}_{\mathbf{k}'} \cdot (\nabla \cdot \mathcal{J})_{-\mathbf{k}'}/[\tau_P k'^2 E^{p,m}(k')]. \qquad (2.11)$$

The inset of Fig. 2.4 shows that $\Delta\nu(k) > 0$ for $k < 15$, but $\Delta\nu(k) < 0$ around $k = 20$. This explains why $E^{p,m}(k)$ is suppressed relative to $E^{f,m}(k)$ at small k, rises above it in the deep-dissipation range, and crosses over from its small-k to large-k behaviours around the value of k where $\Delta\nu(k)$ goes through zero.

2.5.4 Small scale structure: the hyperflatness and Iso-$|\omega|$ surfaces

A good measure of the intermittency in turbulence is the hyperflatness $\mathcal{F}_6(r)$, which is defined by the following ratio of the sixth-order velocity structure function to the second-order velocity structure function:

$$\mathcal{F}_6(r) = S_6(r)/(S_2(r))^3. \qquad (2.12)$$

For a Gaussian random variable $\mathcal{F}_6(r) = 15$. In Fig. 2.7 we plot $\mathcal{F}_6(r)$ versus r without and with polymers. This plot shows that $\mathcal{F}_6(r)$ grows as $r \to 0$, signalling small-scale intermittency at dissipation range scales. Note that the addition of polymers slows down the growth of $\mathcal{F}_6(r)$ as $r \to 0$: This provides evidence for the reduction of small-scale intermittency. Furthermore, the iso-$|\omega|$ surfaces shown in Fig. 2.8 show that, if no polymers are present, these surfaces are filamentary [30] for large $|\omega|$; however, the addition of polymers suppresses a significant fraction of these filaments.
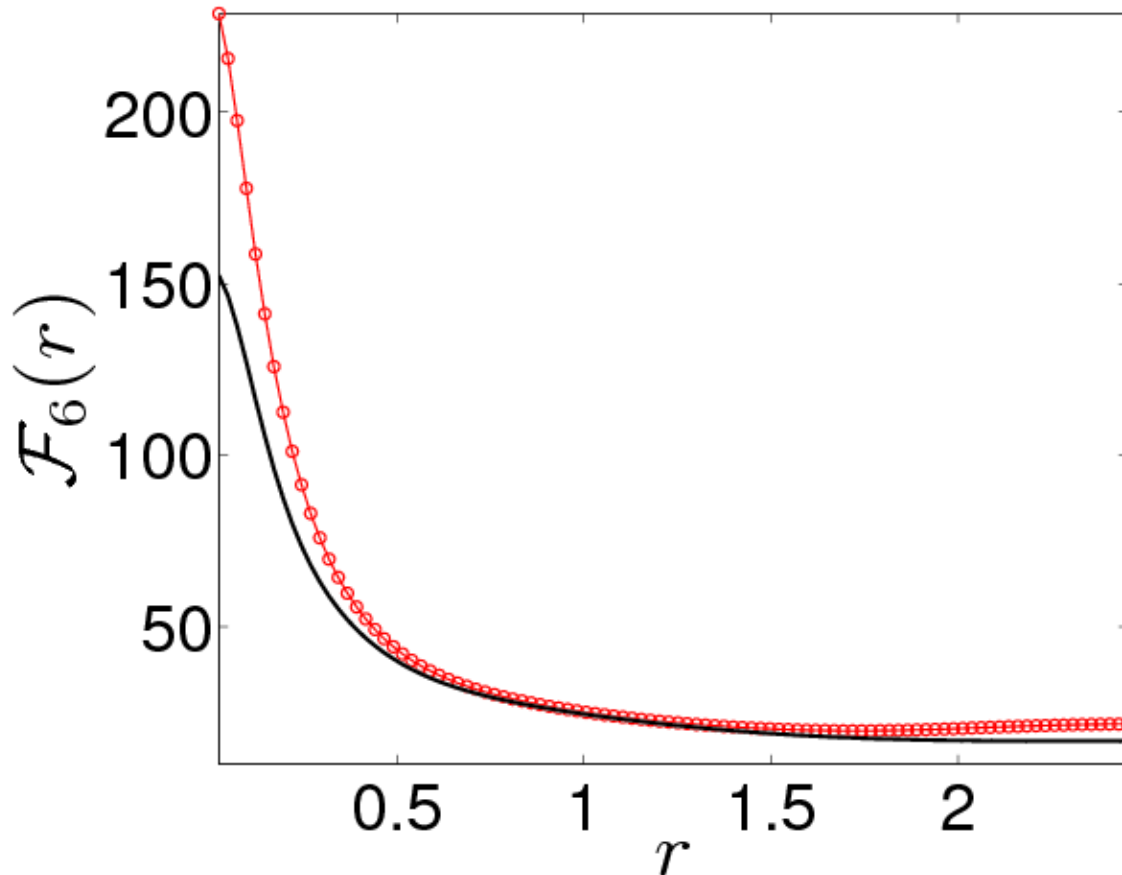
Figure 2.7: The hyper-flatness $\mathcal{F}_6(r)$ as a function of r (run NSP-256B) and concentration $c = 0.4$(solid line). The corresponding plot with $c = 0$ ($o-$) is shown for comparison. For the run NSP-256B the Kolmogorov scale $\eta \equiv (\nu^3/\epsilon^{f,m})$ at the cascade completion is $\eta = 0.036$.
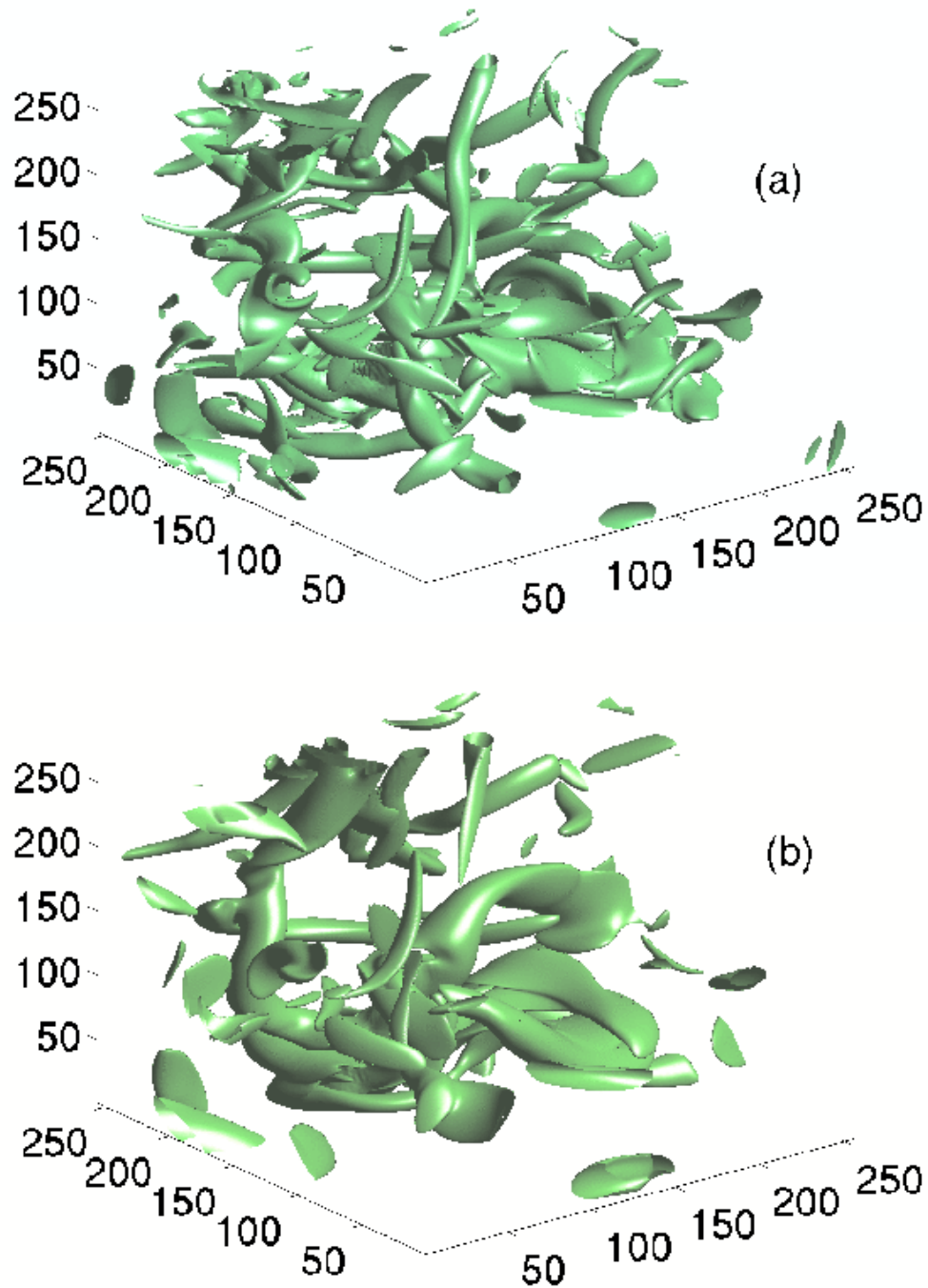
Figure 2.8: Constant-$|\omega|$ isosurfaces for $|\omega| = \langle|\omega|\rangle + 2\sigma$ at t_m without (a) and with (b) polymers, (run NSP-256B) and $c = 0.4$; $\langle|\omega|\rangle$ is the mean and σ the standard deviation of $|\omega|$.

2.5.5 Small-scale structures: structural studies

We now study how the polymers affect the structure of homogeneous, isotropic turbulence and make specific comparisons with the experiments of Liberzon *et al.* [25, 26]. In particular, we plot the probability distribution function (PDFs) of the vorticity [$P(|\omega|)$] and the enstrophy production [$P(\omega_i \omega_j S_{ij})$] in Figs. 2.9 and 2.10. These figures show that the addition of polymers causes a decrease in the regions of high vorticity and the enstrophy production. This is in qualitative agreement with the results of Refs. [25, 26] (see Fig. 2 of Ref. [25] and Fig. 3 of Ref. [26]).

The eigenvalues of the rate of strain tensor $S_{ij} = (\partial_i u_j + \partial_j u_i)/\sqrt{2}$ are denoted by Λ_n, $n = 1, 2, 3$, they provide a measure of local stretching and compression of the fluid. In the present study, the eigenvalues are arranged as $\Lambda_1 > \Lambda_2 > \Lambda_3$. By using incompressibility condition we get $\sum_i \Lambda_i = 0$; therefore, for an incompressible fluid, one of the eigenvalues (Λ_1) should be positive and one should be negative (Λ_3). The intermediate eigenvalue Λ_2 can be either positive or negative. In Figs. 2.11 and 2.12 we plot the PDFs of the eigenvalues of the strain tensor. Note that the tail of the PDFs, indicating events of large extension or compression, shrink on the addition of the polymers. This indicates that the addition of the polymers leads to a substantial decrease regions of large strains. The above results are in remarkable qualitative agreement with the experimental results of Refs. [25] for a turbulent flow with weak mean velocity (see Fig. [3(b)] of Ref. [25]).

We use a rank-order method [31] to obtain the cumulative PDF of scaled polymer extensions, namely $P^C(r_P^2/L^2)$. We find that, as c increases (Fig. 2.13), the extension of the polymers decreases. We have checked that, in the passive-polymer version of Eqs. (2.1) and (2.2), the extension of polymers is much more than in Fig. 2.13.
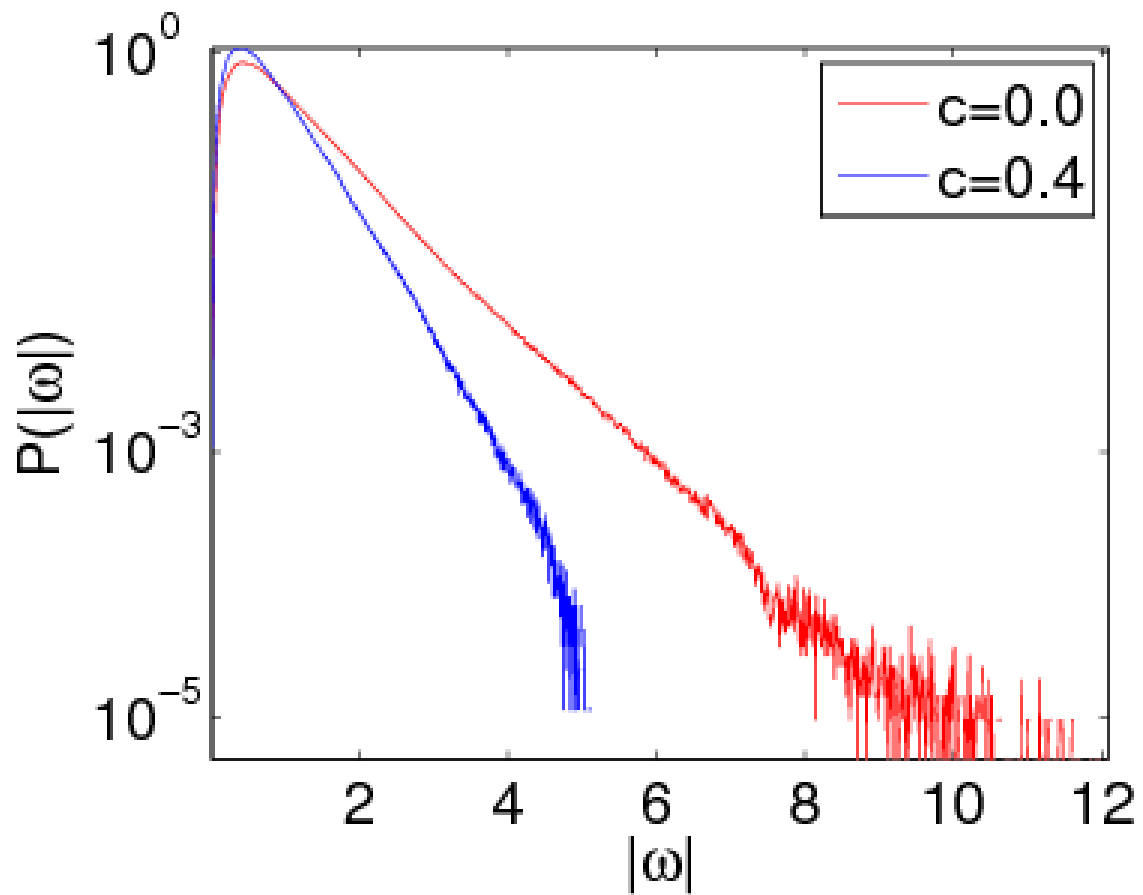
Figure 2.9: The plots of $P(|\omega|)$ versus $|\omega|$, for our run NSP-256B, with [$c = 0.4$ (blue)] and without [$c = 0$ (red)] polymer additives. The plots is normalized such that the area under the curve is unity.
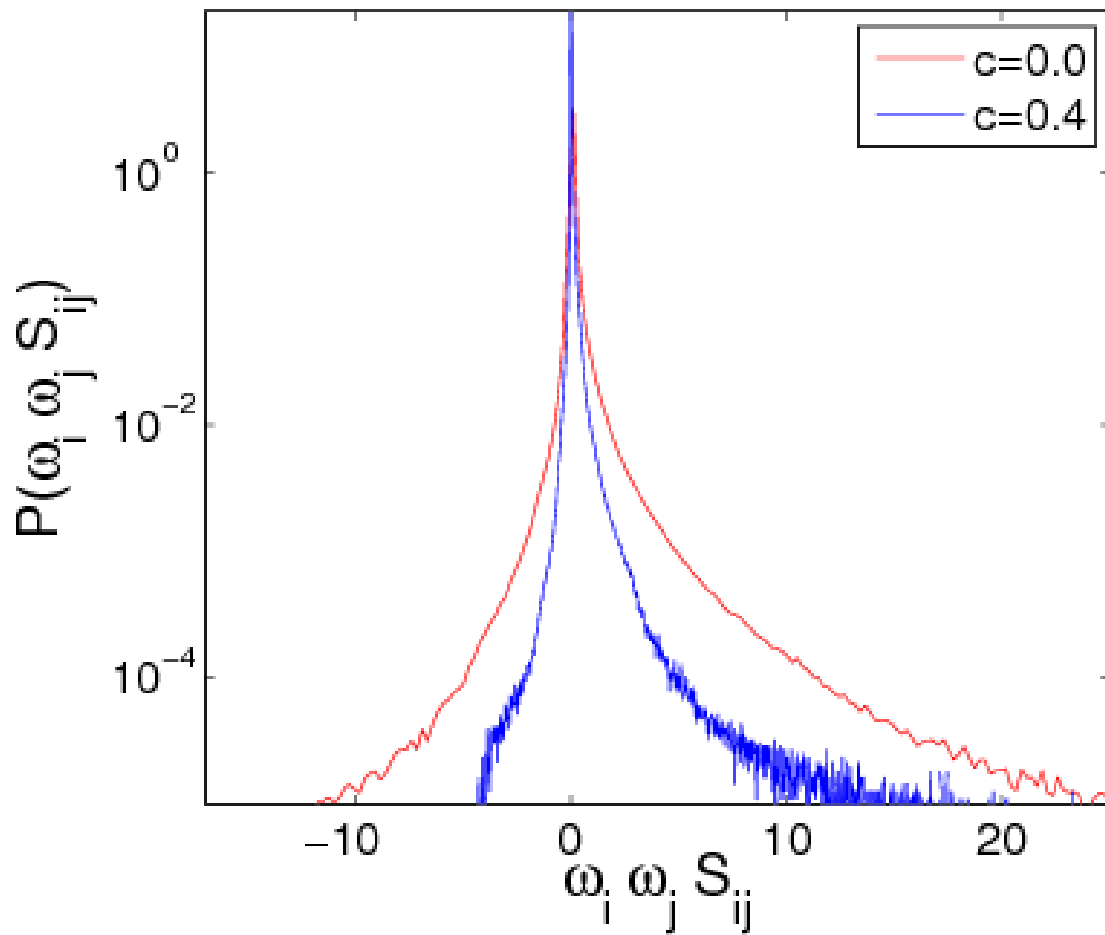
Figure 2.10: The plots of $P(\omega_i \omega_j S_{ij})$ versus $\omega_i \omega_j S_{ij}$, for our run `NSP-256B`, with $[c = 0.4$ (blue)$]$ and without $[c = 0$ (red)$]$ polymer additives. The plots are normalized such that the area under the curve is unity.
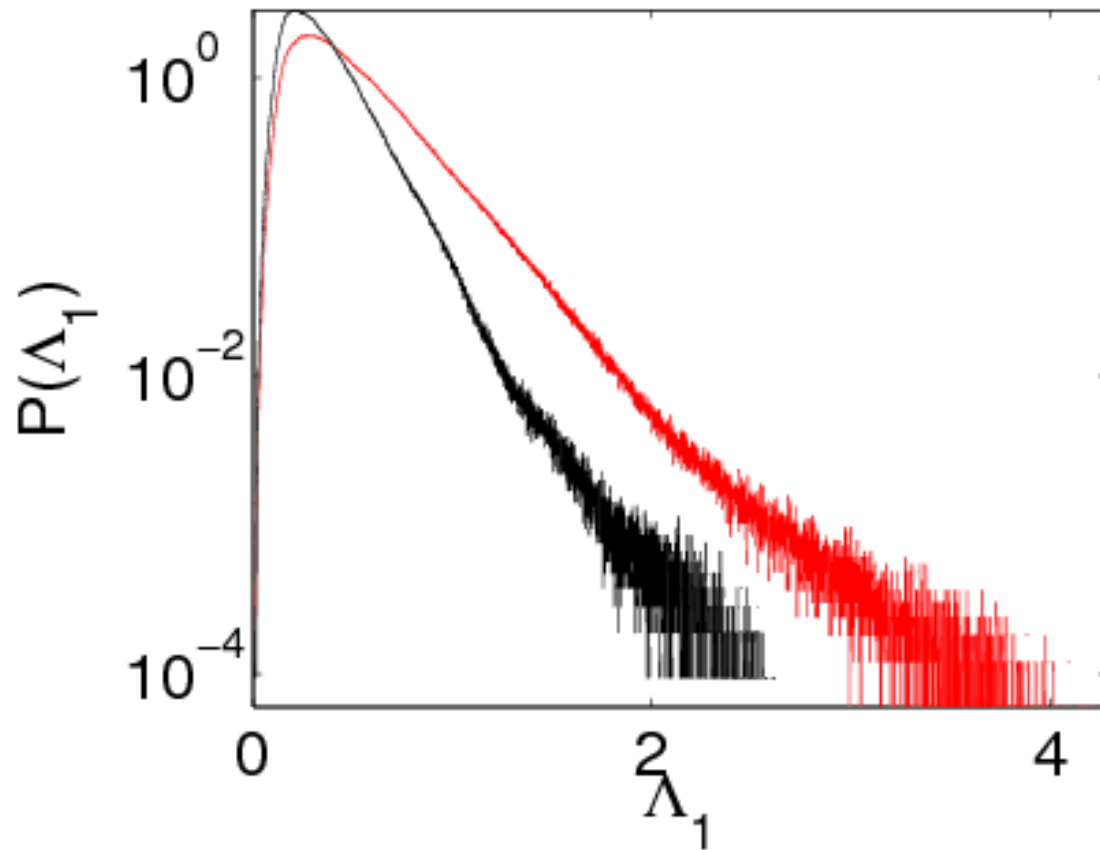
Figure 2.11: Semilog plot of the PDF $P(\Lambda_1)$ versus the first eigenvalue Λ_1 of the rate of strain tensor for the run NSP $-$ 256B, with [$c = 0.4$ (black)] and without [$c = 0.0$ (red)] polymer additives. The plot is normalized such that the area under the curve is unity.
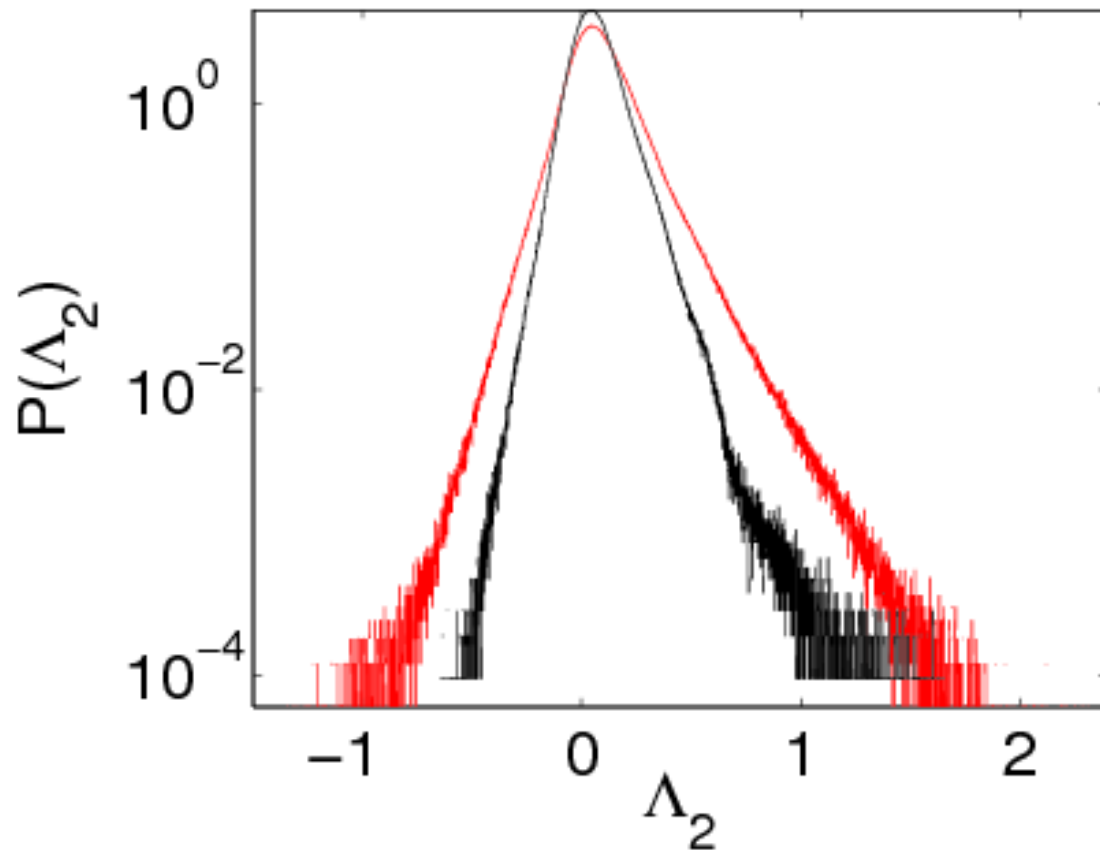
Figure 2.12: Semilog plot of the PDF $P(\Lambda_2)$ versus the second eigenvalue Λ_2 of the rate of strain tensor for the run $\mathtt{NSP-256B}$, with $[c = 0.4$ (black)$]$ and without $[c = 0.0$ (red)$]$ polymer additives. The plot is normalized such that the area under the curve is unity.
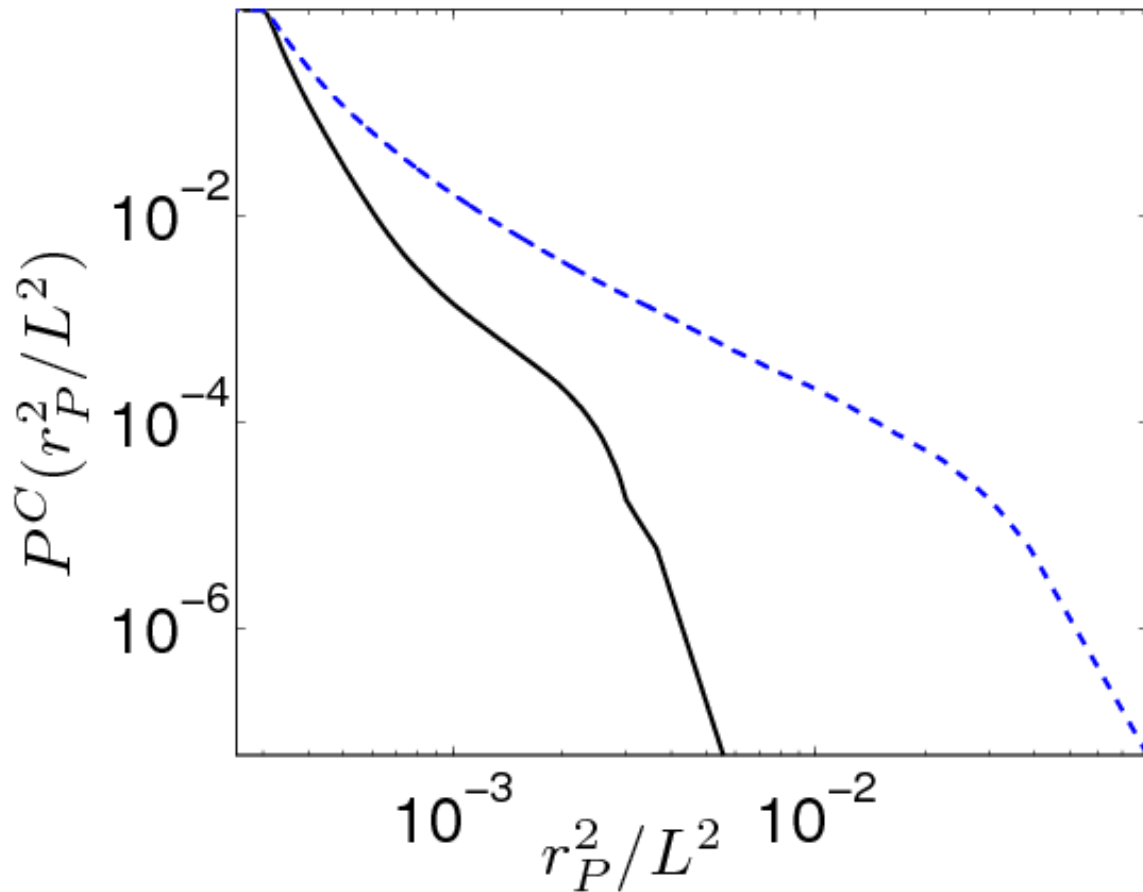
Figure 2.13: The cumulative PDF of scaled polymer extension $P^C(r_P^2/L^2)$ versus r_P^2/L^2 for $c = 0.1 (--)$ and $c = 0.4$ (solid line) (run NSP-256B). Note that increasing the polymer concentration leads to a shrinking of the PDF. The maximum extension (the points where the PDFs make an intercept at the x-axis) for $c = 0$ is around a decade more than that of $c = 0.4$.

2.6 Conclusion

Our study contrasts clearly dissipation-reduction phenomena in homogeneous, isotropic, turbulence and drag reduction in wall-bounded flows. In both these cases the polymers increase the overall viscosity of the solution (see, e.g., Fig. 2.4 and Ref.[14]). In wall-bounded flows the presence of polymers inhibits the flow of the stream-wise component of the momentum into the wall, which, in turn, increases the net throughput of the fluid and thus results in drag reduction, a mechanism that can have no analog in homogeneous, isotropic turbulence. However, the decrease of $\epsilon(t)$ with increasing c (Fig. 2.2) yields a natural definition of DR [Eq. (2.8)] for this case [1]. Thus, if the term *drag reduction* must be reserved for wall-bounded flows, then we suggest the expression *dissipation reduction* for homogeneous, isotropic, turbulence. We have shown that ν_e must be scale-dependent; its counterpart in wall-bounded flows is the position-dependent viscosity of Refs. [5, 8]. Furthermore, as in wall-bounded flows, an increase in c leads to an increase in DR (Fig. 2.2). In channel flows an increase in We leads to an increase in DR, but we find that DR falls marginally as We increases (Fig. 2.2). The reduction in the small-scale intermittency (Fig. 2.7) and in the constant-$|\omega|$ isosurfaces (Fig. 2.8) is in qualitative agreement with channel-flow studies [3], where a decrease in the turbulent volume fraction is seen on the addition of the polymers, and water-jet studies [32], where the addition of the polymers leads to a decrease in small-scale structures. Furthermore, we find that the PDFs of the moduli of the vorticity, the tensor product $\omega_i \omega_j S_{ij}$, and the distribution of the eigenvalues of the rate-of strain tensor are in qualitative agreement with the experiments of Liberzon, *et al.* [25, 26]. We hope our work will stimulate more experi-

---

[1]In some steady-state simulations [24, 13] DR is associated with $E^p(k) > E^f(k)$, for small k. We obtain this for type II, but not type I, initial conditions; but Eq. (2.8) yields drag reduction for both of these initial conditions.

mental studies of dissipation-reduction phenomena in homogeneous, isotropic turbulence.

In next Chapter we investigate such phenomena for forced, statistically steady, homogeneous, isotropic turbulence.

	N	δt	L	ν	τ_P	c
NSP-96	96	1.0×10^{-2}	100	10^{-2}	$0.1 - 3$	0.1, 0.2, 0.3, 0.4
NSP-192	192	1.0×10^{-2}	100	10^{-2}	1	0.1, 0.4
NSP-128A	128	1.0×10^{-2}	100	10^{-2}	1	0.1
NSP-256A	256	1.0×10^{-2}	100	10^{-2}	1	0.1, 0.4
NSP-256B	256	4.0×10^{-3}	100	10^{-3}	1	0.1, 0.4

Table 2.1: The parameters N, δt, L, ν, τ_P and c for our four runs NSP $-$ 96, NSP $-$ 192, NSP $-$ 128A, NSP $-$ 256A, and NSP $-$ 256. NSP $-$ 96, NSP $-$ 192, NSP $-$ 128A, NSP $-$ 256A use type I initial conditions; NSP $-$ 256B uses an initial condition of type II. We also carry out DNS studies of the NS equation with the same numerical resolutions as our NSP runs. $Re \equiv \sqrt{20}\mathcal{E}^{f,m}/\sqrt{3\nu\epsilon^{f,m}}$ and $We \equiv \tau_P\sqrt{\epsilon^{f,m}/\nu}$; NSP $-$ 96: $Re = 47.1$ and $We = 0.03, 0.17, 0.24, 0.28, 0.31, 0.41, 0.48, 0.55, 0.62, 0.68, 1.03$; NSP $-$ 128A, NSP $-$ 192, and NSP $-$ 256A: $Re = 47.1$ and $We = 0.35$; NSP $-$ 256B: $Re = 126.6$ and $We = 0.76$. The Kolmogorov length scale $\eta \equiv (\nu^3/\epsilon)^{1/4}$. For our runs NSP $-$ 192, $\eta \approx 5.3\delta x$ and for our runs NSP $-$ 256A and NSP $-$ 256B, $\eta \approx 1.5\delta x$ where $\delta x = \mathbb{L}/N$ is the grid resolution.

Appendix A

A.1 Finite-difference schemes

The second-order, fourth-order, and sixth-order explicit finite-difference approximations of the derivative of a function $f \in \mathbb{R}^1$ that we use are:

$$f' = (-f_{i-1} + f_{i+1})/(2\Delta x), \tag{A1}$$

$$f' = (f_{i-2} - 8f_{i-1} + 8f_{i+1} - f_{i+2})/(12\Delta x), \text{ and} \tag{A2}$$

$$f' = (-f_{i-3} + 9f_{i-2} - 45f_{i-1} + 45f_{i+1} - 9f_{i+2} + f_{i+3})/(60\Delta x). \tag{A3}$$

A.2 Time marching scheme for Navier-Stokes equation

In this Appendix we illustrate the numerical scheme used for the time evolution of the Navier-Stokes equations. For simplicity, we consider a much simpler ordinary differential equation

$$\frac{dq}{dt} = -\alpha q + f(t) \tag{A4}$$

for which we have the identity

$$e^{\alpha(t+\delta t)}q(t+\delta t) - e^{\alpha t}q(t) = \int_{t}^{t+\delta t} e^{\alpha s}f(s)ds. \tag{A5}$$

The slaved scheme is obtained by writing similar equations for $q(t)$ and $q(t - \delta t)$, and then adding them up to obtain the exact relation

$$q(t + \delta t) = e^{-2\alpha\delta t} q(t - \delta t) + \int_{t-\delta t}^{t+\delta t} e^{-\alpha(t+\delta t - s)} f(s) ds \qquad \text{(A6)}$$

We now replace $f(s)$ under the integral by $f(t)$ to obtain the slaved-frog scheme,

$$q_{n+1} = e^{-2\alpha\delta t} q_{n-1} + \frac{1 - e^{-2\alpha\delta t}}{\alpha} f_n. \qquad \text{(A7)}$$

The slaved-Adam-Bashforth scheme replaces $f(s)$ under the integral by $(3/2)f(t) - (1/2)f(t - \delta t)$, to yield

$$q_{n+1} = e^{-2\alpha\delta t} q_{n-1} + \frac{1 - e^{-2\alpha\delta t}}{\alpha} [(3/2) f_n - (1/2) f_{n-1}]. \qquad \text{(A8)}$$

We use Adams-Bashforth method Appendix A.3 for the time evolution of the polymer-conformation tensor [Eq. (2.7)]; Spatial derivatives are evaluated by using a sixth-order finite-difference scheme of Appendix A.1.

A.3 Adams-Bashforth method

In this Appendix we illustrate the numerical scheme used for the time evolution of the polymer conformation tensor. For simplicity, we consider a much simpler equation:

$$\frac{dq}{dt} = f(q, t) \qquad \text{(A9)}$$

The Adams-Bashforth scheme for Eq. (A9) is

$$q_{n+1} = q_n + [(3/2) f_n - (1/2) f_{n-1}] \delta t. \qquad \text{(A10)}$$

A.4 Pseudo-spectral method

In this Appendix we illustrate the pseudo-spectral method that we have used to solve the Navier-Stokes equation. Our discussion follows

the book of Canuto *et al.* [28]. Recall, the three dimensional Navier-Stokes equations are

$$\frac{\partial \mathbf{u}}{\partial t} = (\mathbf{u} \times \boldsymbol{\omega}) - \nabla p + \nabla^2 \mathbf{u}, \tag{A11}$$

$$\nabla \cdot \mathbf{u} = 0, \tag{A12}$$

where $\mathbf{u}(\mathbf{x}, t)$ and $\boldsymbol{\omega}$ is the velocity and the vorticity field at the position $\mathbf{x}$ and at time t, ν is the viscosity, and $p(\mathbf{x}, t)$ is the pressure at the position $\mathbf{x}$ and at time t. We use a cubic domain with periodic boundary conditions for $\mathbf{u}$, $\boldsymbol{\omega}$, and p, and N^3 collocation points (side $\mathbb{L} = 2\pi$).

Since the fields are periodic, substituting the Fourier series representations for

$$\mathbf{u}(\mathbf{x}, t) = \sum_{\mathbf{k}} \hat{\mathbf{u}}_{\mathbf{k}}(t) \exp(\iota \mathbf{k} \cdot \mathbf{x}), \tag{A13}$$

$$\boldsymbol{\omega}(\mathbf{x}, t) = \sum_{\mathbf{k}} \hat{\boldsymbol{\omega}}_{\mathbf{k}}(t) \exp(\iota \mathbf{k} \cdot \mathbf{x}), \text{ and} \tag{A14}$$

$$p(\mathbf{x}, t) = \sum_{\mathbf{k}} \hat{p}_{\mathbf{k}}(t) \exp(\iota \mathbf{k} \cdot \mathbf{x}), \tag{A15}$$

in Eqs. [(A11) and (A12)] we get

$$\frac{\partial \mathbf{u}_{\mathbf{k}}}{\partial t} = \widehat{(\mathbf{u} \times \boldsymbol{\omega})}_{\mathbf{k}} - \iota \mathbf{k} p_{\mathbf{k}} - \nu k^2 \mathbf{u}_{\mathbf{k}}, \tag{A16}$$

$$\iota \mathbf{k} \cdot \mathbf{u}_{\mathbf{k}} = 0. \tag{A17}$$

Here $\widehat{(\mathbf{u} \times \boldsymbol{\omega})}_{\mathbf{k}}$ is the Fourier transform of the nonlinear advection term in Eq. (A11). We remove the pressure term by taking dot product of Eq. (A16) with $\iota \mathbf{k}$ and using Eq. (A17) to get,

$$\frac{\partial \mathbf{u}_{\mathbf{k}}}{\partial t} = \mathbb{P} \cdot \widehat{(\mathbf{u} \times \boldsymbol{\omega})}_{\mathbf{k}} - \nu k^2 \mathbf{u}_{\mathbf{k}}, \tag{A18}$$

where $\mathbb{P} \equiv \left(\mathcal{I} - \frac{\mathbf{k}\mathbf{k}}{k^2} \right)$ is the transverse projection operator which ensures incompressibility. The nonlinear term $\widehat{(\mathbf{u} \times \boldsymbol{\omega})}_{\mathbf{k}}$ involves convolution operation of $\mathbf{u}_{\mathbf{k}}$ and $\boldsymbol{\omega}_{\mathbf{k}}$ in Fourier space. Evaluating convolutions numerically is computationally very expensive therefore, the following method is used to evaluate the convolution:

1. We inverse Fourier transform $\mathbf{u_k}$ and $\boldsymbol{\omega}_\mathbf{k}$ to real space,

2. We then take the product of $N = \mathbf{u} \times \boldsymbol{\omega}$,

3. The Fourier transform of N gives $\widehat{(\mathbf{u} \times \boldsymbol{\omega})}_\mathbf{k}$.

With $\widehat{(\mathbf{u} \times \boldsymbol{\omega})}_\mathbf{k}$ and $\mathbf{u_k}$ known at every time step we use the method outlined in Appendix A.2 to time integrate Eq. (A18).

Since the convolution term is evaluated in the real space before taking its Fourier transform, the above method of numerically solving the Navier-Stokes equations is called a pseudo-spectral method.

The errors in the pseudo-spectral method occur mainly because of the procedure described above to evaluate the nonlinear term and are known as aliasing errors. To understand the origin of these aliasing errors, we consider the example problem of calculating the Fourier transform $\hat{w}_k$ of a scalar $w(x) = f(x)g(x)$ where $f(x)$ and $g(x)$ are two scalars (see Section-3.2 of Ref. [28]). On an N-point collocation grid, with $x_j, j = 0, \cdots, N-1$, the product becomes:

$$w_j = f_j g_j, \tag{A19}$$

where $w_j \equiv w(x_j)$, $f_j \equiv f(x_j)$, and $f_j \equiv f(x_j)$. Introducing discrete Fourier transforms

$$f_j = \sum_{m=-N/2}^{N/2-1} \hat{f}_m \exp(\iota m x_j), \tag{A20}$$

$$g_j = \sum_{n=-N/2}^{N/2-1} \hat{g}_n \exp(\iota n x_j), \text{and} \tag{A21}$$

$$\hat{w}_k = \frac{1}{N} \sum_{j=0}^{N-1} w_j \exp(-\iota k x_j), \tag{A22}$$

where $k = -N/2, \cdots, N/2 - 1$ and $x_j = 2\pi j/N$, and using Using the discrete orthogonality relation

$$\frac{1}{N} \sum_{j=0}^{N-1} \exp(\iota k x_j) = \begin{cases} 1 & \text{if } k = Np, \ p = 0, \pm 1, \pm 2, \cdots \\ 0 & \text{otherwise} \end{cases}$$

we get,

$$\hat{w}_k = \sum_{m+n=k} \hat{f}_m \hat{g}_n + \sum_{m+n=k\pm N} \hat{f}_m \hat{g}_n. \tag{A23}$$

The first term on the right-hand side is the convolution whereas, the second term on the right-hand side is the aliasing error. This aliasing error can be removed by setting the coefficients $\hat{f}_m$ and $\hat{g}_n$ to zero for all $|m|, |n| \geq N/3$. In three dimensions this can be ensured by setting all the Fourier modes for which $k = \sqrt{k_x^2 + k_y^2 + k_z^2} \geq N/3$ to zero. This de-aliasing technique is referred to as the $2/3$-rule.

Bibliography

[1] P. Perlekar, D. Mitra, and R. Pandit, *Phys. Rev. Lett.* **97**, 264501 (2006).

[2] P. Virk, *AIChE* **21**, 625 (1975).

[3] P.H.J. vanDam, G. Wegdam, and J. van der Elsken, *J. Non-Newtonian Fluid Mech.* **53**, 215 (1994).

[4] J.M.J. Den Toonder, M.A. Hulsen, G.D.C. Kuiken, and F.T.M. Nieuwstadt, *J. Fluid. Mech.* **337**, 193 (1997).

[5] J.L. Lumley, *J. Polymer Sci.* **7**, 263 (1973).

[6] K.R. Sreenivasan and C.M. White, *J. Fluid Mech.* **409**, 149 (2000).

[7] P.K. Ptasinski, F.T.M. Nieuwstadt, B.H.A.A. Van den Brule, and M.A. Hulsen, *J. Fluid Mech.* **490**, 251 (2003).

[8] V.S. L'vov, A. Pomyalov, I. Procaccia, and V. Tiberkevich, *Phys. Rev. Lett.* **92**, 244503 (2004).

[9] I. Procaccia, V.S. Ĺvov, and R. Benzi, *Rev. Mod. Phys.* **80**, 225 (2008).

[10] G. Boffetta, A. Celani, and A. Mazzino, *Phys. Rev. E* **71**, 036307 (2005).

[11] M. Tabor and P.G. De Gennes, *Europhys. Lett.* **2**, 519 (1986).

[12] J.K. Bhattacharjee and D. Thirumalai, *Phys. Rev. Lett.* **67**, 196 (1991).

[13] R. Benzi, E. De angelis, R. Govindarajan, and I. Procaccia, *Phys. Rev. E* **68**, 016308 (2003).

[14] R. Benzi, E. Ching, and I. Procaccia, *Phys. Rev. E* **70**, 026304 (2004).

[15] C. Kalelkar, R. Govindarajan, and R. Pandit, *Phys. Rev. E* **72**, 017301 (2004).

[16] E. De angelis, C.M. Casicola, R. Benzi, and R. Piva, *J. Fluid Mech.* **531**, 1 (2005).

[17] S. Berti, A. Bistagnino, G. Boffertta, A. Celani, and S. Musacchio, *Europhys. Lett.* **76**, 63 (2006).

[18] T. Peters and J. Schumacher, *Phys. Fluids* **19**, 065109 (2007).

[19] E. van Doorn, C.M. White, and K.R. Sreenivasan, *Phys. Fluids* **11**, 2387 (1999).

[20] W. McComb, J. Allan, and C. Greated, *Phys. Fluids* **20**, 873 (1977).

[21] C. Friehe and W. Schwarz, *J. Fluid Mech.* **44**, 173 (1970).

[22] D. Bonn, Y. Couder, P.H.J. van Dam, and S. Douady, *Phys. Rev. E* **47**, R28 (1993).

[23] D. Bonn, Y. Amarouchene, C. Wagner, S. Douady, and O. Cadot, *J. Phys. CM* **17**, S1219 (2005).

[24] T. Vaithianathan and L.R. Collins, *J. Comput. Phys.* **187**, 1 (2003).

[25] A. Liberzon, M. Guala, B. Luthi, W. Kinzelbach, and A. Tsinober, *Phys. Fluids* **17**, 031707 (2005).

[26] A. Liberzon, M. Guala, W. Kinzelbach, and A. Tsinober, *Phys. Fluids* **18**, 125101 (2006).

[27] A. Peterlin, *J. Polym. Sci., Polym. Lett.* **4**, 287 (1966).

[28] C. Canuto, M.Y. Hussaini, A. Quarteroni, and T.A. Zang, *Spectral methods in Fluid Dynamics* (Spinger-Verlag, Berlin, 1988).

[29] A. Vincent and M. Meneguzzi, *J. Fluid Mech.* **225**, 1 (1991).

[30] Y. Kaneda, T. Ishihara, M. Yokokawa, K. Itakura, and A. Uno, *Phys. Fluids* **15**, L21 (2003).

[31] D. Mitra, J. Bec, R. Pandit, and U. Frisch, *Phys. Rev. Lett.* **94**, 194501 (2005).

[32] J. Hoyt and J. Taylor, *Phys. Fluids* **20**, S253 (1977).

Chapter 3

Effect of polymer additives on statistically steady turbulence

In the last Chapter we carried out a study that revealed the effects of polymers on decaying turbulence; in this Chapter we carry forward our study to the case of statistically steady, forced, homogeneous, isotropic turbulence. As in the last Chapter, our study reveals clear manifestations of dissipation-reduction phenomena: On the addition of polymers to the turbulent fluid, we obtain a reduction in the energy dissipation rate, a significant modification of the fluid energy spectrum especially in the deep-dissipation range, a suppression of small-scale intermittency, and a decrease in small-scale vorticity filaments.

3.1 Introduction

A recent experiment [1] has studied the effects of polymers on the second-order longitudinal velocity structure function at very high Reynolds numbers ($Re_\lambda \simeq 200 - 350$). This experiment shows that the inertial-range exponent is not modified by the polymers but the energy content of the dissipation range is dramatically reduced. In another set of experiments, Liberzon, *et al.*; have studied the effects of polymer additives on statistically steady turbulence at moderate Reynolds number ($Re_\lambda \simeq 40$). These experiments have investigated

how the polymers affect the topological properties of the turbulent fluid by measuring the PDFs of the strain and its tensorial products. They have shown thereby that polymer additives suppress small-scale structures in turbulent flows [2, 3].

These experimental studies have motivated us to extend our DNS of decaying fluid turbulence with polymer additives to the case of forced, homogeneous, isotropic turbulence. Our study is divided into two parts.

In Part-I (Secs. 3.5.1-3.5.3), we carry out a numerical study of statistically steady forced turbulence at moderate Reynolds numbers ($Re_\lambda \simeq 80$). The forcing used is designed such that the energy injected into the fluid remains fixed [4], both with and without polymers, to mimic the experiments of Liberzon, *et al.* [2, 3]. We find that, on the addition of polymers, the steady-state energy and the energy dissipation rate are reduced. This dissipation reduction (defined for decaying turbulence in our earlier work [5]) increases with an increase in c (or We) at fixed We (or at fixed c). In the energy spectrum we find that the fluid energy content at small wavevectors is marginally increased on the addition of polymers, but it decreases for intermediate wavevectors. In this study we are not able to resolve the deep-dissipation range because of the relatively low grid-resolution, $N = 256$ i.e., 256^3 collocation points, and moderate Reynolds numbers $Re_\lambda \simeq 80$. We also study the structural properties of the fluid with and without polymers and show that the effect of the polymers is to suppress the large-vorticity and large-strain events. We find our results to be in qualitative agreement with the experiments of Liberzon, *et al.* [2, 3]. Finally, we have also studied the effect of the polymer relaxation time τ_P on the polymer extensions. As in our study of decaying turbulence, we find that the polymer extension increases with an increase in the polymer relaxation time.

In Part-II (Sec. 3.6) we carry out the highest-resolution direct numerical simulation of statistically steady forced fluid turbulence with polymer additives that has been attempted so far. The fluid is driven by an external stochastic forcing [6]. Our study has been designed to uncover the effect of polymers on the deep-dissipation range, so our Reynolds numbers are small $Re_\lambda \simeq 16$. On comparing the energy spectrum, with and without polymers, we find that the polymers suppress the energy content in the dissipation range but, in the deep-dissipation range, the energy content of the fluid in the presence of polymers is increased. Finally, we calculate the second-order velocity structure function $S_2(r)$ directly from the energy spectrum. In contrast to the velocity energy spectrum in Fourier space, which shows an increase in the energy content at deep-disspation-range wavevectors: $S_2(r)$ with polymers is smaller than $S_2(r)$ without polymers in this range.

3.2 Model and Equations

As in Chapter-2 we model the polymeric fluid solution by using the Navier-Stokes equations for the fluid coupled with the Finitely Extensible Nonlinear Elastic-Peterlin (FENE-P) equation for the polymer additives. The polymer contribution to the fluid is modelled by an extra stress term in the NS equations. The FENE-P equation approximates a polymer molecule by a nonlinear dumbbell, which has a single relaxation time and an upper bound on the maximum extension. The NS and FENE-P (henceforth NSP) equations are

$$D_t\mathbf{u} \;=\; \nu\nabla^2\mathbf{u} + \frac{\mu}{\tau_P}\nabla.[f(r_P)\mathcal{C}] - \nabla p + \mathbf{f}; \qquad (3.1)$$

$$D_t\mathcal{C} \;=\; \mathcal{C}.(\nabla\mathbf{u}) + (\nabla\mathbf{u})^T.\mathcal{C} - \frac{f(r_P)\mathcal{C} - \mathcal{I}}{\tau_P}. \qquad (3.2)$$

Here $\mathbf{u}(\mathbf{x}, t)$ is the fluid velocity at point $\mathbf{x}$ and time t, incompressibility is enforced by $\nabla.\mathbf{u} = 0$, $D_t = \partial_t + \mathbf{u}.\nabla$, ν is the kinematic viscosity of the

fluid, μ the viscosity parameter for the solute (FENE-P), τ_P the polymer relaxation time, ρ the solvent density (set to 1), p the pressure, $\mathbf{f}(\mathbf{x}, t)$ the external forcing at point $\mathbf{x}$ and time t, $(\nabla\mathbf{u})^T$ the transpose of $(\nabla\mathbf{u})$, $\mathcal{C}_{\alpha\beta} \equiv \langle R_\alpha R_\beta \rangle$ the elements of the polymer-conformation tensor $\mathcal{C}$ (angular brackets indicate an average over polymer configurations), $\mathcal{I}$ the identity tensor with elements $\delta_{\alpha\beta}$, $f(r_P) \equiv (L^2 - 3)/(L^2 - r_P^2)$ the FENE-P potential that ensures finite extensibility, $r_P \equiv \sqrt{Tr(\mathcal{C})}$ and L the length and the maximum possible extension, respectively, of the polymers, and $c \equiv \mu/(\nu + \mu)$ a dimensionless measure of the polymer concentration [7]; $c = 0.1$ corresponds, roughly, to 100ppm for polyethylene oxide [8]. Table 3.1 lists the parameters of our simulations.

3.3 Numerical Scheme

In earlier numerical studies of homogeneous, isotropic turbulence with polymer additives it was shown that sharp gradients are formed in the time-evolution of the polymer conformation tensor which can lead to dispersion errors [7, 9]. To avoid these dispersion errors, shock-capturing schemes were used to evaluate the polymer-advection term $[(\mathbf{u} \cdot \nabla)\mathcal{C}]$ [9]. In our simulations we have modified the Cholesky–decomposition scheme (see Ref. [7] and Sec. 2.3 of the last Chapter), which preserves the symmetric positive definite nature of the tensor $\mathcal{C}$, to incorporate the large gradients of the polymer conformation tensor. This is easily achieved by evaluating the polymer-advection term $[(\mathbf{u} \cdot \nabla)\ell]$ by using the Kurganov-Tadmor shock capturing scheme (see Appendix B.2).

3.4 Initial conditions

We use the following initial conditions (superscript 0): $\mathcal{C}^0_{mn}(\mathbf{x}) = \delta_{mn}$ for all $\mathbf{x}$; and $u^0_m(\mathbf{k}) = P_{mn}(\mathbf{k})v^0_n(\mathbf{k})\exp(\iota\theta_n(\mathbf{k}))$, with $m, n = x, y, z$,

$P_{mn} = (\delta_{mn} - k_m k_n / k^2)$ the transverse projection operator, k the wave-vector with components $k_m = (-N/2, -N/2 + 1, \ldots, N/2)$, $k = |\mathbf{k}|$, $\theta_n(\mathbf{k})$ random numbers distributed uniformly between 0 and 2π, and $v_n^0(\mathbf{k})$ chosen such that the initial kinetic-energy spectrum is $E(k) = k^4 \exp(-2.0k^2)$. Physically this initial conditions correspond to a state in which the fluid energy is concentrated, to begin with, at small k (large length scales). For our run $\texttt{NSP} - 512$, initially the polymers are in a coiled state. The simulation runs for $45T_{\mathrm{eddy}}$ and a steady state is reached in $10T_{\mathrm{eddy}}$. For our runs $\texttt{NSP} - 256\texttt{A}$ and $\texttt{NSP} - 256\texttt{B}$ we conduct a pure-fluid simulation till a steady state is reached (around $10 - 15T_{\mathrm{eddy}}$, where $T_{\mathrm{eddy}} \equiv u_{rms}/l_{int}$, u_{rms} is the root-mean-square velocity and $l_{in} \equiv \sum_k k^{-1} E(k) / \sum_k E(k)$ is the integral length scale.). Once a steady state is reached we add the polymers to the fluid at $27T_{\mathrm{eddy}}$. The statistics for the polymers are collected after another $5 - 6T_{\mathrm{eddy}}$ have elapsed so that transients die down. We collect data for averages for $25T_{\mathrm{eddy}}$ for our runs $\texttt{NSP} - 256\texttt{A}$ and $\texttt{NSP} - 256\texttt{B}$.

3.5 Results

We now present the results that we have obtained from our DNS. In addition to $\mathbf{u}(\mathbf{x}, t)$, its Fourier transform $\mathbf{u_k}(t)$, and $\mathcal{C}(\mathbf{x}, t)$, we monitor the vorticity $\boldsymbol{\omega} \equiv \nabla \times \mathbf{u}$, the kinetic-energy spectrum $E(k, t) \equiv \sum_{k-1/2 < k' \leq k+1/2} |\mathbf{u}_{\mathbf{k}'}^2(t)|$, the total kinetic energy $\mathcal{E}(t) \equiv \sum_k E(k, t)$, the energy-dissipation-rate $\epsilon(t) \equiv \nu \sum_k k^2 E(k, t)$, the probability distribution of scaled polymer extensions $P(r_P^2/L^2)$, the PDF of the strain and the modulus of the vorticity, and the eigenvalues of the strain tensor. For notational convenience, we do not display the dependence on c explicitly.

3.5.1 Time evolution of E and ϵ

In this Subsection we study the effects of polymer additives on the time evolution of the energy E and the energy dissipation rate ϵ for our runs $\mathtt{NSP-256A}$ and $\mathtt{NSP-256B}$. Figure 3.1 shows the time evolution of the energy. The polymers are added to the fluid at $t = 27T_{\mathrm{eddy}}$. We find that the addition of polymers leads to a new steady state. For $We = 3.5$ and $We = 7.1$ the average energy of the fluid with polymers is reduced in comparison to the average energy of the fluid without polymers.

By using Eq. (3.1), the energy-balance equation for the fluid with polymer additives is:

$$\frac{dE}{dt} = \epsilon_\nu + \epsilon_P + \epsilon_{inj},$$
$$\text{where}$$
$$\epsilon_\nu = -\nu\frac{1}{V}\int \mathbf{u}\cdot\nabla^2\mathbf{u},$$
$$\epsilon_P = (\frac{\mu}{\tau_P})\left\{\frac{1}{V}\int \mathbf{u}\cdot\nabla[f(r_P)\mathcal{C}]\right\},$$
$$\epsilon_{inj} = \frac{1}{V}\int \mathbf{f}\cdot\mathbf{u}.$$

In the steady state $\frac{dE}{dt} = 0$ and the energy injected is balanced by the fluid dissipation rate ϵ_ν and the polymer dissipation ϵ_P. Our simulations are designed to keep energy injection fixed. Therefore, we can now address the question of how the dissipation gets distributed between the fluid and polymer subsystems in forced turbulence. In Fig. 3.2 we present plots of $\epsilon_\nu(t)$ versus t for $We = 3.5$ and $We = 7.1$. The polymer concentration is kept fixed at $c = 0.1$. We find that the averages ϵ_ν decreases on increasing We.

This suggests the following natural definition of the percentage dissipation reduction for forced, homogeneous, isotropic turbulence:

$$\mathrm{DR} \equiv \left(\frac{\langle \epsilon^f \rangle - \langle \epsilon^p \rangle}{\langle \epsilon^f \rangle}\right) \times 100\%; \tag{3.3}$$
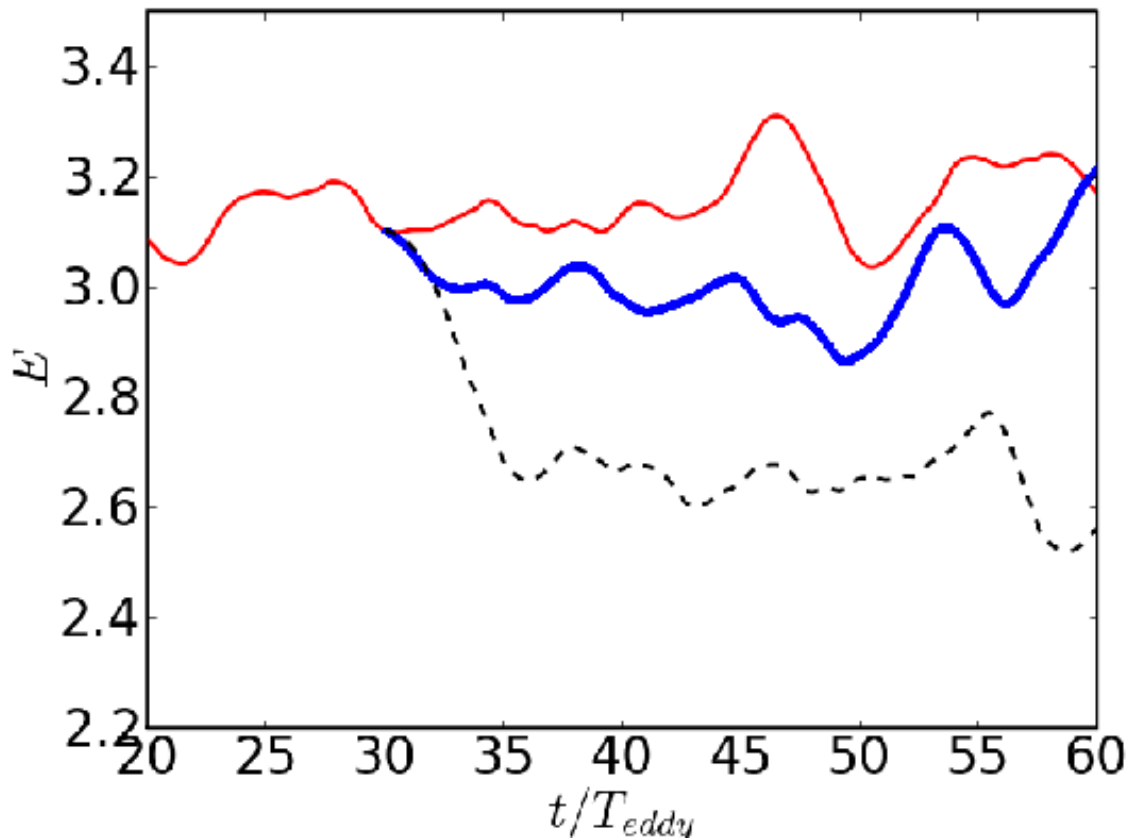
Figure 3.1: Temporal evolution of the energy E versus $t/Teddy$ (runs `NSP-256A` and `NSP-256B`) for Weissenberg numbers $We = 3.5$ (blue circles) and $We = 7.1$ (black dashed line). The corresponding plot for the pure fluid case is also shown for reference (red line). The polymers are added to the fluid at $t = 27T_{\text{eddy}}$.
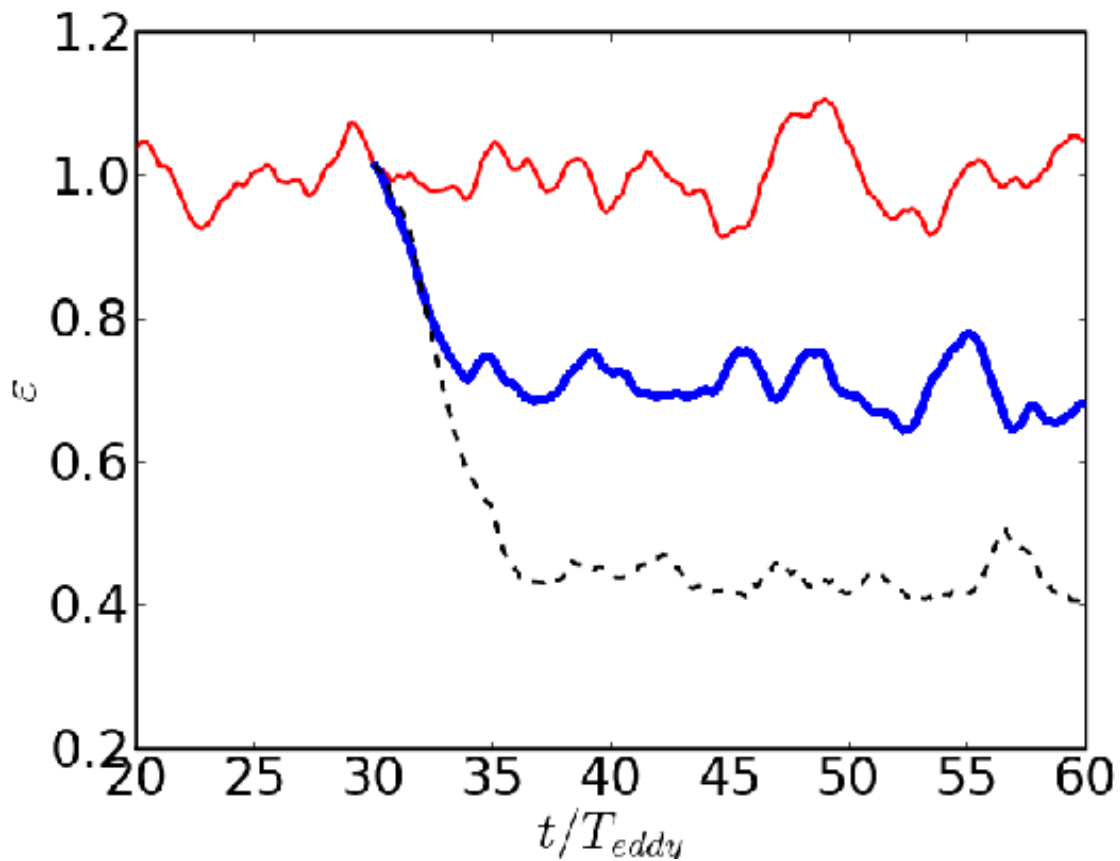
Figure 3.2: Temporal evolution of the energy dissipation rate ϵ versus t/T_{eddy} (runs `NSP-256A` and `NSP-256B`) for Weissenberg number $We = 3.5$ (blue circles) and $We = 7.1$(black dashed line). The corresponding plot for the pure fluid case is also shown for reference (red line). The polymers are added to the fluid at $t = 27T_{\text{eddy}}$.

here (and henceforth) the superscripts f and p stand, respectively, for the fluid without and with polymers. The increase in DR with We clearly indicates that the polymer dissipation increases with and increase in We. By using the above definition, we find that, in contrast to our decaying-turbulence studies (Chapter 2 and Ref. [5]), DR increases with an increase in the Weissenberg number. For $We = 3.5$, DR $\simeq 30\%$ and, for $We = 7.1$, DR $\simeq 50\%$. We believe that this increase of DR with We arises because the polymer extension and, therefore, the polymer stresses are much stronger in forced turbulence in comparison to decaying turbulence. The plot in Fig. 3.3 shows the cumulative PDF of the scaled polymer extension (see Figure 2.13 in the last Chapter for a comparison with decaying turbulence).

3.5.2 Energy spectra

In this Section we study effects of the polymer additives on the fluid energy spectrum for two different values of We. We find that the energy content of the intermediate wave-vectors decreases with an increase in the Weissenberg number. At small k, we observe a small increase in the spectrum on the addition of the polymers, but this increase is within our numerical errorbars, so we cannot draw any conclusion from it.

3.5.3 Small scale structures

We now study how polymers affect the structure of homogeneous, isotropic turbulence and make specific comparisons with the experiments of Liberzon, *et al.* [2, 3]. In particular, we plot the PDFs of the modulus of the vorticity $|\boldsymbol{\omega}|$ and the local energy dissipation rate $\epsilon_{loc} = \sum_{i,j} (\partial_i u_j + \partial_j u_i)^2/2$ in Figs. 3.5. We find that the addition of polymers causes a decrease in the regions of high vorticity and high dissipation [Figs. 3.5]. Furthermore, on normalising any $|\boldsymbol{\omega}|$ or ϵ_{loc} by
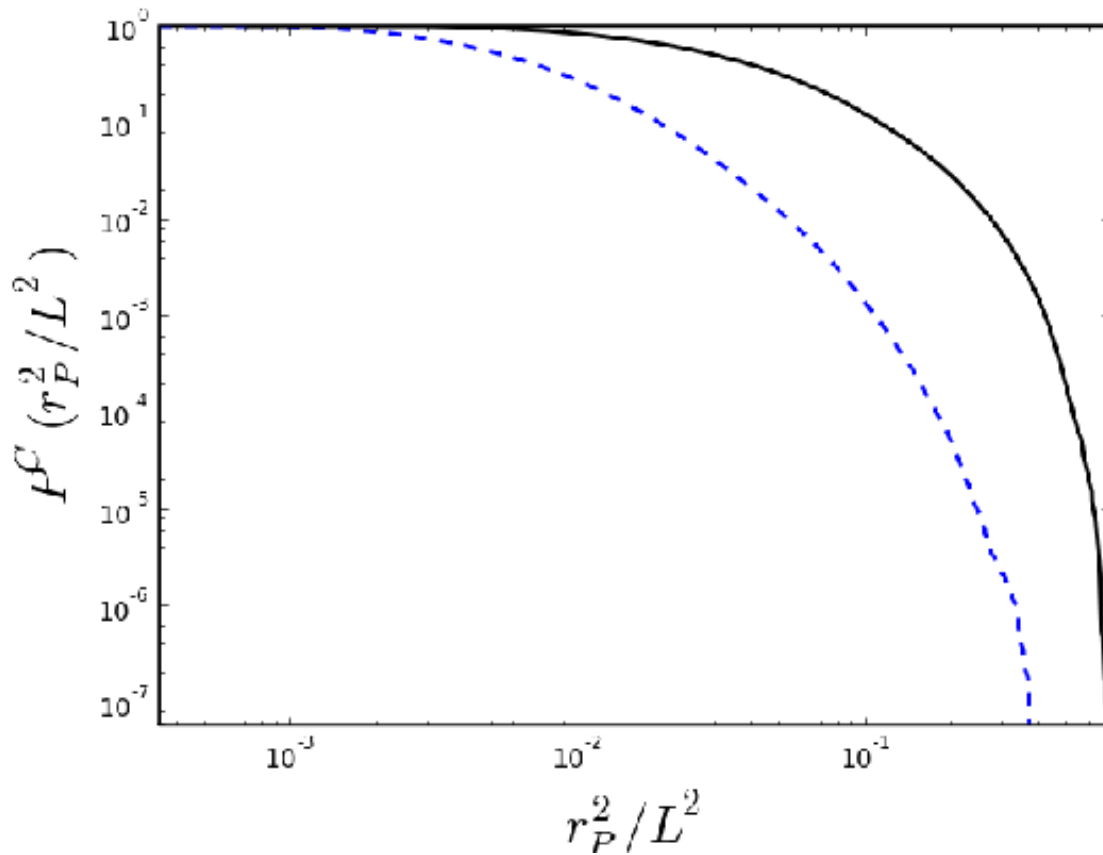
Figure 3.3: Log-log plot of the cumulative PDF of scaled polymer extension $P^C(r_P^2/L^2)$ versus r_P^2/L^2 for $We = 3.5$ (- -) (run `NSP-256A`) and $We = 7.1$ (solid line) (run `NSP-256B`). Note that increasing the polymer Weissenberg leads to larger polymer extensions. The plots are made from the polymer configuration at $t = 60T_{\text{eddy}}$.
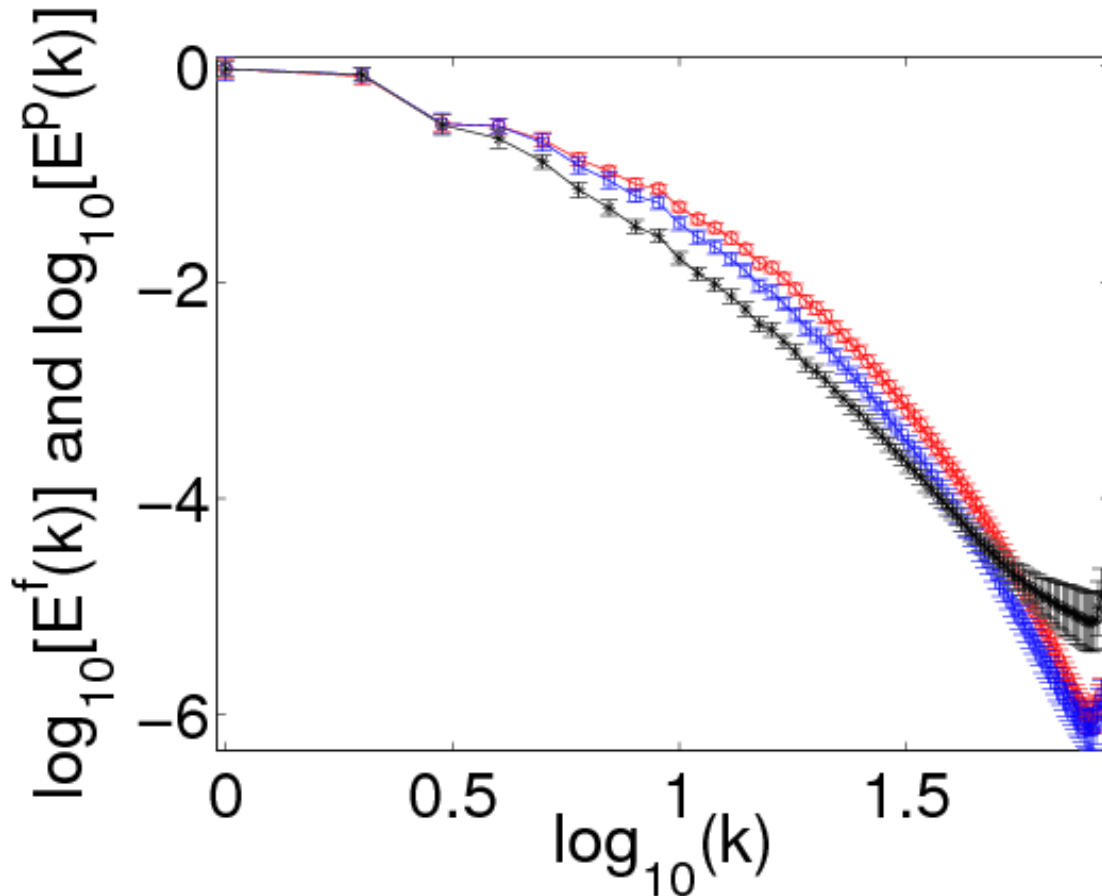
Figure 3.4: Log-log plots of the energy spectra $E^f(k)$ and $E^p(k)$ versus k (runs `NSP-256A` and `NSP-256B`) for different polymer Weissenberg numbers $We = 3.5$ (square), $We = 7.1$ (star) and $c = 0.1$ with two-standard-deviation error bars. The corresponding pure-fluid spectrum (circles) is shown for comparison.

their standard deviations, the PDFs of the pure fluid and those with the polymers collapse onto each other (Figs. 3.6). The above results are in qualitative agreement with the results of Refs. [2, 3] (see Fig. 2 of Ref. [2] and Fig. 3 of Ref. [3]).

In the high-Re_λ, high-resolution, DNS studies [10, 11], it is found that iso-$|\boldsymbol{\omega}|$ surfaces are filamentary for large values of $\boldsymbol{\omega}$. In Fig. 3.7 we plot iso-$|\boldsymbol{\omega}|$ surfaces for the fluid with ($c = 0.1$; $We = 3.5$ or 7.1) and without polymer additives. In the absence of polymers, the large-$|\boldsymbol{\omega}|$ surfaces are filamentary in agreement with earlier studies [5, 10]. On the addition of polymers a significant fraction of these filaments are suppressed.

The eigenvalues of the rate-of-strain tensor $S_{ij} = (\partial_i u_j + \partial_j u_i)/\sqrt{2}$ (denoted by Λ_n, $n = 1, 2, 3$) provide a measure of the local stretching and compression of the fluid. In our study, the eigenvalues are arranged as $\Lambda_1 > \Lambda_2 > \Lambda_3$. By using the incompressibility condition we get $\sum_i \Lambda_i = 0$; therefore, for an incompressible fluid, one of the eigenvalues (Λ_1) should be positive and one should be negative (Λ_3). The intermediate eigenvalue Λ_2 can be either positive or negative. In Figs. (3.8) and (3.9) we plot the PDFs of the eigenvalues of the S. As in our earlier study on decaying turbulence (see Chapter 2), the tails of the PDFs shrink on the addition of polymers. This indicates that the addition of the polymers leads to a substantial decrease in the regions of large strain. The above result is in qualitative agreement with the experiments of Liberzon, *et al.* [2] (see Fig. 3(b) of Ref. [2]).

In Chapter 1 we have shown that the topological properties of a three-dimensional turbulent fluid can be classified by the $Q - R$ plot, where $Q = -\text{Tr}(A^2)/2$ and $R = -\text{Tr}(A^3)/3$ are the invariants of the velocity-gradient tensor $\nabla \mathbf{u}$. In Fig. 3.10 we plot the joint PDFs $P(R, Q)$ for the fluid with and without polymers; although the qualitative structure of the PDFs remains the same, the regions of large R
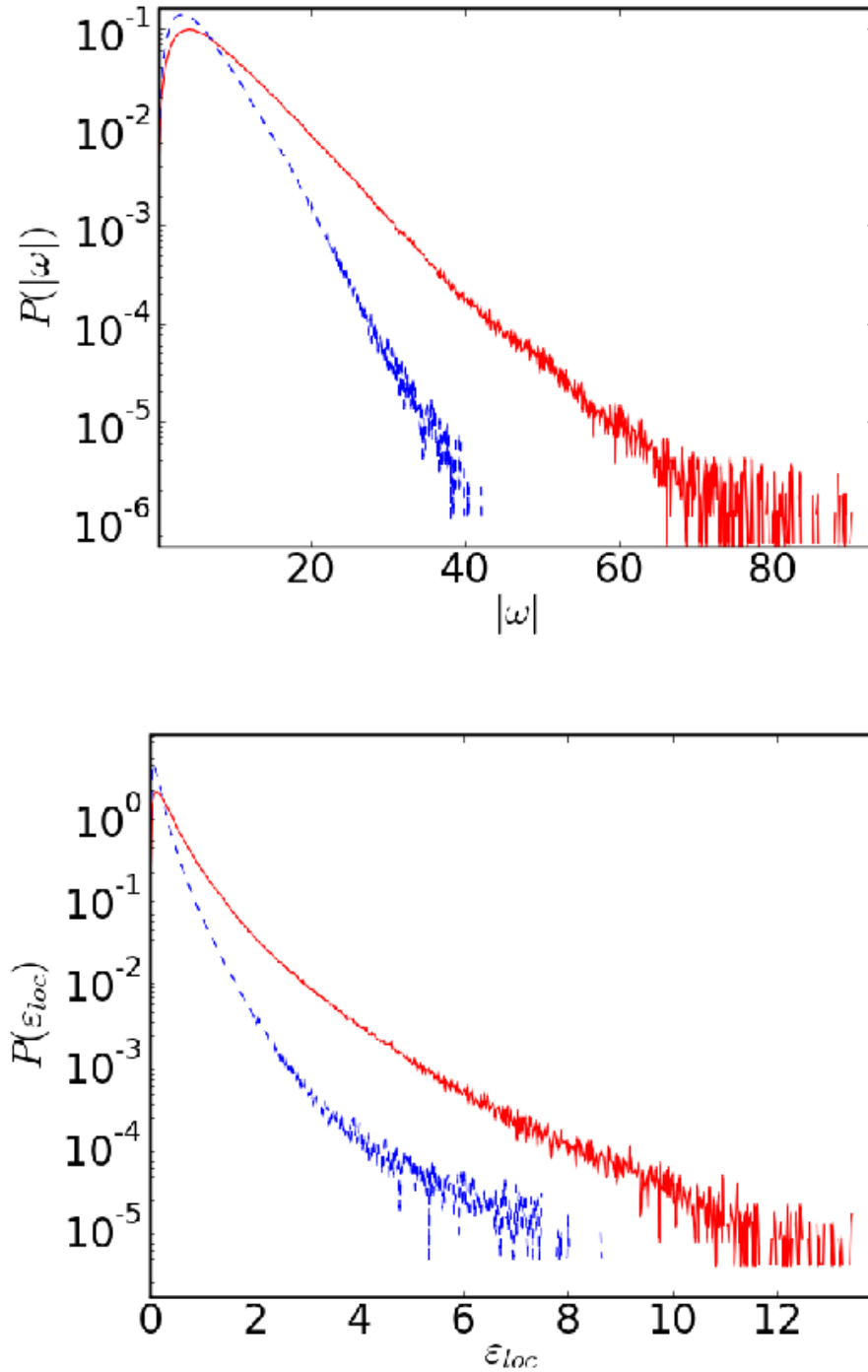
Figure 3.5: Semilog plots of the PDFs $P(|\boldsymbol{\omega}|)$ versus $|\boldsymbol{\omega}|$ (top panel) and $P(\epsilon_{loc})$ versus ϵ_{loc} (bottom panel), for our run NSP-256B, with [$c = 0.1$, $We = 7.1$ (dashed line)] and without [$c = 0$ (red)] polymer additives.
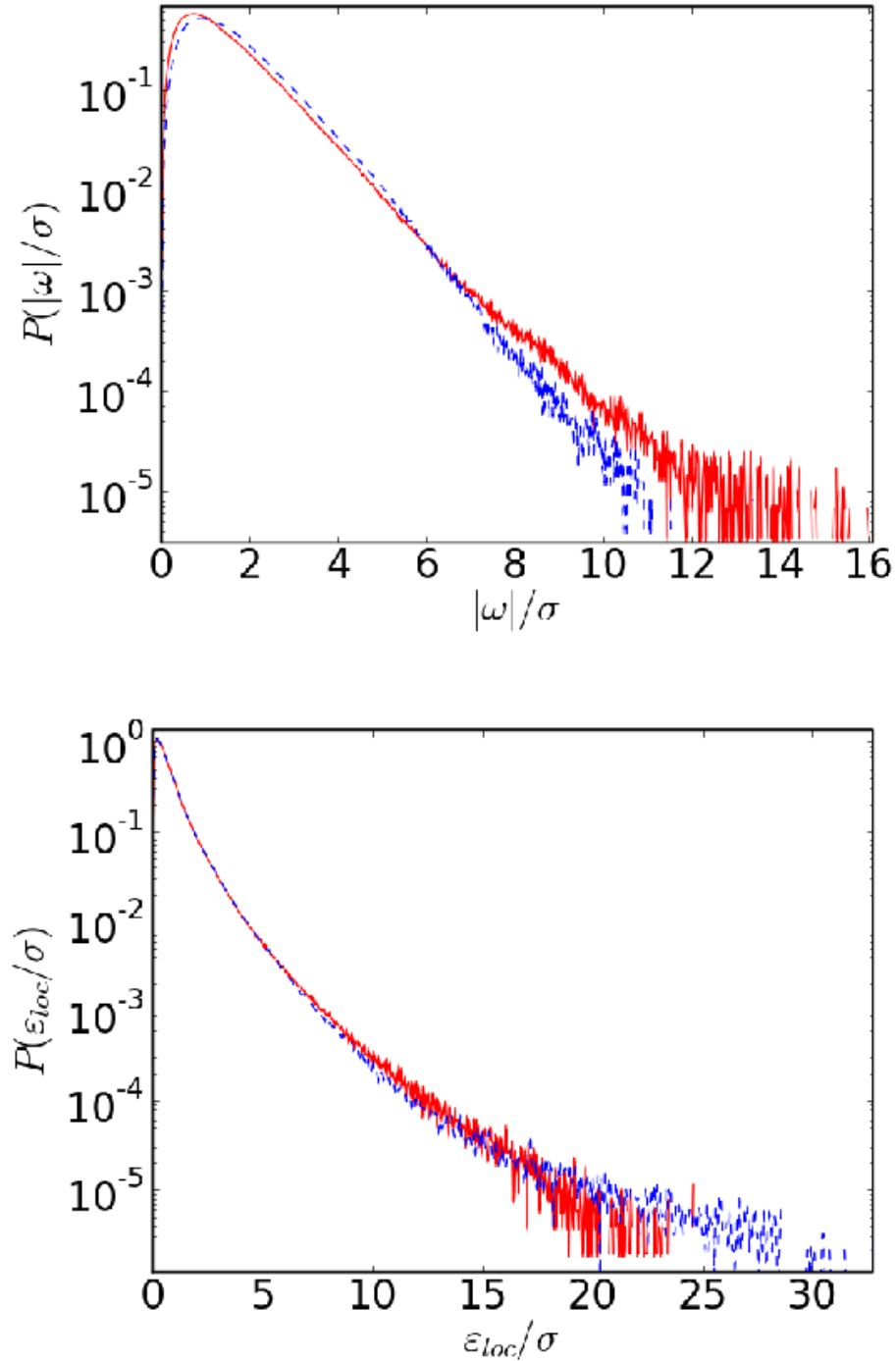
Figure 3.6: Semilog plots of the scaled PDFs $P(|\boldsymbol{\omega}|/\sigma)$ versus $|\boldsymbol{\omega}|/\sigma$ (top panel) and $P(\epsilon_{loc}/\sigma)$ versus $\epsilon_{loc}/sigma$ (bottom panel), where σ is the standard deviation for the respective fields, for our run NSP-256B, with [$c = 0.1$, $We = 7.1$ (dashed line)] and without [$c = 0$ (line)] polymer additives. The plots are normalized such that the area under the curve is unity.
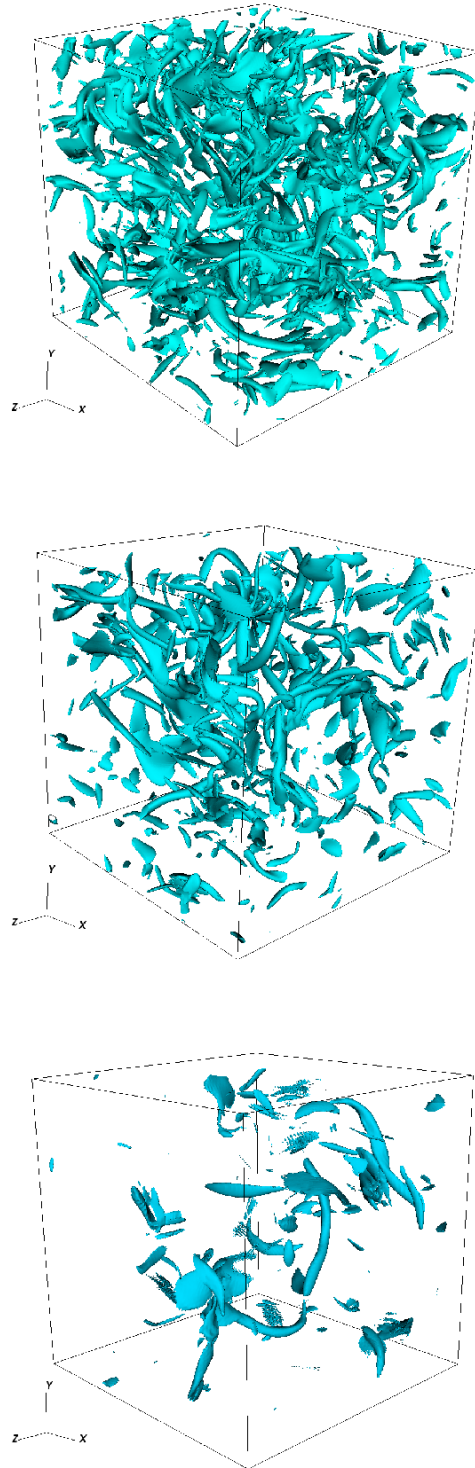
Figure 3.7:   Constant-$|\boldsymbol{\omega}|$ isosurfaces for $|\boldsymbol{\omega}| = \overline{|\boldsymbol{\omega}|} + 2\sigma$ at $t \approx 60T_{\text{eddy}}$ without (Top) and with polymers [Middle $We = 3.5$ (`NSP-256A`) and Bottom $We = 7.1$ (run `NSP-256B`)]; $\overline{|\boldsymbol{\omega}|}$ is the mean and σ the standard deviation of $|\boldsymbol{\omega}|$.
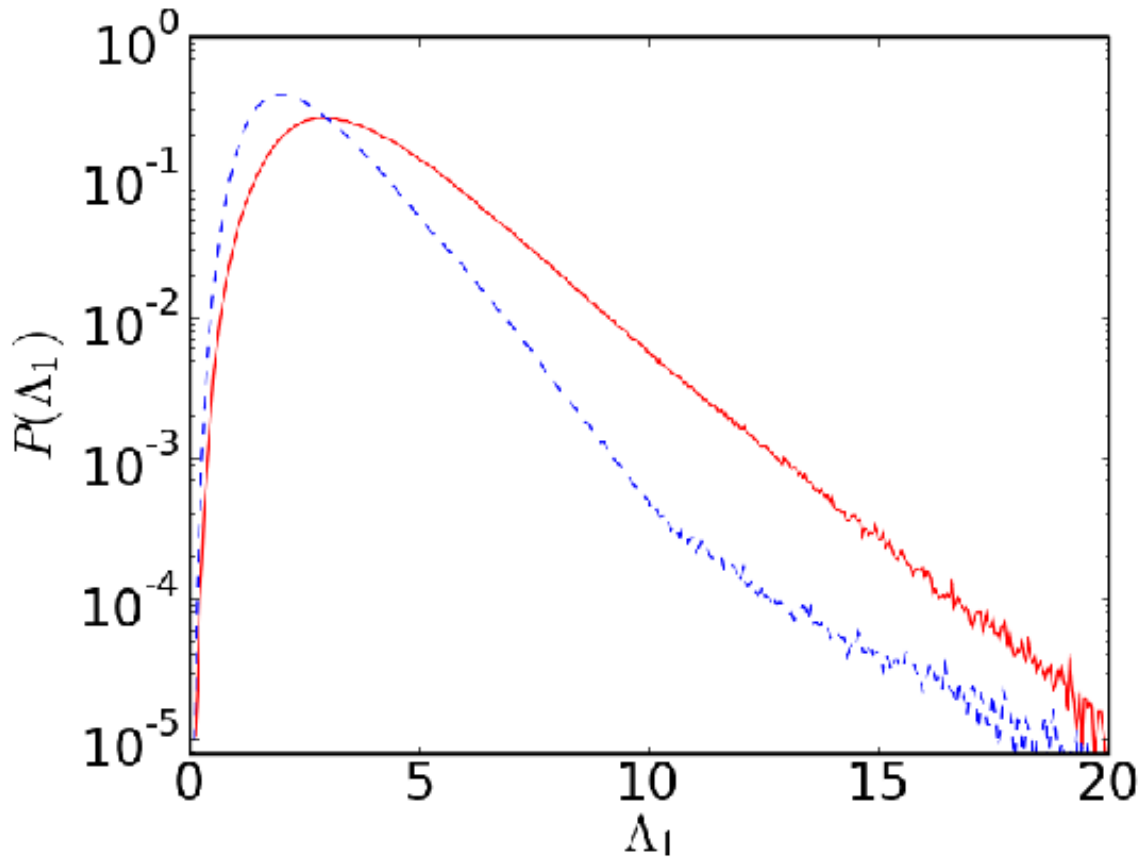
Figure 3.8: Semilog plots of the PDF $P(\Lambda_1)$ versus the first eigenvalue Λ_1 of the strain-rate tensor S for the run NSP$-$256B, with [$We = 7.1$ (dashed line)] and without [$c = 0$ (line)] polymer additives. The plot is normalized such that the area under the curve is unity.
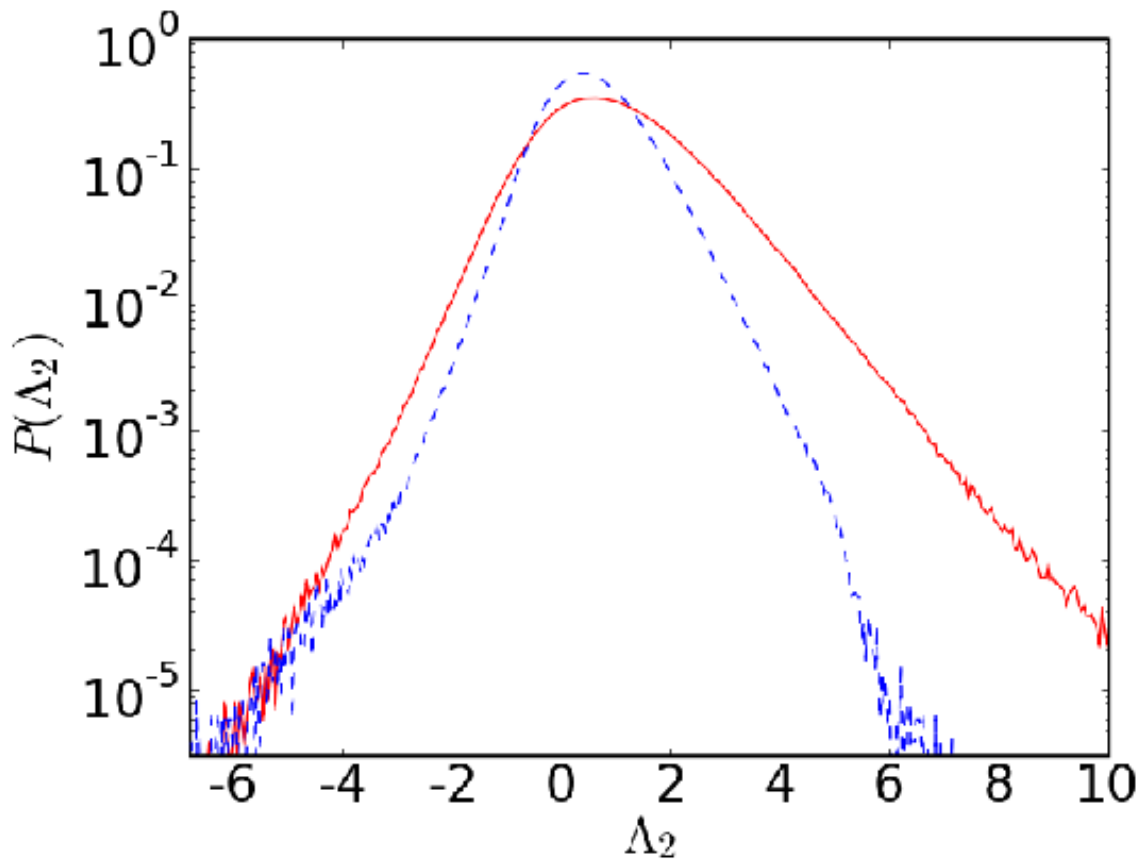
Figure 3.9: Semilog plots of the PDF $P(\Lambda_2)$ versus the second eigenvalue Λ_2 of the strain-rate tensor S for the run $\texttt{NSP}-\texttt{256B}$, with [$We = 7.1$ (dashed line)] and without [$c = 0$ (line)] polymer additives. The plot is normalised such that the area under the curve is unity.

and Q are dramatically reduced on the additions of polymers. This is another indicator of the reduction of small-scale structures.

3.6 Effects of polymer additives on the deep dissipation range

In the previous Section we have studied the effects of the polymer additives on the structural properties of the fluid at moderate Reynolds numbers. In this section we investigate the effects of polymer additives on the deep-dissipation range. To uncover such dissipation-range effects, we conduct a very high-resolution, low-$Re_\lambda = 16$ DNS study NSP − 512. The parameters used in our run NSP − 512 are given in Table 3.1. The fluid is driven by using a stochastic forcing of Ref. [6]. In Fig. 3.11 we plot the fluid energy spectrum with and without polymer additives. The behaviour of the energy spectrum is similar to that in our decaying-turbulence study (see Chapter 1 and Ref. [5]). We find that, on the addition of polymers, the energy content of the intermediate wave-vectors is decreases, whereas the energy content at large wave-vectors is increased. Furthermore, to check whether the rise in the energy spectrum in the deep-dissipation range is because of the aliasing errors, we also plot the corresponding enstrophy spectrum $k^2 E(k)$ versus k in Fig. 3.12. Since this also decays at large k we conclude that we have resolved the dissipation range adequately.

For homogeneous, isotropic turbulence, the relationship between the second-order structure function and the energy spectrum is [12]

$$S_2(r) = \int_0^\infty \left[1 - \frac{\sin(kr)}{kr} \right] E(k) dk. \tag{3.4}$$

By using Eq. (3.4) and the data in Fig. 3.11 we have obtained the second-order structure function $S_2(r)$ for our run NSP − 512. We find that the addition of polymers leads to a decrease in the magnitude of $S_2(r)$. In our simulations we are able to reach much smaller values of
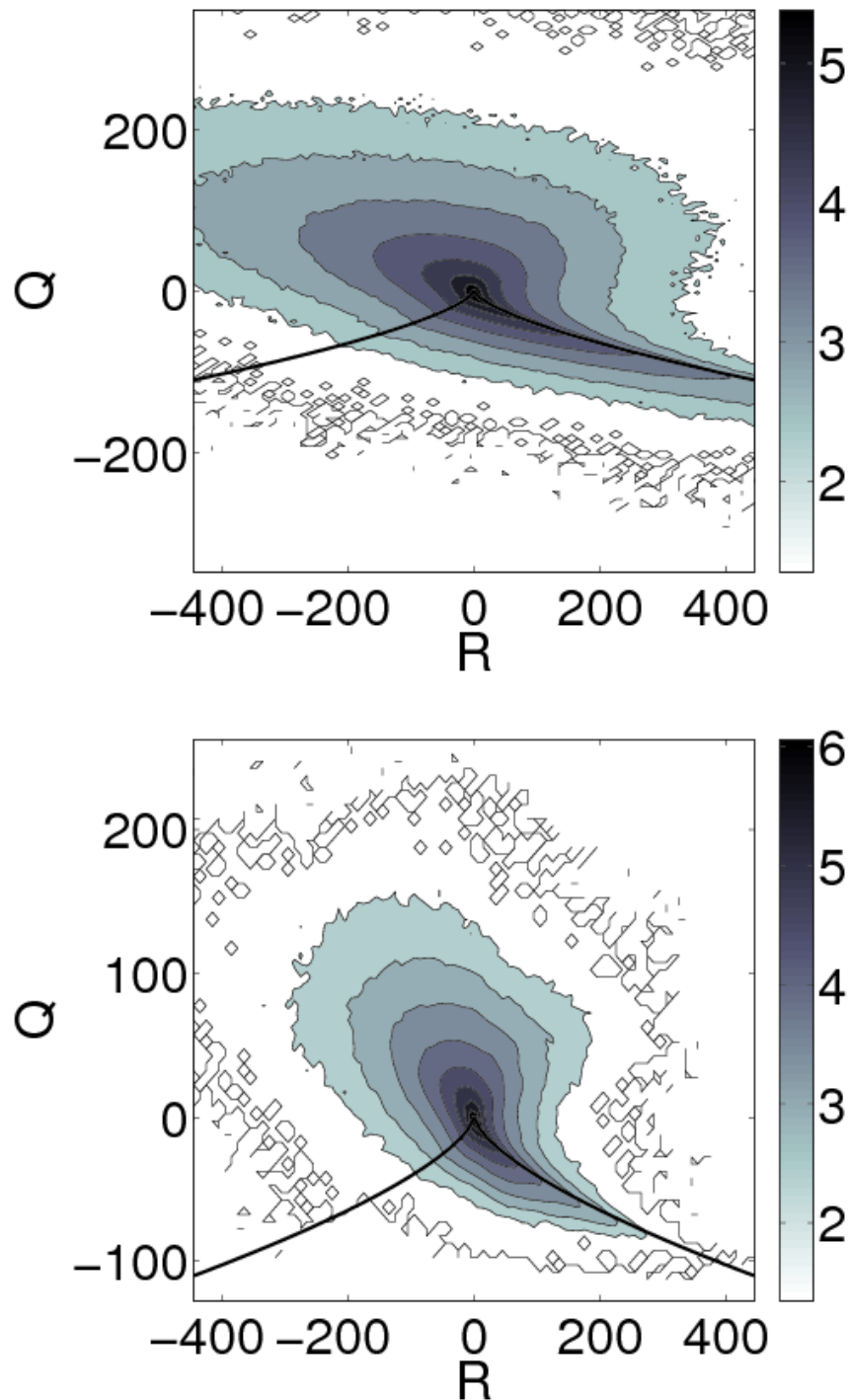
Figure 3.10: The joint probability distribution $P(R,Q)$ for the fluid with (top) and without (bottom) polymer additives. Note that $P(R,Q)$ shrinks on the addition of polymers; this indicates a depletion of small-scale structures. The contour levels are logarithmically spaced and are drawn at values $1.3, 2.02, 2.69, 3.36, 4.04, 4.70, 5.38,$ and 6.05.

	N	δt	L	ν	τ_P	c	We
NSP-256A	256	5.0×10^{-4}	100	5×10^{-3}	0.5, 1	0.1	3.5
NSP-256B	256	5.0×10^{-4}	100	5×10^{-3}	0.5, 1	0.1	7.1
NSP-512	512	1.0×10^{-2}	100	10^{-2}	0.1	1.0	0.9

Table 3.1: The parameters N, δt, L, ν, τ_P and c for our four runs $\mathtt{NSP-256A}$, $\mathtt{NSP-256B}$ and $\mathtt{NSP-512}$. We also carry out DNS studies of the NS equation with the same numerical resolutions as our NSP runs. Taylor micro-scale Reynolds number $Re_\lambda \equiv \sqrt{20\mathcal{E}^f}/\sqrt{3\nu\epsilon^f}$ and $We \equiv \tau_P\sqrt{\epsilon^f/\nu}$; $\mathtt{NSP-256A}$ and $\mathtt{NSP-256B}$: $Re_\lambda \approx 80$ and $\mathtt{NSP-512}$: $Re_\lambda \approx 16$; the Kolmogorov length scale $\eta \equiv (\nu^3/\epsilon^f)^{1/4}$. For our runs $\mathtt{NSP-256A-B}$, $\eta \approx 1.07\delta x$ and for our runs $\mathtt{NSP-512}$, $\eta \approx 19\delta x$ where $\delta x \equiv \mathbb{L}/N$ is the grid resolution of our simulations. The integral length scale $l_{int} \equiv (3\pi/4)\sum k^{-1}E(k)/(\sum E(k))$ and $T_{\mathrm{eddy}} \equiv u_{rms}/l_{int}$; $\mathtt{NSP-256A}$ and $\mathtt{NSP-256B}$: $l_{int} \approx 1.3$ and $T_{\mathrm{eddy}} \approx 1.2$, for $\mathtt{NSP-512}$: $l_{int} \approx 2.05$ and $T_{\mathrm{eddy}} \approx 4.0$.
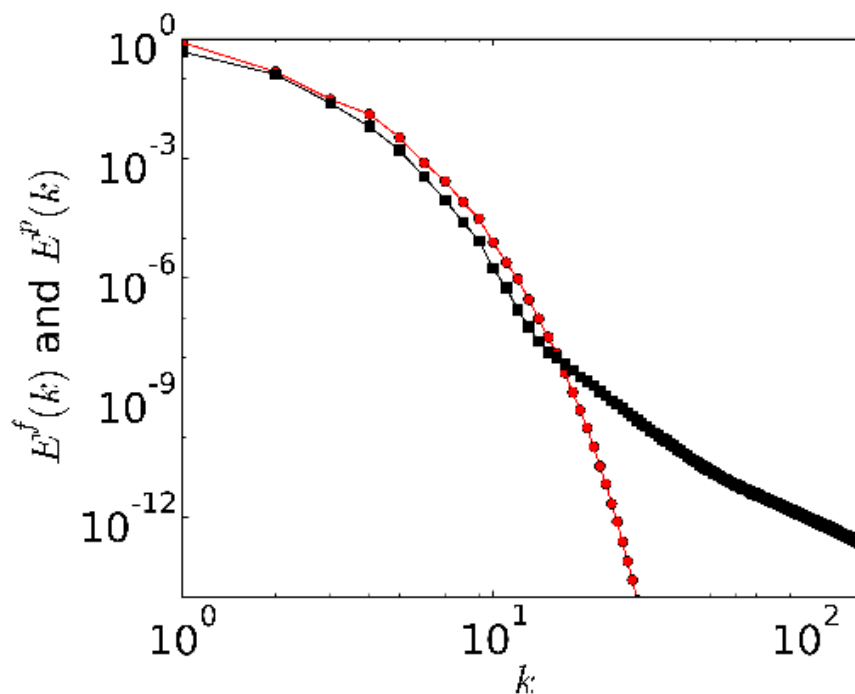
Figure 3.11: Log-log plots of the energy spectrum $E(k)$ versus the wave vector k for our run $\mathtt{NSP=512}$ (black circle) for $c = 0.1$ and $\tau_P = 1$. The corresponding plot for the pure fluid (red line) is also shown for comparison.
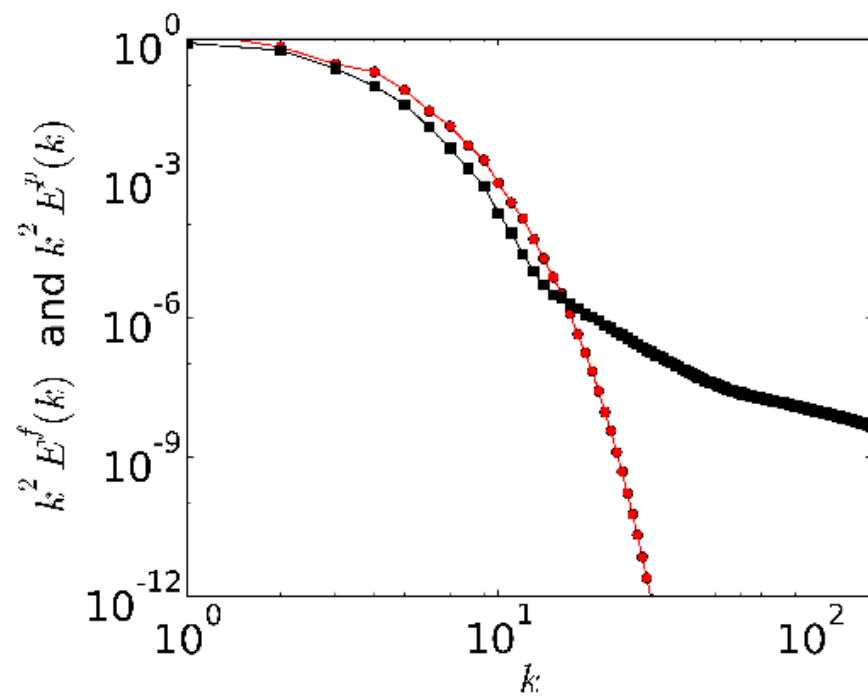
Figure 3.12: Log-log plots of the enstrophy spectrum $k^2 E(k)$ versus the wave vector k for our run $\mathtt{NSP} = 512$ (black circle) for $c = 0.1$ and $\tau_P = 1$. The corresponding plot for the pure fluid (red line) is also shown for comparison.

r/η than has been possible in earlier studies on these systems. However, because we have concentrated on dissipation-range, we cannot resolve the inertial range. Note that, unlike $E^f(k)$, where a cross-over is observed on the addition of polymer, we do not observe any cross-over in the plot of $S_2(r)$. This can be understood by realizing that $S_2(r)$ mixes the information in $E^f(k)$ from large and small k [13]. This behaviour of $S_2(r)$ is similar to the experimental observations of Ref. [1]; this reference resolves much larger length scales than we do, but not small ones.

3.7 Conclusion

In this Chapter we have carried forward our decaying-turbulence study with polymer additives to the case of statistically steady turbulence. We find that the average viscous dissipation decreases on the addition of polymers. This allows us to extend the definition of dissipation reduction to the regime of statistically steady turbulence. We find that the dissipation reduction increases with an increase in the Weissenberg number We at fixed polymer concentration. The PDFs of the moduli of the vorticity, the tensor product $\omega_i\omega_j S_{ij}$, the distribution of the eigenvalues of the rate-of-strain tensor, and the QR-plot are in qualitative agreement with the experiments of Liberzon, *et al.* [2, 3]. In the deep-dissipation range, the energy spectrum shows a behaviour similar to that in our earlier decaying turbulence study [14]. We have carried out a high-resolution study in the dissipation range too. By using the energy spectrum have also calculated $S_2(r)$ and find trends in qualitative agreement with the experiments.
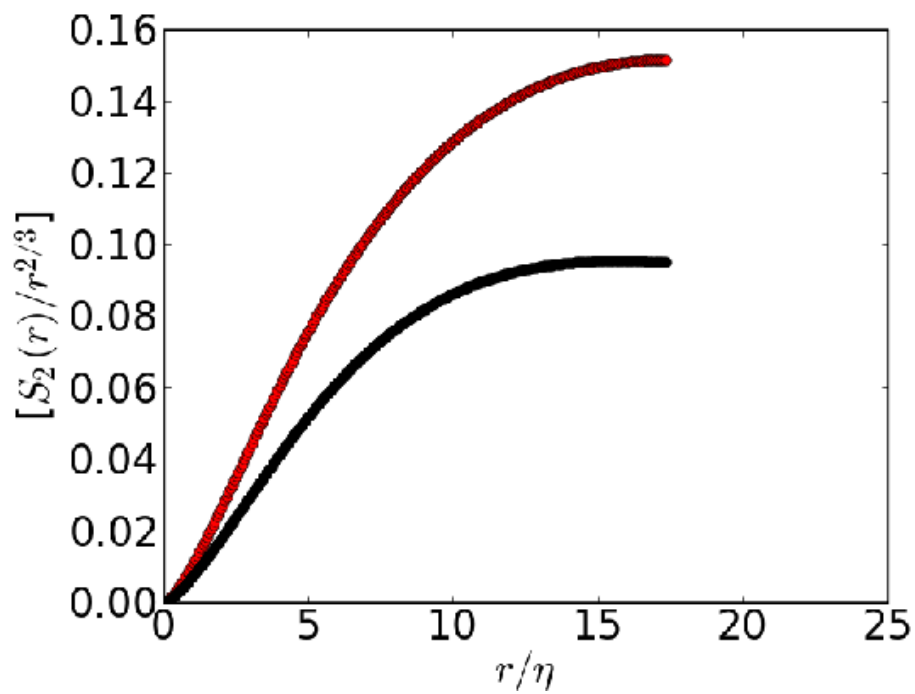
Figure 3.13: Plot of the compensated energy spectrum $S_2(r)/r^{2/3}$ versus r/η with (black circles) and without (red circles) polymer additives for our run NSP − 512. In contrast to the energy spectrum we do not observe any cross over in the structure function.

Appendix B

B.1 Finite-difference schemes

The second-order, fourth-order, and sixth-order explicit finite-difference approximations of the derivative of a function $f \in \mathbb{R}^1$ that we use are:

$$f' = (-f_{i-1} + f_{i+1})/(2\Delta x), \tag{B1}$$

$$f' = (f_{i-2} - 8f_{i-1} + 8f_{i+1} - f_{i+2})/(12\Delta x), \text{ and} \tag{B2}$$

$$f' = (-f_{i-3} + 9f_{i-2} - 45f_{i-1} + 45f_{i+1} - 9f_{i+2} + f_{i+3})/(60\Delta x). \tag{B3}$$

B.2 Kurganov-Tadmor scheme

In this Appendix we illustrate the Kurganov-Tadmor (KT) numerical scheme used for solving the advection term in the FENE-P equation. We then solve the problem of advection of polymers in two dimensional Taylor-Green flow and show that the KT scheme resolves the gradients properly [1] whereas the use of sixth-order, centered, explicit finite difference scheme leads to spurious modes which pollute the large wave-vectors.

For simplicity, let us consider one dimensional conservation law:

$$\frac{\partial u}{\partial t} = \frac{\partial f(u)}{\partial x}. \tag{B4}$$

---

[1]by adding numerical diffusion at the regions of large gradients

where $u, f(u) \in \mathbb{R}$. Using the KT scheme the above equation is discretized on a grid of length $\mathbb{L}$ (with grid points $j = 0, \cdots, N-1$ and grid spacing $\delta x = \mathbb{L}/N$ as:

$$
\begin{aligned}
\frac{du}{dt} &= -\frac{H_{j+1/2} - H_{j-1/2}}{\delta x}, \\
H_{j+1/2} &= \frac{f(u^+_{j+1/2}) - f(u^-_{j+1/2})}{2} - \frac{a_{j+1/2}[u^+_{j+1/2} - u^-_{j+1/2}]}{2}, \\
u^\pm_{j+1/2} &= u_{j+1} \mp \frac{\delta x}{2}(\partial_x u)_{j+1/2\pm1/2}, \\
a_{j+1/2} &= max_{u \in [u^-_{j+1/2}, u^+_{j+1/2}]} |\partial_u f(u)|.
\end{aligned}
$$

As a test problem, we now study the effect of different spatial discretization schemes of the polymer advection term. The analysis is conducted in two dimensions. We consider Taylor-Green flow $[u_x = \sin(x)\cos(y), \ u_y = -\cos(x)\sin(y)]$ as the velocity field at all times. We study the polymer extension spectrum and the contours of the polymer extensions, once a steady state is reached. For one run we evaluate the polymer advection term using a sixth order centered finite-difference scheme, whereas, in another run we evaluate the polymer advection term using a KT scheme. The plot in Fig. B1 shows the polymer spectrum $E_P(k) \equiv \sum_{k-1/2 \le k' k+1/2} |(r_P)_{\mathbf{k}'}|^2$ and the corresponding contours for the polymer extensions r_P^2 as a function of the increasing grid resolution N. We make the following observations:

1. The explicit scheme leads to spurious modes at large-k. These spurious modes move to larger wave-vectors on increasing the resolution.

2. The shock capturing scheme resolves the structures even at low resolutions and the large-k spectrum is also well resolved.
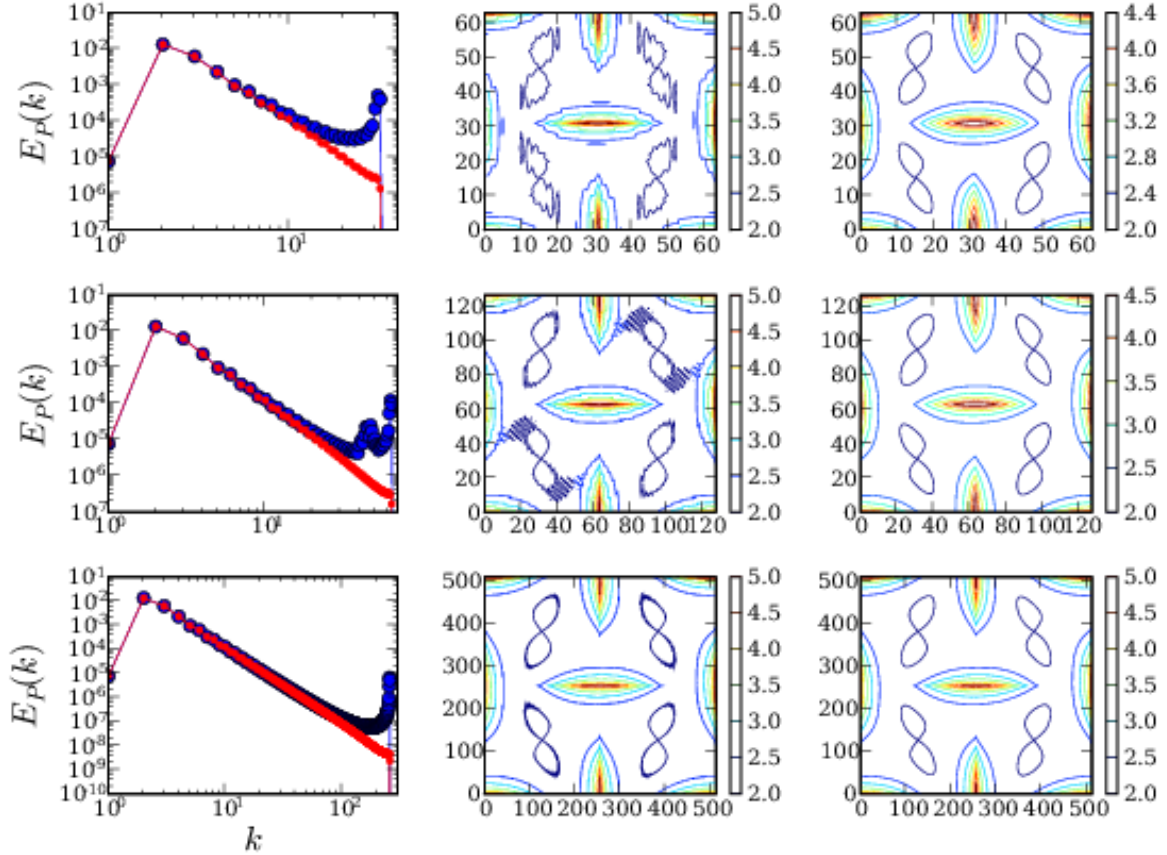
Figure B1: Left: Polymer extension spectrum using sixth-order explicit finite-differences for the advection term (circles) and the polymer spectrum obtained by using KT scheme for the advection term (dots); Middle: the corresponding contours of r_P^2 for the scheme which uses sixth-order finite differences for the advection term; Right: contours of r_P^2 for the scheme which uses KT scheme for the advection term. The different resolutions used are (a) $N = 64$ (top), (b) $N = 128$ (middle), and (c) $N = 512$ (bottom). We keep $\tau_P = 0.4$ fixed.

Bibliography

[1] N.T. Ouellette, H. Xu, and E. Bodenschatz, *J. Fluid Mech.* **629**, 375 (2009).

[2] A. Liberzon, M. Guala, B. Luthi, W. Kinzelbach, and A. Tsinober, *Phys. Fluids* **17**, 031707 (2005).

[3] A. Liberzon, M. Guala, W. Kinzelbach, and A. Tsinober, *Phys. Fluids* **18**, 125101 (2006).

[4] A.G. Lamorgese, D.A. Caughey, and S.B. Pope, *Phys. Fluids* **17**, 015106 (2005).

[5] P. Perlekar, D. Mitra, and R. Pandit, *Phys. Rev. Lett.* **97**, 264501 (2006).

[6] V. Eswaran and S.B. Pope, *Comput. Fluids* **16**, 257 (1988).

[7] T. Vaithianathan and L.C. Collins, *J. Comput. Phys.* **187**, 1 (2003).

[8] P. Virk, *AIChE* **21**, 625 (1975).

[9] T. Vaithianathann, A. Robert, J.G. Brasseur, and L.C. Collins, *J. Non-newtonian Fluid Mech.* **140**, 3 (2006).

[10] Y. Kaneda, T. Ishihara, M. Yokokawa, K. Itakura, and A. Uno, *Phys. Fluids* **15**, L21 (2003).

[11] R. Pandit, P. Perlekar, and S.S. Ray, *Pramana* **73**, 179 (2009).

[12] G.K. Batchelor, *The theory of homogeneous turbulence* (Cambridge University Press, Cambridge, 1953).

[13] P.A. Davidson, *Turbulence* (Oxford University Press, New York, 2004), pp. 386–410.

[14] P. Perlekar and R. Pandit, *New J. Phys.* **11**, 073003 (2009).

Chapter 4

Statistically steady turbulence in thin films with Ekman friction

In this chapter we present the results of a detailed direct numerical simulation (DNS) of the two-dimensional Navier-Stokes equation with the incompressibility constraint and air-drag-induced Ekman friction. This chapter follows the version of the paper that we have just published in the *New Journal of Physics*, 11, 073003, (2009). Our DNS has been designed to investigate the combined effects of walls and such friction on turbulence in forced thin films. We concentrate on the forward-cascade regime and show how to extract the isotropic parts of velocity and vorticity structure functions and thence the ratios of multiscaling exponents. We find that velocity structure functions display simple scaling whereas their vorticity counterparts show multiscaling; and the probability distribution function of the Okubo-Weiss parameter Λ, which distinguishes between regions with centers and saddles, is in quantitative agreement with experiments.

4.1   Introduction

The pioneering work of Kraichnan [1, 2, 3] showed that fluid turbulence in two dimensions (2D) is qualitatively different from that in three dimensions (3D): in the former we have an infinity of extra con-

served quantities, in the inviscid, unforced case; the first of these is the enstrophy. It turns out, therefore, that 2D turbulence displays an inverse cascade of energy, from the length scale at which the force acts to larger length scales, and a forward cascade of enstrophy, from the forcing length scale to smaller ones; by contrast, 3D turbulence is characterized by a forward cascade of energy [4]. Kraichnan's predictions were first confirmed in atmospheric experiments in quasi-two-dimensional, stratified flows [5]; subsequent experiments have studied systems ranging from large-scale geophysical flows to soap films [5, 6, 7, 8, 9, 10, 11, 12]. The latter have proved to be especially useful in characterizing 2D turbulence.

We present the first direct numerical study (DNS) that has been designed specifically to explore the combined effects of the air-drag-induced Ekman friction α and walls on the forward cascade in 2D turbulence; and we employ the Kolmogorov forcing used in many soap-film experiments [9, 10, 11, 12]. Since we use the two-dimensional Navier-Stokes equation with the incompressibility constraint, we cannot explore the effects of changes in the thickness of soap-films, Marangoni stresses, and compressibility [13, 14]. Nevertheless, as we show in detail below, our study is able to reproduce several results that have been obtained in the soap-film experiments of Refs. [9, 10, 11, 12].

In particular, if we use values of α that are comparable to those in experiments, we find that the energy dissipation rate because of the Ekman friction is comparable to the energy dissipation rate that arises from the conventional viscosity. We show how to extract the isotropic parts [15] of velocity and vorticity structure functions and then, by using the extended self-similarity (ESS) procedure [16], we obtain ratios of multiscaling exponents whence we conclude that velocity structure functions show simple scaling whereas their vorticity counterparts display multiscaling. Most important, our probability

distribution function (PDF) of the Okubo-Weiss parameter Λ [17, 18] is in quantitative agreement with that found in experiments [10, 11].

The remaining part of this Chapter is organized as follows. Section 4.2 contains a description of the model we use and the numerical methods we employ. Section 4.3 is devoted to our results: In Section 4.3.1 we examine the temporal evolution of the energy and the dissipation rates because of the viscosity and Ekman-friction; in Section 4.3.2 we study the structure functions of the velocity and the vorticity in the forward-cascade regime; and in Section 4.3.3 we study the topological properties of two-dimensional turbulence and their dependence on the Ekman friction. The concluding Section 4.4 contains a discussion of our results and suggestions for some experiments that should be conducted to confirm our numerical findings.

4.2   Model and Numerical Technique

Soap-film dynamics is governed by the equations derived in Refs. [13, 14]. These equations account for mass, momentum, and soap-film-concentration conservation, and the boundary condition for the free, air-film interfaces. However, for the low-Mach-number flows, which are relevant to the experiments of Refs. [6, 9, 10, 11, 12], these equations reduce to the incompressible, 2D Navier-Stokes equations [13, 14] albeit with an extra Ekman friction term. The experiments of Ref. [9] showed the validity of these equations by testing the Karman-Howarth-Monin relation.

Thus we use the 2D, incompressible Navier-Stokes equations with an additional Ekman friction term to model soap-film dynamics [9, 14]:

$$(\partial_t + \mathbf{u} \cdot \nabla)\omega \;=\; \nu\nabla^2\omega - \alpha\omega + F_\omega/\rho; \qquad (4.1)$$

$$\nabla^2\psi \;=\; \omega. \qquad\qquad (4.2)$$

Here $\mathbf{u} \equiv (-\partial_y \psi, \partial_x \psi)$, ψ, and $\omega \equiv \nabla \times \mathbf{u}$ are, respectively, the velocity, stream function, and vorticity at the position $\mathbf{x}$ and time t; we choose the uniform density $\rho = 1$; α is the Ekman friction coefficient, ν is the kinematic viscosity, and $F_\omega \equiv k_{inj} F_0 \cos(k_{inj} y)$, a Kolmogorov-type forcing term, with amplitude F_0, and injection wave vector k_{inj} (the injection length scale $\ell_{inj} \equiv 2\pi/k_{inj}$). We impose no-slip ($\psi = 0$) and no-penetration ($\nabla \psi \cdot \hat{n} = 0$) boundary conditions on the walls, where $\hat{n}$ is the outward normal to the wall. If we non-dimensionalize $\mathbf{x}$ by k_{inj}^{-1}, t by k_{inj}^{-2}/ν, and F_ω by $2\pi/(k_{inj}||F_\omega||_2)$, with $||F_\omega||_2 \equiv (\int_A |F_\omega|^2 d\mathbf{x})^{1/2}$ and A the area of the film, then we have two control parameters, namely, the Grashof [19] number $\mathcal{G} = 2\pi||F_\omega||_2/(k_{inj}^3 \rho \nu^2)$ and the non-dimensionalized Ekman friction $\gamma = \alpha/(k_{inj}^2 \nu)$. For a given set of values of $\mathcal{G}$ and γ, the system attains a nonequilibrium statistical steady state after a time $t/\tau \simeq 2.8$, where $\tau = L/u_{rms}$ is the box-size time, L the side of our square simulation domain, and u_{rms} the root-mean-square velocity. In this state the Reynolds number $Re \equiv u_{rms}/(k_{inj}\nu)$, the energy, etc., fluctuate; their mean values, along with one-standard-deviation error bars, are given in Tables 4.1 and 4.2 that list the values of the parameters in our runs R1−7.

We use a fourth-order Runge-Kutta scheme (Appendix C.1) with step size $\delta t = 10^{-4}$ for time marching in Eq. (4.1) and evaluate spatial derivatives via second-order and fourth-order, centered, finite differences, respectively, for points adjacent to the walls and for points inside the domain (Appendix C.2). The Poisson equation Eq. (4.2) is solved by using a fast-Poisson solver [20] (see Appendix C.3) and ω is calculated at the boundaries by using Thom's formulae [21] that are given below:

$$\omega_{i,1} = 2\psi_{i,2}/\delta_x^2 \text{ (bottom wall)},$$
$$\omega_{i,N} = 2\psi_{i,N-1}/\delta_x^2 \text{ (top wall)},$$
$$\omega_{1,j} = 2\psi_{2,j}/\delta_x^2 \text{ (left wall)},$$
$$\omega_{N,j} = 2\psi_{N-1,j}/\delta_x^2 \text{ (right wall)},$$

	N	α	F_0	γ	$\mathcal{G}(\times 10^4)$	Re	E
R1	1025	0.45	45	0.25	3.5	23.3 ± 0.4	15.1 ± 0.5
R2	1025	1.25	45	0.71	3.5	19.6 ± 0.3	10.7 ± 0.3
R3	1025	1.25	60	0.71	4.7	24.0 ± 0.5	15.9 ± 0.6
R4	2049	0.45	45	0.25	3.5	23.2 ± 0.4	15.1 ± 0.5
R5	2049	1.25	45	0.71	3.5	19.6 ± 0.4	10.8 ± 0.4
R6	2049	1.25	60	0.71	4.7	23.8 ± 0.4	15.9 ± 0.6
R7	3073	0.45	45	0.25	3.0	26.5 ± 0.4	20.0 ± 1.0

Table 4.1: Parameters for our runs R1-7: N, the number of grid points along each direction, γ, $\mathcal{G}$, Re (we use $\nu = 0.016$, $\ell_{inj} = 0.6$, and a square simulation domain with side $L = 7$, uniform grid spacing $\delta_x = \delta_y = L/N$, area A, and boundary ∂A), and the time-averaged kinetic energy E.

where $1 \leq (i, j) \leq N$ are the Cartesian indices of points in our simulation domain with $N \times N$ grid points.

To evaluate spatiotemporal averages, we store $\psi(\mathbf{x}, t_n)$ and $\omega(\mathbf{x}, t_n)$, with $t_n = (4 + n\Delta)\tau$, $n = 0, 1, 2, \ldots, n_{max}$, and $96 \leq n_{max} \leq 200$; $\Delta = 0.28$ for runs R1-6 and $\Delta = 0.13$ for run R7.

4.3 Results

Our results are of three types and are given, respectively, in Sections 4.3.1, 4.3.2, and 4.3.3. We begin with a short overview of these before we present details. In Section 4.3.1 we study the time evolutions of the kinetic energy $E(t) \equiv (\int_A \mathbf{u}^2 d\mathbf{x})/A$, viscous energy-dissipation rate $\epsilon_\nu(t) \equiv -\nu(\int_A |\omega|^2 d\mathbf{x})/A$, and energy-dissipation rate because of the Ekman friction $\epsilon_e(t) = -2\alpha E(t)$ and their time averages $E \equiv \langle E(t) \rangle$, $\epsilon_\nu \equiv \langle \epsilon_\nu(t) \rangle$, and $\epsilon_e \equiv \langle \epsilon_e(t) \rangle$. We show that there are important qualitative differences, not emphasized earlier, between runs in which $\mathcal{G}$ is held fixed and those in which Re is held fixed (by varying $\mathcal{G}$ and γ). In particular, for runs with constant $\mathcal{G}$, ϵ_ν turns out to be independent of the Ekman friction, whereas, for runs in which Re

	ϵ_ν	ϵ_e	$\tilde{\Lambda}(\times 10^2)$	b	$\delta_b(\times 10^{-2})$
R1	-28 ± 2	-13.6 ± 0.5	5.3 ± 0.3	0.32 ± 0.01	3.1 ± 0.1
R2	-28 ± 1	-26.8 ± 0.9	4.8 ± 0.2	0.33 ± 0.01	3.1 ± 0.1
R3	-40 ± 2	-39.9 ± 1.4	7.2 ± 0.4	0.33 ± 0.01	2.8 ± 0.1
R4	-28 ± 2	-13.6 ± 0.4	5.3 ± 0.3	0.31 ± 0.01	3.2 ± 0.2
R5	-28 ± 1	-27.0 ± 1.0	4.8 ± 0.2	0.33 ± 0.01	3.1 ± 0.1
R6	-40 ± 2	-40.0 ± 1.5	7.2 ± 0.4	0.33 ± 0.01	3.1 ± 0.1
R7	-26 ± 2	-17.8 ± 0.6	5.0 ± 0.4	0.31 ± 0.01	3.7 ± 0.3

Table 4.2: Parameters for our runs R1-7: viscous-energy-dissipation rate ϵ_ν, the energy-dissipation rate because of Ekman friction ϵ_e, $\tilde{\Lambda} \equiv [\langle \overline{(\partial_x u'_y)^2} \, \overline{(\partial_y u'_x)^2} \rangle]^{1/2}$, $b \equiv -\langle \overline{\partial_x u'_y \partial_y u'_x} \rangle / \tilde{\Lambda}$, and the boundary-layer thickness $\delta_b \propto \langle (\oint_{\partial A} \omega^2 / \oint_{\partial A} ((\nabla \omega).\hat{n})^2)^{1/2} \rangle$ [22, 23]. Angular brackets denote time averages whereas overbars indicate spatial averages over the whole simulation domain.

is held fixed, E remains fixed. In Section 4.3.2 we present a detailed analysis of velocity and vorticity structure functions with a view to elucidating their scaling and multiscaling properties. We then carry out a detailed study of the topological properties of 2D turbulence in Section 4.3.3 and compare our simulations with experimental results. In particular, we examine the dependence of the PDF $P(\Lambda)$ on γ and we study the joint PDFs of velocity and vorticity differences with Λ. We obtain excellent agreement with experiments.

4.3.1 Energy and dissipation

Figures 4.1(a)-(f) show the time evolution of $E(t)$, normalized by $\mathcal{N}_E \equiv (\nu k_{inj})^2$, and $\epsilon_\nu(t)$ and $\epsilon_e(t)$, normalized by $\mathcal{N} \equiv -k_{inj}^4 \nu^3$. The mean values E, ϵ_ν, and ϵ_e, given in Table 4.1, are comparable to those in experiments; note that ϵ_ν and ϵ_e are of similar magnitudes. By comparing data from runs R1 (red circles) and R2 (black lines) in Figs. 4.1(a), (c), and (e) we see that, if we fix $\mathcal{G}$ and increase γ, E decreases, ϵ_ν remains unchanged (within error bars), and ϵ_e increases. If we change both $\mathcal{G}$ and γ, we can keep the mean Re fixed, as in runs R1 and R3 in
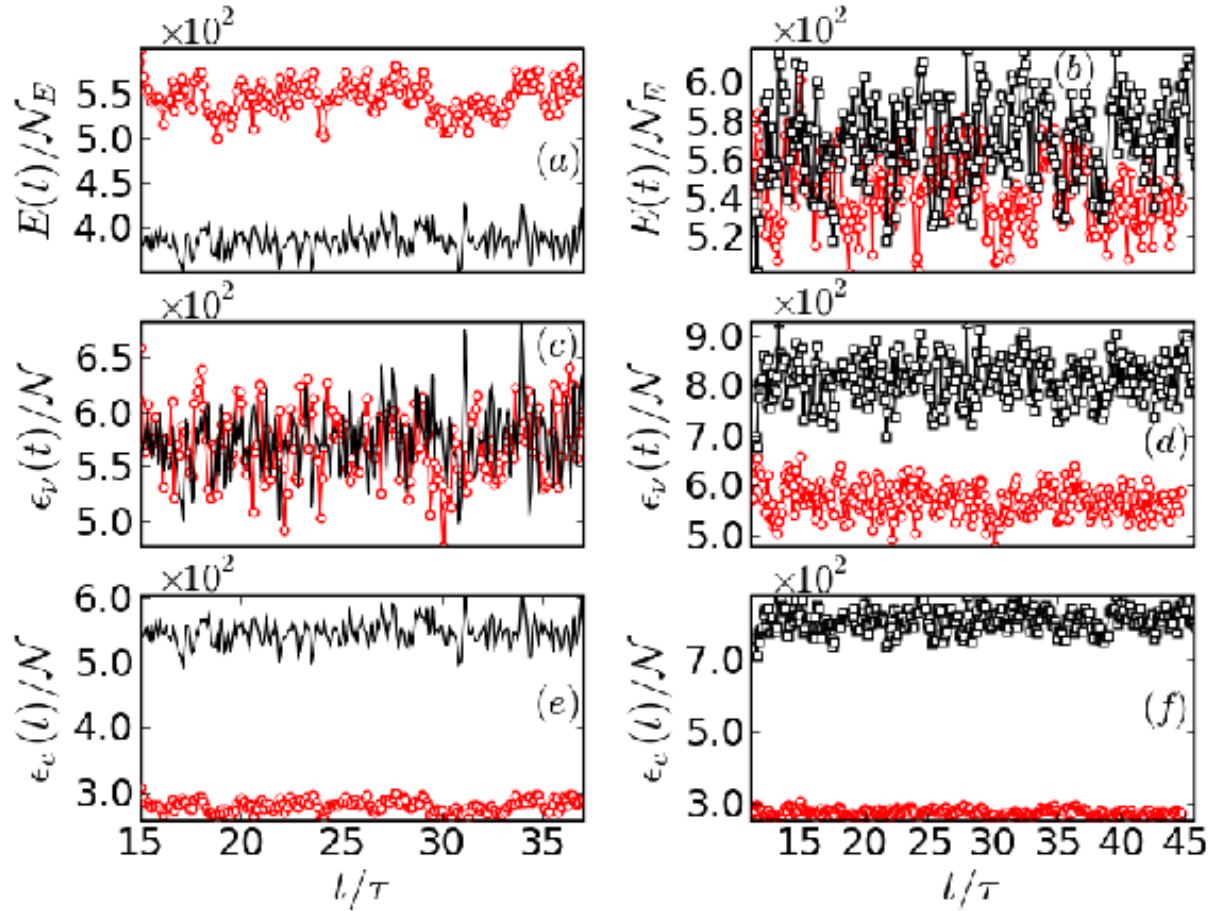
Figure 4.1: Representative plots from runs R1 (red circles), R2 (black lines), and R3 (black squares), showing the time evolution of $E(t)/\mathcal{N}_E$ [(a) and (b)], $\epsilon_\nu(t)/\mathcal{N}$ [(c) and (d)], and $\epsilon_e(t)/\mathcal{N}$ [(e) and (f)]. In (a), (c), and (e) we keep $\mathcal{G}$ fixed and vary γ ($\gamma = 0.25$ (red circles) and $\gamma = 0.71$ (black line)). In (b), (d), and (f) we maintain $Re \simeq 21.2$ by varying γ ($\gamma = 0.25$ (red circles) and $\gamma = 0.71$ (black squares)) and $\mathcal{G}$.

Table 4.1, by compensating an increase in γ with an increase in $\mathcal{G}$ (cf. Ref. [10]); in Figs. 4.1(b), (d), and (f) we see, by comparing runs R1 (red circles) and R3 (black squares), that E remains unchanged (within error bars), whereas both ϵ_ν and ϵ_e increase as γ and $\mathcal{G}$ increase in such a way that Re is held fixed.

4.3.2 Structure functions of the velocity and the vorticity

Since Kolmogorov forcing is inhomogeneous, we use the decomposition $\psi = \langle \psi \rangle + \psi'$ and $\omega = \langle \omega \rangle + \omega'$, where the angular brackets denote a time average and the prime the fluctuating part. The inhomogeneous forcing F_ω and the no-slip boundary conditions that we use generate the patterns shown via the pseudocolor plots of the time averages of $\langle \psi \rangle$ and $\langle \omega \rangle$ [Figs. 4.2(a) and (b)] respectively [1]. We use $u'_x \equiv -\partial_y \psi'$, $u'_y \equiv \partial_x \psi'$, and ω' to calculate the order-p velocity and vorticity structure functions $S_p(\mathbf{r_c}, \mathbf{R}) \equiv \langle |(\mathbf{u}'(\mathbf{r_c} + \mathbf{R}) - \mathbf{u}'(\mathbf{r})) \cdot \mathbf{R}/R|^p \rangle$ and $S_p^\omega(\mathbf{r_c}, \mathbf{R}) \equiv \langle |\omega'(\mathbf{r_c} + \mathbf{R}) - \omega'(\mathbf{r})|^p \rangle$, respectively, where $\mathbf{R}$ has magnitude R and $\mathbf{r_c}$ is an origin. Figures 4.3(a) and (c) show pseudocolor plots of $S_2(\mathbf{r_c}, \mathbf{R})$ and $S_2^\omega(\mathbf{r_c}, \mathbf{R})$, respectively, for $\mathbf{r_c} = (2, 2)$; other values of $\mathbf{r_c}$ yield similar results so long as they do not lie near the boundary layer (Table 4.1) of thickness δ_b ($\mathbf{r_c}$ is chosen at least $5\delta_b$ away from all boundaries). We now calculate $S_2(\mathbf{R}) \equiv \langle S_2(\mathbf{r_c}, \mathbf{R}) \rangle_{\mathbf{r_c}}$ and $S_2^\omega(\mathbf{R}) \equiv \langle S_2^\omega(\mathbf{r_c}, \mathbf{R}) \rangle_{\mathbf{r_c}}$, where the subscript $\mathbf{r_c}$ denotes an average over the origin (we use $\mathbf{r_c} = (i, j), 2 \leq i, j \leq 5$, where $\mathbf{r_c}$ indicates the displacement vector relative to origin of the simulation domain); these averaged structure functions [Figs. 4.3(b) and (d)] are nearly isotropic for $R < \ell_{inj}$ but not so for $R > \ell_{inj}$.

To obtain the isotropic parts in an $SO(2)$ decomposition of these structure functions [15] we integrate over the angle θ that $\mathbf{R}$ makes

---

[1]Experiments [9, 10, 11] achieve homogeneity via a periodic, square-wave forcing with amplitude F_0; this introduces another time-scale in the problem; to avoid this complication we work with a time-independent force.
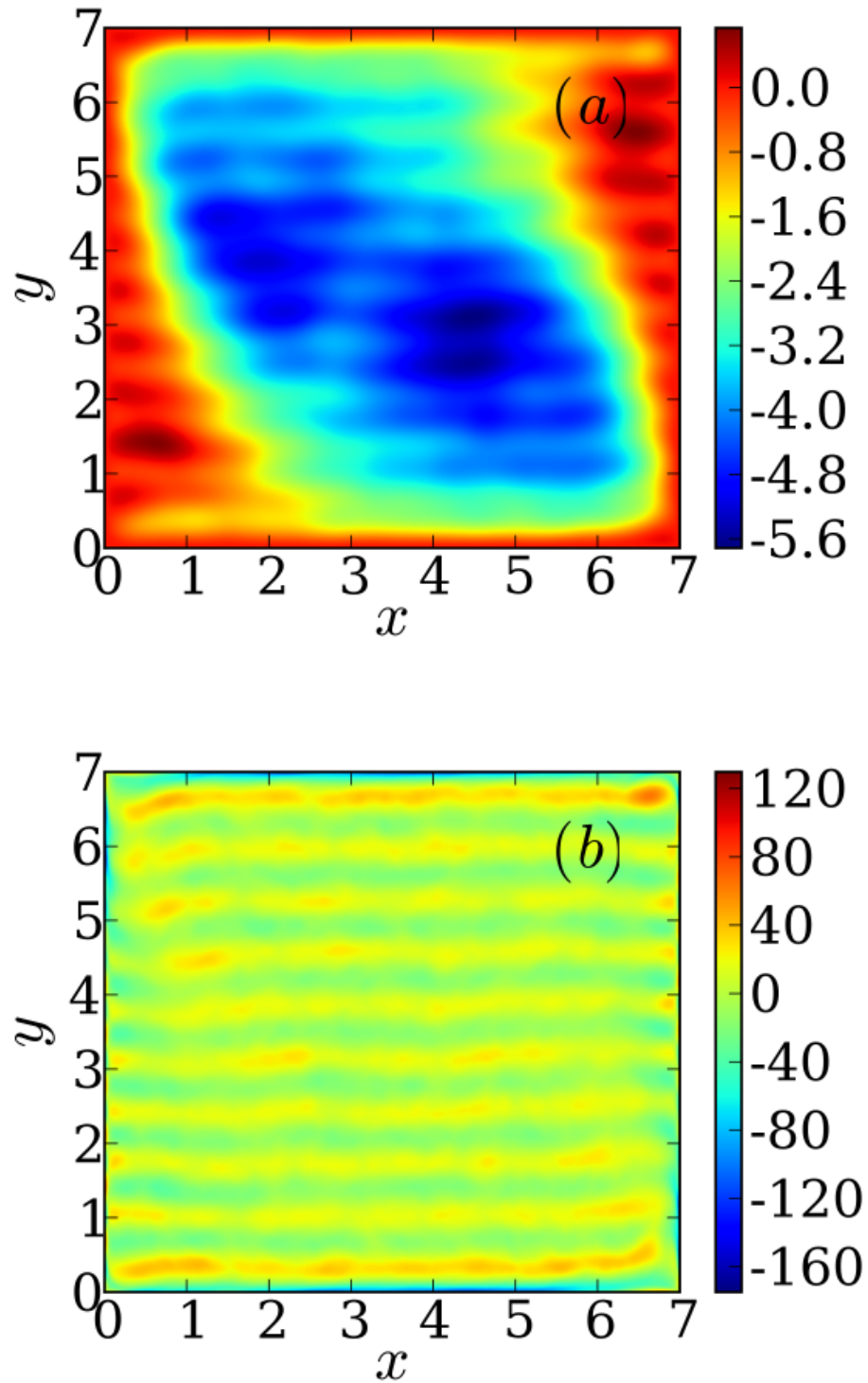
Figure 4.2: Representative pseudocolor plots of (a) the time-averaged streamfunction $\langle\psi\rangle$ and (b) the time-averaged vorticity $\langle\omega\rangle$ for our run R7.
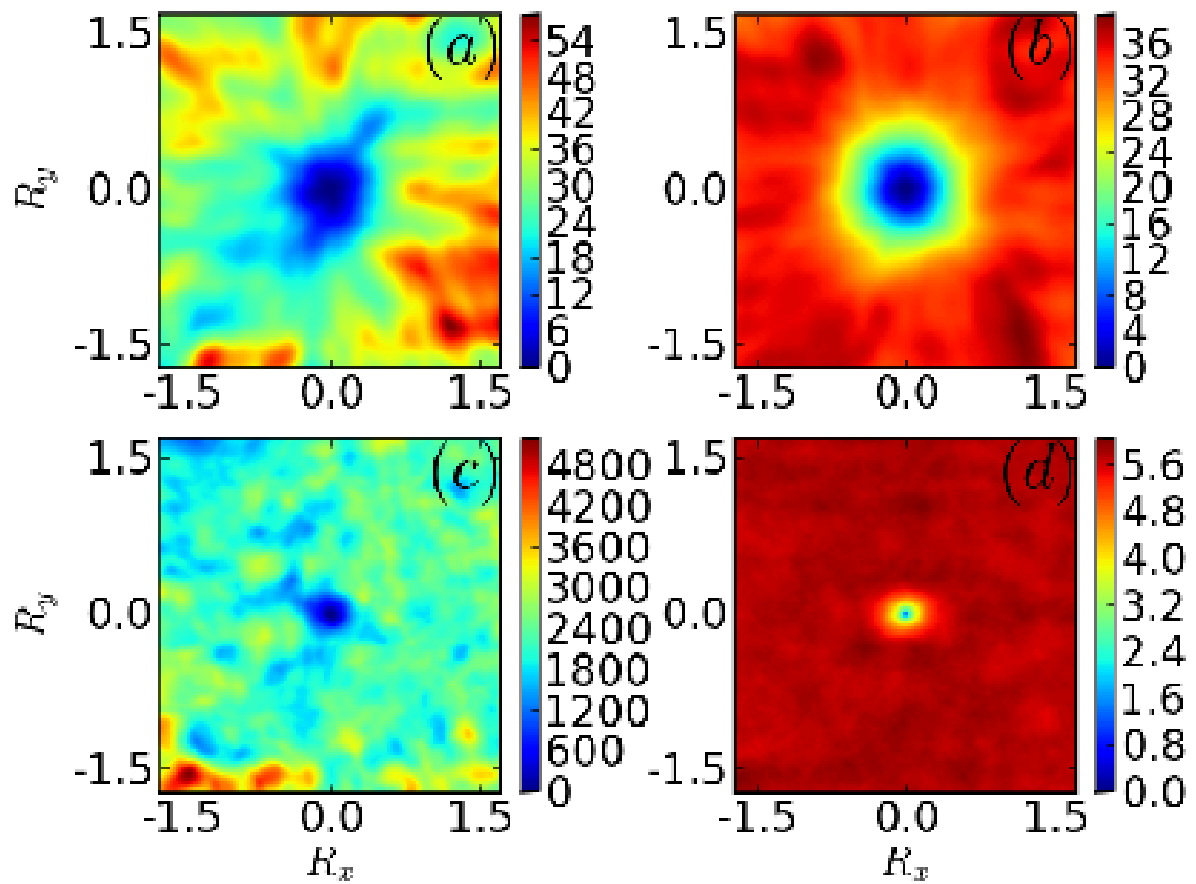
Figure 4.3: Pseudocolor plots of (a) $S_2(\mathbf{r_c}, \mathbf{R})$, for $\mathbf{r_c} = (2, 2)$, (b) $S_2(R)$ (average of $S_2(\mathbf{r_c}, \mathbf{R})$ over $\mathbf{r_c}$), (c) $S_2^\omega(\mathbf{r_c}, \mathbf{R})$, for $\mathbf{r_c} = (2, 2)$, and (d) $S_2^\omega(R)$ (average of $S_2^\omega(\mathbf{r_c}, \mathbf{R})$ over $\mathbf{r_c}$).
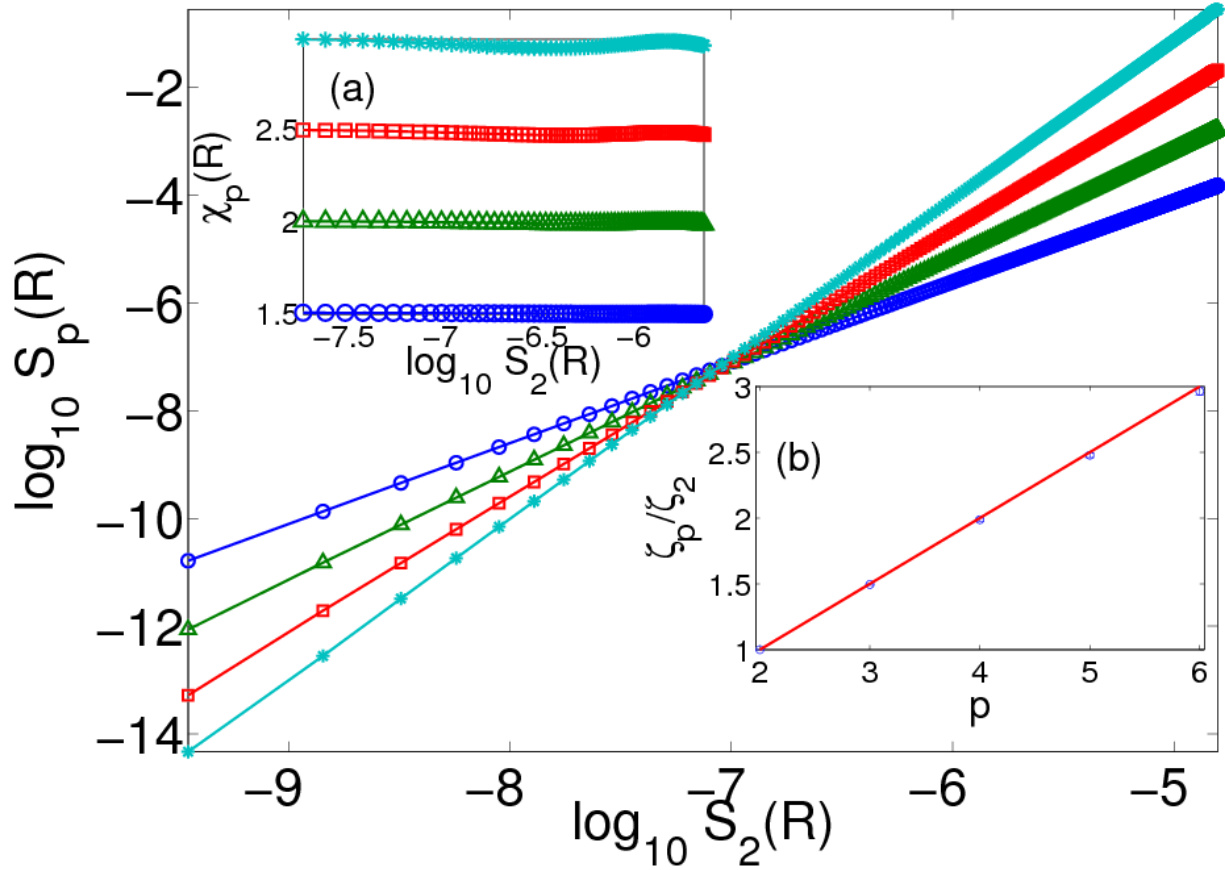
Figure 4.4: Log-log ESS plots of the isotropic parts of the order-p velocity structure functions $S_p(R)$ versus $S_2(R)$; $p = 3$ (blue line with circles), $p = 4$ (green line with triangles), $p = 5$ (red line with squares), and $p = 6$ (cyan line with stars); plots of the local slope χ_p (see text), in the forward-cascade inertial range: (a) χ_p versus $\log_{10} S_2(R)$ and (b) plots versus p of the exponent ratios ζ_p/ζ_2 and error bars from the local slopes (see text), along with the KLB prediction (red line). All plots are for run R7.

with the x axis to obtain $S_p(R) \equiv \int_0^{2\pi} S_p(\mathbf{R})d\theta$ and $S_p^\omega(R) \equiv \int_0^{2\pi} S_p^\omega(\mathbf{R})d\theta$. Given $S_p(R)$ and $S_p^\omega(R)$ we use the extended-self-similarity (ESS) procedure [16] to extract the multiscaling-exponent ratios ζ_p/ζ_2 and $\zeta_p^\omega/\zeta_2^\omega$, respectively, from the slopes (in the forward-cascade inertial range) of log-log plots of $S_p(r)$ versus $S_2(r)$ [Fig. 4.4] and $S_p^\omega(R)$ versus $S_2^\omega(R)$ [Fig. 4.5] [2].

The insets Figs. 4.4(a) and Figs. 4.5(a) show, respectively, plots of the local slopes $\chi_p \equiv d\log_{10} S_p(R)/d\log_{10} S_2(R)$ versus $\log_{10} S_2(R)$ and $\chi_p^\omega \equiv d\log_{10} S_p^\omega(R)/d\log_{10} S_2^\omega(R)$ versus $\log_{10} S_2^\omega(R)$ in the forward-cascade regime; the mean values of χ_p and χ_p^ω, over the ranges shown, yield the exponent ratios ζ_p/ζ_2 and $\zeta_p^\omega/\zeta_2^\omega$ that are plotted versus p in Figs. 4.4 and Figs. 4.5, respectively, in which the error bars indicate the maximum deviations of χ_p and χ_p^ω from their mean values. The Kraichnan-Leith-Batchelor (KLB) predictions [1, 2, 3] for these exponent ratios, namely, $\zeta_p^{KLB}/\zeta_2^{KLB} \sim r^{p/2}$ and $\zeta_p^{\omega,KLB}/\zeta_2^{\omega,KLB} \sim r^0$, agree with our values for ζ_p/ζ_2 but not $\zeta_p^\omega/\zeta_2^\omega$: velocity structure functions do not display multiscaling [Fig. 4.4 (b)] whereas their vorticity analogs do [note the curvature of the plot in Fig. 4.5 (b)]. This is in consonance with the results of DNS studies with periodic boundary conditions [24, 25, 26, 27]. Indeed, if we use the same values of γ as in Ref. [24], we obtain the same exponent ratios (within error bars); thus our method for the extraction of the isotropic parts of the structure functions suppresses boundary and anisotropy effects efficiently.

4.3.3 Topological properties of soap-film turbulence

For an inviscid, incompressible 2D fluid the local flow topology can be characterized via the Okubo-Weiss criterion [17, 18] that uses the invariant

$$\Lambda \equiv (\omega^2 - \sigma^2)/4, \tag{4.3}$$

---

[2]We employ ESS since forward-cascade inertial ranges have very modest extents even in the largest DNS studies [24, 25] that use periodic domains and hyperviscosity.
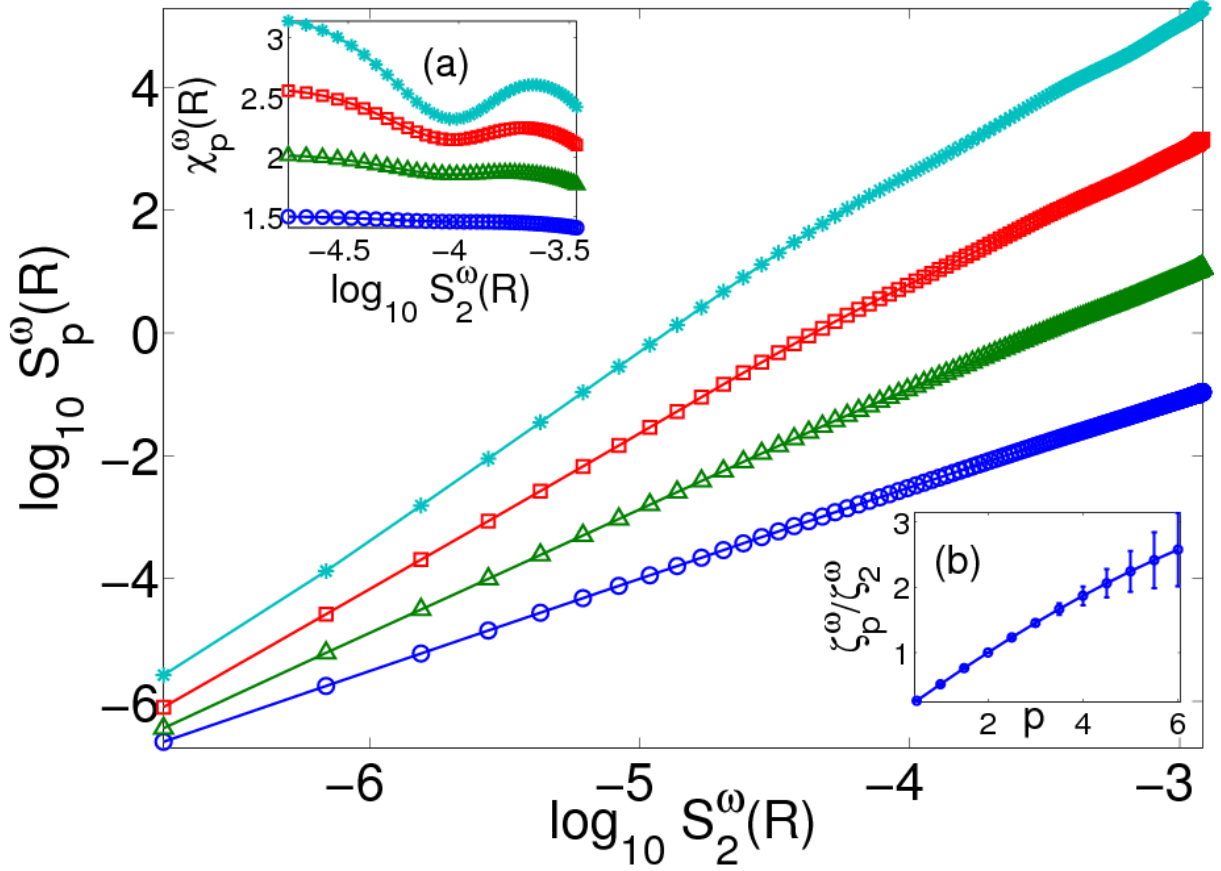
Figure 4.5: Log-log ESS plots of the isotropic parts of the order-p vorticity structure functions $S_p^\omega(R)$ versus $S_2^\omega(R)$; $p = 3$ (blue line with circles), $p = 4$ (green line with triangles), $p = 5$ (red line with squares), and $p = 6$ (cyan line with stars); plots of the local slope χ_p^ω (see text), in the forward-cascade inertial range: (a) χ_p^ω versus $\log_{10} S_2^\omega(R)$ and (b) plots versus p of the exponent ratios $\zeta_p^\omega/\zeta_2^\omega$ and error bars from the local slopes (see text). All plots are for run R7.

where $\sigma^2 \equiv \sum_{i,j} \sigma_{ij}\sigma_{ji}$ and $\sigma_{ij} \equiv (\partial_i u_j + \partial_j u_i)/\sqrt{2}$. This criterion provides a useful measure of flow properties even if $\nu > 0$ as noted in the experiments of Ref. [10]: Regions with $\Lambda > 0$ and $\Lambda < 0$ correspond, respectively, to centers and saddles as we show in Fig. 4.6 by superimposing, at a representative time, a pseudocolor plot of Λ on contours of ψ; an animated version of this plot is given as a multimedia file mov_lam.mpg (MPEG file, 3.5MB, in the attached CDROM). This result is in qualitative accord with experiments [see, e.g., Fig. 1 of Ref. [10] and also earlier DNS studies [17, 18], which do not use Ekman friction]. In Fig. 4.7 we compare the scaled PDFs $P_2(\Lambda/\Lambda_{rms})$ with data obtained from points near the walls (black curve) and from points in the bulk (red curve); the clear difference between these, not highlighted before, indicate that the regions of large Λ are suppressed in the boundary layers.

This is because near-wall regions (say within one-boundary-layer thickness δ_b from the walls) are dominated by the strain, i.e., $\sigma^2 > \omega^2$ as shown in Fig. 4.8. For the temporal evolution of the σ^2, ω^2, and Λ fields in the region near the wall see the movie mov_snw_sig2_omg2_lam
.mpg (see the attached CDROM). This explains the skewness of the near-wall $P_2(\Lambda/\Lambda_{rms})$ in Fig. 4.7. For the following discussion, to analyse the topological properties of the flow in the bulk, we evaluate Λ from the fluctuating part of the streamfunction.

Figures 4.9 (a) and (d) show the PDF $P_1(\Lambda)$ and the scaled PDF $P_2(\Lambda/\Lambda_{rms})$ for runs R4 (red line) and R5 (blue dashed line), with $\gamma = 0.25$ and $\gamma = 0.71$, respectively, and $\mathcal{G} = 3.5 \times 10^4$; by comparing these figures we see that both P_1 and P_2 overlap (within error bars) for runs R4 and R5. We believe this is because, in fixed-$\mathcal{G}$ runs like R4 and R5, ϵ_ν does not change [Table 4.1] even though γ changes. By contrast, if we compare P_1 and P_2 [Figs. 4.9 (c) and (d)] for runs R4 (red line) and R6 (blue dashed line), in which the mean Re is held fixed by tuning both γ
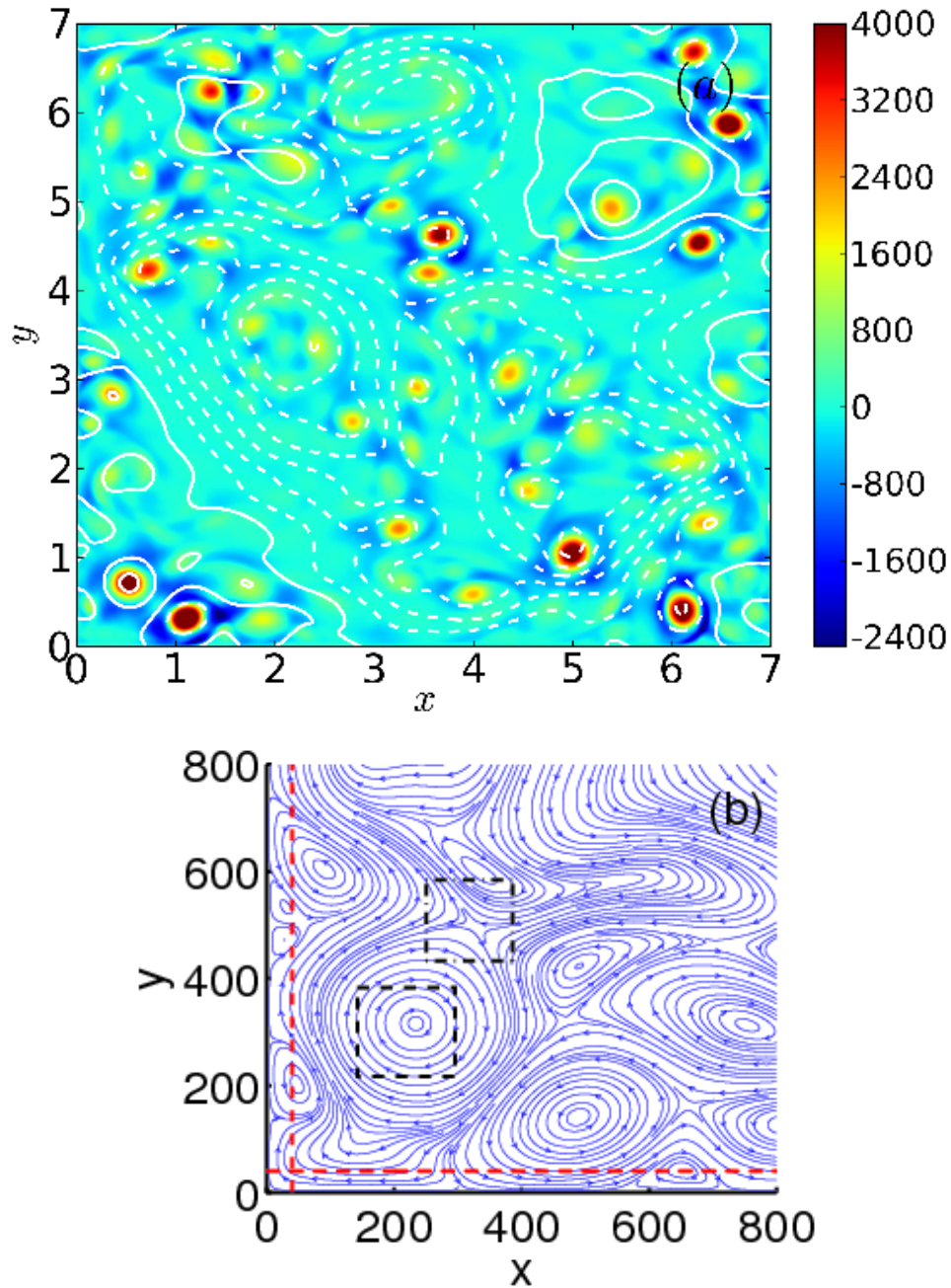
Figure 4.6: (a) Representative pseudocolor plot of Λ superimposed on a contour plot of the stream function ψ in the statistical steady state. Contours of $\psi > 0$ are shown as continuous lines whereas contours of $\psi < 0$ are indicated by dashed lines. Regions with $\Lambda > 4000$ are shown in dark-red color and with $\Lambda < -2400$ in dark-blue color. For intermediate values of Λ, the colors used are as indicated in the color bar. For the temporal evolution of the Λ field see the movie mov_lam.mpg (MPEG file, 3.5MB, in the attached CDROM) from our DNS. (b) A representative plot of the velocity field in the left corner of the simulation domain; the border with the red boundary is of width $2\delta_b$ and the two square boxes show one center and one saddle. Both plots are for the run R7.
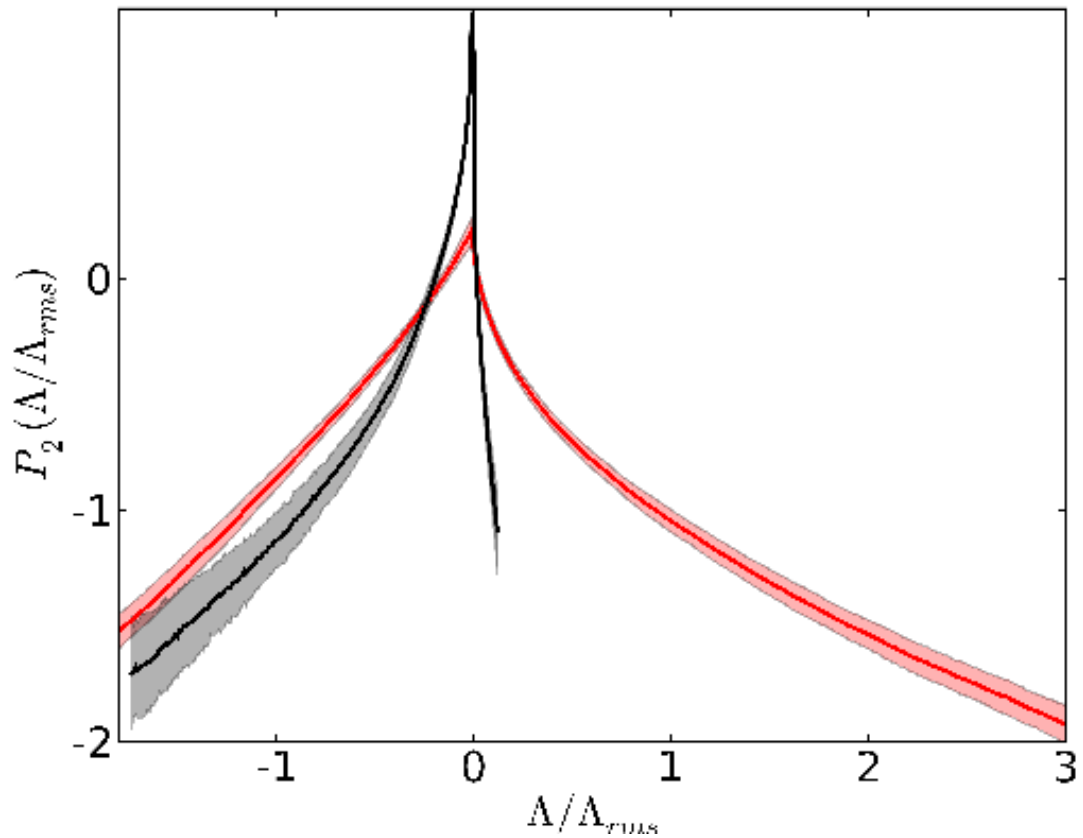
Figure 4.7: The PDF $P_2(\Lambda/\Lambda_{rms})$ obtained from points in the bulk $\delta_b < x, y < L - \delta_b$ (red line) and from points within a distance δ_b from the boundaries (black line) for our run R7. One-standard-deviation error bars are indicated by lightly shaded regions that straddle the curves of $P_2(\Lambda/\Lambda_{rms})$.
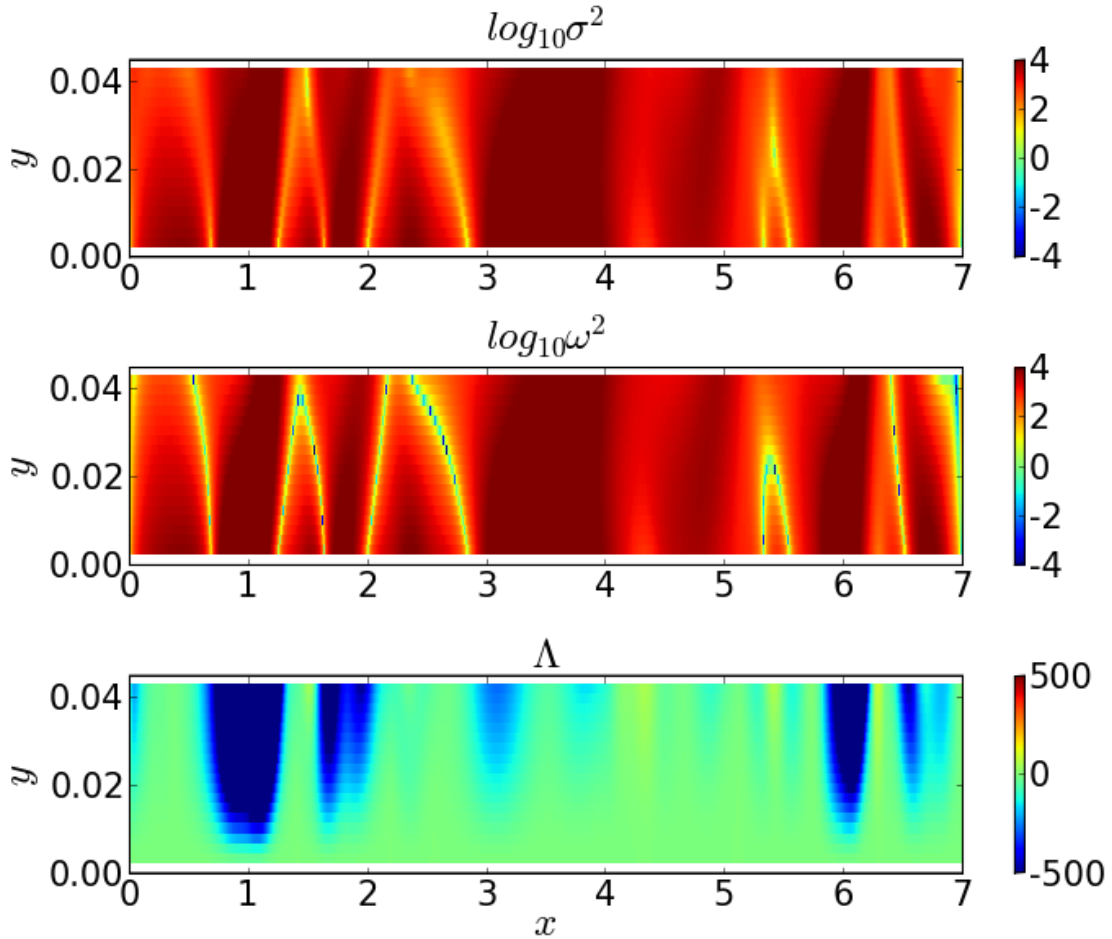
Figure 4.8: Representative pseudocolor plot of $log_{10}(\sigma^2)$ (top frame), $log_{10}(\omega^2)$ (middle frame), and Λ (bottom frame) in a region that is one-boundary-layer thick, i.e., of width δ_b, and which lies near the bottom wall. The plot shows that, although $log_{10}\sigma^2$ and $log_{10}\omega^2$ have very similar profiles, in most of the region $log_{10}\sigma^2 > log_{10}\omega^2$. This explains the skewness of the near-wall $P_2(\Lambda/\Lambda_{rms})$. Regions with $\Lambda > 1000$ and $log_{10}\sigma^2, log_{10}\omega^2 > 4$ are shown in dark red and regions with $\Lambda < -1000$ and $log_{10}\sigma^2, log_{10}\omega^2 > -4$ are shown in dark blue. For intermediate values of $log_{10}\sigma^2, log_{10}\omega^2$, and Λ, the colors used are as in the color bar.
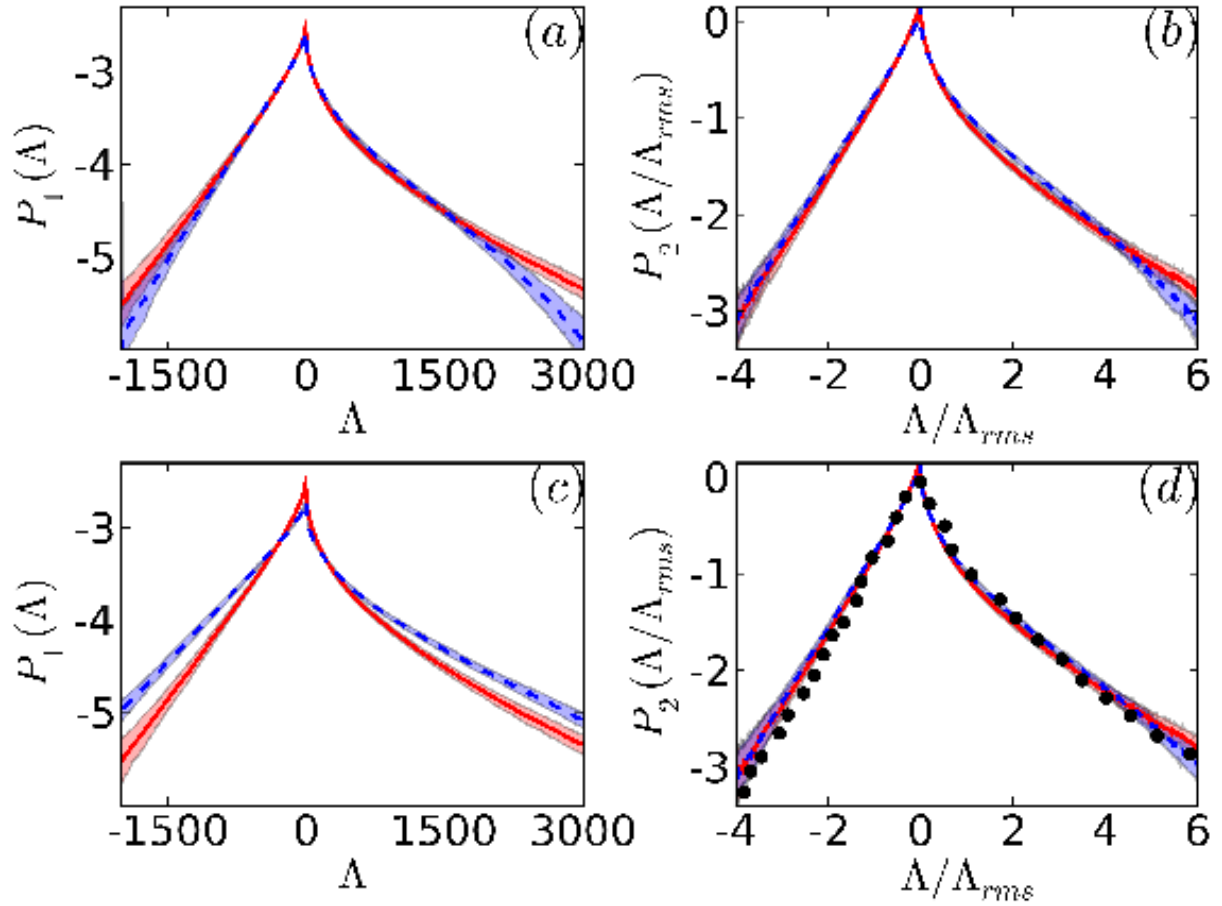
Figure 4.9: Plots of (a) $P_1(\Lambda)$ versus Λ and (b) $P_2(\Lambda/\Lambda_{rms})$ versus Λ/Λ_{rms} for fixed $\mathcal{G}$ and $\gamma = 0.25$(red line) and $\gamma = 0.71$(blue dashed line) [runs R4 and R5]; plots of (c) $P_1(\Lambda)$ versus Λ and (d) $P_2(\Lambda/\Lambda_{rms})$ versus Λ/Λ_{rms} [runs R4 and R6 with $Re \simeq 23.5$] and $\gamma = 0.25$(red line) and $\gamma = 0.71$(blue dashed line) and points (black dots) extracted from Fig. 2(d) of Ref. [10]. The fluctuating part of the velocity is used to calculate Λ. One-standard-deviation error bars are indicated by the shaded regions.

and $\mathcal{G}$, we find, in agreement with experiments [10], that the PDFs P_1 do not agree for these runs, but the PDFs P_2 overlap within error bars. Our results for P_2 in Fig. 4.9(d) are in quantitative agreement with experiments: we have obtained the points in this plot by digitizing data points [see http://www.frantz.fi/software/g3data.php] in Fig. 2(d) of Ref. [10]; the errors in these points are comparable to the spread of data in [10]. The differences between Figs. 4.9(a) and (b) can be understood by the following heuristic argument: For homogeneous, isotropic turbulence

$$\overline{\Lambda} = (\overline{\omega^2} - \overline{\sigma^2})/4 = 0$$

because the spatial averages of ω^2 and σ^2 are both $2|\epsilon_\nu|/\nu$. Even for the flow we consider the PDFs of Figs. 4.9(a)-(d) yield $\overline{\Lambda} \simeq 0$ whence $\overline{\omega^2} \simeq \overline{\sigma^2}$. On taking the square and then the spatial average of Eq. (4.3) we get

$$\overline{\Lambda^2} = [\overline{\omega^4} + \overline{\sigma^4} - 2\overline{\omega^2\sigma^2}]/16;$$

and if we make the approximations $\overline{\omega^4} \simeq 3\overline{\omega^2}^2$ and $\overline{\sigma^4} \simeq 3\overline{\sigma^2}^2$ then

$$\overline{\Lambda^2} \simeq \frac{3|\epsilon_\nu|^2}{2\nu^2}(1 - \frac{2\overline{\omega^2\sigma^2}}{\overline{\omega^4} + \overline{\sigma^4}}),$$

$$\overline{\Lambda^2} \simeq 0.33\frac{3|\epsilon_\nu|^2}{2\nu^2}, \text{whence}$$

$$\Lambda_{rms} = \sqrt{\overline{\Lambda^2} - (\overline{\Lambda})^2} \simeq |\epsilon_\nu|/\nu, \tag{4.4}$$

where the second line in Eq. (4.4) follows from the last column of Table 4.3; this Table shows the degree to which the approximations made above agree with the the results from our DNS.

Note that in all our runs R1 − 7 $\nu = 0.016$. So, if we hold the Grashof number $\mathcal{G}$ fixed (runs R4 and R5), then $|\epsilon_\nu|$ is independent of γ [Fig. 4.1(c) and Table4.2] and, therefore, Λ_{rms} [Eq. (4.4)] is also independent of γ. In contrast, if we hold Re fixed (runs R4 and R6), $|\epsilon_\nu|$ increases with increasing γ [Fig. 4.1(d) and Table 4.2] so Λ_{rms} [Eq. (4.4)] also increases as γ increases. This explains why the the unscaled PDFs P_1
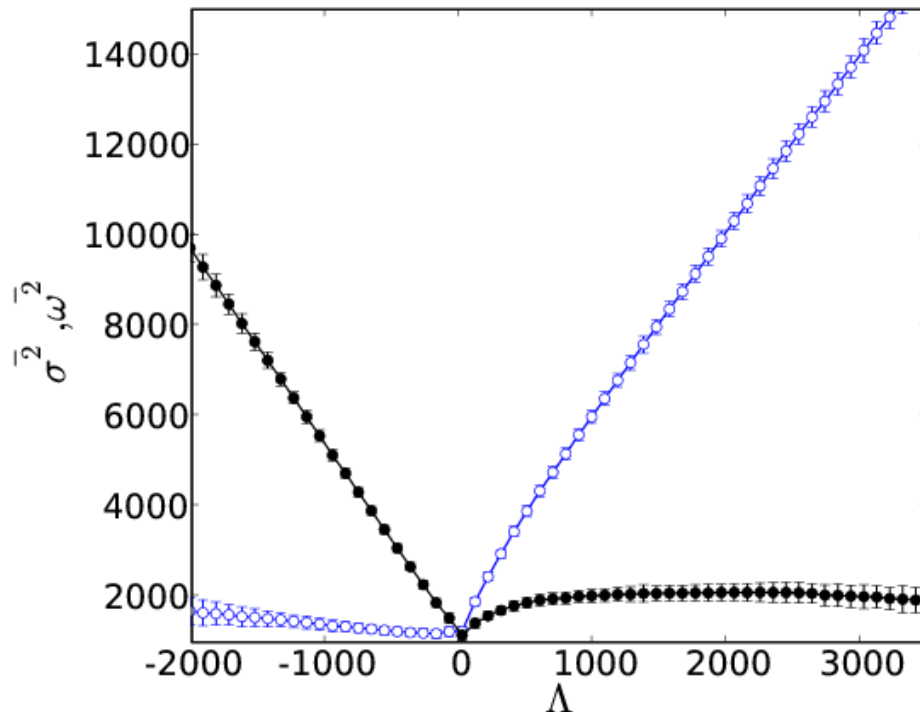
Figure 4.10: Plots of conditional expectation values, with one-standard-deviation error bars, of $\overline{\sigma^2}$(black dots) and $\overline{\omega^2}$(blue circles) for a given Λ for our run R5. A comparison of this figure with Fig. 3 of Ref. [10] shows that our results are in excellent qualitative agreement with the experiments.

of Fig. 4.9(a) overlap ($\mathcal{G}$ fixed) but those in Fig. 4.9(c) do not (Re fixed). Only when we normalise Λ by Λ_{rms} do the scaled PDFs P_2 overlap [Figs. 4.9(b) and (d)].

Conditional expectation values of $\overline{\sigma^2}$ and $\overline{\omega^2}$, for a given value of Λ, also agree well with experiments as can be seen by comparing Fig. 4.10 with Fig. 3 of Ref. [10].

We also present in Figs. 4.11 (a-c) pseudocolor plots of the joint PDFs of

$$
\begin{aligned}
\delta\omega(r) &\equiv \omega'(\mathbf{x} + r\hat{e}_x) - \omega'(\mathbf{x}), \\
\delta u_L(r) &\equiv u_x'(\mathbf{x} + r\hat{e}_x) - u_x'(\mathbf{x}), \text{ or} \\
\delta u_T(r) &\equiv u_y'(\mathbf{x} + r\hat{e}_x) - u_y'(\mathbf{x})
\end{aligned}
\tag{4.5}
$$

with $\Lambda' \equiv \det(M)$. **Here**

$$M^{\alpha\beta} \equiv \frac{1}{A_r} \int_\Omega m^{\alpha\beta} \mathbf{d}r, \tag{4.6}$$

$$A_r \equiv \int_\Omega \mathbf{d}r, \text{and} \tag{4.7}$$

$$m^{\alpha\beta} \equiv \partial_\alpha \mathbf{u}'_\beta, \tag{4.8}$$

Ω a circular disc with center at $\mathbf{x} + (r/2)\hat{e}_x$ and radius $r/2$, and r in the forward-cascade regime. In Figs. 4.11(a-c) we present pseudocolor plots of the joint PDFs $P(\delta\omega(r = 0.12), \Lambda'/\Lambda'_{rms})$, $P(\delta u_L(r = 0.12), \Lambda'/\Lambda'_{rms})$, and $P(\delta u_T(r = 0.12), \Lambda'/\Lambda'_{rms})$. Figures 4.11(b-c) are in striking agreement with Figs. 1-2 of Ref. [11]. Figure 4.11(a) predicts that regions of large $\delta\omega$ and small Λ'/Λ'_{rms} (and vice-versa) are correlated; this result awaits experimental confirmation.

Finally, we calculate

$$\tilde{\Lambda} \equiv [\langle \overline{(\partial_x u'_y)^2} \ \overline{(\partial_y u'_x)^2} \rangle]^{1/2} \text{ and} \tag{4.9}$$

$$b \equiv -\langle \partial_x u'_y \partial_y u'_x \rangle / \tilde{\Lambda} \tag{4.10}$$

(see Table 4.2). Our simulations yield $b \simeq 0.3$ which is the same as that obtained in the experiments for the Kolmogorov forcing in Table I of Ref. [10]. We find $530 \leq \tilde{\Lambda} \leq 720$, which is close to the experimental range $712 \leq \tilde{\Lambda} \leq 1282$; our values of $\tilde{\Lambda}$ are somewhat smaller than those in experiments since our Reynolds numbers are not as large as in these experiments. We find δ_b, the boundary-layer thickness, to be small and it does not depend significantly on α ($\delta_b \sim 0.031 \pm 0.001$), which suggests that the bulk-flow properties are only weakly affected by the boundaries in such a soap-film.

4.4 Conclusion

Some earlier numerical studies of 2D, wall-bounded, statistically steady turbulent flows [22, 23] use forcing functions that are not

	$\dfrac{\overline{\omega^2}}{\overline{\sigma^2}}$	$\dfrac{\overline{\omega^4}}{3\overline{\omega^2}^2}$	$\dfrac{\overline{\sigma^4}}{3\overline{\sigma^2}^2}$	$\dfrac{\overline{\omega^2\sigma^2}}{\overline{\omega^4}+\overline{\sigma^4}}$
R4	1 ± 10^{-5}	1.4 ± 0.2	1.0 ± 0.2	0.32 ± 0.03
R5	1 ± 10^{-5}	1.1 ± 0.1	0.8 ± 0.1	0.34 ± 0.03
R6	1 ± 10^{-5}	1.3 ± 0.1	0.9 ± 0.1	0.32 ± 0.02
R7	0.99 ± 10^{-4}	1.7 ± 0.3	1.3 ± 0.1	0.34 ± 0.03

Table 4.3: The ratios $\frac{\overline{\omega^2}}{\overline{\sigma^2}}$, $\frac{\overline{\omega^4}}{3\overline{\omega^2}^2}$, $\frac{\overline{\sigma^4}}{3\overline{\sigma^2}^2}$, $\frac{\overline{\omega^2\sigma^2}}{\overline{\omega^4}+\overline{\sigma^4}}$ obtained from our DNS.
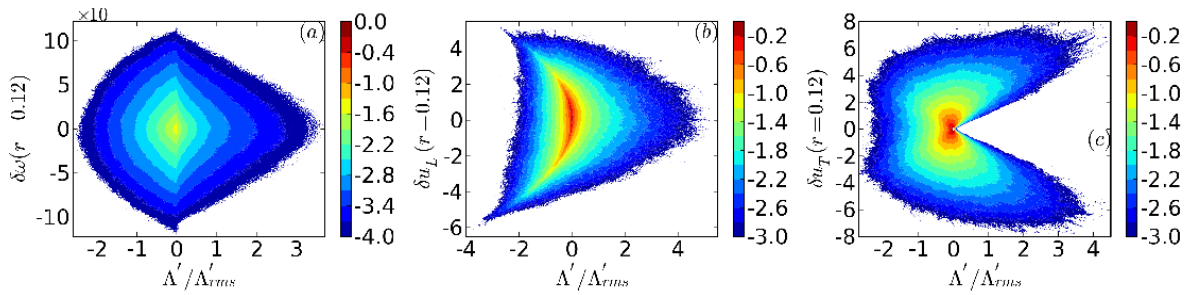
Figure 4.11: Pseudocolor plots of (a) the joint PDF $P(\delta\omega(r = 0.12), \Lambda'/\Lambda'_{rms})$, (b) the joint PDF $P(\delta u_L(r = 0.12), \Lambda'/\Lambda'_{rms})$, and (c) the joint PDF $P(\delta u_T(r = 0.12), \Lambda'/\Lambda'_{rms})$ for our run R7. The contours and the shading are for the logarithms of the joint PDFs. A comparison of (b) and (c) with Figs. 1(b) and 2 of Ref. [11] show that our results agree very well with experiments.

of the Kolmogorov type; furthermore, they do not include air-drag-induced Ekman friction. Other numerical studies, which include the Ekman friction and Kolmogorov forcing, employ periodic boundary conditions [24, 25, 28]. To the best of our knowledge our study of 2D *turbulent* flows is the first one that accounts for the Ekman friction, realistic boundary conditions, and Kolmogorov forcing. We show that, for values of α that are comparable to those in experiments, the energy dissipation rate because of the Ekman friction is comparable to the energy dissipation rate that arises from the conventional viscosity. We extract the isotropic part of the structure functions in the forward-cascade regime. We find that velocity structure function exponent ratios show simple scaling whereas their vorticity counterparts show multiscaling. We also study the topological properties of two-dimensional turbulence by using the Okubo-Weiss criterion and we find excellent agreement with PDFs that have been obtained experimentally. We hope our results will stimulate experimental studies designed to extract (a) the isotropic parts of structure functions (and thereby to probe the multiscaling of vorticity structure functions [Fig. 4.5 (b)] or (b) the PDF $P_2(\Lambda/\Lambda_{rms})$ (Fig. 4.7) near soap-film boundaries.

In Ref. [29] it was argued that, if the Ekman friction is nonzero and in the limit of vanishing viscosity, the third-order velocity structure function shows an anomalous behavior. In our calculations of structure functions of odd orders, we have employed moduli of velocity increments; without these moduli the error bars are too large in our wall-bounded DNS to obtain good statistics for structure functions of odd order. Thus we cannot compare our results directly with those of Ref. [29]. The main point of our study is to mimic, as closely as possible, parameters and boundary conditions in soap-film experiments such as those of Ref.[12]. Hence our viscosity is much higher (and the Reynolds number much lower) than in the DNS of Ref. [27], which was

designed to investigate some of the issues raised in Ref. [29]. Therefore, a direct comparison of our structure-function results with those of Ref. [27] is not possible especially for odd orders because, as mentioned above, we use moduli of velocity increments. We have, however, checked that our velocity structure functions show simple scaling as in the experiments of Ref. [12]; it would be interesting to explore if these experiments can be extended to confirm the multiscaling of vorticity structure functions that we describe above; such experimental studies might well benefit from the procedures we have used to extract the isotropic parts of structure functions.

Appendix C

C.1   Numerical scheme

In this appendix we describe the fourth-order Runge-Kutta (RK4) scheme that is used for the time evolution of Eq. (4.1).
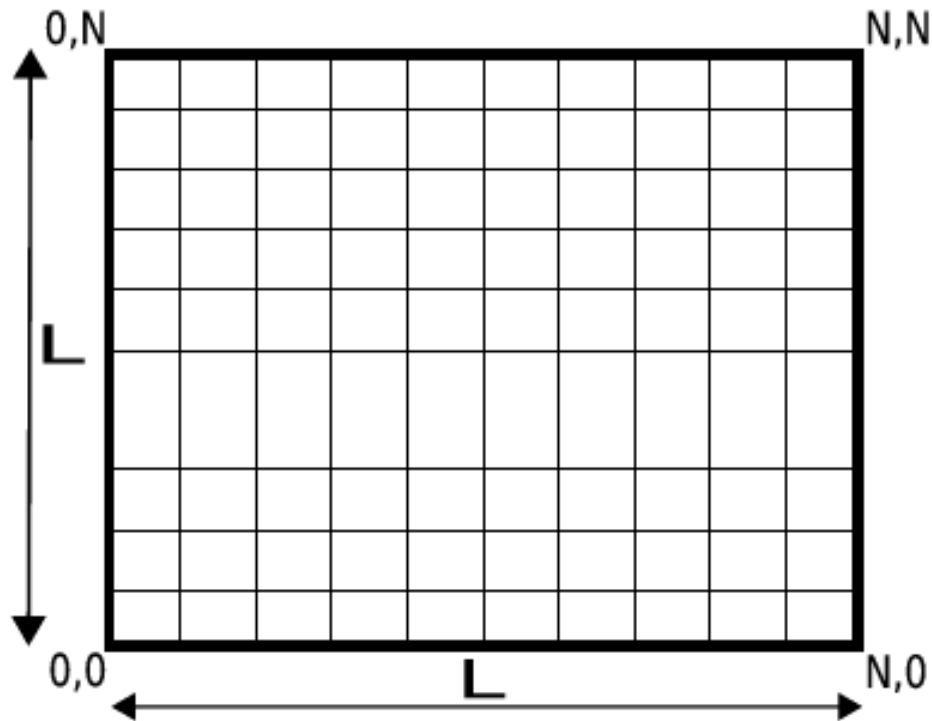
Figure C1: A schematic diagram of the equispaced spatial grid in a square domain used in our simulations. The grid spacings along the x and y directions are $\delta x = \delta y = L/N$.

In Fig. C1 we show a schematic diagram of the equispaced grid used in our simulations. We have used no-slip and no-penetration boundary conditions at the wall. In terms of the streamfunction these boundary conditions are $\psi = 0$ and $\nabla \psi \cdot \hat{n} = 0$. In the interior of the domain $(2,2) \leq (i,j) \leq (N-1, N-1)$ we solve the vorticity evolution Eq. (4.1) equation by using a fourth-order Runge-Kutta (RK4) scheme as follows:

$$
\begin{aligned}
\omega_1 &= \omega^n + \delta t R(\omega^n, \mathbf{u}^n)/2; \\
\nabla^2 \psi_1 &= \omega_1; \\
\omega_2 &= \omega^n + \delta t R(\omega_1, \mathbf{u}_1)/2; \\
\nabla^2 \psi_2 &= \omega_2; \\
\omega_3 &= \omega^n + \delta t R(\omega_2, \mathbf{u}_2); \\
\nabla^2 \psi_3 &= \omega_3; \\
k_4 &= -\delta t R(\omega_3, \mathbf{u}_3); \\
\omega^{n+1} &= (-\omega^n + \omega_1 + 2\omega_2 + \omega_3) + k_4/6; \\
\nabla^2 \psi^{n+1} &= \omega^{n+1}.
\end{aligned}
$$

Here ω_1, ω_2, and ω_3 are the intermediate values of ω at the intermediate time steps of the RK4 scheme. The superscripts n and $n+1$ indicate the discrete time indices such that t at the nth iteration step is $t \equiv n\delta t$, and $R(\omega, \mathbf{u}) = -\mathbf{u}.(\nabla \omega) + \nu \nabla^2 \omega$.

At every step of the RK4 scheme, first the vorticity is updated at the interior nodes ($1 \leq (i,j) \leq N-1$). Next the Poisson equation, with boundary condition $\psi = 0$ at the walls, is solved to obtain ψ (see Appendix C.3). Finally, the vorticity at the walls is updated by using Thom's formulae [21] and Eq. (4.3). This completes the numerical solution procedure that we use to solve Eq. (4.1).

C.2 Finite-difference schemes

In this Appendix we describe the finite-difference schemes we use for first and second derivatives. The centered second- and fourth-order explicit finite-difference approximations of the derivative of a function $f \in \mathbb{R}^1$ are:

$$f' = (-f_{i-1} + f_{i+1})/(2\Delta x); \tag{C1}$$
$$f' = (f_{i-2} - 8f_{i-1} + 8f_{i+1} - f_{i+2})/(12\Delta x). \tag{C2}$$

The centered second- and fourth-order explicit finite-difference approximations of the second derivative of a function $f \in \mathbb{R}^1$ are:

$$f'' = (-f_{i-1} - 2f(i) + f_{i+1})/(\Delta x)^2; \tag{C3}$$
$$f'' = (-f_{i-2} + 16f_{i-1} - 30f_i + 16f_{i+1} - f_{i+2})/(12(\Delta x)^2). \tag{C4}$$

C.3 The Poisson-equation solver

In Appendix C.1 we discussed the numerical procedure to solve Eq. (4.1). To implement the numerical scheme discussed in Appendix C.1 we need to solve the Poisson equation

$$\partial_{xx}\psi + \partial_{yy}\psi = \omega, \tag{C5}$$

with the Dirichlet boundary condition $\psi = 0$ at the walls at every time step. The numerical scheme used by us is similar to the one discussed on pages $849 - 852$ of Ref. [20].

We take the sine transform (see Appendix C.4) of Eq. (C5) along the x-direction to get

$$-(n\pi/L)^2\hat{\psi}_n(y) + \partial_{yy}\hat{\psi}_n(y) = \hat{\omega}_n(y), \tag{C6}$$

where $n = 0, \ldots, N - 1$ and the caret denotes the sine transform. If we now use the second-order, centered, finite-difference approximation

for the derivative Appendix C.2 on our simulation grid, we get,

$$\hat{\psi}_{n,j+1} - [2 + (n\pi/L)^2(\delta y)^2]\hat{\psi}_{n,j} + \hat{\psi}_{n,j-1} = \hat{\omega}_{n,j}(\delta y)^2. \qquad \text{(C7)}$$

For a fixed value of n, Eq. (C7) is a linear system of the form $\mathcal{A}X = \mathcal{B}$, where the tridiagonal matrix $\mathcal{A}$ has the elements $\mathcal{A}_{\alpha,\alpha} = -[2 + (n\pi/L)^2(\delta y)^2]$, $\mathcal{A}_{\alpha,\alpha+1} = \mathcal{A}_{\alpha+1,\alpha} = 1$, and all other elements of $\mathcal{A}$ are 0. The column vectors X and $\mathcal{B}$ have the elements $\hat{\psi}_{n,j}$ and $\hat{\omega}_{n,j}(\delta y)^2$, respectively. We solve the above tridiagonal system for all $n = 0, \cdots, N - 1$ by using the Thomas tridiagonal matrix algorithm (see page-43 of Ref. [20]) or

http://www.cfd-online.com/Wiki/Tridiagonal_matrix_algorithm_-_TDMA_(Thomas_algorithm).

The final step involves taking the inverse sine transform (see Appendix C.4) along the x-direction to get ψ.

C.4 Fast sine transforms

We use the FFTW3 software (`http://www.fftw.org/fftw3\_doc`) to take the sine transforms in Appendix C.3. Below give the definition of sine transform as given in the FFTW3 manual.

Consider a real array $\mathcal{X}$ of length N. Its sine transform to a real array $\hat{\mathcal{Y}}$ of length N is:

$$\hat{\mathcal{Y}}_n = 2 \sum_{j=0}^{N-1} \mathcal{X}_j \sin[\pi(j+1)(n+1)/(N+1)], \qquad \text{(C8)}$$

and the corresponding inverse sine transform is

$$\mathcal{X}_j = \frac{1}{N+1} \sum_{n=0}^{N-1} \hat{\mathcal{Y}}_n \sin[\pi(j+1)(n+1)/(N+1)]. \qquad \text{(C9)}$$

Bibliography

[1] R.H. Kraichnan, *Phys. Fluids* **10**, 1417 (1967).

[2] C. Leith, *Phys. Fluids* **11**, 671 (1968).

[3] G.K. Batchelor, *Phys. Fluids Suppl.* II **12**, 233 (1969).

[4] U. Frisch, *Turbulence the legacy of A.N. Kolmogorov* (Cambridge University Press, Cambridge, 1996).

[5] G.J. Boer and G.T. Shepherd, *J. Atmos. Sci.* **40**, 164 (1983).

[6] W.B. Daniel and M.A. Rutgers, *arXiv:nlin/005008v1* (2000).

[7] H. Kellay and W.I. Goldburg, *Rep. Prog. Phys.* **65**, 845 (2002).

[8] P. Tabeling, *Phys. Rep.* **362**, 1 (2002).

[9] M. Rivera and X.L. Wu, *Phys. Rev. Lett.* **85**, 976 (2000).

[10] M. Rivera, X.L. Wu, and C. Yeung, *Phys. Rev. Lett.* **87**, 044501 (2001).

[11] W.B. Daniel and M.A. Rutgers, *Phys. Rev. Lett.* **89**, 134502 (2002).

[12] M. Rivera and R.E. Ecke, *arXiv:0710.5888v1* (2007).

[13] J.M. Chomaz and B. Cathalau, *J. Fluid Mech.* **442**, 387 (2001).

[14] J.M. Chomaz, *J. Fluid Mech.* **442**, 387 (2001).

[15] E. Bouchbinder, I. Procaccia, and S. Sela, *Phys. Rev. Lett.* **95**, 255503 (2005).

[16] R. Benzi, S. Ciliberto, R. Tripiccione, C. Baudet, F. Massaioli and S. Succi *Phys. Rev. E* **48**, R29 (1993).

[17] J. Weiss, *Physica D* **48**, 273 (1992).

[18] A. Provenzale and A. Babiano, *J. Fluid Mech.* **257**, 533 (1993).

[19] C.R. Doering and J.D. Gibbon, *Applied Analysis of the Navier-Stokes equations* (Cambridge University Press, Cambridge, 1995).

[20] W.H. Press, B.P. Flannery, S.A. Teukolsky, and W.T. Vetterling, *Numerical Recipes in Fortran* (Cambridge University Press, Cambridge, 1992).

[21] E. Weinan and J.-G. Liu, *J. Comp. Phys.* **124**, 368 (1996).

[22] H.J.H. Clercx, G.J.F. Heijst, D. Molenaar, and M.G. Wells, *Dyn. Atmos. and Oceans* **40**, 3 (2005).

[23] G.J.F. van Heijst, H.C.H. Clercx, and D. Molenaar, *J. Fluid Mech.* **554**, 411 (2006).

[24] Y.-K. Tsang, E. Ott, T.M. Antonsen, and P.N. Guzdar, *Phys. Rev. E* **71**, 066313 (2005).

[25] G. Boffetta, *J. Fluid Mech.* **589**, 253 (2007).

[26] K. Nam, E. Ott, T.M. Antonsen, and P.N. Guzdar, *Phys. Rev. Lett.* **84**, 5134 (2000).

[27] G. Boffetta, A. Celani, S. Musacchio, and M. Vergassola, *Phys. Rev. E* **66**, 026304 (2002).

[28] M. Bandi and C. Connaughton, *Phys. Rev. E* **77**, 036318 (2008).

[29] D. Bernard, *Europhs. Lett.* **50**, 333 (2000).

Chapter 5

Turbulence-induced melting of a nonequilibrium vortex lattice in a forced soap film

We perform a DNS of the two-dimensional Navier-Stokes equations. The forcing is chosen such that, at low Reynolds (Re) numbers, the steady state of the soap film is a square lattice of vortices. We find that, as we increase Re, this lattice undergoes a series of nonequilibrium phase transitions, first to a crystal with a different reciprocal lattice and then to a sequence of crystals that oscillate in time. Initially the temporal oscillations are periodic; this periodic behavior becomes more and more complicated with increasing Re until the soap film enters a spatially disordered nonequilibrium statistical steady that is turbulent. We study this sequence of transitions by using fluid-dynamics measures, such as the Okubo-Weiss parameter, ideas from nonlinear dynamics, e.g., Poincaré maps, and theoretical methods that have been developed to study the melting of an equilibrium crystal or the freezing of a liquid, for instance, the behavior of the autocorrelation function $G(r)$ in crystalline and liquid phases.

5.1 Introduction

A crystal melts into a disordered liquid when the temperature is raised beyond the melting point T_M; and when the liquid is cooled below T_M it freezes again. This melting or freezing transition, one of the most common equilibrium phase transitions, has been studied extensively; and the Ramakrishnan-Yussoff density-functional theory [1, 2, 3, 4], which uses a suitable variational free energy, has led to a good understanding of such freezing. It is natural to ask whether there are nonequilibrium analogues of this transition. One example is shear-induced melting of colloidal crystals [5]. In this Chapter we investigate another example of a nonequilibrium transition in which dynamically generated turbulence plays the role of temperature and disorders a crystal consisting of an array of vortices, of alternating sign, imposed on a thin fluid film by an external force.

Recent experiments [6, 7] have explored this transition from a low-Reynolds-number nonequilibrium vortex crystal, imposed on a thin fluid film by a force that is periodic in space, to a high-Reynolds-number, disordered, nonequilibrium liquid-type phase. This problem has been studied earlier by using linear-stability analysis [8, 9] and direct numerical simulations (DNS) [10, 11]. The former is well-suited to the study of the first instability of the vortex crystal with increasing Reynolds number Re; the latter have (a) studied the route to chaos, by using techniques from nonlinear dynamics [10, 11] to analyse the temporal evolution of this system, or (b) have mimicked [12] the experiments of Ref. [6] to study the creation and annihilation of vortices.

In this Chapter we revisit the problem of turbulence-induced melting of the vortex by conducting a direct numerical simulation of the two-dimensional Navier-Stokes equations. We show how to combine methods from turbulence, nonlinear dynamics, and statistical physics to elucidate the nature of nonequilibrium phases and transitions in

this system. Our approach leads to a characterisation of these transitions in terms of order parameters like those in the density-functional theory of freezing [1, 2, 3, 4].

In particular, we use the two-dimensional (2D) Navier-Stokes equation with Ekman friction to model the thin fluid films used in experiments [6, 7, 13]; as we have shown in Chapter-4 and Ref. [14], this is a good model for flows in such thin films so long as the Mach number is small and the corrections arising from the finite thickness of the film and from the Marangoni effect can be neglected [15, 16]. We force this 2D NS equation in a manner that mimics the forcing used in experiments and which yields, at low Re, a stationary, periodic array of vortices of alternating signs; we will refer to this array as the vortex crystal.

We then investigate the stability of this array as we increase the amplitude of the force and, therefore, the Reynolds number. We use methods from nonlinear dynamics, including time-series analysis, power spectra, and Poincaré-type maps, to examine the temporal behaviour of this system as it undergoes a sequence of transitions. This part of our study complements the work of Refs. [10, 11].

Furthermore, we elucidate the natures of the transitions from the spatially ordered crystal to the disordered, turbulent state by borrowing ideas from the density-functional theory of the freezing of a liquid into a crystal [1, 2, 3, 4]. Since the density field of a crystal is *periodic*, this theory uses the coefficients in the Fourier decomposition of the density as *order parameters*. Specifically, in a conventional crystal, ρ admits the Fourier decomposition

$$\rho(\mathbf{r}) = \sum_{\mathbf{G}} \rho_{\mathbf{G}} \exp(\imath \mathbf{G} \cdot \mathbf{r}), \tag{5.1}$$

where the sum is over the vectors $\mathbf{G}$ of the *reciprocal lattice*; in the density-functional theory of freezing [1, 2] the Fourier coefficients $\rho_{\mathbf{G}}$ are taken to be the order parameters of the liquid-to-crystal transi-

tion since their mean values vanish in the liquid phase for all nonzero reciprocal lattice vectors **G**; moreover, $\rho_{\mathbf{G}=0}$ is the mean density and, because most liquids are nearly incompressible, it shows a very small change at this transition. Spatial correlations in the isotropic liquid phase can be characterized conveniently by the autocorrelation function $g(r) = \langle \overline{[\rho(\mathbf{x} + \mathbf{r})\rho(\mathbf{x})]} \rangle$, where the angular brackets denote Gibbsian thermal averages and the overline denotes spatial averaging over x; the Fourier transform of $g(r)$ is related [1, 2] to the static structure factor $S(k)$. [The crystalline phase is not isotropic so the arguments of g and S are vectors in that phase.]

We use the Okubo-Weiss field $\Lambda \equiv \det(A)$ as the analogue of the density $\rho(\mathbf{r})$ in the density-functional theory of freezing; here A is the velocity-derivative matrix that has components $A_{ij} \equiv \partial_i u_j$, with u_j the jth component of the velocity. As we have shown in Chapter-4, Λ distinguishes between vortical regions and strain-dominated ones; it is positive in the former and negative in the latter. Thus, in the nonequilibrium vortex crystal, $\Lambda(\mathbf{r})$ is a periodic function; so, like $\rho(\mathbf{r})$ in a conventional crystal, it admits the Fourier decomposition

$$\Lambda(\mathbf{r}) = \sum_{\mathbf{k}} \hat{\Lambda}_{\mathbf{k}} \exp(i\mathbf{k} \cdot \mathbf{r}), \tag{5.2}$$

where the sum is over the reciprocal-lattice vectors k and it is natural to think of $\hat{\Lambda}_{\mathbf{k}}$ as the order parameters that characterise the vortex crystal. In terms of these order parameters we can define the analogue of the static structure factor $S(\mathbf{k})$ for a conventional crystal; for the vortex crystal this is the two-dimensional spectrum

$$E_\Lambda(\mathbf{k}) \equiv \langle \hat{\Lambda}_{\mathbf{k}} \hat{\Lambda}_{-\mathbf{k}} \rangle; \tag{5.3}$$

here the angular brackets do not imply a Gibbsian thermal average, as in equilibrium melting, but denote an average over the nonequilibrium statistical steady state of our system. The autocorrelation function

$$G(\mathbf{r}) = \langle \overline{\Lambda(\mathbf{x} + \mathbf{r})\Lambda(\mathbf{x})} \rangle, \tag{5.4}$$

is related to $E_\Lambda(\mathbf{k})$ by a spatial Fourier transform. The turbulent phase is isotropic so G depends only on $r \equiv | \mathbf{r} |$; and it characterises the short-range order in the system exactly as $g(r)$ does in an isotropic liquid.

We also make comparisons with the recent experiments of Ref. [6]. Our main results are: (i) For the parameter range explored by us, on increasing the Reynolds number we observe a series of transitions from steady states with structures larger than the forcing state, to time periodic solutions, and finally for large values of Reynolds number spatio-temporal chaos sets in; (ii) In agreement with the earlier numerical simulations [10, 17] we observe the formation of large scale-structures and periodic orbits. We quantify the above by not only looking at the projection of Poincaré sections in Fourier space and the Fourier analysis of the time series but also by E_Λ and the autocorrelation function $G(r)$.

5.2   Equations

In this section we give an overview of the model and the numerical methods we use. The 2D Navier-Stokes (NS) equations can be written in the following non-dimensional form [17]:

$$(\partial_t + \mathbf{u} \cdot \nabla)\omega = \nabla^2\omega/\Omega - \alpha\omega + F_\omega; \quad \nabla^2\psi = \omega. \tag{5.5}$$

Here $\mathbf{u} \equiv (-\partial_y\psi, \partial_x\psi)$, ψ, and $\omega \equiv \nabla \times \mathbf{u}$ are, respectively, the velocity, stream function, and vorticity at the position $\mathbf{x}$ and time t; we choose the uniform density $\rho = 1$; α is the Ekman friction coefficient, ν is the kinematic viscosity, and $F_\omega \equiv -n^3[\cos(nx) + \cos(ny)]/\Omega$, is the force with injection wave vector n. We denote the x and y components of the velocity as $u_1 \equiv u$ and $u_2 \equiv v$, respectively. The above non-dimensional form of the 2D NS equations is obtained by using the normalizations of Ref. [17] given which we have $\Omega \equiv nF_{amp}/(\nu^2 k^3)$,

and $\alpha = n\nu\alpha'k/F_{amp}$, where F_{amp} is the forcing amplitude, α' is the Ekman friction, and lengths are non-dimensionalised via a factor k/n with k a wave vector or inverse length. The spatially periodic force F_ω yields, at low Ω, a vortex crystal that is also referred to as a cellular flow. A linear-stability analysis of this flow indicates that it has a primary instability [9] at a critical Reynolds number $Re_c \equiv \sqrt{2}$ which translates into a threshold value $\Omega_{s,n} \equiv nRe_c$. This primary instability yields another vortex crystal, which is steady in time but whose unit cell is larger than that of the original vortex crystal [9, 18].

We solve Eq. (5.5) numerically by using a pseudo-spectral code with a $2/3$ dealiasing cut-off and a second-order Runge-Kutta scheme for time marching (Appendix D.1) with a time step $\delta t = 0.01$. We use N^2 collocation points; in most of our studies we use $N = 128$; we have checked in representative cases that our results are unchanged if we use $N = 256$. Our main goal has been to obtain long time series for several variables (see below) to make sure that the temporal evolution of our system is obtained accurately; most of our runs are at least as long as $3 \times 10^6 \delta t$. We monitor the time-evolution of (a) the kinetic energy $E(t) \equiv \overline{\mathbf{u}^2}$, (b) the stream function ψ, (c) the vorticity ω, (d) the Okubo-Weiss parameter Λ, and (e) the $\mathbf{k} = (1,0)$ component of the Fourier transform $\hat{v}$ of the y component v of $\mathbf{u}$. Given these time series we obtain $E_\Lambda(\mathbf{k})$ at representative times and $G(r)$, which is obtained by averaging over 20 configurations of $\Lambda(x,y)$ separated from each other by $10^5 \delta t$, after transients in the first 10^6 time steps have been removed. From the time series of $E(t)$ we obtain its temporal Fourier transform $E(f)$ and thence the spectrum $|E(f)|$ that helps us to distinguish between periodic, quasiperiodic, and chaotic temporal behaviours. We also augment this charaterisation by using Poincaré-type sections in which we plot $\Im\hat{v}_{(1,0)}$ versus $\Re\hat{v}_{(1,0)}$ at successive times (see, e.g., Ref. [17] for the Kolmogorov flow).

As we show below, the vortex crystal melts, as we increase Ω, via a complicated sequence of transitions. The principal effect of the Ekman friction is to delay the onsets of these transitions; we have checked this explicitly in some cases. However, to make contact with earlier linear-stability and DNS studies of this problem, the results we present below have been obtained with no Ekman friction. Our qualitative conclusions are not affected by this.

So long as $\Omega < \Omega_{s,n}$, the steady-state solution [17], indicated by the subscript s, of Eq. (5.5) is $\omega_{s,n} = -n[cos(nx) + cos(ny)]$. We examine the destabilisation of this state, with increasing Ω, for two representative values of n, namely, $n = 4$ and $n = 10$; for both these cases we choose the initial velocity field to have the form $\omega = \omega_{s,n} + 10^{-4} \sum_{m_1=0,m_2=0}^{2,2} [\sin(m_1 x + m_2 y) + \cos(m_1 x + m_2 y)] m_2^2 / \sqrt{(m_1^2 + m_2^2)}$; and then we let the system evolve under the application of the force F_ω. We increase Ω from $2.26\Omega_{s,n}$ to $3.67\Omega_{s,n}$ in steps of 0.5, for $n = 4$(runs `R4-1` to `R4-7` in Table 5.1), and from $1.9\Omega_{s,n}$ to $19.44\Omega_{s,n}$ in steps of 1, for $n = 10$ (runs `R10-1` to `R10-4` in Table 5.1). We have benchmarked our numerical scheme by comparing our results with those of Ref. [17], which deals with a Kolmogorov flow imposed by an external force of the form $F_\omega = n \cos(ny)$.

5.3 Initial state and the Λ field

For an inviscid, incompressible 2D fluid the local flow topology can be characterized via the Okubo-Weiss criterion [19]. This criterion provides a useful measure of flow properties even if viscosity and Ekman friction are present, as noted in earlier experiments and simulations [13, 14, 20]: Regions with $\Lambda > 0$ and $\Lambda < 0$ correspond, respectively, to centers and saddles [19]. In particular, for $\Omega < \Omega_{s,n}$, we obtain the Λ field, with alternating centres and saddles, arranged in a two-dimensional square lattice, which we illustrate via pseudocolour

	n	Ω	Comments
R4 − 1	4	$\Omega < \Omega_{s,n}$	Square array
R4 − 2	4	$\Omega_{s,n} < \Omega \le 6.5$	Steady state, large structures
R4 − 3	4	$\Omega = 8.202$	Periodic orbit
R4 − 4	4	$9.05 < \Omega < 15.3$	Steady state, large structures
R4 − 5	4	$15.3 < \Omega < 17.3$	Periodic orbits
R4 − 6	4	$\Omega = 17.8$	Quasiperiodic + chaos
R4 − 7	4	$\Omega \ge 18.3$	Chaotic
R10 − 1	10	$\Omega < \Omega_{s,n}$	Square array
R10 − 2	10	$\Omega_{s,n} < \Omega < 22.6$	Steady state
R10 − 3	10	$24 < \Omega < 28$	Periodic orbits
R10 − 4	10	$\Omega \ge 29$	Chaotic

Table 5.1: Table indicating the values of Ω and the route to chaos observed in our simulations.

plots for $n = 4$ and $n = 10$ in Figs. 5.1 (a) and (b), respectively. [These patterns are reminiscent of a two-dimensional version of a perfectly ordered binary alloy, with two kinds of atoms, whose analogues here are centers and saddles.] We show corresponding pseudocolour plots of ψ in Figs. 5.2 (a) and (b), respectively.

5.4   Results

In this section we present the results for our numerical simulations for $n = 4$ and $n = 10$ for the ranges of parameters given in Table 5.1. In the first subsection we present our results for $n = 4$; the next subsection contains our results for $n = 10$.

5.4.1   The case $n = 4$

When we increase Ω beyond $\Omega_{s,n}$, the steady-state solution $\omega_{s,n}$ becomes unstable. From the range of values of Ω in our runs R4 − 2 (Table 5.1) we observe that a new steady state is attained, which we
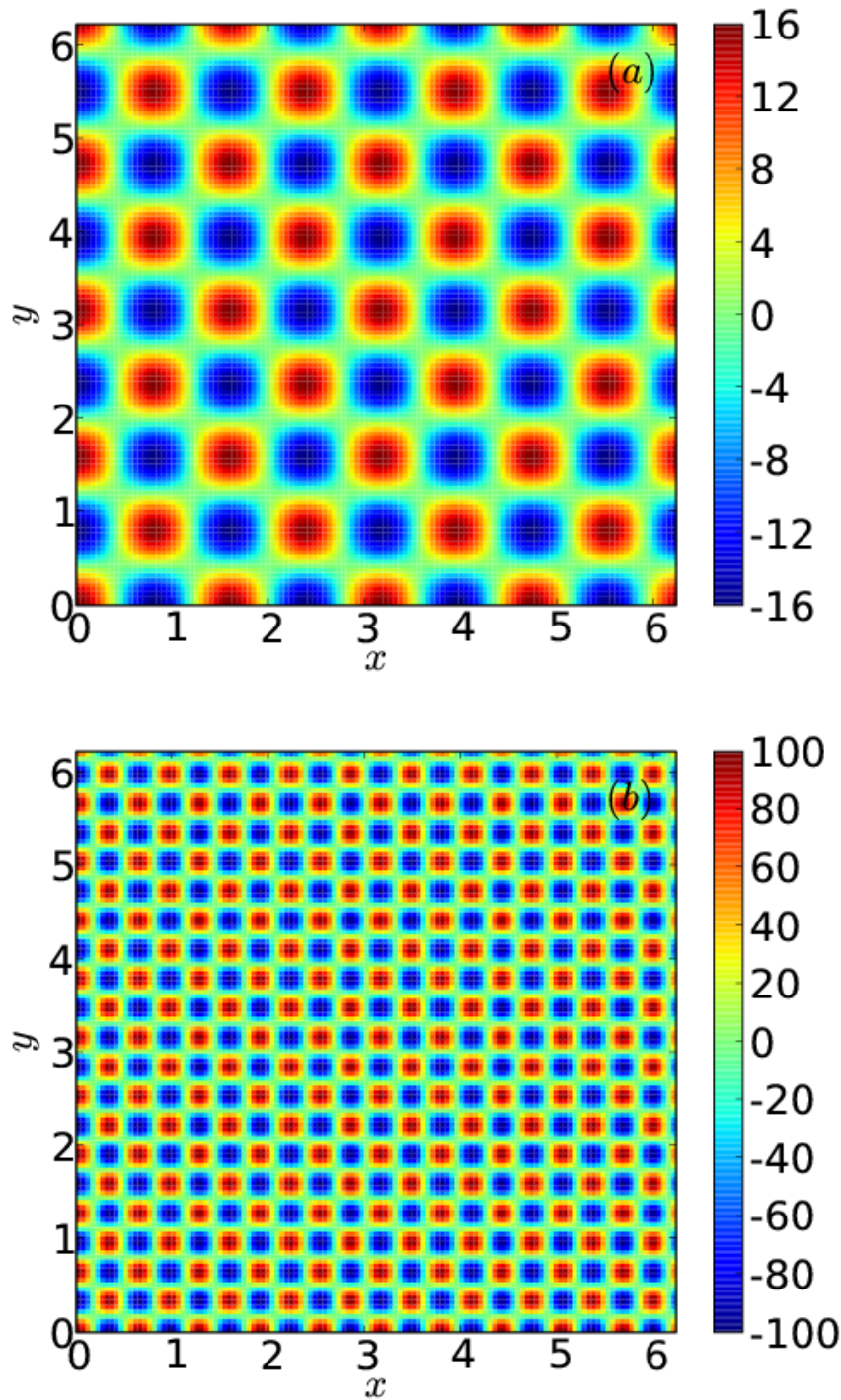
Figure 5.1: Pseudocolour plots, illustrating the vortex crystal for $\Omega < \Omega_{s,n}$, of the Okubo-Weiss field Λ for (a)$n = 4$, and (b) $n = 10$. Given our colour bar, vortical regions, i.e., centres, appear red whereas strain-dominated regions, i.e., saddles, appear dark blue.
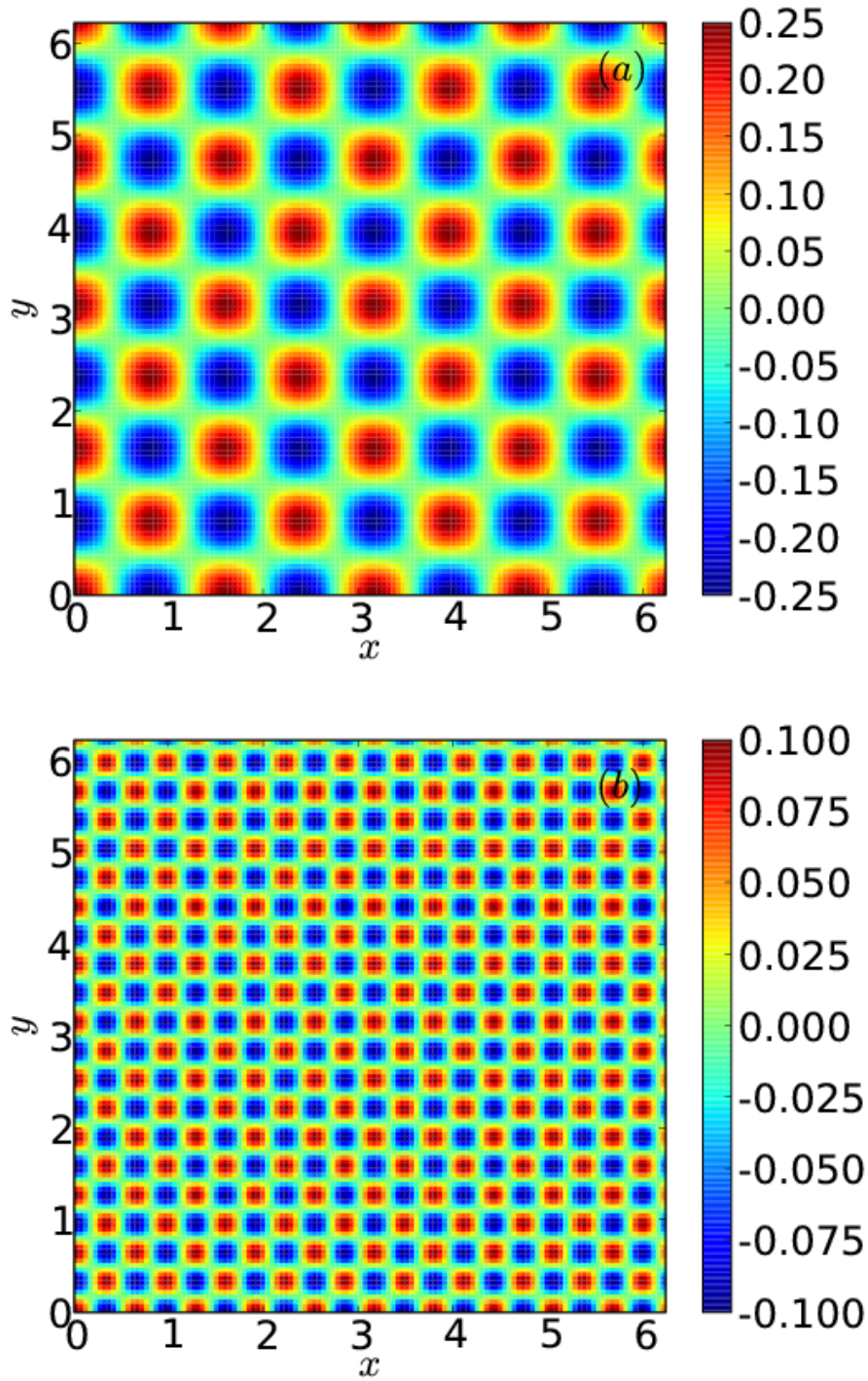
Figure 5.2: Pseudocolour plots, illustrating the vortex crystal for $\Omega < \Omega_{s,n}$, of the streamfunction field ψ for (a)$n = 4$, and (b) $n = 10$.

illustrate, for $\Omega = 6.5$, via pseudocolour plots of ψ and Λ in Figs. 5.3(a) and (b), respectively. The new steady state is also a vortex crystal; however, it is different from the original vortex crystal as can be seen especially clearly by comparing the pseudocolour plots of ψ in Figs. 5.2 (a) and 5.3(a). This difference also shows up as a very slight distortion of the crystalline structure in the pseudocolour plot Λ shown in Fig. 5.3(b). To use the language of solid state physics, this is an example of a very weak *structural phase transition*. Normally such a phase transition is mirrored in new *superlattice peaks* that appear in the reciprocal-space spectrum E_Λ in addition to the dominant peaks associated with the original crystal structure; however, given the weakness of the distortion, such superlattice peaks are not visible, given our resolution in Fig. 5.3(c). Clear examples of such superlattice peaks appear as we increase Ω as we show below.

At $\Omega = 8.202$, a new regime appears (runs R4 − 3). The time-series of the energy $E(t)$ now shows a periodic array of spikes. This regime has no analogue in a conventional crystal; indeed it is a crystal that oscillates periodically in time and, to that extent, it can be thought of as a *spatiotemporal crystal*. The time between successive spikes is very large ($\simeq 10^4 \delta t$) as shown by the plot of $E(t)$ in Fig. 5.4(a); this is why our DNS runs must be very long to distinguish this state from one that is steady; we have also checked that the time between successive spikes is the same (to three-figure accuracy) for $N = 64$ and $N = 128$. In Figs. 5.4(b) and (c) we show pseudocolour plots of ψ and Λ, respectively; the former shows a large-scale undulation and the latter some deformation relative to the original crystal. This deformation is also mirrored in the distortion, relative to Fig. 5.3(c), of the dominant peaks in the reciprocal-space spectrum $E_\Lambda(\mathbf{k})$ shown in Fig.5.4(d).

For runs R4 − 4, i.e., $9.05 \leq \Omega < 15.3$, we find a new crystalline state that is steady in time. It has a large-scale spatial undulation relative to the original vortex crystal as illustrated, for $\Omega = 11.3$, by
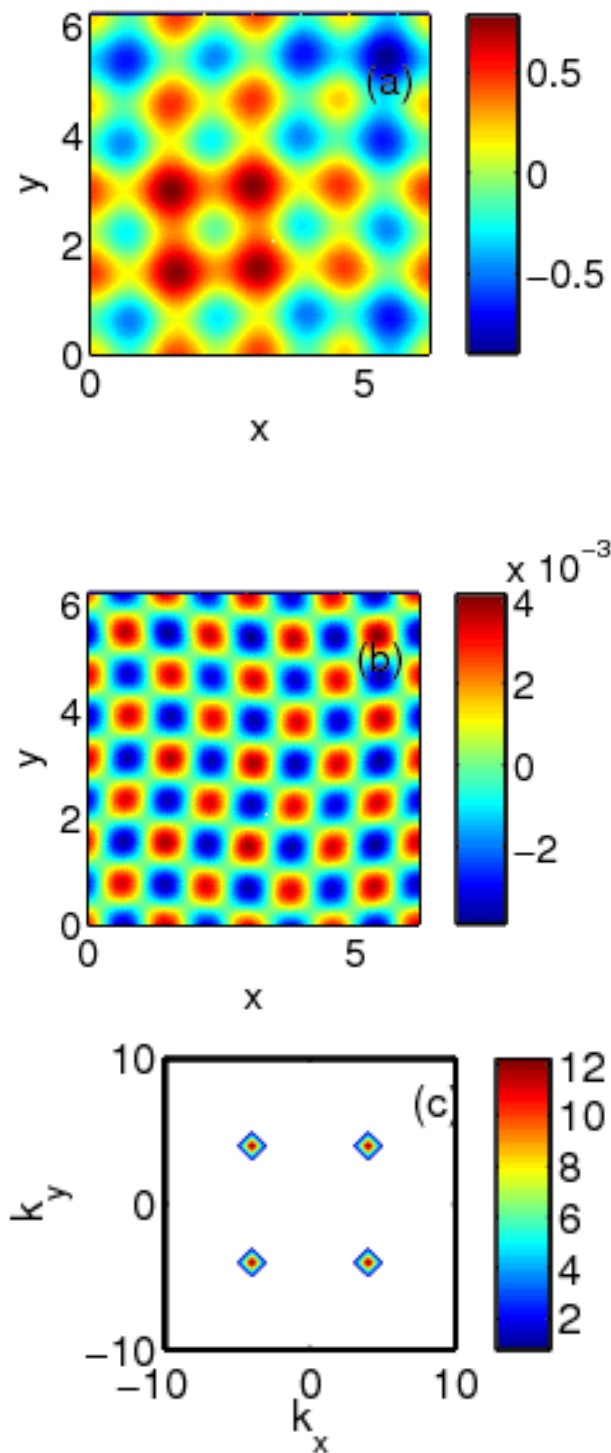
Figure 5.3: Pseudocolour plots for $\Omega = 6.5$ of (a) the streamfunction ψ and (b) the Okubo-Weiss parameter Λ with superimposed contour lines. (c) A filled contour plot the reciprocal-space energy spectrum E_Λ showing clear, dominant peaks at the forcing wave vectors.
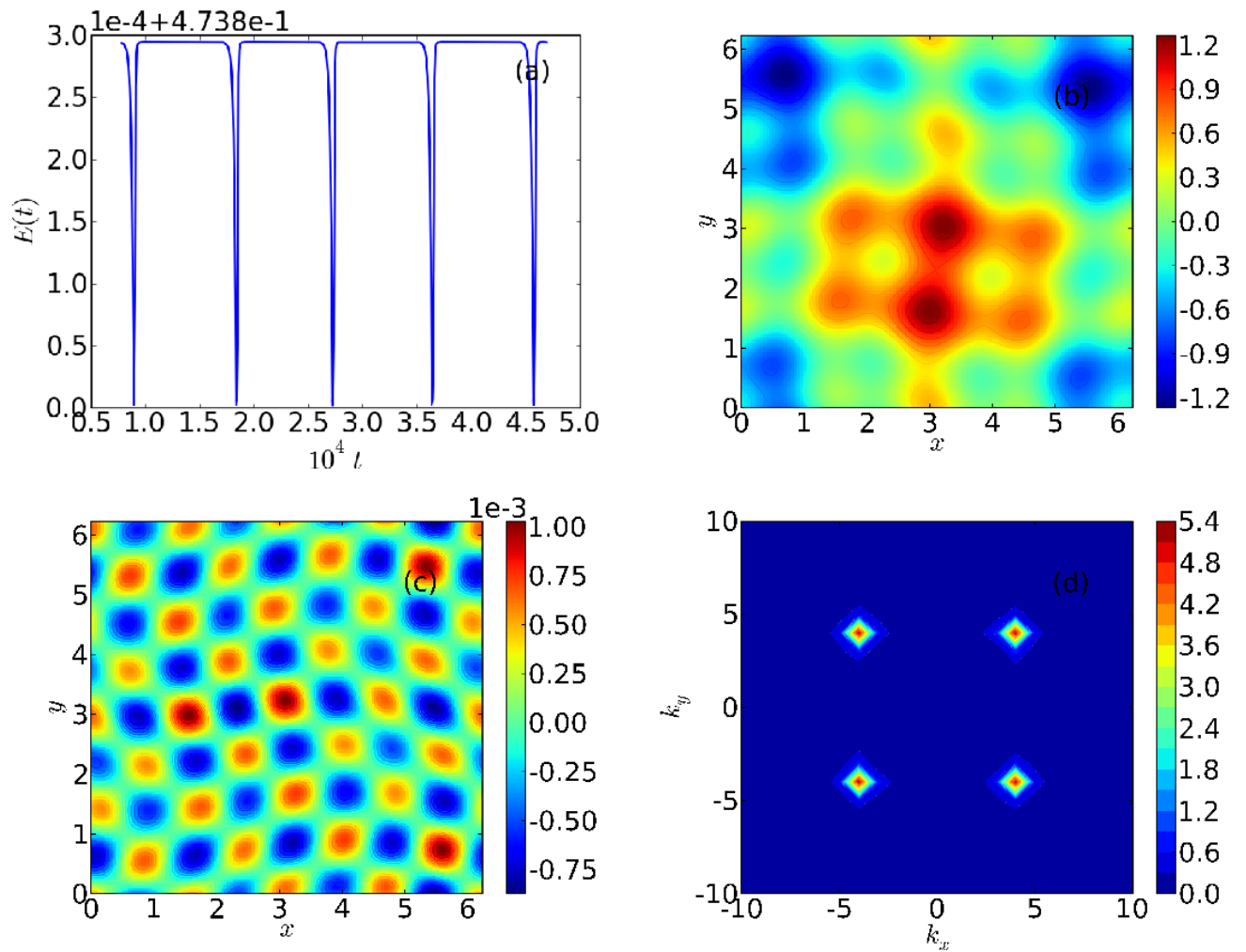
Figure 5.4: The plots for $\Omega = 8.202$ of (a) The time evolution of the energy $E(t)$ for $\Omega = 8.202$. Pseudocolour plots of (b) the streamfunction ψ and (c) the Okubo-Weiss parameter Λ with superimposed contour lines. (d) A filled contour plot the reciprocal-space energy spectrum E_Λ showing the distortions of peaks at the forcing wave vectors.

the pseudocolour plots of ψ and Λ in Figs. 5.5(a) and (b), respectively. This undulation leads to a distortion of the dominant peaks in the the reciprocal-space spectrum $E_\Lambda(\mathbf{k})$ of Figs. 5.5(c), which also shows new superlattice peaks that occur at smaller values of (k_x, k_y) relative to the dominant peaks.

On further increasing Ω we enter a new regime (runs R4 − 5, i.e., $15.3 \leq \Omega < 17.3$) in which we have a spatiotemporal crystal, i.e., a spatially periodic Λ that oscillate in time. The time-series $E(t)$ displays a periodic array of spikes as shown in Fig. 5.6(a); this leads to the frequency-space $\mid E(f) \mid$ of Fig. 5.6(b). The peaks in this spectrum can be labelled as ℓf_0, where ℓ is a positive integer and f_0 is the fundamental frequency that can be obtained from the inverse of the temporal separation between successive spikes in Fig. 5.6(a); this is a clear signature of periodic temporal evolution. The Poincaré-type map in the $(\Re[\hat{u}_y(1,1)], \Im[\hat{u}_y(1,1)])$ plane, Fig. 5.6(c), shows that there is a closed-loop attractor in this case. Pseudocolour plots of ψ and Λ [Figs. 5.7(a)-(b)] are similar, respectively, to those in Figs. 5.5(a)-(b) if we look at their spatial patterns; however, they oscillate in time as can be seen most clearly from their animated versions [mpeg files files psi_movie_R5.mpeg-lam_movie_R5.mpeg in the attached CDROM]. The associated reciprocal-space spectrum E_Λ also oscillates between the spectra shown in Figs. 5.7(c) and (d) as can be clearly seen from its animated version [avi file lamf_movie_R5.avi in the attached CDROM].

The time between successive spikes in $E(t)$ decreases as Ω increases. To quantify this, we define the inter-spike interval T_i as follows: $T_i \equiv t_{i+1} - t_i$, where t_i is the time at which $E(t)$ crosses, for the ith time, its mean value, $\langle E(t) \rangle$, from below; we can think of i as the spike index. In Fig. 5.8(a) we plot T_i versus i; this shows that the mean value of T_i decreases as Ω increases [Fig. 5.8(b)]; furthermore, T_i oscillates slightly about its mean value for any given value of Ω. The
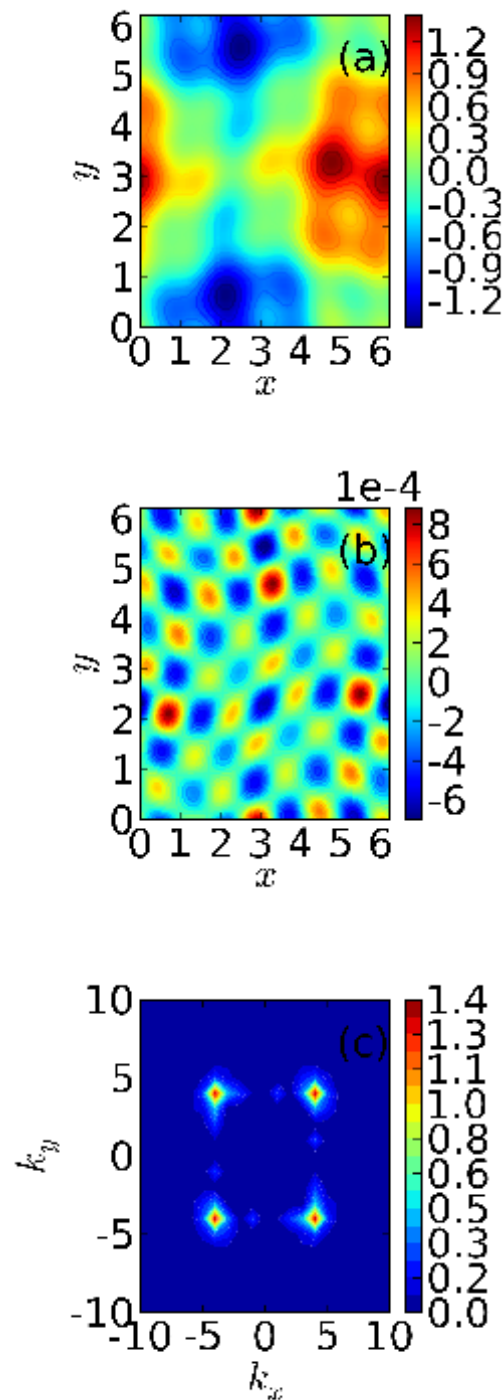
Figure 5.5: Pseudocolour plots for $\Omega = 11.3$ of (a) the streamfunction ψ and (b) the Okubo-Weiss parameter Λ with superimposed contour lines. (c) A filled contour plot the reciprocal-space energy spectrum E_Λ showing clear, dominant peaks, at the forcing wave vectors, and subdominant superlattice peaks at smaller wave vectors.
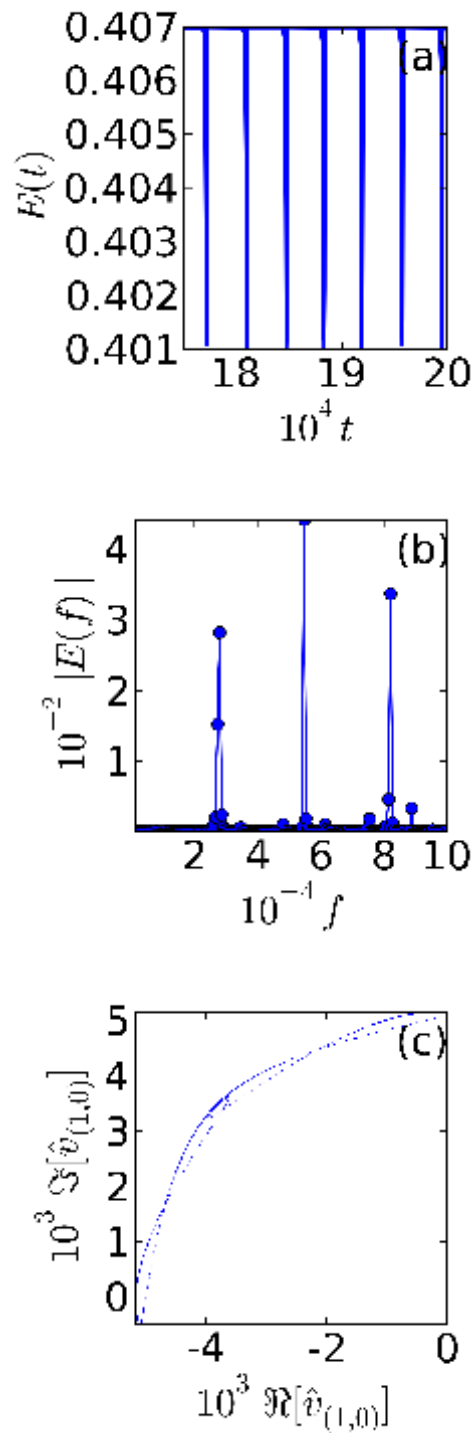
Figure 5.6: Plots for $\Omega = 15.3$ of (a) the time evolution of the energy $E(t)$, (b) $| E(f) |$ versus the frequency f, and (c) the Poincaré-type section in the $(\Re[\hat{\omega}(1,0)], \Im[\hat{\omega}(1,0)])$ plane.
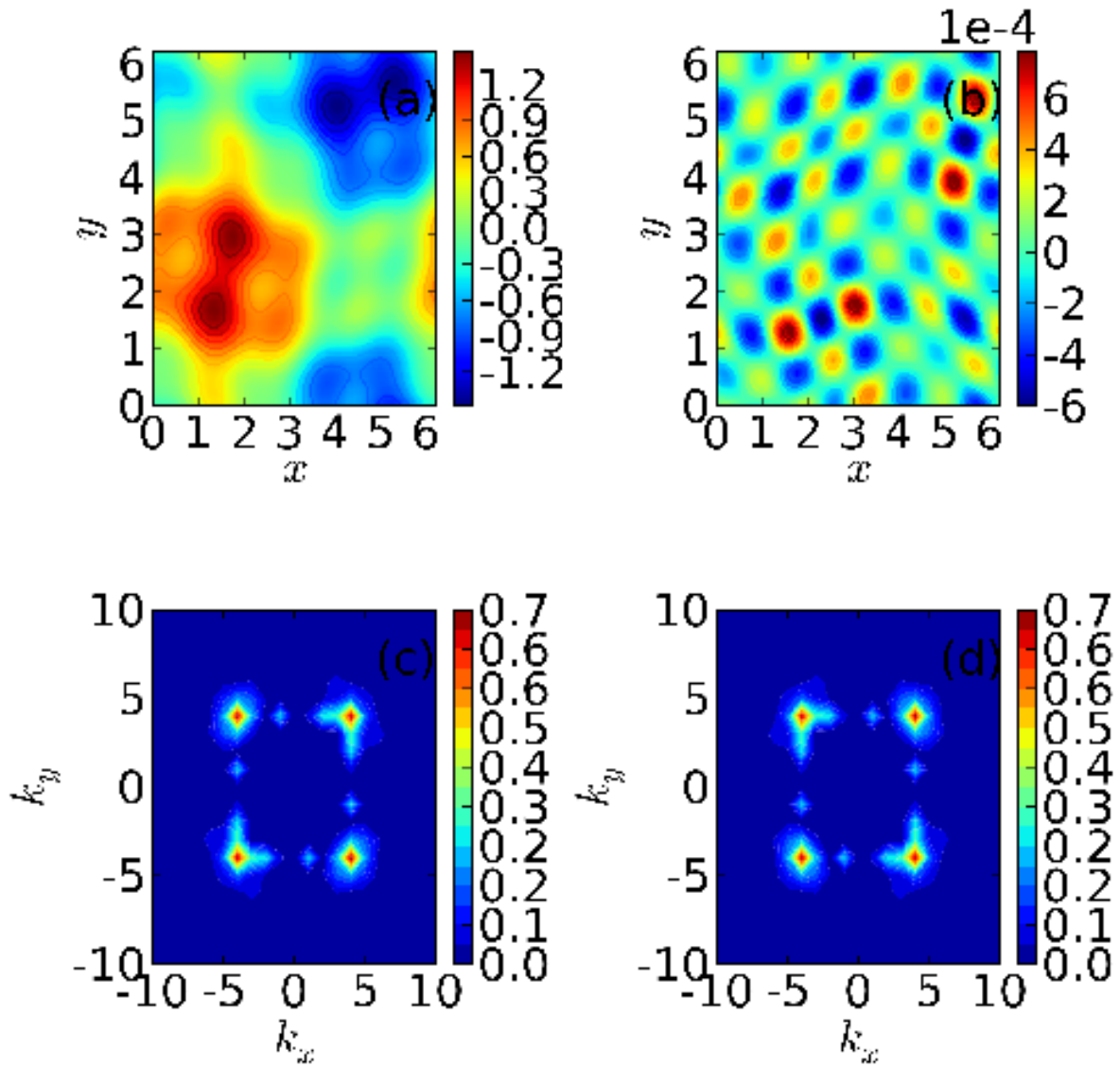
Figure 5.7: Pseudocolour plots for $\Omega = 15.3$ of (a) the streamfunction ψ and (b) the Okubo-Weiss parameter Λ with superimposed contour lines. (c) and (d) Filled contour plots of E_Λ showing the two spectra between which it oscillates in time.

magnitude of these oscillations, which we have used for the error bars in Fig. 5.8(b), decreases as Ω increases. We have checked explicitly that our results here do not change when we increase the resolution of our pseudo-spectral study from $N = 128$ to $N = 256$.

At $\Omega = 17.8$, i.e., run $R4 - 6$, another transition occurs: The time series of energy $E(t)$ and its frequency spectrum $\mid E(f) \mid$ are shown, respectively, in Figs. 5.9(a) and (b). The latter displays peaks superimposed on a noisy background signal; these peaks can be indexed as $f_0, f_1, f_1 - 2f_0, f_0 - 2f_1$, and $3f_0 - 2f_1$, within our numerical accuracy and with $f_0 = 0.001653$ and $f_1 = 0.001707$. Since f_0/f_1 is not a simple rational number, we conclude that Fig. 5.9(b) indicates principally quasiperiodic temporal evolution with a small chaotic admixture, the former associated with the peaks indexed above and the latter with the noisy background signal. We believe the chaotic part of the signal comes from transitions between the elliptical islands in the Poincaré-type section of Fig. 5.9(c). The plot of the inter-spike interval T_i versus the spike index i in Fig. 5.9(d) confirms the complicated temporal evolution of this state.

As we increase Ω further ($R4 - 7$) the temporal evolution of the system becomes ever more chaotic; this is associated with a disordered pattern of vortices in space too. Thus we obtain a state with spatiotemporal chaos and turbulence, which is our analogue of the liquid state. We illustrate this for $\Omega = 50$. We begin with the time series of $E(t)$ and the spectrum $\mid E(f) \mid$ in Figs. 5.10(a) and (b), respectively; the latter clearly shows a broad background that is indicative of temporal chaos. This is further confirmed by the nearly uniform spread of points in the Poincaré-type section [Fig. 5.10(c)] in the $(\Re[\hat{u}_y(1,1)], \Im[\hat{u}_y(1,1)])$ plane. The disordered spatial organisation of this state is illustrated by the pseudocolour plots of ψ and Λ [Figs. 5.11(a)-(b), respectively] and the reciprocal-space spectrum $E_\Lambda(k$ of Fig. 5.11(c) that shows several new modes in addition to the
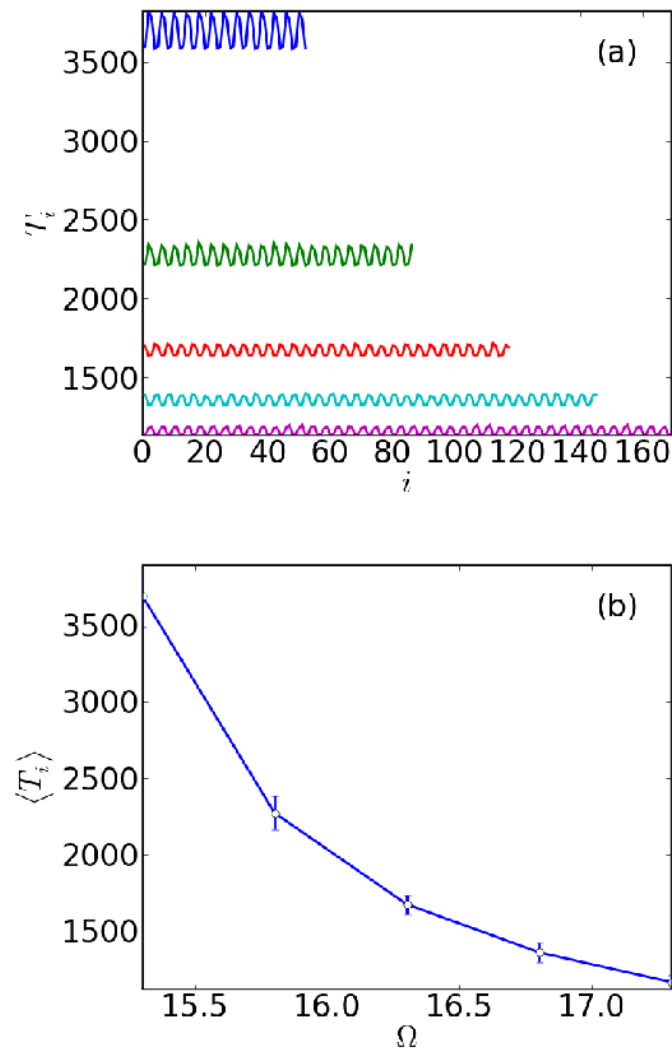
Figure 5.8: Plots of (a) the inter-spike interval T_i versus the spike index i for $\Omega = 15.3$ (blue curve), $\Omega = 15.8$ (green curve), $\Omega = 16.3$ (red curve), $\Omega = 16.8$ (cyan curve), and $\Omega = 17.3$ (purple curve) and (b) the time mean value of T_i versus Ω (see text for error bars).
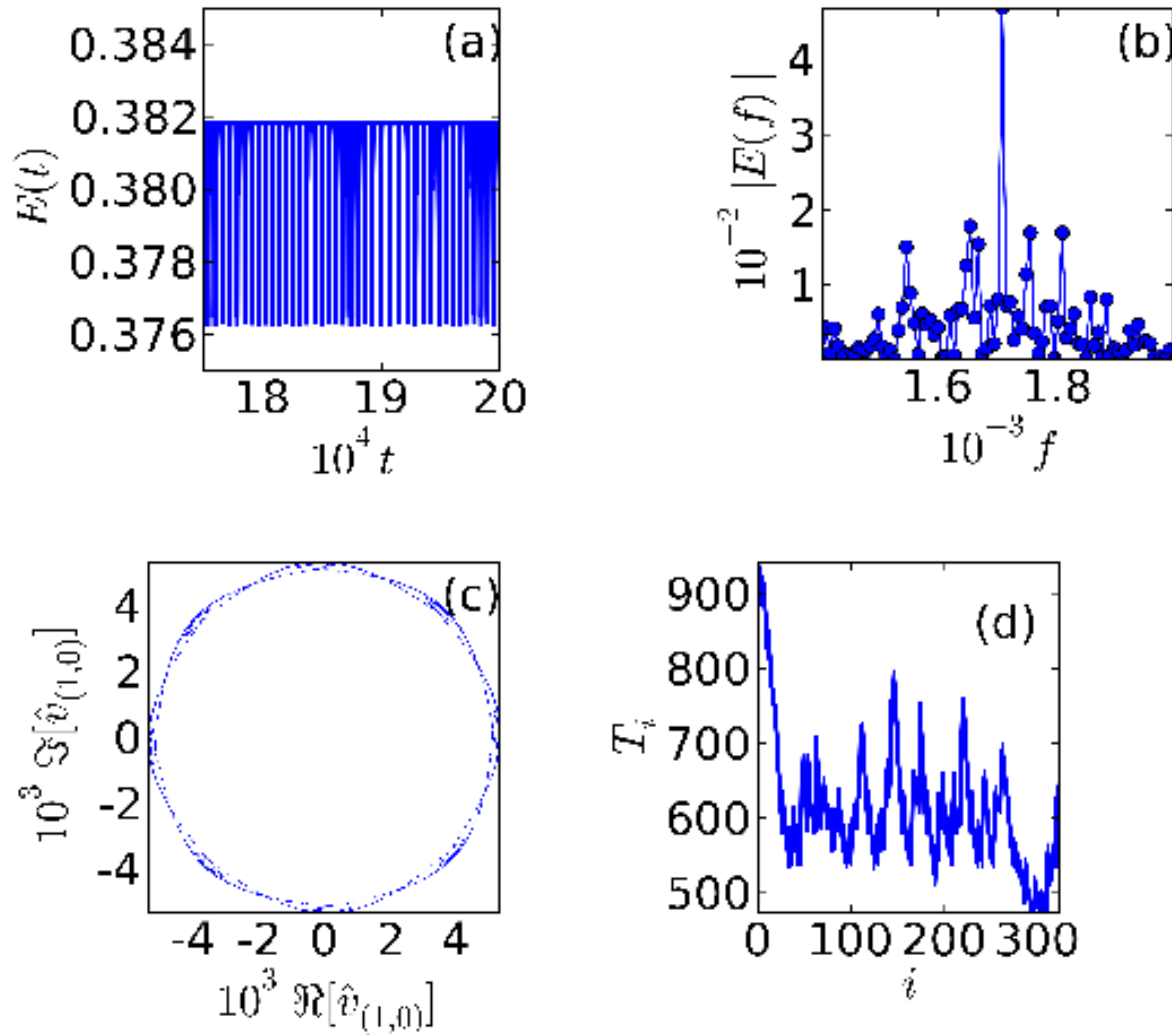
Figure 5.9: Plots for $\Omega = 17.8$ of (a) the time evolution of the energy $E(t)$, (b) the spectrum $E(f)$ versus f, (c) the Poincaré-type section in the plane $(\Re[\hat{v}(1,0)], \Im[\hat{v}(1,0)])$, and (d) the inter-spike interval T_i versus the spike index i.

original peaks, which are still visible since F_ω continues to act on the system.

Thus we see that turbulence-induced melting of our nonequilibrium vortex crystal is far richer than its equilibrium counterpart. For the case $n = 4$ investigated above it proceeds as described by the comments in Table 5.1. Before we present an analysis of the disordered state in terms of the spatial autocorrelation function $G(r)$ and the evolution of the order parameters $\langle \hat{\Lambda}_k \rangle$ with Ω, we give below a short summary of our results for $n = 10$; the route to turbulence is different for this case.

5.4.2   n=10

Our results for $n = 10$ are based on the runs R10 $- 1$ to R10 $- 5$ in Table 5.1.

For $\Omega < \Omega_{s,n}$ the steady vortex crystal is shown by the pseudo-colour plot of Λ in Fig. 5.1(b). As we increase Ω beyond $\Omega_{s,n}$ we find in runs R10 $- 2$, (i.e., the range $\Omega_{s,n} < \Omega < 22.6$) a new steady state in which pseudocolour plots of ψ and Λ show large-scale spatial undulations caused by small deformations of the original vortex crystal [Figs. 5.12 (a) and (b), respectively]; consequently the dominant peaks in the reciprocal-space spectrum E_Λ are slightly distorted.

Around $\Omega = 24$(R10 $- 3$) another transition occurs: the time series of $E(t)$ is periodic [Fig. 5.13(a)] and its spectrum $\mid E(f) \mid$ [Fig. 5.13(b)] shows one dominant peak, i.e., higher harmonics are nearly absent. Thus the Poincaré-type plot in the $(\Re[\hat{u}_y 1, 1], \Im[\hat{u}_y 1, 1])$ plane [Fig. 5.13(c)] displays a simple attractor. The spatial structure of this state is illustrated by the the pseudocolour plots of ψ and Λ shown, respectively, in Figs. 5.14(a) and (b); the associated reciprocal-space spectrum E_Λ is shown in Fig. 5.14(c). Given the temporal behaviour of this state, these structures, in real or reciprocal space, oscillate in time at the frequency given by the temporal evolution of $E(t)$. For
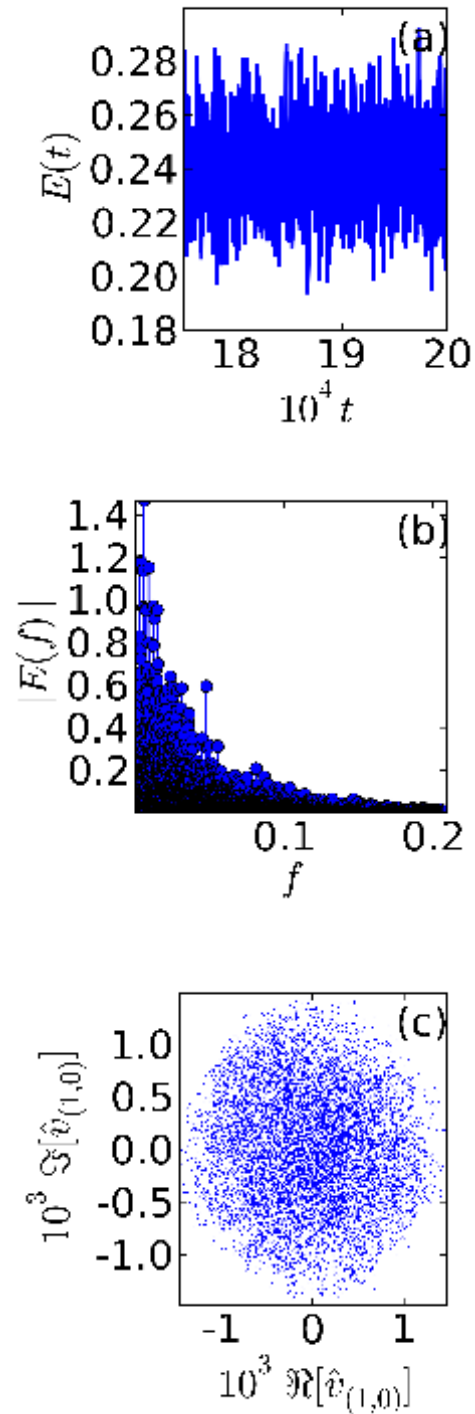
Figure 5.10: Plots for $\Omega = 50$ of (a) the time evolution of the energy $E(t)$, (b) the spectrum $|E(f)|$ versus f, and (c) the Poincaré-type section in the $(\Re[\hat{v}(1,0)], \Im[\hat{v}(1,0)])$ plane.
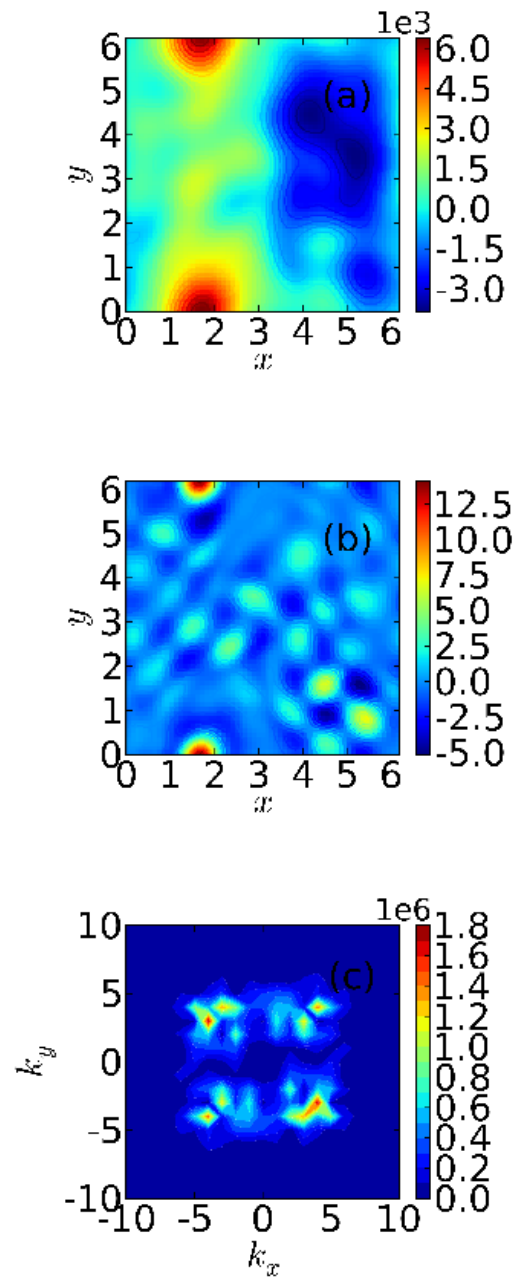
Figure 5.11: Pseudocolour plots for $\Omega = 50$ of (a) the streamfunction ψ and (b) the Okubo-Weiss parameter Λ with superimposed contour lines. (c) A filled contour plot the reciprocal-space energy spectrum E_Λ which shows that a large number of modes are excited.
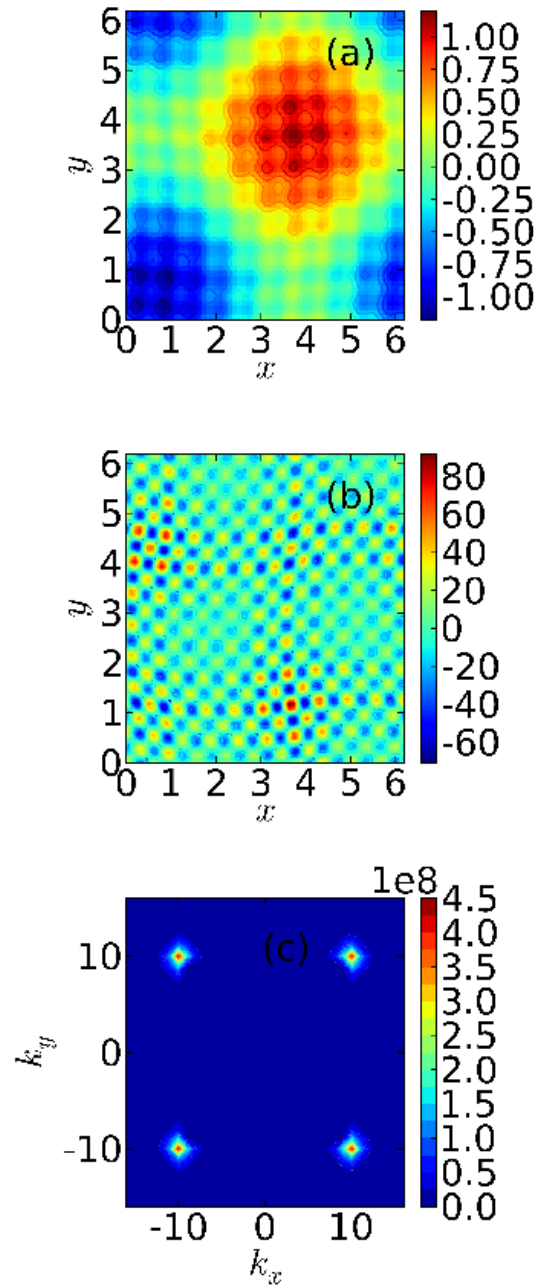
Figure 5.12: Pseudocolour plots for $\Omega = 22.62$ of (a) the streamfunction ψ and (b) the Okubo-Weiss parameter Λ with superimposed contour lines. (c) A filled contour plot the reciprocal-space energy spectrum E_Λ showing clear, but slightly distorted, dominant peaks at the forcing wave vectors.

$\Omega = 24$ the large spatial structures in ψ oscillate around their mean positions; but, for $25 \leq \Omega \leq 28$, we find a travelling-wave type pattern, which reenters our simulation by virtue of the periodic boundary conditions that we use in our pseudo-spectral method. If we compare the frequency spectra $| E(f) |$ for the cases $\Omega = 24$ and $\Omega = 28$, we find higher harmonics in the latter but they are all multiples of one fundamental frequency.

In Fig. 5.15(a) we show plots of T_i versus i (cf. Fig. 5.8(a) for $n = 4$) for various values of Ω. From these we obtain the plot of the mean value $\langle T_i \rangle$ versus Ω shown in Fig. 5.15(b). This first decreases, as we increase Ω, and then increases mildly at $\Omega = 28$.

For $\Omega \geq 29$ the time-series of $E(t)$ appears chaotic and the associated frequency spectrum $| E(f) |$ displays a broad background, we as show in the illustrative Figs. 5.16 (a) and (b) for $\Omega = 225$. The associated Poincaré-type section in Fig. 5.16(c) confirms that the temporal behaviour is chaotic. The spatial patterns are also disordered as we show via the pseudocolour plots of ψ and Λ in Figs. 5.17(a) and (b), respectively. The corresponding reciprocal-space spectrum E_Λ shows that a large number of modes are excited. Thus we have both spatial disorder and temporal chaos; as in the case $n = 4$, the analogue of the liquid state is a turbulent one with spatiotemporal chaos. However, given the resolution in Ω that we have been able to obtain in our calculations, the route to this state of spatiotemporal chaos is different for $n = 10$ and $n = 4$ as can be seen from the comments in Table 5.1.

5.5 Order parameters and autocorrelation functions

We now return to ideas borrowed from the density-functional theory [1, 2, 3, 4] of freezing by examining the behaviour of the order parameters $\langle \hat{\Lambda}_\mathbf{k} \rangle$ as functions of Ω. Recall that, in equilibrium melt-
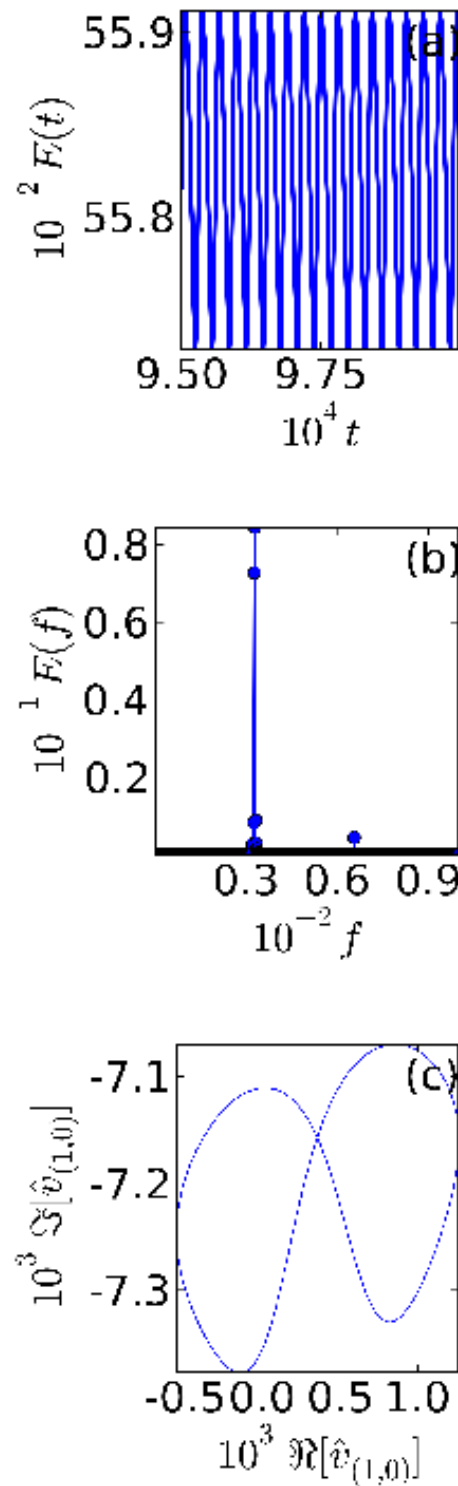
Figure 5.13: The plots for $\Omega = 24$ of (a) the time evolution of energy $E(t)$ versus t, (b) the power spectrum $E(f)$ versus f, and (c) the Poincaré section $\Im[\hat{v}(1,0)]$ versus $\Re[\hat{v}(1,0)]$.
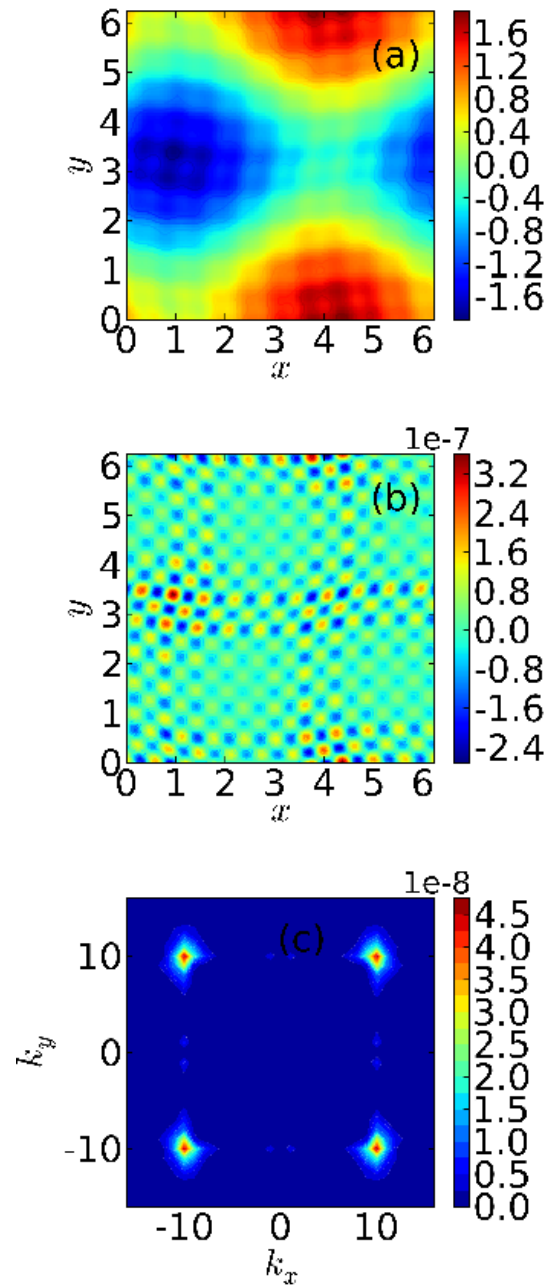
Figure 5.14: Pseudocolour plots for $\Omega = 24$ of (a) the streamfunction ψ and (b) the Okubo-Weiss parameter Λ with superimposed contour lines. (c) A filled contour plot the reciprocal-space energy spectrum E_Λ showing clear, dominant peaks at the forcing wave vectors.
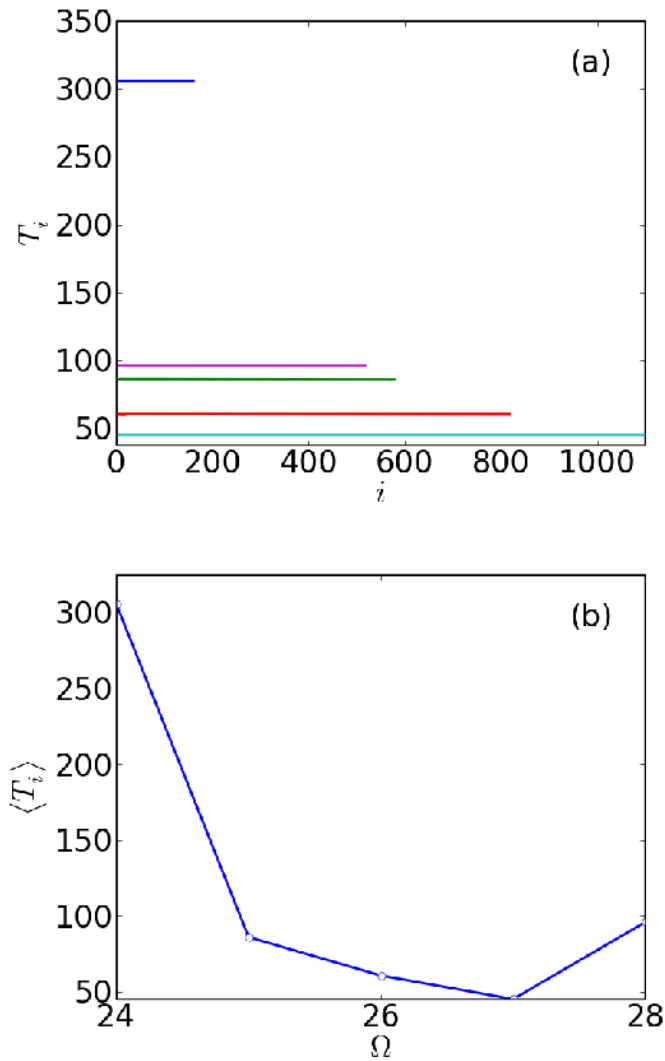
Figure 5.15: Plots of (a) the inter-spike interval T_i versus the spike index i for $\Omega = 24$ (blue curve), $\Omega = 25$ (purple curve), $\Omega = 26$ (green curve), $\Omega = 27$ (red curve), and $\Omega = 28$ (cyan curve) and (b) the time mean value of T_i versus Ω (see text for error bars).
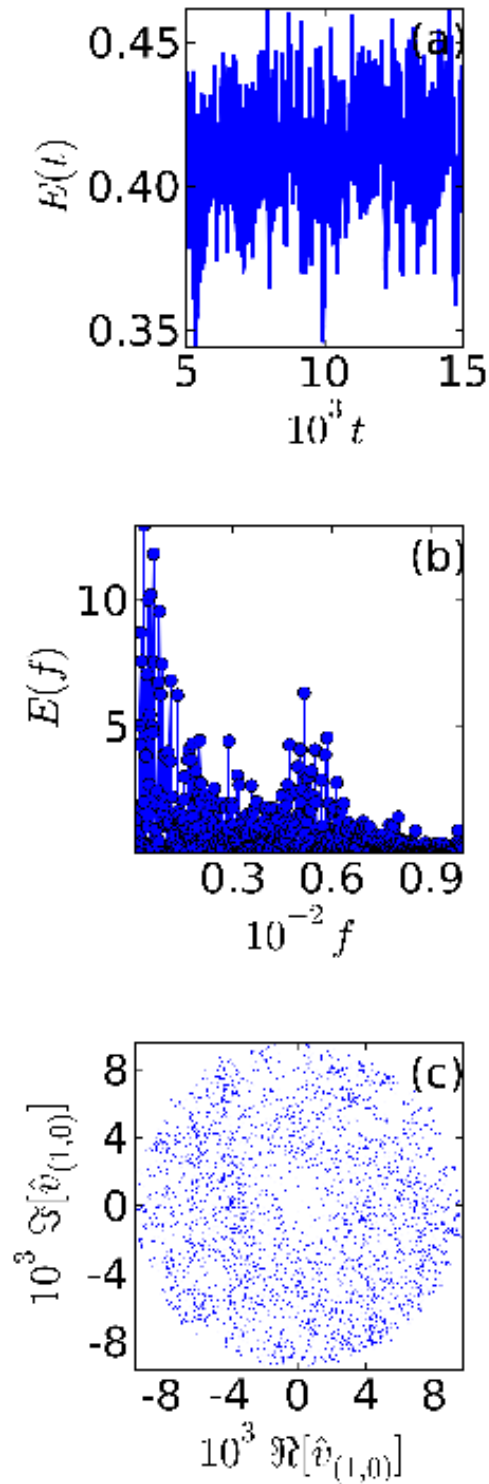
Figure 5.16: Plots for $\Omega = 225$ of (a) the time evolution of $E(t)$, (b) the spectrum $|E(f)|$ versus f, and (c) the Poincaré-type section in the $(\Re[\hat{v}(1,0)], \Im[\hat{v}(1,0)])$ plane.
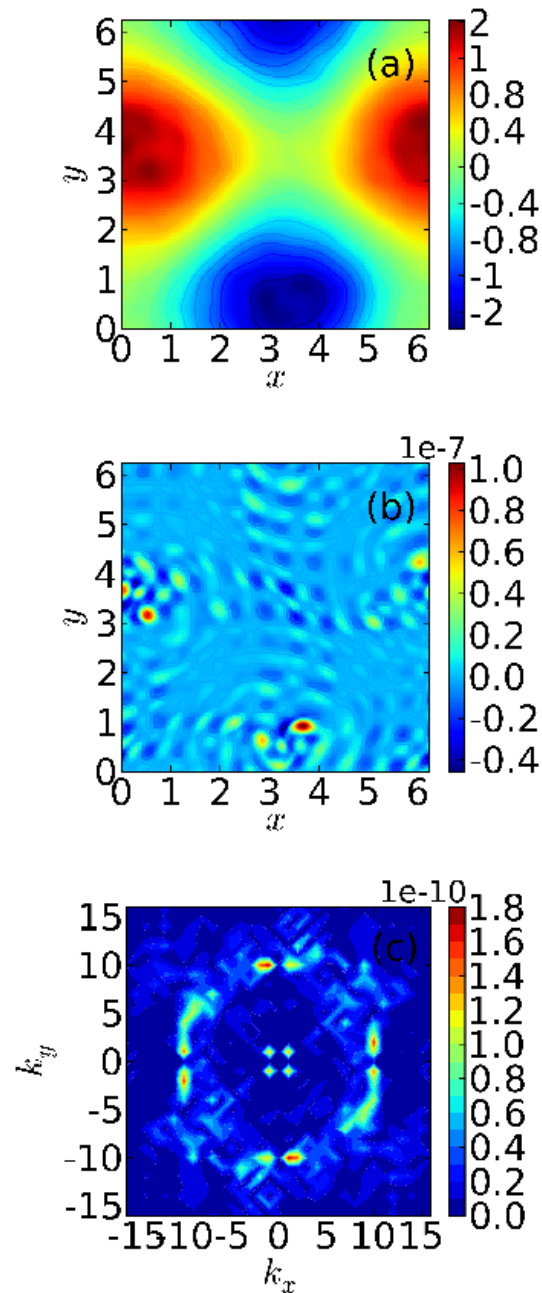
Figure 5.17: Pseudocolour plots for $\Omega = 225$ of (a) the streamfunction ψ and (b) the Okubo-Weiss parameter Λ with superimposed contour lines. (c) A filled contour plot the reciprocal-space energy spectrum E_Λ showing that a large number of modes are excited.

ing, ρ_G jumps discontinuously from a nonzero value in the crystal to zero in the liquid at the first-order melting transition. As we have noted above, the turbulence-induced melting of our vortex crystal is far more complicated; it proceeds via a sequence of transitions. Thus $\langle \hat{\Lambda}_k \rangle$ changes with Ω as shown, respectively, for (a) $n = 4$ and $k = (4, 4)$ and (b) $n = 10$ and $k = (10, 10)$ in Figs. 5.18 (a) and (b); if we sum $\langle \hat{\Lambda}_k \rangle$ over the four forcing wave vectors, we obtain a real number that is $\Re\langle \hat{\Lambda}_k \rangle$; we show this in our figures.

The short-range order in the disordered, turbulent phase can be characterised by the auto-correlation function $G(r)$. Representative plots are shown, respectively, for $n = 4$ and $n = 10$ in Figs. 5.19 (a)-(d). For the crystalline case we evaluate $G(r)$ along the line connecting $r = (\pi/2, \pi/2)$ and $r = (\pi/2, \pi)$; this shows a periodic array of peaks [Figs. 5.19 (a) and (b) for $n = 4$ and $n = 10$, respectively]; the widths of these peaks are related to the widths of vortical or strain-dominated regions. In the turbulent phase we present data obtained by a circular average of G [Figs. 5.19 (c) and (d) for $n = 4$ and $n = 10$, respectively]; here the peaks decay over a length scale that indicates the degree of short-range order. This is similar to the behaviour of spatial correlation functions in a disordered liquid.

5.6 Conclusions

We have carried out a detailed numerical study of turbulence-induced melting of a nonequilibrium vortex crystal in a forced, thin fluid film. We use ideas from the density-functional theory of freezing [1, 2, 3, 4], nonlinear dynamics, and turbulence to characterise this. Ideas from liquid-state theory have been used by some recent experiments to analyse the short-range order in the turbulent phase; nonlinear-dynamics methods, such as Poincaré-type maps, have been used in the numerical studies of Ref. [10]; experimental studies have used
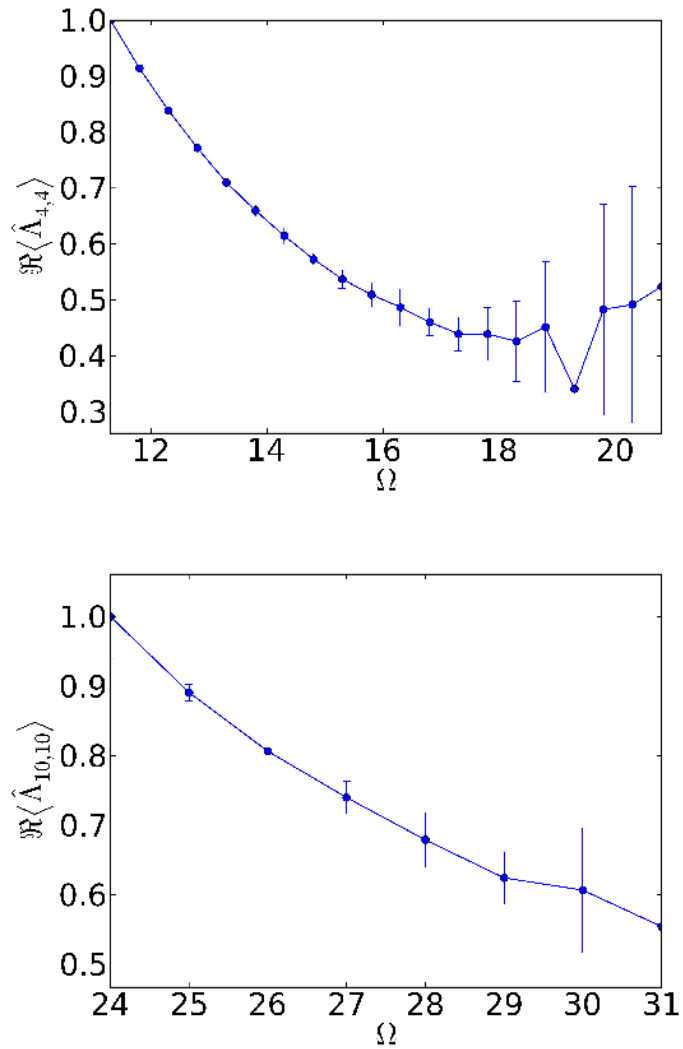
Figure 5.18: Plot showing a decrease in $\langle \hat{\Lambda}_{\mathbf{k}} \rangle$ with increasing Ω for (a) $n = 4$ and $\mathbf{k} = (4, 4)$ and (b) $n = 10$ and $\mathbf{k} = (10, 10)$.
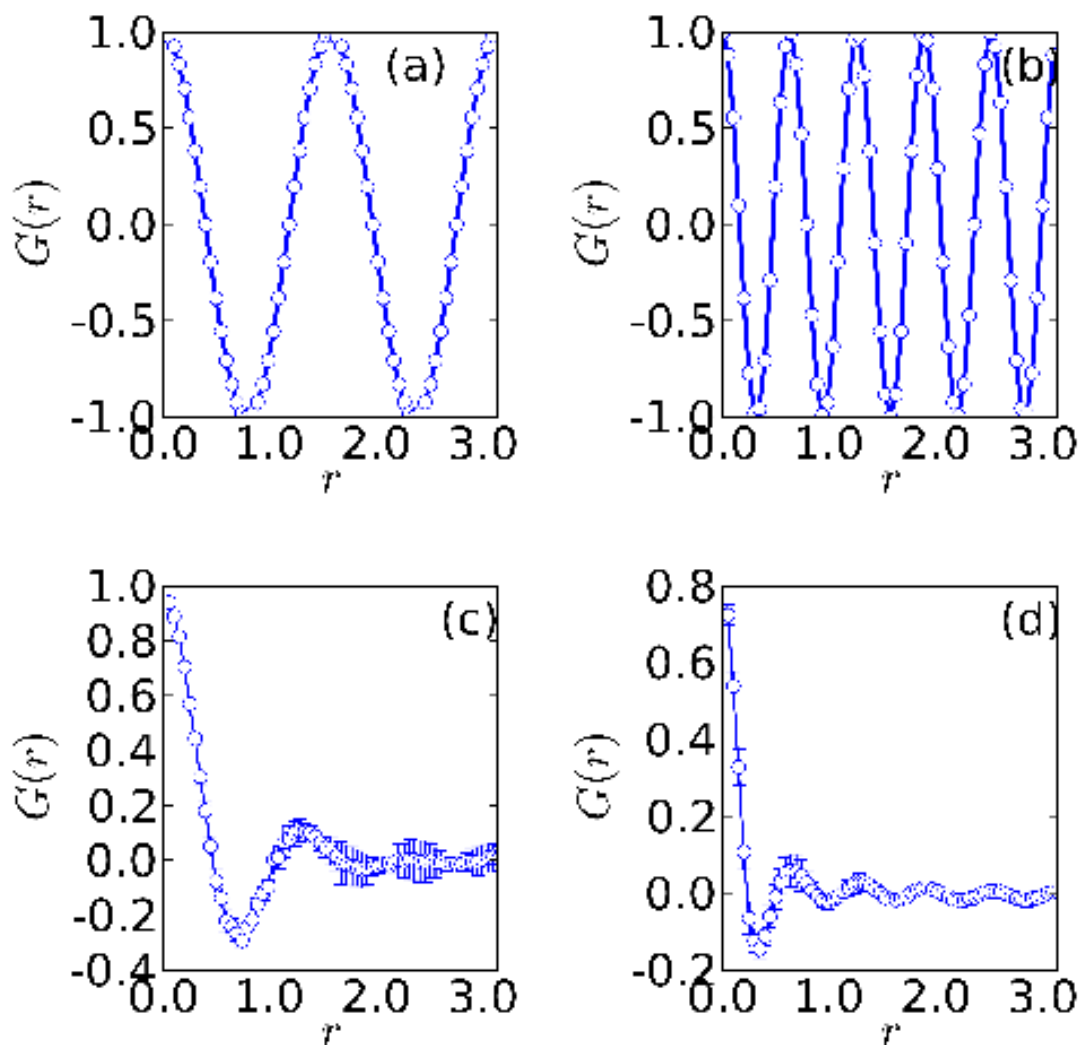
Figure 5.19: Plots of $G(r)$ in (i) crystalline state: (a) $n = 4, \Omega < \Omega_{s,n}$ and (b) $n = 10, \Omega < \Omega_{s,n}$ and (ii) melt state: (c) $n = 4$, $\Omega = 20.81$ and (d) $n = 10, \Omega = 225$.

the curvature of Lagrangian trajectories to identify extrema in vortical and strain-dominated regimes. To the best of our knowledge, there is no study that brings together the methods we do to analyse turbulence-induced melting.

The advantages of our approach are as follows: (a) it helps us to identify the order parameters for turbulence-induced melting and thus contrast it with conventional melting; (b) the sequence of transitions can be characterised completely in terms of the Eulerian fields ψ and Λ and the total energy $E(t)$ and suitable Fourier transforms of these; (c) the short-range order in the turbulent phase can be studied conveniently in terms of G.

Equilibrium phase transitions occur strictly only in the thermodynamic limit that is, roughly speaking, the limit of infinite size. It is interesting to ask how we might take the thermodynamic limit for vortex crystals we have studied here. There seem to be at least two ways to do this: (a) in the first the system size should be taken to infinite in such a way that the areal density of the vortical and strain-dominated regimes remains the same in the ordered, crystalline phase; (b) we can increase the parameter n in the forcing F_ω so that more and more unit cells occur in the simulation domain (cf., e.g., Figs. 5.1(a) and (b) for $n = 4$ and $n = 10$, respectively). Such issues have not been addressed in detail by any study, partly because, for large system sizes, it is not possible to obtain the long time series that are required to characterise the temporal evolution of the system (especially in the states we have referred to as spatiotemporal crystals). In particular, it is quite challenging to investigate the system-size dependence of the transitions summarised for $n = 4$ and $n = 10$ in Table 5.1.

As we have shown above, the array of transitions that comprise turbulence-induced melting of a vortex crystal is far richer than conventional equilibrium melting. There is another important way in which the former differs from the latter: To maintain the steady

states, statistical or otherwise, of our system, we always have a force F_ω; thus, in the language of phase transitions, we always have a symmetry breaking field, both in the ordered and disordered phases. Strictly speaking, therefore, there is no symmetry difference between the "disordered" turbulent state and the vortex crystal, as can be seen directly from the remnants of the dominant peaks in the reciprocal-space spectra $E_\Lambda(\mathbf{k})$ in Figs. 5.11 and 5.17(c) for $n = 4$ and $n = 10$, respectively. One consequence of this is that the order parameters $\langle \hat{\Lambda}_{\mathbf{k}} \rangle$, with $\mathbf{k}$ equal to the forcing wave vectors, do not vanish identically in the disordered, turbulent phase; however, they do assume very small values. Moreover, in the case of turbulence-induced melting the crystal undergoes a transition from an ordered state to an undulating crystal to a fully turbulent state. Thus there is noise and hence no fluctuations in the crystalline state; i.e., it is equivalent to a crystal at zero temperature. This has no analogue in the equilibrium melting of a crystal.

In equilibrium, different ensembles are equivalent; we can, e.g., use either the canonical or grand-canonical ensemble to study the statistical mechanics of a system and, in particular, the phase transitions in it. However, this equivalence cannot be taken for granted when we consider nonequilibrium statistical steady states (see, e.g., Ref. [21]). We have seen an example of this in Chapter 4 and in Ref. [14] where certain PDFs show slightly different behaviours depending on whether we keep the Grashof number fixed or whether we keep the Reynolds number fixed. Turbulence-induced melting offers another example of the inequivalence of dynamical ensembles: the precise sequence of transitions that we encounter in going from the vortex crystal to the turbulent state depends on whether we do so by changing the Grashof number (i.e., the amplitude of the force) as in Ref. [10] or whether we do so by changing Ω as we have done here. We have checked explicitly that we can reproduce the sequence

of transitions in Ref. [10] if we tune the Grashof number rather than Ω.

Investigations of similar transitions, such as in the route Kolmogorov flow [17] can also benefit by using the combination of methods we have used above. Detailed studies of the effects of confinement air-drag induced Ekman friction on turbulence-induced melting, initiated, e.g., in Refs. [11, 22], can also benefit from the use of our methods but that lies beyond the scope of this Chapter. We hope, too, that our study will encourage experimental groups to analyse turbulence-induced melting by using the set of techniques and ideas that we have described above.

Appendix D

D.1 Numerical scheme

In this section we describe the numerical scheme that is used for the time evolution of Eq. (5.5). We use periodic boundary conditions and therefore use a pseudo-spectral method. We start with an initial Fourier space $\hat{\omega}$ field and evaluate the stream function, and thus the two-component velocity field, from it :

$$\hat{\psi} = -\frac{1}{k^2}\hat{\omega}; \tag{D1}$$

$$\hat{u}_x = \imath k_y \hat{\psi}; \tag{D2}$$

$$\hat{u}_y = -\imath k_x \hat{\psi}. \tag{D3}$$

$$\tag{D4}$$

Fast Fourier Transform routines are used to go back and forth between real and Fourier space. If we define the nonlinear term

$$\hat{\mathcal{N}} = \imath(k_x\widehat{u_x\omega} + k_y\widehat{u_y\omega}) \tag{D5}$$

the evolution equation becomes:

$$\partial_t\hat{\omega} = \hat{\mathcal{N}} - \nu k^2\hat{\omega}. \tag{D6}$$

This equation is then solved numerically by using the second-order Runge–Kutta scheme:

$$\hat{\omega}_1 = e^{-\nu k^2 \delta t/2}\left\{\hat{\omega}^n + \frac{\delta t}{2}\hat{\mathcal{N}}[\hat{\omega}^n]\right\};$$

(D7)

$$\hat{\omega}^{n+1} = e^{-\nu k^2 \delta t}\hat{\omega}_n + \delta t e^{-\nu k^2 \delta t/2}\hat{\mathcal{N}}[\hat{\omega}_1].$$

(D8)

Bibliography

[1] T.V. Ramakrishnan and M. Yussouff, *Phys. Rev. B* **19**, 2775 (1979).

[2] P.M. Chaikin and T.C. Lubensky, *Principles of condensed matter physics* (Cambridge, Cambridge University Press, UK, 1998).

[3] D.W. Oxtoby, in *Liquid, Freezing, and the Glass Transition*, edited by J.P. Hansen, D. Levesque, and J. Zinn-Justin (North-Holland, Elsevier, New York, 1990).

[4] Y. Singh, *Phys. Rep.* **207**, 351 (1991).

[5] M. Das, S. Ramaswamy, and G. Ananthakrishna, *Europhys. Lett.* **20**, 636 (2002).

[6] N.T. Ouellette and J. Gollub, *Phys. Rev. Lett.* **99**, 194502 (2007).

[7] N.T. Ouellette and J. Gollub, *Phys. Fluids* **20**, 064104 (2008).

[8] K. Gotoh and M. Yamada, *J. Phys. Soc. Japan* **53**, 3395 (1984).

[9] K. Gotoh and M. Yamada, *Fluid Dynam. Res.* **1**, 165 (1986).

[10] R. Braun, F. Feudel, and N. Seehafer, *Phys. Rev. E* **55**, 6979 (1997).

[11] D. Molenaar, H.J.H. Clercx, G.J.F. van Heijst, and Z. Yin, *Phys. Rev. E* **75**, 036309 (2007).

[12] M. Brons, A. Skajaa, and O. Skovgaard, *arXiv:0806.4757* (2008).

[13] M. Rivera, X.L. Wu, and C. Yeung, *Phys. Rev. Lett.* **87**, 044501 (2001).

[14] P. Perlekar and R. Pandit, *New J. Phys.* **11**, 073003 (2009).

[15] J.M. Chomaz and B. Cathalau, *J. Fluid Mech.* **442**, 387 (2001).

[16] J.M. Chomaz, *J. Fluid Mech.* **442**, 387 (2001).

[17] N. Platt, L. Sirovich, and N. Fitzmaurice, *Phys. Fluids A* **3**, 681 (1991).

[18] A. Thess, *Phys. Fluids A* **4**, 1396 (1992).

[19] J. Weiss, *Physica D* **48**, 273 (1992).

[20] A. Provenzale and A. Babiano, *J. Fluid Mech.* **257**, 533 (1993).

[21] M. Acharyya, A. Basu, R. Pandit, and S. Ramaswamy, *Phys. Rev. E* **61**, 1139 (2000).

[22] A. Thess, *Phys. Fluids* **4**, 1385 (1992).

Chapter 6

Lifetime of topological structures in two-dimensional turbulence

For a nonequilibrium fluctuating field persistence is the probability $P_0(\tau)$ that the sign of the field at a point in space does not change upto time τ [1]. This probability can be determined analytically for a number of models, e.g., the simple diffusion equation with Gaussian random initial conditions [1, 2]. Such questions have also been studied for several other models including reaction-diffusion systems, fluctuating interfaces, granular media, and population dynamics. In all these cases the persistence probability shows a power-law decay for large τ, i.e., $P_\theta(\tau) \sim \tau^\theta$, where θ is negative; it is often called the persistence exponent [3, 4].

Any turbulent flow in two dimensions displays vortical regions and strain-dominated or extensional regions (see Chapters 4 and 5). In this Chapter we examine the *persistence* of such regions in time. We show, in particular, that the Okubo-Weiss parameter Λ (whose sign determines whether a region is vortical or extensional), which we had introduced in Chapter 4, provides us with a natural way of studying such persistence. We distinguish two types of persistence: (A) In the Eulerian framework we consider a point (x, y) and determine how long the flow at this point remains vortical (extensional) if the flow at this point became vortical (extensional) at some earlier time; (B) in the

Lagrangian framework we consider how long a Lagrangian particle resides in a vortical (extensional) region if this particle entered that vortical (extensional) region at an earlier time. Our study shows that, in the Eulerian framework, the persistence PDFs show an exponential tail. In the Lagrangian framework the persistence PDF for the residence time of the particle in vortical regions shows a power-law whereas the persistence PDF for the residence time of the particle in straining regions shows an exponential tail. Our study of the autocorrelation functions of Λ and $\nabla \mathbf{u}$ shows that the correlation time in the Lagrangian frame is shorter than in the Eulerian frame.

The rest of the Chapter is organised as follows: Section 6.1 contains an Introduction; Section 6.2 describes the equations and the model; results and conclusions are presented in Section 6.3 and Section 6.4, respectively.

6.1 Introduction

Topological structures in a two-dimensional flow field are classified by the eigenvalues of the velocity-gradient tensor A [5]. If, at a point in space, the eigenvalues of A are complex (real), then in the plane formed by the eigenvectors of A the flow is a center (a saddle) and the topological structure is vortical (extensional). Whether the eigenvalues of A are real or complex can be determined by $\Lambda \equiv \det(A)$. If the eigenvalues of A are complex then $\Lambda > 0$ and the flow is vortical, whereas if the eigenvalues are real, then $\Lambda < 0$ and the flow is extensional [see Fig. 4.6(a), Chap. 4]. Furthermore, the PDF of Λ for two-dimensional turbulent flows is asymmetrical about $\Lambda = 0$, i.e., vortical regions are more likely to occur than strain-dominated regions (see Fig. 4.9, Chap. 4).

We investigate the temporal evolution of Λ in both Eulerian and Lagrangian frames: (i) To collect data for Eulerian statistics, we mon-

itor the evolution of Λ at N_{p} (randomly chosen) points that are fixed in the simulation domain [1]; (ii) to collect data for Lagrangian statistics, we seed the flow with N_{p} (see Table 6.1) neutrally buoyant Lagrangian particles and monitor the evolution of Λ along their trajectories. A typical Lagrangian particle track superimposed on a representative pseudocolour plot of the streamfunction is shown in Fig. 6.1. In Fig. 6.2 we plot a typical time-series of Λ at an Eulerian point and along a Lagrangian trajectory.

We now outline the method we have used to determine different persistence PDFs in two-dimensional ($2D$) turbulence. We first consider persistence in the Eulerian framework by monitoring the sign of Λ at a given point (x, y). We find the probability $P_E^+(\tau)$ [resp., $P_E^-(\tau)$] that Λ remains positive (resp., negative) upto a time τ if it had entered a region with $\Lambda > 0$ (resp., $\Lambda < 0$) at an earlier time. We show that the PDFs $P_E^+(\tau)$ and $P_E^-(\tau)$ show exponential tails (see Figs. 6.3,6.4,6.5, and 6.6).

Next we consider persistence in the Lagrangian framework by monitoring the sign of Λ along a Lagrangian particle trajectory. We find the probability $P_L^+(\tau)$ (resp., $P_L^-(\tau)$) that Λ remains positive (resp., negative) upto a time τ if it had entered a region with $\Lambda > 0$ (resp., $\Lambda < 0$) at an earlier time. We show that the PDF $P_L^+(\tau)$ of the persistence times of Lagrangian particles in vortical regions shows a power-law tail with an exponent $\theta = -3.1 \pm 0.1$ (see Fig. 6.10). By contrast, the PDF of the persistence time of a Lagrangian particle in strain-dominated regions shows an exponential decay. Furthermore, we find that, on rescaling the PDF $P_L^-(\tau)$ with τ_{rms} plots for different runs collapse onto each other (within our errorbars).

In an earlier experiment [6] the waiting time of a particle in a vortex trap in a two-dimensional soap-film found a persistence PDF of the form $\tau^{-5/3}$. The numerical simulations of Ref. [7] have studied the

---

[1]Although we have the full Eulerian field at every time-step storing it is computationally very expensive.
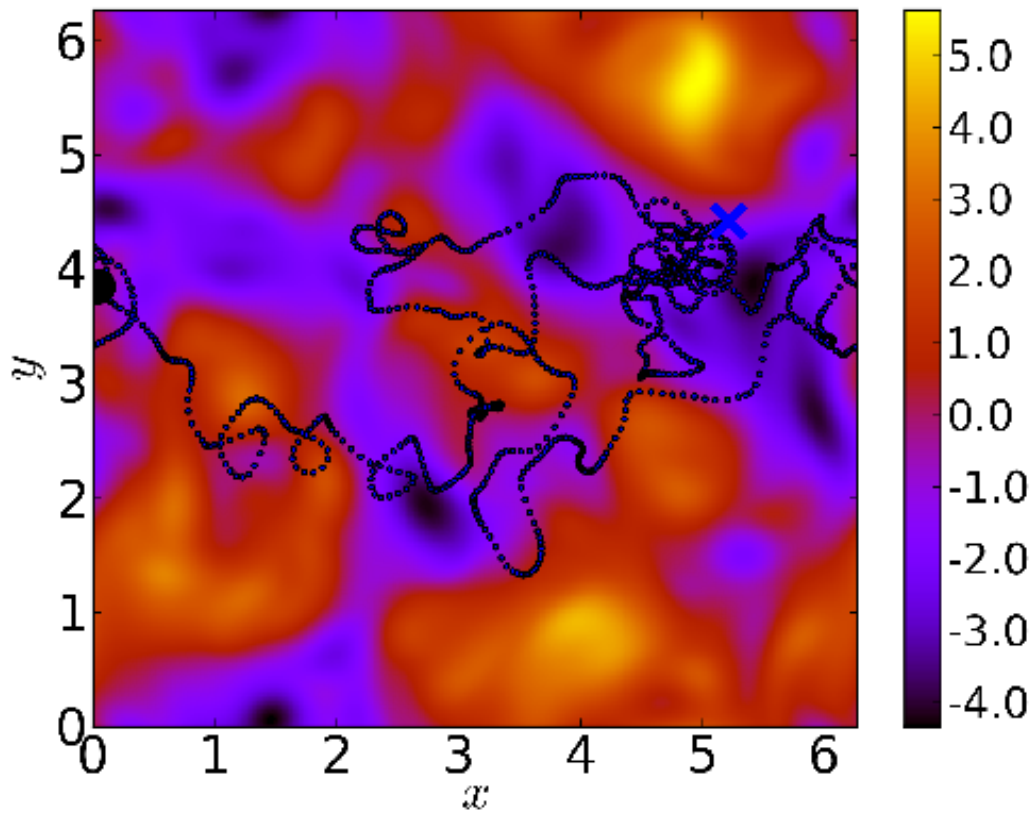
Figure 6.1: Representative pseudocolour plot of the streamfunction field and a representative particle track from our run R2. The symbol o indicates the beginning of the trajectory and the × sign marks its end.
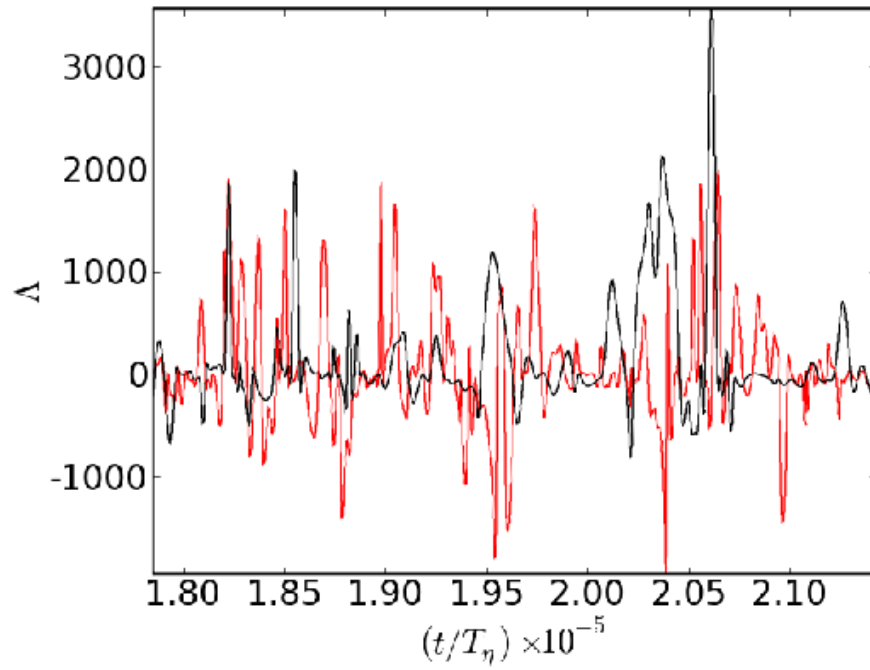
Figure 6.2: Plot of the typical time-series of Λ at an Eulerian point and along a Lagrangian particle for our run R2.

waiting time of particles in a region of a vortex trap in laminar and chaotic Kolmogorov flows. This study predicted a $\tau^{-2.48}$ behaviour for the persistence exponent in the turbulent regime. Both these studies require an adhoc measure to estimate the size of a trap. In another set of numerical studies [8, 9] the persistent streamline topology was studied in two-dimensional turbulence in the inverse-cascade regime. This study predicted a t^3 law for particle pair-dispersion.

As we have mentioned above we show that, because the Okubo-Weiss parameter Λ presents a natural way to determine whether a particle is in a vortical or strain dominated, region it allows us to study persistence times in both Lagrangian and Eulerian framework. We also study the autocorrelation of Λ, and the velocity derivatives $\partial_x u_x$, $\partial_x u_y$, and $\partial_y u_x$ in both Eulerian and Lagrangian frameworks. Our study reveals that the characteristic time scale of the Lagrangian autocorrelation function is shorter than the Eulerian one and that both of them are comparable to the Kolmogorov time scale. Our study has been designed with soap-film experiments in mind [10, 11] (see also Chapter-4), so we also take into account the air-drag induced Ekman friction α and drive the fluid by using a Kolmogorov forcing.

6.2 Equations

We perform direct numerical simulations (DNS) of the incompressible Navier-Stokes equation

$$\partial_t \omega - J(\psi, \omega) = \nu \nabla^2 \omega + f_\omega - \alpha \omega \qquad (6.1)$$

with periodic boundary conditions in two dimensions by using a pseudospectral method (see Appendix D.1 in Chapter 5). Here ψ is the streamfunction, ω the vorticity, $J(\psi, \omega) \equiv (\partial_x \psi)(\partial_y \omega) - (\partial_x \omega)(\partial_y \psi)$ is the Jacobean operator and ν is the kinematic viscosity and α the coefficient of Ekman friction. The two spatial coordinates are x and y.

The velocity $\mathbf{u}$ is uniquely determined by the stream-function ψ as $\mathbf{u} \equiv (-\partial_y \psi, \partial_x \psi)$ and $\omega = \nabla^2 \psi$. f_ω is an external forcing which acts on intermediate Fourier modes with $\mid \mathbf{k} \mid = k_{\mathrm{inj}}$. We implement deterministic forcing with $f_\omega = -F_0 k_{\mathrm{inj}} \cos(k_{\mathrm{inj}} x)$. The injected energy displays an inverse cascade to small k. Ekman friction removes energy from all Fourier modes; in particular, it removes energy from small Fourier modes in such a way that the system reaches a nonequilibrium statistical steady state.

To calculate the Lagrangian quantities we track N_{p} particles. The evolution equation for the Lagrangian particles is:

$$\frac{d\mathbf{x}_L(t)}{dt} = \mathbf{u}(\mathbf{x}_L, t). \tag{6.2}$$

Here $\mathbf{x}_L(t)$ denotes the position of the Lagrangian particle at time t; $\mathbf{u}(\mathbf{x_L}, t)$, the velocity at the Lagrangian particle position, is evaluated from the Eulerian velocity field $\mathbf{u}(\mathbf{x}, t)$ by using a bilinear-interpolation scheme [12]. The time evolution of the particles is done along with Eq. (6.1) by using a second-order Runge-Kutta method [12]. Initially all the particles are seeded randomly in the flow. To calculate Λ at the Lagrangian particle position we use the method described in Appendix E.1. A list of parameters used in our simulations, including the values of k_{inj}, F_0 and α, is given in Table (6.1).

In all our simulations we wait for a time T_{tran} [Table (6.2)] to allow transients to die out and to allow our system to reach a statistically steady state.

6.3 Results

We now present the results that we have obtained from our DNS. We monitor the time-series of Λ in both the Eulerian and Lagrangian framework and calculate the respective persistence PDFs. We also study the autocorrelation functions of Λ and A.

Run	N	N_{p}	ν	α	F_0	k_{inj}	l_d	λ	Re_λ
R1	512	1000	0.016	0.1	45	10	0.023	0.17	59.2
R2	512	1000	0.016	0.45	45	10	0.021	0.11	26.8
R3	1024	1000	10^{-5}	0.01	0.005	10	0.0043	0.125	827.3
R4	1024	1000	10^{-5}	0.01	0.005	4	0.0054	0.198	1318.8

Table 6.1: Parameters for our runs R1-4: N is the number of grid points along each direction, N_{p} the number of Lagrangian particles and Eulerian positions (at which we monitor Λ), ν the viscosity, α the Ekman friction, F_0 the forcing amplitude, k_{inj} the forcing wavenumber, $l_d \equiv (\nu^3/\varepsilon)^{1/4}$ the dissipation scale, $T_\eta \equiv \sqrt{\nu/\varepsilon}$ the Kolmogorov time scale, $\lambda \equiv \sqrt{\nu E/\varepsilon}$ the Taylor microscale, $Re_\lambda \equiv u_{\mathrm{rms}}\lambda/\nu$ the Taylor microscale Reynolds number.

Run	T_{eddy}	T_η	T_{E}^-	T_{L}^-	T_{E}^+	T_{mean}^+	T_{inj}	τ_{rms}
R1	0.12	0.034	0.6	0.12	0.34	0.028	0.27	0.042
R2	0.11	0.027	0.4	0.15	0.28	0.042	0.22	0.071
R3	10.8	1.89	20.0	9.9	14.28	1.81	20	3.74
R4	7.34	2.97	33.3	12.5	25.0	2.52	30.2	5.63

Table 6.2: Time scales for our runs R1-4: $T_{\mathrm{eddy}} \equiv [\pi \sum_k (E(k)/k)/(2u_{rms}^2)]$, the eddy turn-over time and $T_\eta \equiv \sqrt{\nu/\varepsilon}$ the Kolmogorov time scale. The tail of the PDF of the persistence time in the Eulerian framework in strain-dominated regions behaves as $P_E^-(\tau) = \exp(-t/T_{\mathrm{E}}^-)$, and its Lagrangian analogue as $P_L^-(\tau) = \exp(-t/T_{\mathrm{L}}^-)$. The tail of the PDF of the persistence time in the Eulerian framework in regions of vorticity behaves as $P_E^+(\tau) = \exp(-t/T_{\mathrm{E}}^+)$. The decay rates T_{E}^-, T_{L}^-, and T_{E}^+ for different runs are as shown in the table above. T_{mean}^+ is the average time spent by a Lagrangian particle in a vortical region, $T_{inj} \equiv (l_{inj}^2/E_{inj})^{2/3}$ is the energy-injection time scale, where $E_{inj} = <\mathbf{f} \cdot \mathbf{u}>$ is the energy injection rate and $l_{inj} = 2\pi/k_{inj}$ is the energy-injection length scale, and τ_{rms} is the root-mean-square value of τ. We do not use data for the first $T_{\mathrm{tran}} = 100T_{\mathrm{eddy}}$ times to remove transients. We use a square simulation domain with side $L = 2\pi$, grid spacing $\delta_x = L/N$, area A, and boundary ∂A.

6.3.1 Persistence times

In this Subsection we study the persistence PDFs in both Eulerian and Lagrangian frameworks. The persistence PDFs P_{E}^+ and P_{E}^- in the Eulerian framework for our runs $\mathrm{R}1 - 4$, along with the corresponding fits, are shown in Figs. 6.3, 6.4, 6.5, and 6.6. The PDFs P_{E}^+ and P_{E}^- show exponentially decaying tails for all the runs. Therefore, we can define the characteristic time scales T_{E}^+ and T_{E}^- for vortical and strain dominated regions, respectively, from these PDFs. The time-scales T_{E}^+ and T_{E}^- for our different runs are given in Table (6.2). The plots for the persistence PDF of a Lagrangian particle in a region of strain for our runs $\mathrm{R}1 - 4$ along with the fits are shown in Fig. 6.7.

The persistence PDF of a Lagrangian particle in a vortical region P_{L}^+ is very different from those discussed above and so it warrants a separate discussion. To highlight the difference between P_{L}^+ and the other PDFs, in Figs. 6.8(a)-(b) we present the log-log plots of the PDFs P_{L}^+, P_{L}^-, P_{E}^+, and P_{E}^- for our runs $\mathrm{R}2$ and $\mathrm{R}4$. We find that P_{L}^+ shows a power-law tail in contrast to the exponential tails of the PDFs for the other three cases.

Since P_{L}^+ shows the power-law behavior $P_{\mathrm{L}}^+ \sim \tau^\theta$, in what follows we study this exponent for our different runs $\mathrm{R}1 - 4$. In Fig. 6.9(a) we plot the PDF P_{L}^+ for our runs $\mathrm{R}1 - \mathrm{R}4$. On scaling τ with τ_{rms} we find that the PDFs for all the runs collapse [Fig. 6.9(b)], demonstrating that the scaling exponent θ does not depend on the parameters α, F_0, and k_{inj}. Since the exponent $\theta < -1$, a mean value of this distribution is well defined. Therefore an average lifetime of a particle in a vortex can be calculated from the PDF P_{L}^+. This average lifetime T_{mean}^+, given in Table (6.2) for different runs, is nearly equal to the Kolmogorov time scale T_η.

We follow the convention in nonequilibrium statistical mechanics [4] and call θ the persistence exponent. Let us first describe our method of getting the best estimate for θ. In general, the calcula-
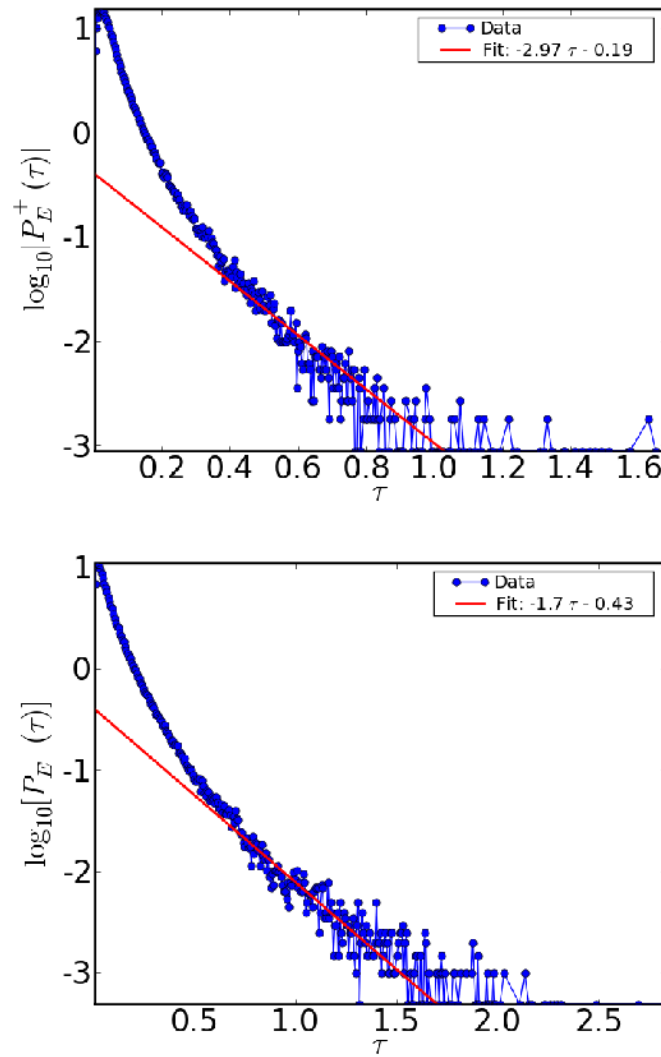
Figure 6.3: Semilog plots of the persistence PDFs: (a) P_{E}^{+} versus τ and (b) P_{E}^{-} versus τ for our run R1. The red lines indicate fits to the data.
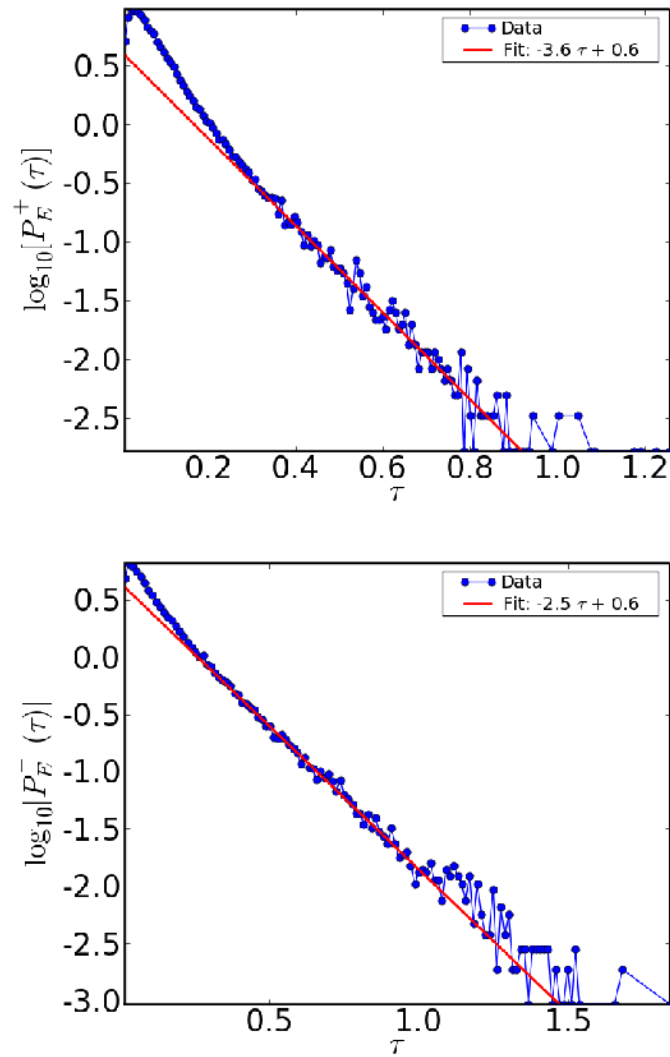
Figure 6.4: Semilog plots of the persistence PDFs: (a) P_E^+ versus τ and (b) P_E^- versus τ for our run R2. The red lines indicate fits to the data.
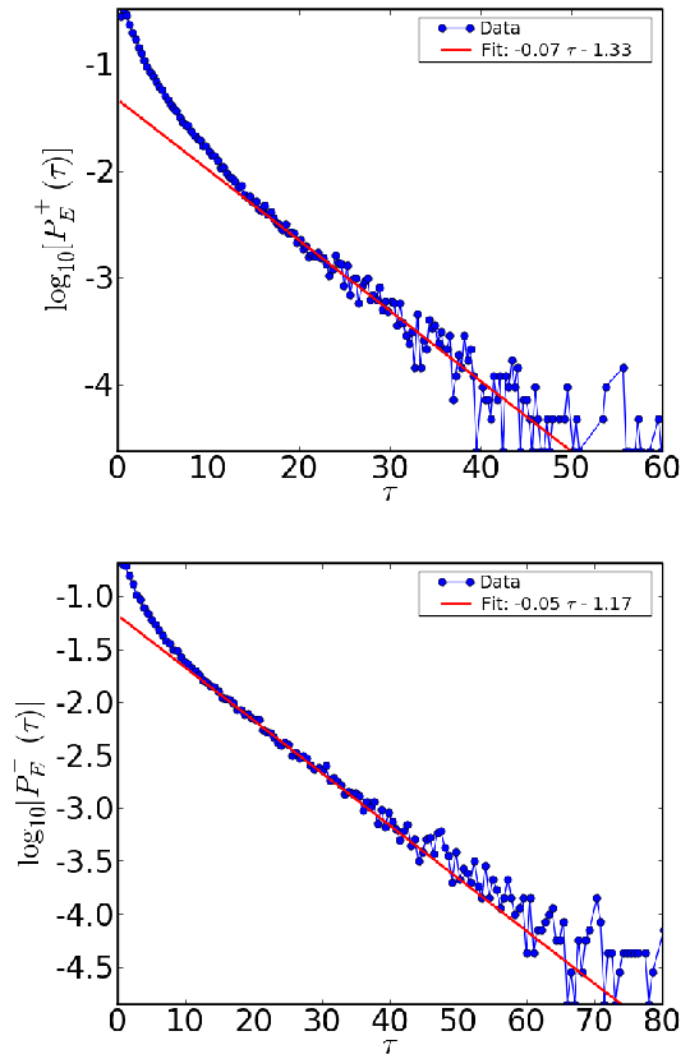
Figure 6.5: Semilog plots of the persistence PDFs: (a) P_{E}^{+} versus τ and (b) P_{E}^{-} versus τ for our run R3. The red lines indicate fits to the data.
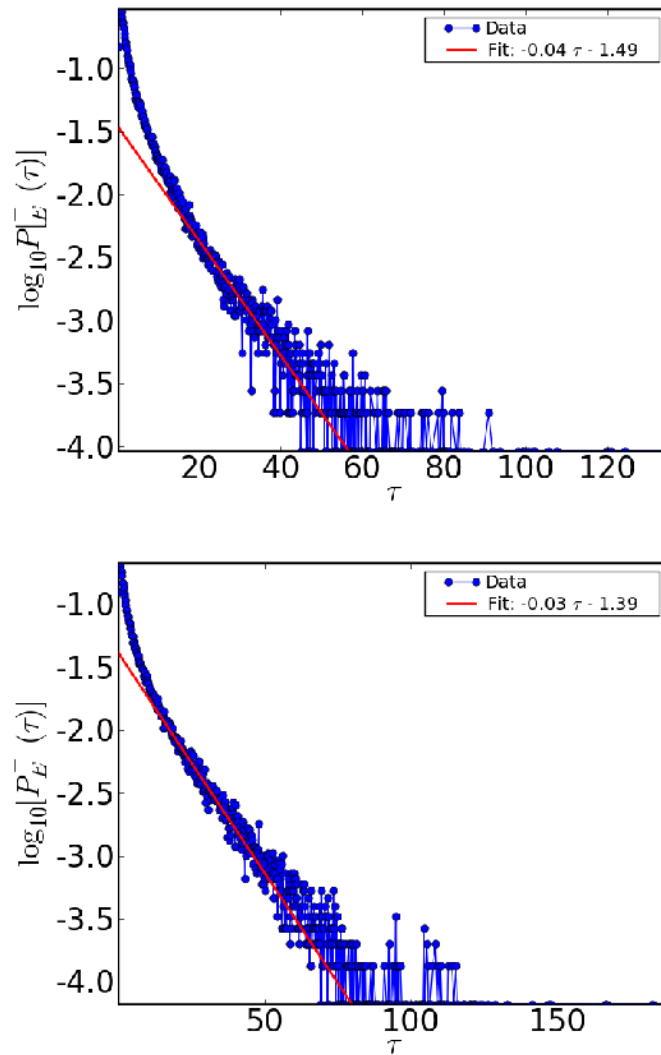
Figure 6.6: Semilog plots of the persistence PDFs: (a) P_{E}^{+} versus τ and (b) P_{E}^{-} versus τ for our run R4. The red lines indicate fits to the data.
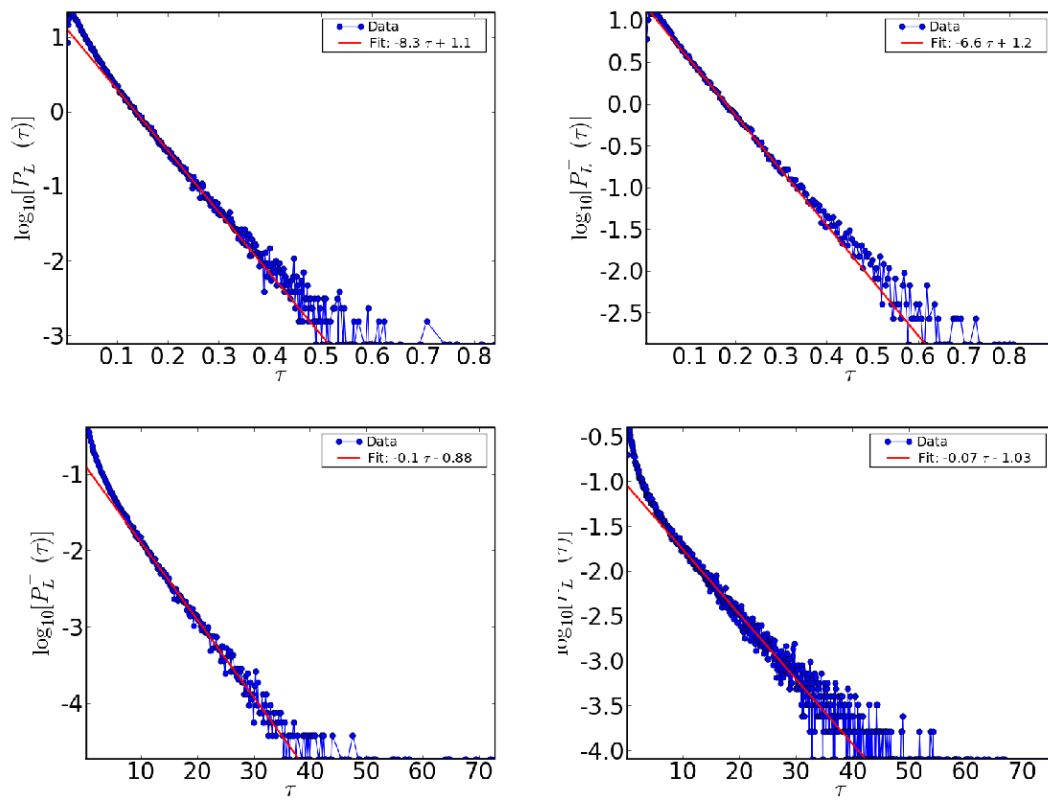
Figure 6.7: Semilog plots of the persistence PDFs for a Lagrangian particle in a region of strain for our runs: R1 (top left); R2 (top right); R3 (bottom left); R4 (bottom right). The red lines indicate fits to the data.
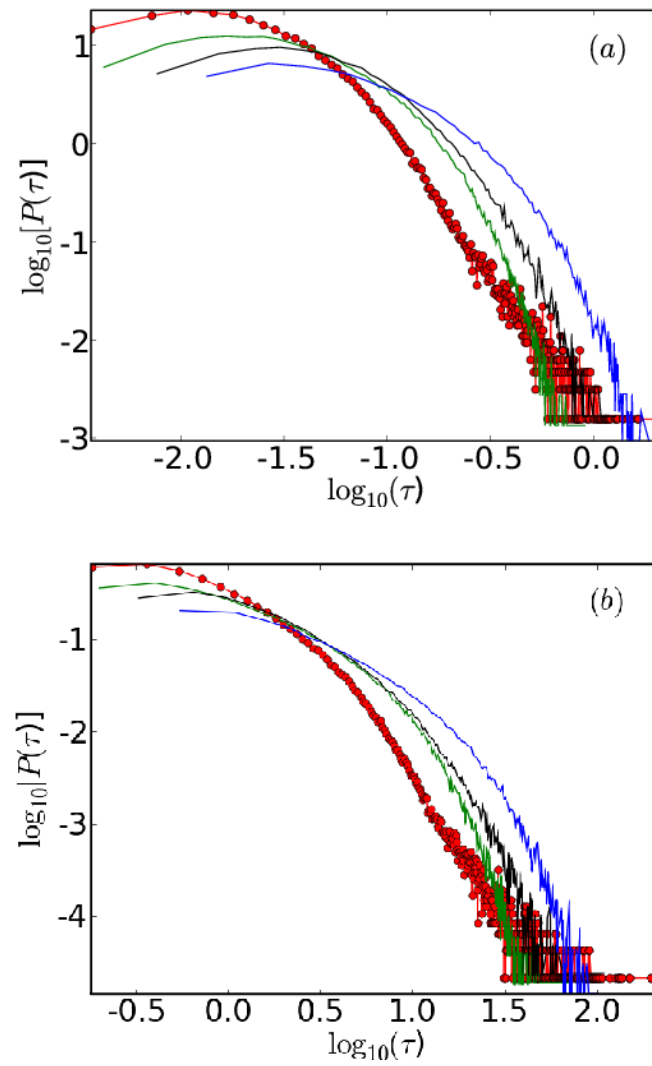
Figure 6.8: Log-log plots of the PDFs P_L^+ (red dots), P_L^- (green line), P_E^+ (black line), and P_E^- (blue line). The probability distribution function(PDF) for our runs (a) R2 and (b) R4.
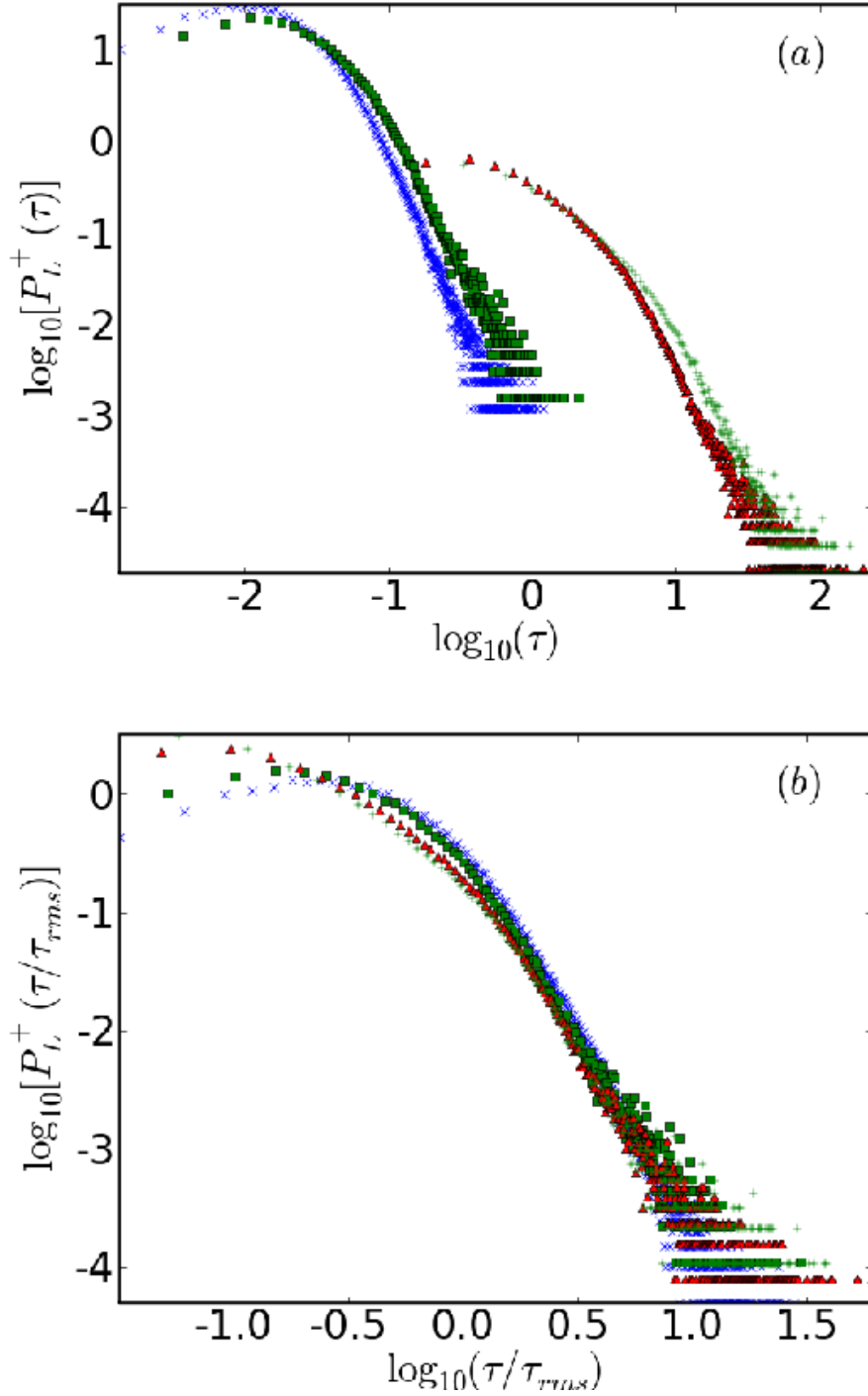
Figure 6.9: Log-log plots of (a) the PDF $P_{\mathrm{L}}^+(\tau)$ versus τ and (b) the normalized PDF $P_{\mathrm{L}}^+(\tau/\tau_{rms})$ versus τ/τ_{rms} for our runs R1 − R4; the symbols used for different runs are × (R1), ■ (R2), ▲ (R3), and + (R4). The values of τ_{rms} for different runs is given in Table 6.2.

tion of PDFs from numerical data is plagued by errors originating from the binning of the data to make histograms. Thus exponents such as θ cannot be obtained reliably from such PDFs. A reliable estimate of such an exponent can be obtained by using the rank-order method [13] to calculate the corresponding cumulative probability distribution function. A plot of the cumulative probability distribution function of the persistence time of the Lagrangian particle in a vortical region is shown, for our run R4, in Fig. 6.10. The scaling exponent $\theta + 1$ is obtained by fitting a power-law to the tail of the cumulative PDF. To find the best estimate for $\theta + 1$ we evaluate the local slope $\chi = d \log_{10} P_C(\tau) / d \log_{10}(\tau)$ in the region shown in the inset of Fig. 6.10. Our estimate for $\theta + 1$ is the average value of χ over the region indicated in the inset; and the standard deviation yields the error. Finally we obtain $\theta = -3.0 \pm 0.1$.

6.3.2   Auto-correlation of Λ

We now study how Λ is correlated over a Lagrangian particle track and at a given Eulerian point. For this we have calculated the auto-correlation function of Λ

$$C_\Lambda(t) = \langle \Lambda(0)\Lambda(t) \rangle, \tag{6.3}$$

in both the Eulerian and the Lagrangian frameworks from our simulations. Here $\langle \cdot \rangle$ denotes averaging over the origin of time and also over N_{p} different Lagrangian particles or over N_{p} different Eulerian positions. In Figure 6.11 we plot $C_\Lambda(t/T_\eta)$ versus t/T_η for our run R1. The plots from other runs are similar and are not shown here. We find that the characteristic time of decay in the Lagrangian framework is shorter than in the Eulerian framework; but they are both of the same order as the Kolmogorov time scale T_η. This provides quantitative support to the qualitative notion [14, 15] that the characteristic
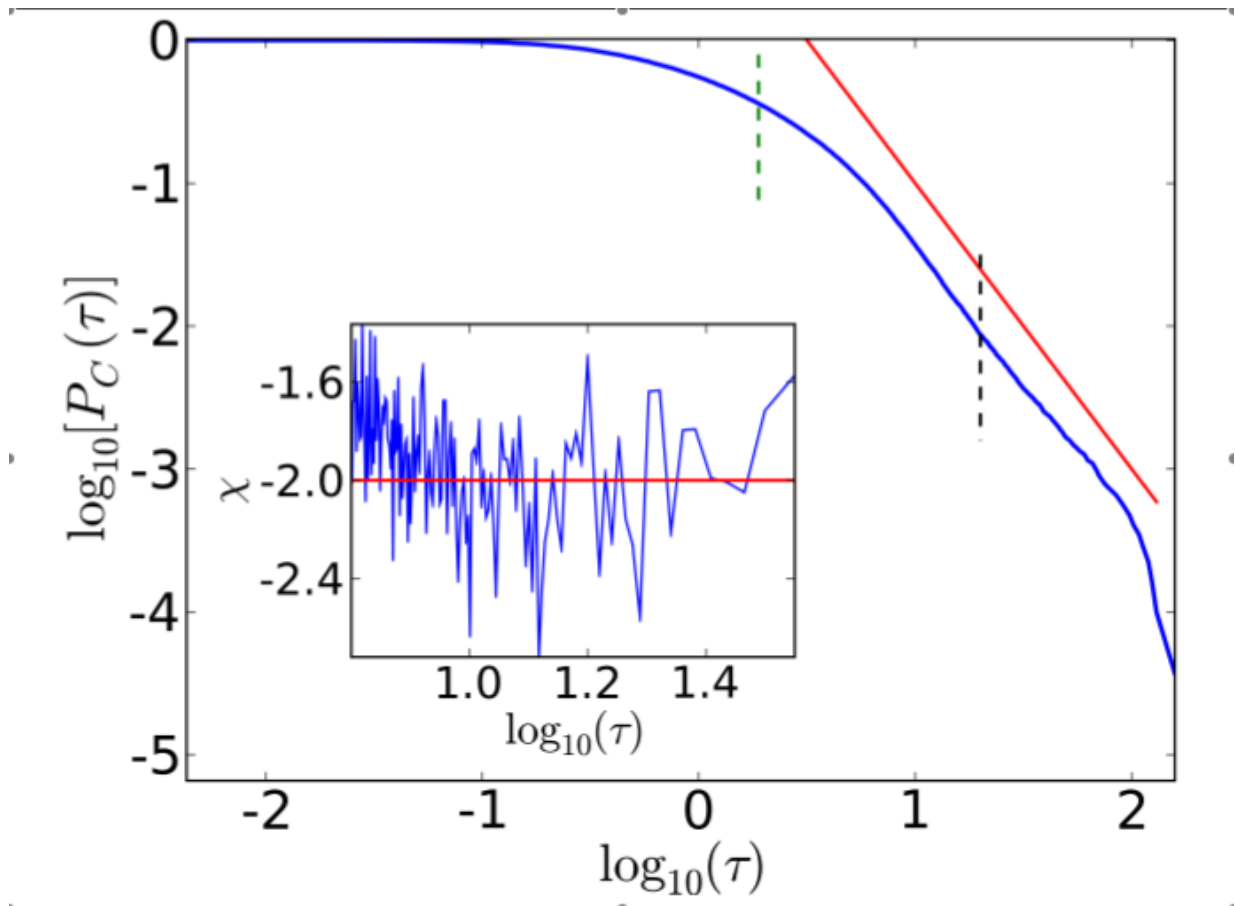
Figure 6.10: Log-log plot of the cumulative PDF $P_C(\tau)$ versus τ for our run R4. The dashed red line is drawn for reference and has a slope equal to -2; the dashed green vertical line indicates the Kolmogorov time scale; and the dashed black vertical line indicates the energy injection time scale. The inset shows the local slope $\chi = d\log_{10} P_C(\tau)/d\log_{10}(\tau)$ versus τ. The red line at $\chi = -2$ is drawn for reference.
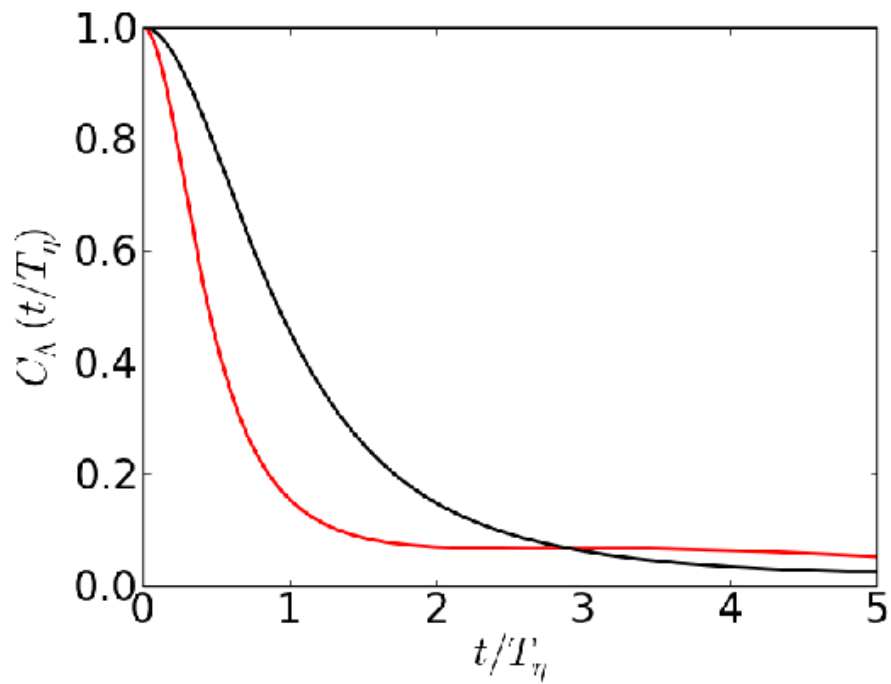
Figure 6.11: Plots of $C_\Lambda(t/T_\eta)$ versus t/T_η for our run R1. The red curve is for the Lagrangian autocorrelation and the black curve is for the Eulerian autocorrelation (see text).

lifetime of topological structures (e.g., vortices) is of the same order as the Kolmogorov time.

Different models have been proposed to study the dynamics of the velocity gradient tensor [14, 15] in three dimensions. In Ref. [15], the dynamics of the velocity gradient tensor is modelled along Lagrangian trajectories. One of the central assumptions of these models is that the velocity gradient tensor is correlated upto time T_η. Thus we now study the autocorrelation of the components of the velocity gradient tensor, namely,

$$C_{\mathrm{ij}}(t) = \langle \partial_i u_j(0) \partial_i u_j(t) \rangle, \tag{6.4}$$

where the subscripts ij indicate different components of the velocity gradient tensor. In Figs. 6.12(a), 6.12(b), and Fig. 6.12 (c) we plot the autocorrelations of C_{xx}, C_{xy}, and C_{yx}.

We find that, for $t < T_\eta$, C_{ij} remains close to unity whereas, for $t > T_\eta$, C_{ij} decays sharply like the correlation function of Λ. To the best of our knowledge this is the first time this result has been shown in a direct numerical simulation. This result can also be used as a benchmark for models in two-dimensions which study the time-evolution of the velocity gradient tensor but do not make a priori assumptions on the correlation time of the velocity gradient tensor.

6.4 Conclusions

To summarise, we have numerically calculated persistence times and autocorrelation functions for the parameter Λ in Eulerian and Lagrangian frameworks. We observe qualitatively different behaviours for the probability distribution functions for persistence times in different frames. In the Eulerian case, the PDF for residence time in vortical regions shows exponential decay whereas in the Lagrangian case it shows power law tail. Qualitatively such a nontrivial behaviour appears because of the possibility of a passive tracer particle being
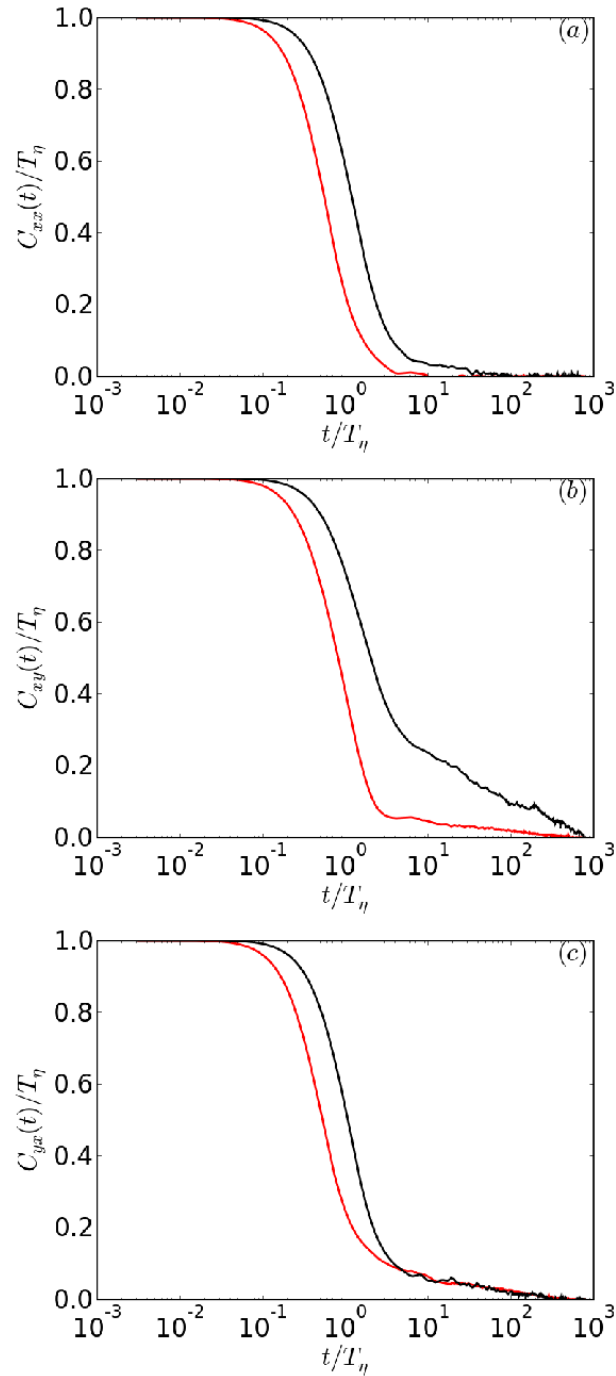
Figure 6.12: Log-lin plot of the autocorrelation functions (a) $C_{xx}(t/T_\eta)$, (b) $C_{xy}(t/T_\eta)$, and (c) $C_{yx}(t/T_\eta)$ versus t/T_η for our run R1. In all the three figures, the red curve is for the Lagrangian autocorrelation and the black curve is for the corresponding Eulerian autocorrelation.

trapped temporarily in a vortical region. Earlier studies [16] have found that passive tracer particles seldom, if at all, escape a strong vortical region, i.e., the lifetime of a particle in a vortical region is the same as the lifetime of a vortical region itself. This is not the case in our simulations as the lifetime of a vortical region, i.e., residence time in the Eulerian frame, is different from the lifetime of passive tracers in vortical region.

Appendix E

E.1 Λ at particle position

In this appendix we describe the method that is used to evaluate $\Lambda \equiv \det(A)$ at the Lagrangian particle position.

Consider the situation in which the tracer particle is at an off-grid position (x, y) as shown in Fig. E1. The neighbouring grid points of the particle are (x_i, y_j), (x_{i+1}, y_j), (x_i, y_{j+1}), and (x_{i+1}, y_{j+1}).
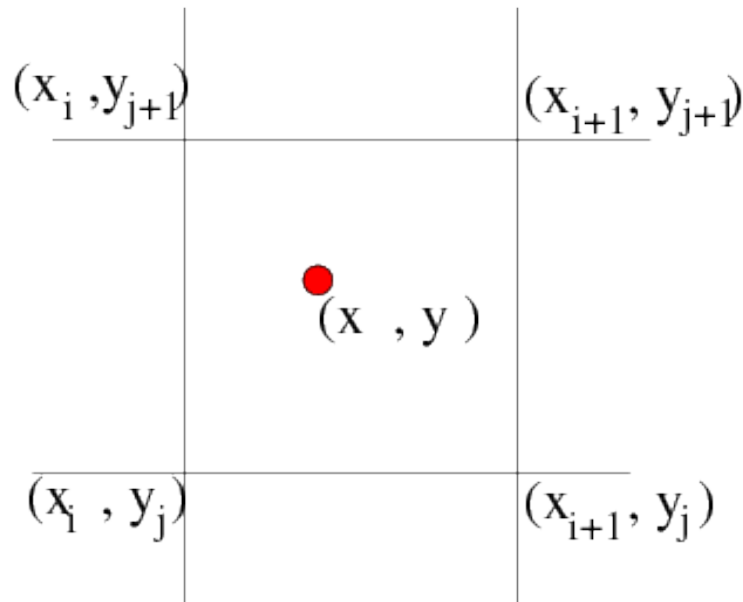
Figure E1: Sketch showing a particle (red dot) at an off-grid position (x, y). The neighbouring grid points are at (x_i, y_j), (x_{i+1}, y_j), and (x_{i+1}, y_{j+1}).

To evaluate Λ at (x, y) we first find out all the components of the velocity gradient tensor A at the neighbouring grid positions of the particle from the velocity field $\mathbf{u}$ using a second-order, centered, finite-difference (see Appendix E.2). Once A is determined at the off-grid positions, we interpolate it to the particle position (x, y) using a bilinear interpolation

$$
\begin{aligned}
A(x, y) = A(x_i, y_j) & \frac{(x_{i+1} - x)(y_{j+1} - y)}{(x_{i+1} - x_i)(y_{j+1} - y_j)} + \\
A(x_{i+1}, y_j) & \frac{(x - x_i)(y_{i+1} - y)}{(x_{i+1} - x_i)(y_{j+1} - y_j)} + \\
A(x_i, y_{j+1}) & \frac{(x_{i+1} - x)(y - y_j)}{(x_{i+1} - x_i)(y_{j+1} - y_j)} + \\
A(x_{i+1}, y_{j+1}) & \frac{(x - x_i)(y - y_j)}{(x_{i+1} - x_i)(y_{j+1} - y_j)}.
\end{aligned}
\tag{E1}
$$

Determinant of this interpolated A gives us Λ at the off-grid position.

E.2 Second order finite-difference scheme

In this appendix we describe the finite-difference scheme we use for first-derivatives.

The centered second-order explicit finite-difference approximation of the derivative of a function $f \in \mathbb{R}^1$ is:

$$
f' = (-f_{i-1} + f_{i+1})/(2\Delta x).
$$

Bibliography

[1] S. Majumdar, C. Sire, A. Bray, and S. Cornell, *Phys. Rev. Lett.* **77**, 2867 (1996).

[2] B. Derrida, V. Hakim, and R. Zeitak, *Phys. Rev. Lett.* **77**, 2871 (1995).

[3] S. Watanbe, *Proc. Symp. Pure Math.* **57**, 157 (1995).

[4] S. Majumdar, *Curr. Sci.* **77**, 370 (1999).

[5] A.E. Perry and M.S. Chong, *Annu. Rev. Fluid Mech.* **19**, 125 (1987).

[6] O. Cardoso, B. Gluckmann, O. Parcollet, and P. Tabeling, Phys. Fluids **8**, 209 (1996).

[7] P. Beyer and S. Benkadda, *Chaos* **11**, 774 (2001).

[8] S. Goto and J.C. Vassilicos, *New J. Phys.* **6**, 64 (2004).

[9] S. Goto, D.R. Osborne, J.C. Vassilicos, and J.D. Haigh, *Phys. Rev. E* **71**, 015301(R) (2005).

[10] M. Rivera, X.L. Wu, and C. Yeung, *Phys. Rev. Lett.* **87**, 044501 (2001).

[11] P. Perlekar and R. Pandit, *New J. Phys.* **11**, 073003 (2009).

[12] W. Press, B. Flannery, S. Teukolsky, and W. Vetterling, *Numerical Recipes in Fortran* (Cambridge University Press, Cambridge, 1992).

[13] D. Mitra, J. Bec, R. Pandit, and U. Frisch, *Phys. Rev. Lett.* **94**, 194501 (2005).

[14] L. Biferale, L. Chevillard, C. Meneveau, and F. Toschi, *Phys. Rev. Lett.* **98**, 214501 (2007).

[15] M. Afonso and C. Meneveau, *arXiv:0812.3891v1* (2008).

[16] C. Pasquero, A. Provenzale, and J. Weiss, *Phys. Rev. Lett.* **89**, 284501 (2002).